RICE UNIVERSITY

PRODUCTION OF JETS FROM PROTON-NUCLEUS COLLISIONS AT 400 GEV/C

by

ROBERT CHRISTOPHER MOORE

A THESIS SUBMITTED
IN PARTIAL FULFILLMENT OF THE
REQUIREMENTS FOR THE DEGREE

DOCTOR OF PHILOSOPHY

RICE

Houston, Texas

May, 1989

AAAB1882

RICE UNIVERSITY

PRODUCTION OF JETS FROM PROTON-NUCLEUS COLLISIONS AT 400 GEV/C

by

ROBERT CHRISTOPHER MOORE

A THESIS SUBMITTED
IN PARTIAL FULFILLMENT OF THE
REQUIREMENTS FOR THE DEGREE

DOCTOR OF PHILOSOPHY

APPROVED, THESIS COMMITTEE:

Marjorie D. Corcoran, Director
Associate Professor of Physics

Hannu E. Miettinen
Associate Professor of Physics

William L. Wilson Jr.
Professor of Electrical and
Computer Engineering

Houston, Texas

May, 1989

ACKNOWLEDGEMENTS

In nearly eight years of graduate school there have been many people who have guided and encouraged me along the way. My most heartfelt thanks must go to my wife Joan who will probably be even happier to have me out of graduate school than I will.

Marj Corcoran also deserves special laud; her ability to steer me in the right direction and see to the core of a problem still amazes me. The other members of the E609 collaboration deserve thanks along with the staff at Fermilab, and Bonner lab. Several people helped make the many hours spent collecting this data back in 1983 and 1984 very enjoyable, including Larry Cormell, Rod Ditzler, Jack Fleischman, and Ed Gardella. I also appreciate the friendship of Paul Pancella, Damien Gray and Nety Krishna during the long hours required to complete this thesis. John Clement deserves special thanks for tailoring the graphics program, which produced the figures in this thesis, to meet my every whim, as well as for sharing his wisdom on a wide variety of computer related problems.

The list of people who lent aid beyond the call of duty includes all of my extended family. I appreciate my Grandfather's the insights on presenting my thesis data, the computer time at Brown & Root available through my uncle Bob, and the statistics discussions with my father. Shell oil has also assisted, by donating the computer hardware used to perform the analysis and allowing me to finish the time consuming process of rewriting portions of this thesis.

I can never over emphasize the emotional support and love provided by wife as well as my mother, grandmother and mother in-law. Each of them has had to sit through esoteric discussions of what a "jet" really is as well as being told, "I am just about finished" a phrase that was voiced *years* before this final pass through the word processor.

In the final analysis, Joan takes the star position in my list of appreciated contributors. In addition to her unwavering support, her countless hours of spell checking, digitizing and baby sitting allowed this thesis to be finished before I reached retirement age!

Thanks to you too Nicole.

TABLE OF CONTENTS

LIST OF FIGURES

CROSS REFERENCE OF CHAPTER 4 FIGURES

--Variable--	Dist.	vs. ⟨Jet P_T⟩	vs. A	α vs.	Additional
⟨Jet P_T⟩	4.1A,B		4.3A	4.3B	4.13(vs. M_{jj})
⟨Jet E_T⟩	4.1C,D				
E_T of Clusters in Jets	4.32				
Event E_T		4.52A	4.52B		
Raw σ		4.2			
Planarity	4.4	4.6A	4.6B	4.8	4.5(vs. Event E_T)
R=σ(pp)/Aσ(pA)			4.7,4.9		(in Planarity bins)
R=σ(pp)/Aσ(pA) Cronin			4.10		
R=σ(pp)/Aσ(pA) Abramov			4.11		
Total # of Particles			4.12,		
# of Clusters/jet	4.53A	4.53E	4.15,4.53D	4.53B	
⟨# Clusters⟩/jet		4.14A(vs. M_{jj})	4.14B	4.21A	
# of "Particles"/jet		4.18(vs. M_{jj})	4.20		4.19(w/world Data)
⟨# Tracks⟩/jet		4.16A	4.16B	4.21B	
ω_i (angle w/jet)	4.22				
ω_i (leading cluster)		4.30A	4.30B	4.31B	
Ω (jet aperture)	4.23	4.24A	4.24B	4.31A	
$\Delta\phi_{jj}$ (angle btwn jets)	4.41A	4.41E	4.41D	4.41B	
$dN_{cluster}/d\Delta\phi$		4.29A	4.29B		4.17(vs. $\Delta\phi$)
$dE_T/d\Delta\phi$					4.26,4.27(vs. $\Delta\phi$)
$dN_{cluster}/d\Delta\eta$	4.28A				
$dE_T/d\Delta\eta$					4.25(vs. $\Delta\eta$)
η_{jets} (psuedorapidity)	4.28B				
$\theta^*_{clusters}$	4.28C				
θ^*_{jets}			4.46A		
$\Delta\theta^*_{jet}$			4.46B		
Z (momentum fraction)	4.33	4.34A,B	4.34C,D	4.35	
q_T (P_T fraction)	4.36,4.37	4.38A	4.38B	4.38C	4.39(vs. Z)
X_{jet} (E/M ratio)	4.40A	4.40E	4.40D	4.40B	
H_1	4.42A	4.42E	4.42D	4.42B	
H_2	4.43A	4.43E	4.43D	4.43B	
ΔP_{Tjj} (jet P_T imbalance)	4.44A	4.44E	4.44D	4.44B	
M_{jj} (effective jet mass)	4.45A	4.45E	4.45D	4.45B	4.13(vs. ⟨Jet P_T⟩)
Energy in calorimeters			4.47	4.50	
Ring E_T			4.48		
Ring Energy			4.49		
Unused E_T	4.51A	4.51E	4.51D	4.51B	
# Clusters in Rotated Area	4.54A	4.54E	4.54D	4.54B	
Rotated Area P_T	4.55A	4.55E	4.55D	4.55B	
Cluster Density btwn Jets	4.56A	4.56E	4.56D	4.56B	
BackGround Sub P_T	4.57A	4.57E	4.57D	4.57B	
BackGround Sub ω_{jj}	4.58A	4.58E	4.58D	4.58B	
BackGround Sub Ω	4.59A	4.59E	4.59D	4.59B	
BackGround Sub ΔP_{Tjj}	4.60A	4.60E	4.60D	4.60B	

LIST OF TABLES

CHAPTER 1

INTRODUCTION

1.1 INTRODUCTION

Quantum Chromodynamics (QCD), is widely believed to be the correct theory of strong interactions. It is a quantum field theory and analogous in many ways to QED. One important difference is that the gluons, the carriers of the color force, also carry color themselves, unlike the neutral photons which carry the electric force. It is thought that the self-interaction of the gluons leads to color confinement, a property in which "free quarks", partons removed from a color neutral particle, can not exist in nature. Examining color confinement, Bjorken [BJ073] proposed that quarks, torn free from their color neutral particles in a hard collision, should hadronize (the process of creating a jet of hadronic particles from a quark) to produce a collimated spray of daughter particles known as a jet. Because of conservation of momentum, each jet carries total momentum reflecting that of the original quark. Experimental observation of jets in collisions is taken as partial confirmation of QCD.

This thesis explores the quark-nucleon interaction by studying jets produced from a variety of atomic nuclei ranging in size from hydrogen to lead. Motivation of this study comes from several areas.

For fast, high γ particles, the nuclear radii roughly matches the expected distance that a quark travels during its fragmentation into observable particles [CHI83]. In this picture the nucleus serves as a miniature laboratory providing a tool to estimate the distance traveled by a rapidly moving quark before hadronizing. Jet production could change dramatically with nuclear size; a jet resulting from a high γ quark which escaped a small nucleus would be nearly unaffected by the nucleus while a jet resulting from a quark hadronizing within a large nucleus would experience additional intranuclear interactions (cascades). Changing nuclear targets may also affect the properties of the produced jets; quarks passing through large nuclei may experience multiple scatters, for example.

Additional motivation for studying jets from nuclei comes from experiments performed at Fermilab during 1973-1975 by Cronin *et al.* of the Chicago-Princeton collaboration [CRO73,75,KLU77,ANT79]. A proton beam incident on one of 3 nuclear targets (with atomic numbers, A, ranging from 9 to 183) triggered their experiment whenever a particle with large transverse momentum scattered at 90° in the center-of-mass and entered their spectrometer. The ratio of the nuclear target cross section over the hydrogen cross section, $\sigma(pA)/\sigma(pp)$, for the high P_T particle production is often parameterized as A^{α}. In low P_T particle production α has values near 2/3, the expected value from Glauber theory [GLA58] where all protons passing within the nuclear radius scatter, (recall that nuclear radius, r, is proportional to $A^{1/3}$, implying the area of the front face is proportional $A^{2/3}$). In lepton-nuclear collisions the production rate goes roughly as A^{1} [OSB78] indicating leptons scatter off the entire volume of nucleons

in the nucleus. For high P_T particle production α, however, takes values greater than one. Values of α over one imply that the nucleons act collectively to produce a cross section larger than the number of available scatterers; the increased probability of scattering is known either as the Cronin effect or *anomalous nuclear enhancement*. This study examines the nuclear enhancement for high P_T jet production in proton-atomic nuclei (pA) collisions.

This thesis is divided into five chapters. This chapter provides an introduction to jet production and presents the relevant background material on nuclear enhancement. The second chapter describes the Fermilab E609 experimental apparatus and the data collection while the third chapter explains the jet-finding algorithms used to extract the jets from the data. The fourth chapter contains the results of the jet-finding and discusses the jet properties as a function of jet P_T and atomic number. The final chapter draws conclusions about the hadronization length and the nuclear enhancement of jets from atomic nuclei.

1.2 A REVIEW OF QCD IN TWO PARAGRAPHS

The meson-baryon SU(3) group theory, proposed in the early 1960's by Gell-Mann, postulates that hadrons are built from smaller particles call quarks [GEL63] (mesons contain quark-antiquark pairs and baryons contain quark triplets). The physical existence of quarks became severely doubted in the mid-sixties after extensive searches for the fractional -1/3 and +2/3 quark charges proved fruitless. Electron-proton scattering at large angles, known as deep inelastic

scattering, exonerated the quark theory by proving the existence of constituents within hadrons. Electron-positron collisions provided evidence for fractional charges utilizing comparisons between hadron and lepton production rates in e^+e^- annihilation. Furthermore, the ratio of the hadron to lepton production cross section also indicated the existence of a new quantum number called color. Proton-proton scattering at large angles also indicated structure existed inside hadrons since the high P_T cross section falls much more slowly than the total inelastic inclusive cross section which drops as e^{-6P_T} for lower values of P_T. The larger than expected cross section at large angles was reminiscent of Rutherford's clue that the atom had a nucleus.

Hadronic building blocks, dubbed partons by Feynman [FEY69], are now identified as quarks, antiquarks and gluons; a proton is made of three valence quarks, two up (u) quarks and one down (d) quark accompanied by a cloud of gluons ("glueing" the proton together) and the "sea" of virtual quark-antiquark pairs existing as a result of vacuum fluctuations for times shorter than the Heisenberg uncertainty limit. Explanation of the non-observation of quarks comes from Quantum Chromodynamics, a gauge field theory. In QCD, gluons mediate the "color" field, which holds hadrons together, in a similar manner to the way in which the photon transmits the electromagnetic force in Quantum Electrodynamics. Gluons, however, carry color (akin to the electric charge) and therefore interact with other gluons (unlike photons) resulting in a potential whose strength *increases* with distance between the quarks. Furthermore, free quarks never exist since the color field must always remain neutral; they are hidden by a cloud of

gluons-- explaining the non-observation of fractional charges. Quarks knocked free from a hadron however will have a signature; Bjorken [BJO73] first recognized that hard parton scatters manifest themselves as a jet of particles with momentum along the direction of the original parton and with limited momentum transverse to the jet axis. Riordan [RIO87] presents an entertaining historical overview of the events leading to the discovery of the quark.

1.3 JET PRODUCTION

Two balanced jets clearly appear in e^+e^- collisions [WOL80,-HAN82,ALT83,SHAP84]. The annihilation results in a virtual photon which in turn produces a quark anti-quark pair, described by the Feynman diagram in figure 1.1A. Each quark hadronizes into a separate jet of particles which are in turn detected by the experiment. As the center of mass energy of the collision, $\sqrt{s}$, increases the jet collimation increases roughly as $ln(s)/\sqrt{s}$; experiments with 30 GeV of available energy produce spectacular jet events [HOL83].

Hadron-hadron collisions producing particles with large quantities of transverse momentum, schematically shown in figure 1.1B, generate four jets; a pair of jets, resulting from the hard collision, carry the transverse momentum while the remaining portion of the beam and target hadrons produce spectator jets. (Because the two high P_T jets are of primary interest, this type of event is often referred to as a "di-jet" event, in spite of the existence of four separate jets in the full event. This thesis studies events with at least 2 high P_T jets and this pair of jets will often be referred to as the

Figure 1.1 Diagrams for Jet Production

A) Feynman Diagram for $e^+ + e^- \rightarrow$ Jet+Jet

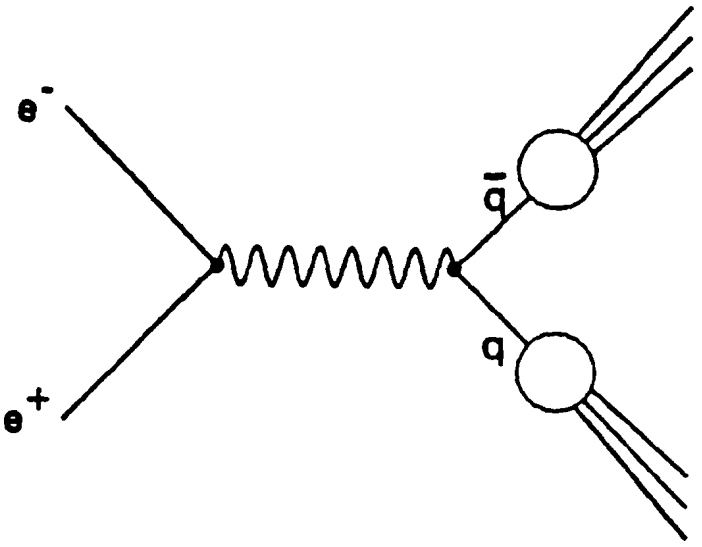

B) Schematic of p+p → 2 Hi P_T Jets + Beam Jet + Target Jet

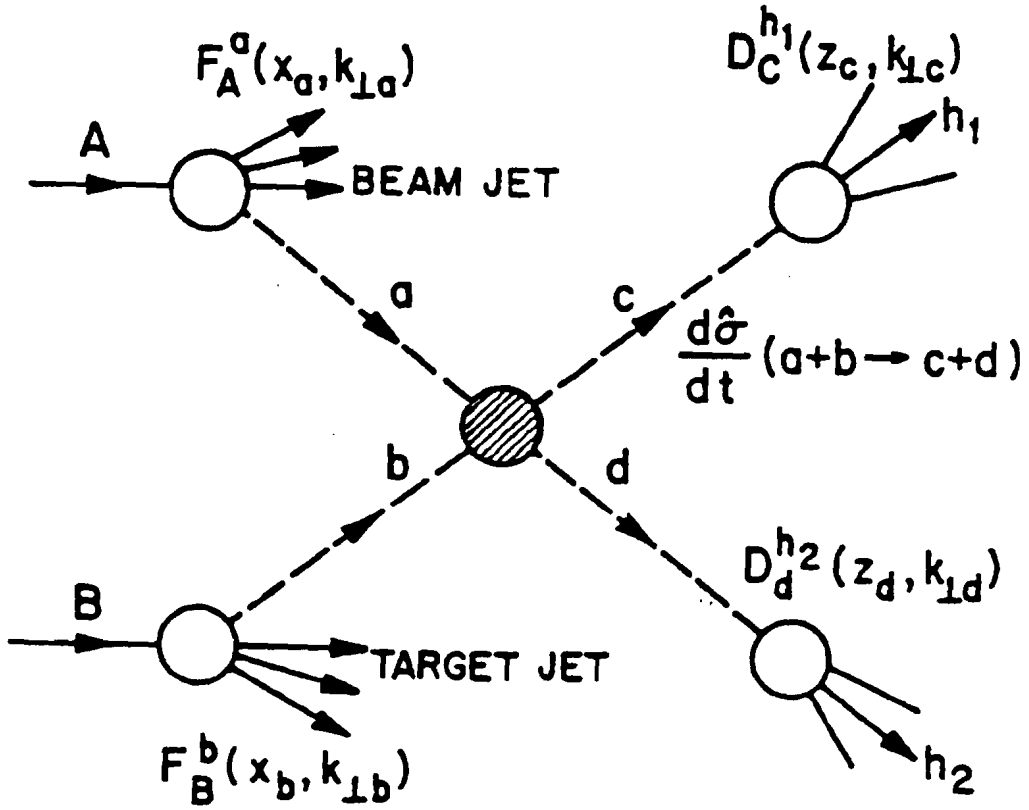

"di-jet" pair.) Substantial hadron-hadron energies are required before the high P_T jet signal dominates the transverse-energy production cross section, much higher energies than required in e^+e^- scattering. Hadron-hadron events with total E_T, the transverse energy sum of all particles in the event, below 10 GeV appear jet-like only occasionally while 99% of the produced events show clear high P_T jet properties for E_T's over 100 GeV [APP85]. (This result depends on $\sqrt{s}$ and was derived at a $\sqrt{s}$ = 630 GeV. At our beam energy, event production for total E_T's below 20 GeV/c (the range of our data) contain only a small fraction of events displaying distinct jets). The increased energy requirement results from the sharing of energy among the many nucleon constituents. The partons that undergo the hard scatters carry only a fraction of the available energy. Experimental results reported here utilized a 400 GeV proton beam on a fixed target, providing $\sqrt{s}$ = 27.4 GeV as the usable proton-proton center-of-mass energy, near the threshold for jet identification. Substantially larger $\sqrt{s}$ requires the use of colliding proton (or anti-proton) beams.

Proton-proton jet production at our threshold energies, difficult because the high P_T jet signal is mixed in with the beam and target jets, explores the lower limit of perturbative QCD. Many of the results from our experiment, E609, have been reported elsewhere [CORM85,ARE85,FLE87]. Fleischman presents a particularly lucid review of the difficulties of working at threshold energies as he traces the development of jet detectors from measurements of single particles at large angles to the advent of large solid angle calorimeters. Enhancement of the jet-like events in the data sample utilize a variety of triggers (discussed more fully in §2.3.3). Large solid

angle detectors typically use a geometrically unbiased "global" trigger, requiring the total E_T to exceed a specific threshold. At high energies ($\sqrt{s} \geq 500$ GeV, $E_T \geq 100$ GeV) this trigger effectively selects jets while at our energy the jet-like events must be extracted from the much larger sample of nearly isotropic events resulting from large-angle spectator jet fragmentation. This analysis utilizes a "two-high" event trigger which enhances the jet sample over that collected by the global trigger. The two-high trigger requires that two ~0.15 sr regions each contain E_T's above threshold (our final analysis requires 1.9 and 1.6 GeV of E_T in the triggering region). From the event sample satisfying the two-high trigger we extract jets using a jet-finding algorithm; the non-jet events passing the two-high trigger are removed by the jet-finders.

1.4 PROTON-NUCLEI COLLISIONS

High energy collisions of protons with large nuclei are practical only for fixed target experiments. (Experiments using colliding beams of α particles provide some p-nuclei information). In our experiment the various solid nuclear targets were mounted on a rotating wheel which changed positions between beam spills. Comparisons between nuclear targets remove many possible systematic errors in our experiment. The introduction to chapter 4 contains a discussion of the systematic errors.

A huge body of data exists documenting hadron-nuclear collisions ranging from cosmic ray studies to heavy-ion collisions, (Fredrikson's data review contains over a thousand references [FRE87]). Data

Figure 1.2 **Cronin's α data**

A^{α} dependence of the invariant cross section vs. P_T of the produced hadron for $\pi^{\pm}$, $K^{\pm}$, p, and $\bar{p}$ from pA collisions at 400 GeV/c [ANT79].

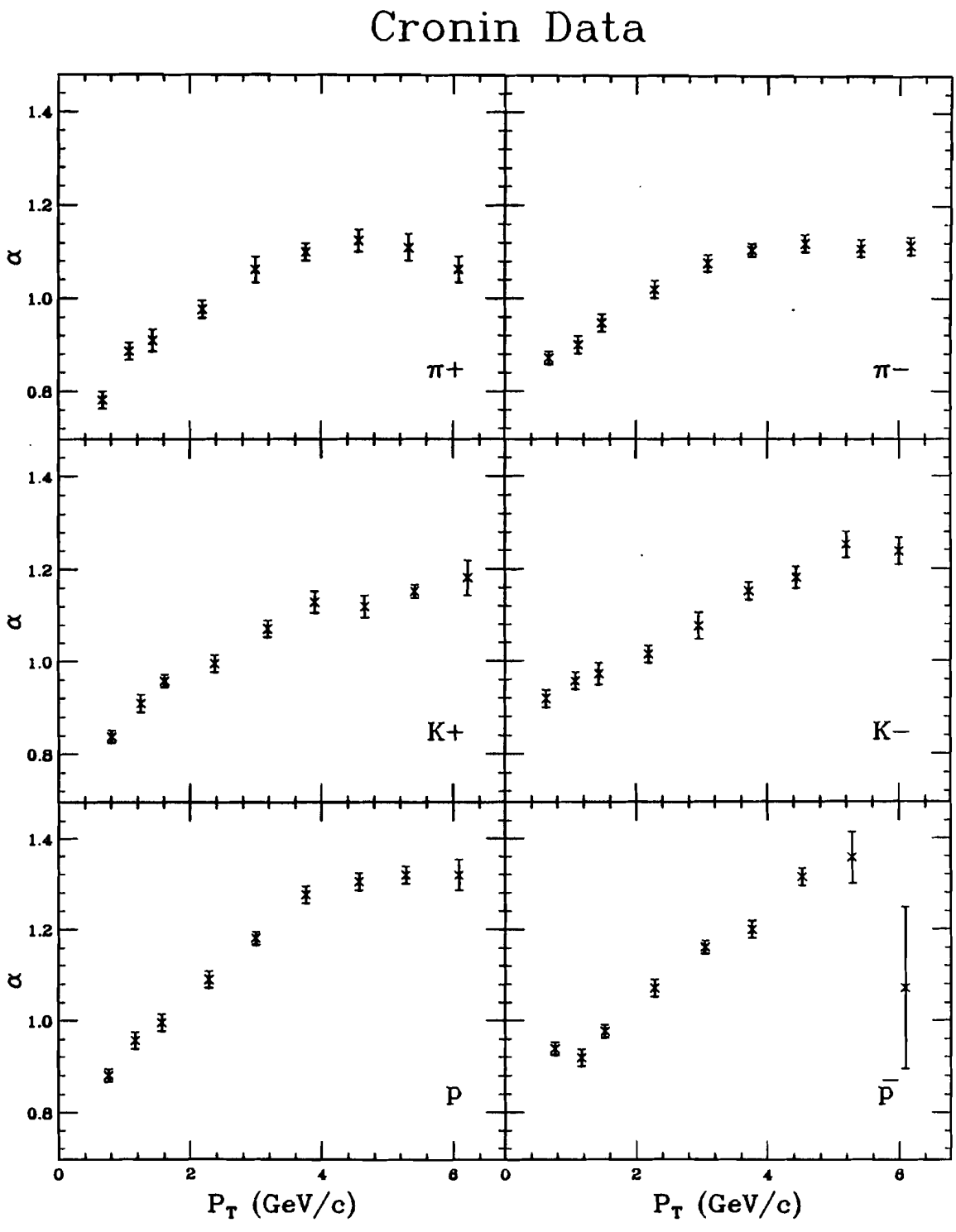

relevant to this thesis, however, finds its roots in the work of Cronin *et al.* [CRO73,75,KLU77,ANT79] and the later experiments confirming nuclear enhancement [BEC76],[GAR77],[FRI83], and [HSI85]. In these experiments the production of specific high P_T hadrons ($\pi^{\pm}$,$K^{\pm}$,p,$\bar{p}$) was studied as a function of atomic number; the slope of the $\sigma(pA)/\sigma(pp)$ ratio was found to increase with particle P_T from α = 0.8 to 1.2, see figure 1.2. Two other experiments, Fermilab E260 [BROM77,78,79a,79c,80] and Fermilab E557/E672 [BROW83,GOM86a,86c,86d,-87,STE88] studied jets from various nuclei. The earlier experiment utilized a relatively limited solid angle calorimeter while E557's calorimeter was very similar to the E609 large solid angle apparatus. Both sets of pA→Jet data will be compared with our results in chapter 4. Jet experiments at the CERN ISR collider, R110, R418, R806 and R807 [FRA82], typically record pp jets; however, data from αp and $\alpha\alpha$ collisions were also collected. They present nuclear effects without the luxury of an A^{α} fit based on more than two points. It should be noted that study of the specific jet properties as a function of α is unique to this thesis.

1.4.1 Current Understanding of pA Collisions

Several interesting points arise from the earlier data. Discussion of jets from nuclear targets for experiments before 1983 all involve the assumption that a limited solid angle calorimeter successfully measures jet properties, a valid assumption if one lets the observed properties of the "jet" be defined by the experiment.

1) The enhanced α value, implying coherent effects in the nucleus, is

not well understood by theory [ZAL85].

2) The total event multiplicity increases with **A**.

3) The value of α depends on the high P_T particle type [ANT79].

4) α is higher for "jet" production than it is for single particle production and is much larger than one [BROM79]. (Again recall that this experiment involved a limited solid angle detector and their definition of a "jet" was all particles hitting their detector).

5) The value of α depends on the trigger used to select the events.

6) The produced particle multiplicity density as a function of momentum along the jet, $D(Z)$, has been reported to show a strong dependence on **A** in [BROM79] and show a clear depression at the highest Z values [STE88], where $Z=(\vec{P}_{T_{particle}} \cdot \vec{P}_{T_{jet}})/|\vec{P}_{T_{particle}}|\,|\vec{P}_{T_{jet}}|$. Stewart infers that decreased $D(Z)$, for large **A** implies that the "core" of the jet vanishes with increasing **A**. Our data is consistent with their data; however we arrive at a contradictory interpretations.

7) Much of the beam energy appears to be transferred to the target nucleus and does not appear in the scattering at large angles [MIE88], (an E609 result).

8) "The hadron formation time (for the high γ partons) far exceeds the transit time through the nucleus" [SZW83], implying that hadronization of this particle type occurs *outside* of the nucleus. This statement is tempered by Kisielewska [KIS84] who points out that in any frame where a quark has a small γ, such as the target rest frame, there is ample opportunity for quark hadronization and subsequent intranuclear cascade. The beam jet demonstrates this effect; as the struck target parton leaves the nucleus it is accompanied by a rapid rise in

particle density in the back scattering angles. Many of these points will be explored further in the results of this thesis.

1.4.2 Models explaining pA Nuclear Enhancement

As noted above the "true" nature of the nuclear enhancement is not well understood [ZAL85]. We follow the lead of Faessler who classifies the dozens of models explaining the nuclear enhancement in three general classes "corresponding to the three ingredients of a hard hadron-hadron interaction: (1) the structure function of the incoming hadrons in terms of partons; (2) the hard-scattering amplitude; and (3) the fragmentation or recombination of the scattered partons to physical hadrons" [FAE82]. Many of the models span the category boundaries, for example Pumplin uses additional Fermi motion coupled to multiple-scattering to explain nuclear enhancement [PUM75]. Several of these models have predictions that can be tested in jet production from nuclei.

Models in category (1) use various mechanisms which increase the parton densities in the nuclei to values higher than A times that of a single nucleon. For example, an increase in the number of partons with large Feynman x_f (the momentum fraction along the beam axis) increases the probability of collisions with a large fraction of the center-of-mass energy involved in the high P_T scatter. Similarly, an increase in the density of particles with large internal Fermi motion increases the probability of producing scatters with large transverse momentum. These models include the enhanced number of "sea" partons inside the nucleus [KRZ76], density fluctuations [LUK77], coherent

interaction of hadrons with nucleon "tubes" [BER76,KAL79], and the addition of Fermi motion to the nucleons [KÜH76,FIS75]. An example is Krzywicki's early model on the anomalous nuclear enhancement which attributed the effect to fluctuations in the partition of the total available momentum. This hypothesis relied on the enhanced number of "sea" quarks in the nucleus (enhanced over the number in a single nucleon) which share a fraction of the total momentum. The increased number of scatters generate the observed increase in the cross section for production of large transverse momentum secondaries. The explanation requires a similar effect in lepton pair production from pA collisions, if this is the true source of the nuclear enhancement. Scattering of pA to produce $\mu^+ + \mu^- + X$ [KAP78] via the Drell-Yan mechanism, however, produces A^{α} with $\alpha \simeq 1.0$. This experimental fact invalidates (at least as the complete picture) models based on density fluctuations or extra "sea" partons as the explanation of the nuclear enhancement [ZMU80a].

Category (2) concerns the hard scattering amplitude. Most of the models in this category contain roots in a low P_T scattering theory by Glauber [GLA58] based on an optical model. This theory assumes that as the parton passes through the nucleus it scatters sequentially on several nucleons, creating the appearance of anomalously high P_T [PUM75,KÜH76,FIS75,77,MIC79,ZMU80a,MCN83]. In the simplest picture, the enhancement builds as a function of the nuclear thickness, $\sim A^{1/3}$, raised to the power of the number of multiple scatters; the cross section is proportional to $A(a+bA^{1/3}+cA^{2/3}+\ldots)$ where a, b, and c are the probabilities for 1, 2, and 3 scatters of the triggering parton. Typical models include multiple scattering

with additional modifications. since the simple model fails to predict the observed α value [FAR75]. The expectation for too small an enhancement arises from the steep drop in cross section with increasing P_T (we observe the decease at a rate of $e^{-1.74P_T}$ [CORM82]); the probability of one collision is small, ergo the probability of a second collision with the same high P_T must be even smaller. McNeil uses the Glauber model in an analytic approximation to predict that α (based on multiple scattering) drops to 1.0 at high P_T's if the exponent in the cross section power-law dependence exceeds $-4.0P_T$ [MCN83]. Extensions to the multiple scattering typically include enhancement mechanisms from category (1).

A second approach in category (2), leading to a similar dependence on **A**, results from multiple partons in the projectile scattering simultaneously [LAN75,TAK79,ZMU80b,TRE80,SUK82]. These models produce an enhancement at high P_T since each collision in the pair can be "soft" while the net collision produces an apparent "hard" P_T collision. Further, these models are particularly good at describing beam and product α dependences as a function of hadron type. For example, Cronin observed a larger α in the production of K^-, p and $\bar{p}$ than he did for $\pi^{\pm}$ and K^+ [CRO77]. Concurrent scatters of three quarks could produce high P_T protons while this channel would be closed for the production of high P_T mesons, providing an explanation of the α dependence on produced hadron type. Similar logic applies to the observed beam dependencies. Multiple scattering models including only consecutive multiple scatters provide no clue as to why α depends on hadron type.

The final category (3) is Faessler's own, in which he points out that the nucleus itself could influence the hadronization process leading to enhanced jet production. "For instance, in terms of a color neutralization picture, a scattered colored quark may pick up a quark with the complementary color {which might be more numerous in higher A targets} on its way through the nucleus and leave the nucleus unhindered in such good company. [FAE82]" Capella and Krzywicki's [CAP78] low E_T model involving a "wounded" target parton which leaves behind a cloud of gluons as it departs from the nucleus may fit into this category. In this model the generated gluons interact with the other nucleons in the nucleus, producing the nuclear enhancement. Brody [BROD83], however, shows that this model works well at low E_T but fails in higher E_T regions. Krzywicki *et al.* (and later Paver *et al.*) extended the multiple scattering model in the high P_T region and include enhanced gluon density in the nucleus [KRZ79,PAV83] to achieve curves that match the data reasonably well. (Well enough to decrease the flow of new models to one every few years). Aurenche utilizes the multiple scattering combined with the produced gluons to explain the difference in the α value observed for production of high P_T p and $\bar{p}$'s and the α value seen in production of π^+ and π^- [AUR79]. (He defers comment on the difference between the K^+ and K^- α values as being too difficult a calculation to provide conclusive results).

Nearly all the multiple scattering models imply that the terms of the expansion will be positive, as the naive model assumes. Krzywicki notes however, that a priori, it is not clear whether the second term (including contributions from the geometrical shadow effect) is necessarily greater than zero [KRZ79].

1.4.3 Predictions of pA Models

Several models explaining anomalous nuclear enhancement make specific predictions, some of which the production of jets from nuclei can address. Krzywicki's [KRZ76,79,CAP78] model of gluon production in the nucleus coupled with multiple scattering as the cause of nuclear enhancement makes several predictions. 1) He expects that jets from large nuclei will be more often created from an escaping gluon than from a quark, resulting in a higher fraction of gluon jets which are characteristically softer and contain more particles. Experiments using e^+e^- collisions at center-of-mass energies similar to ours claim to see no difference in the number of particles associated with quark jets and those resulting from gluon jets. CERN collider experiments, by assuming their jets result from mostly gluons, see a different number of particles per jet and from this they infer a difference between quark and gluon jets. Our experiment lacks individual particle identification, and coupling this with the beam and target jet spread into the calorimeter we do not have a method to test this prediction. 2) Krzywicki suggests that the enhancement will grow as sea quarks and/or gluons represent more of the internal parton momentum, and 3) that the second (softer) jet will tend to follow the direction of the nucleus in the center-of-mass frame (a prediction we can test). Finally, 4) he predicts that the enhancement should vanish for interactions not involving particles from the "sea", indicating α near 1.0.

Takagi's model, where several pairs of quarks from the colliding nucleons interact [TAK79], predicts that the enhancement occurs when

the exiting quarks align to give an apparent single extra high P_T jet. The corresponding prediction for a "single arm" trigger is that the away jet will be much wider than the triggering jet. Landshoff's similar model [LAN75] goes one step further and predicts that the "fan like" away jet will be accompanied by an increased multiplicity.

Zmushko's model, also using multiple scattering from two target quarks [ZMU80b], makes several predictions. His model attributes the nuclear enhancement to two separate high P_T scatters producing overlapping jets which appear as a single jet. His comments were originally directed toward a limited solid angle jet experiment which detected only one jet [BROM79]. Zmushko explores the possibility that some of the high P_T triggers resulted when two (out of the four) high P_T jets combined to appear as a single jet. The first test of his model is to look for events displaying four high P_T jets. In general the center-of-mass energy for our experiment is too low for the clear identification of four separate jets; four jets start to overlap in our detector if they have typical widths. Three of Zmushko's predictions that our experiment can address are: 1) He predicts that α will increase as the jet P_T approaches the kinematic limit $\sqrt{s}/2$. Production of a single di-jet pair is kinematically limited before the multiple di-jet production reaches its limit -- thereby producing an enhanced α. He further states 2) that the multiplicity within both jets will grow with A and 3) that the ϕ angle separating the jets will degrade with A and with P_T since the two di-jet scenario is in effect.

Kastella recently presented a paper combining both the hard and soft scatters, with nuclear enhancement provided by the previously developed multiple scattering mechanism coupled with the additional

gluons available in the nucleus [KAS87,89]. He points out that the soft component, typically ignored in the earlier work, also effects the A dependence of the cross section through the low-x behavior of the gluon distribution.

The focus of this thesis will be to answer several questions. The first asks if our data agrees with the previously observed phenomenon. The second inquires as to what the nucleus can tell us about the hadronization length. We also inquire as to the response of the beam and target jets to increasing A and to changing di-jet properties. Finally, and most importantly, we study the nuclear enhancement in detail and look for enlightenment as to its cause. Table 1.1 list the members of the E609 experimental collaboration.

TABLE 1.1

E609 Collaboration

ARGONNE NATL. LAB.	**RICE UNIVERSITY**	**U. of PENNSYLVANIA**
M. Arenton	R.K. Clark	L. Cormel
W. Ditzler	M.D. Corcoran	M. Dris
T. Fields	K.A. Johns	J. Fleischman
G. Thomas	M.R. Marcin	E. Gardella
	H.E. Miettinen	W. Kononenko
FERMILAB	R.C. Moore	B. Robinson
M. Harrison	C.J. Naudet	W. Selove
	J.B. Roberts	G. Theodosiou
LEHIGH UNIVERSITY	S.R. Tonse	B. Yost
A. Kanofsky		
U. of MICHIGAN		**U. OF WISCONSIN**
R. Gustafson		H. Chen
		A. Erwin
		M. Hasan
		C. Kuehn
		K. Nelson
		M. Thompson
		M. Thompson

CHAPTER 2

EXPERIMENTAL SETUP

Figure 2.1: E609 Detector Plan View

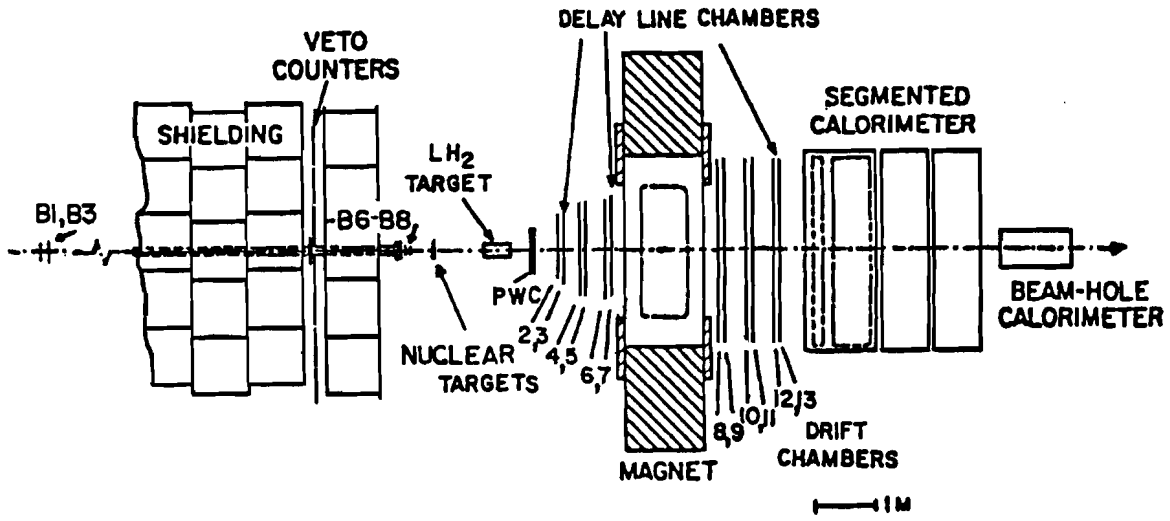

TOP VIEW OF E-609 APPARATUS

Details of the E609 detector, shown in figure 2.1, fill several volumes [JOH83,JOH85,MAR85,MOO85] however this thesis requires an additional overview of the apparatus. After initial beam definition, the detector worked in two stages, the upstream portion consisting of a series of 13 wire chambers to detect the trajectories of charged particles, and the downstream portion consisting of a pair of lead--iron-scintillator calorimeters which measured the particle energy deposition. The wire chambers combine to measure the collision vertex

location and charged particle multiplicities and flow. Ideally the chambers measure the charged particle's momentum; however chamber failure during data collection prevented momentum analysis. The calorimeters measure the total event energy, transverse energy, energy flow and, to some extent, total multiplicity. Additionally the main calorimeter labels reconstructed particles as decaying electro--magnetically or hadronically. Finally the information from the main calorimeter determines, through triggering logic, which events the computer records to magnetic tape.

The coordinate system used in describing the experiment aligns positive Z to point downstream along the beam line, positive X to the horizontal left, positive Y up, the polar angle (θ) with zero angle along the beam line, and the azimuthal angle (ϕ) with zero angle along the positive X axis. The measured polar angle depends on the reference frame; a related variable which is more tractable when changing frames is rapidity, y given by,

$$y = \frac{1}{2} \ln\left[\frac{1 + \frac{P_Z}{E}}{1 - \frac{P_Z}{E}}\right].$$

When the mass of a particle is unknown (as is the case in our experiment) rapidity can be approximated by pseudorapidity, η. Pseudorapidity, using the assumption of massless particles ($E^2 = P^2 + M^2$ becomes $E = P$ so that $P_Z/E \equiv \cos\theta$), is given by,

$$\eta = \frac{1}{2} \ln\left[\frac{1+\cos\theta}{1-\cos\theta}\right].$$

Polar angle discussions use either θ, rapidity or pseudorapidity; our

experiment, not resolving the difference between particle momentum and energy measures θ_{lab} and pseudorapidity. Our references to θ^*, the center-of-mass polar angle, contain uncertainties for particles with $E \lesssim M$.

TABLE 2.1
E609 Targets (1984 Run)

TARGET	TARGET CODE	TARGET LENGTH (cm)	ATOMIC NUMBER	DENSITY (g/cm^3)	NUMBER DENSITY $10^{23}/cm^2$	% of an Interaction length
Hydrogen	20 LH2	45.72	1.01	0.0708	19.300	6.37
Hydrogen-effective		38.00	1.01	0.0708	16.041	5.30
Helium	30 LHE	8.527	4.00	0.125	1.605	1.64
Beryllium	40 BE1	1.179	9.01	1.848	1.456	2.90
Beryllium	41 BE2	1.190	9.01	1.848	1.470	2.92
Carbon	50 C2	1.275	12.01	1.728	1.105	2.55
Carbon	51 C1	1.276	12.01	1.751	1.121	2.59
Aluminum	60 AL1	0.963	26.98	2.700	0.580	2.44
Aluminum	61 AL2	1.947	26.98	2.700	1.173	4.94
Copper	70 CU	0.358	63.54	8.960	0.304	2.38
Tin	80 SN	0.301	118.69	7.310	0.112	1.35
Lead	90 PB1B	0.178	207.19	11.35	0.059	1.04
Lead	91 PB1A	0.192	207.19	11.35	0.063	1.12
Lead	95 PB2B	0.366	207.19	11.35	0.121	2.14
Lead	96 PB2C	0.366	207.19	11.35	0.121	2.14
Lead	97 PB2A	0.368	207.19	11.35	0.121	2.15

Experiment E609 collected data during a three month run at Fermilab spanning late 1983 and early 1984 on the Meson West beam line. An incident 400 GeV/c proton beam collided with a series of targets ranging from liquid hydrogen to lead, listed in table 2.1. This table also lists for each target its length (L), atomic number (A), atomic density (ρ), number density (N=Avogadro's number$\cdot\rho\cdot$L/A),

and percent interaction length. Typical spills contained 1 to 10 million protons (often fluctuating another order of magnitude) spread over ten seconds, with one spill per minute. We collected nuclear target data at ten times lower intensities than the bulk of the hydrogen data. Vertex cuts on the hydrogen target, excluding both background and hydrogen events near the container walls, reduce the total hydrogen length by 7.7 cm. The 6% reduction in target length results from the vertex resolution (~2 cm) and the 4 hydrogen vessel walls in the beam line.

Solid nuclear targets, mounted on a wheel, were changed between each spill to reduce systematic errors. Each of the four different target wheel combinations contained both the copper and 0.96 cm aluminum targets to help monitor systematic drifts occurring between nuclear data collection runs. Comparisons between the liquid helium target and the solid nuclear targets contain systematic errors due to the larger helium background and the difference in time of data collection, allowing possible instrument drift. Helium background, estimated as 5% (see §2.2.5.1), plus the calorimeter consistency throughout the nuclear data collection imply that the systematic uncertainties between the nuclear targets fall below the statistical uncertainty. Comparisons with the hydrogen data incur similar errors, although vertex reconstruction effectively removes the background. An additional complication arises since the hydrogen target-to--calorimeter distance was a meter shorter than the nuclear target-to--calorimeter separation. We attempt to correct for this difference, which changes the calorimeter acceptance, by including θ^*'s (assuming zero mass particles) in our calculations and comparing targets in P_T

regions where all targets have similar data. A 15% hydrogen to nuclear target cross section uncertainty still remains.

2.1 BEAM DEFINITION

TABLE 2.2
Beam Telescope --Dimensions & Position
(Zero at center of LH_2 target)
(Positive Z in downstream direction)

Element	Dimensions (cm^3)	Position (meters)
B1	2.54 X 2.54 X .32	-40.
B2	10.16 X 10.16 X .32	-40.
Muon Veto	335. X 244. X 1.3	-5.
B7	15.24 X 15.24 X .64	-2.95
B6	5.08 X 5.08 X .64	-2.93
B8	15.24 X 15.24 X .64	-2.45
Nuclear Targets		-0.996
Hydrogen Target		0.000
Calorimeter (1^{st} layer)		6.063
Calorimeter (2^{nd} layer)		6.690
Calorimeter (3^{rd} layer)		7.554
Calorimeter (4^{th} layer)		8.458

Scintillation counters recorded the beam position and condition to define a usable beam particle. Two counters, B1 and B3, just downstream of the beam transport magnets, defined the initial beam. After passing through a beam pipe inside a 4.6 meter steel wall, the beam crossed another pair of counters B6 and B7 and passed though a 1.59 cm hole in counter B8. Counter B6, a thick dE/dx counter,

discriminated between one and two particles in the accelerator's radio-frequency accelerator bucket (RF bucket), while B8, used in the veto mode, eliminated particles from the beam halo. A final beam particle requirement, to help minimize the background particles created in the beam line, came from a 7 meter^2 veto counter built into the steel shielding wall. This counter, μ veto, vetoed all events containing coincidental particles which survived the traverse through the steel wall (primarily muons). In logic notation the raw-beam--trigger (RBT), the product of the above requirements, appears as

$$RBT=B1\cdot B3\cdot B6(1\text{ particle})\cdot\overline{B6(2+\text{ particles})}\cdot B7\cdot\overline{B8}\cdot\overline{\mu\text{ veto}}.$$

Table 2.2 lists the dimensions and positions of these scintillators as well as the target-to-calorimeter layer distances.

A series of four small wire chambers (Sense Wire Integrating Chambers or SWICs) monitored the average beam location during a spill. The SWICs, (positioned near the last beam transport magnet, in front of the target, in front of the main calorimeter, and behind the beam calorimeter) measured the beam centroid and recorded the beam steering through the detector. SWIC information, written to tape after each beam spill, determined any apparent transverse momentum imbalance due to an off-axis beam. Visual displays generated by the SWICs during the run allowed on-line monitoring of beam steering and indicated the beam remained consistently on axis so that off-line analysis was not necessary.

2.2 TRACK AND VERTEX RECONSTRUCTION

Track and vertex reconstruction utilize the wire chambers to record the charged particles' tracks. We use several stages of analysis to extract the charged particle multiplicities and vertex location from the raw chamber data. Our tracking algorithm combines the chamber hits to reconstruct tracks and vertices. Further refinements come through measurements of the chamber efficiencies, by way of a Monte Carlo, and the correction of these inefficiencies.

Particles resulting from a 400 GeV collision spread out at all angles in the center-of-mass reference frame. In the lab frame the particles experience a forward Lorentz boost and most particles' trajectories lie within 10° of the beam line. Our experiment utilizes this reference frame transformation in studying particles at 90° in the center-of-mass. Measurements made with modest X and Y distances from the beam cover both forward and backward scattering; 3° from the beam line in the lab corresponds to 90° in the center-of-mass frame.

Wire chambers, placed at various fixed Z positions, record charged particle trajectories using an array of vertical wires with specific X positions. The chambers detect the ionization of charged particles by presenting a gas in a region of high voltage to the particles. Charged particles traversing the gas produce ions within the gas which eventually create an electric pulse on a wire being monitored. Knowledge of which wire recorded the signal, (plus additional data manipulation described below), gives the particle's X position at the chamber's Z position. Our widest wire chambers spanned center-of-mass polar angles out to 150°. Determination of a particle's path utilizes information recorded in different chambers

joined together to reconstruct a track. Multiple reconstructed tracks combine to give the event vertex.

2.2.1 Chamber Description

The chamber array consisted of 3 proportional wire chamber planes, 3 delay-line chambers and 9 drift chambers. A detailed description of the chamber array exists in [KUE84,MOO85]; discussion here focuses on the particulars of the second E609 run. Much of the downstream half of the chamber array remained inoperable throughout the data run, rendering individual charged particle momentum analysis impossible, (out of 787 drift cells only 360 were active). This analysis utilized the seven chambers in front of the magnet and one chamber behind the magnet. Chamber positions, measured by survey and modified to optimize vertex reconstruction, appear in table 2.3, while table 2.4 lists the physical properties pertaining to the chambers.

2.2.1.1 Multi-Wire Proportional Chamber -

The first chamber, a three plane proportional wire chamber (PWC), operated well, recording over 99% of the separated particles incident upon it and producing the particles X and associated Y locations. In the analysis we assume the sum number of hits counted in all three PWC planes divided by 3,

$$\text{Charged Multiplicity} = \left(\sum_{i=1}^{3} \text{Hits in Plane}_i \right)/3$$

characterizes the event charged multiplicity (see §2.2.2 for the

TABLE 2.3
Physical Chamber Locations (1984)
(Zero at center of target)

CHAMBER		*X* shift (cm)	Z location (cm)	Rotation (rad)	Y *Shift* (cm)	*X* Size (cm)	*Y* Size (cm)
1	PWC	-.090	95.81	-.0063	1.0	62.6	35.6
2	Drift	-.175	141.29	-.0130		93.1	47.2
3	Delay	-.164	145.86	-.0064	3.15	97.4	47.2
4	Drift	-.665	185.53	-.0062		122.3	74.7
5	Drift	-.679	190.19	-.0070		128.3	74.7
6	Drift	-.247	232.16	-.0030		155.3	74.7
7	Delay	-.252	236.88	-.0056	3.5	159.7	74.7
8	Drift	.282	403.87	.0047		246.4	147.2
9	Drift	dead	dead	dead		250.4	147.2
10	Drift	.264	450.54	.0022		246.4	147.2
11	Drift	.268	456.41	.0032		250.4	147.2
12	Drift	.076	499.19	.0002		246.4	147.2
13	Delay	.054	504.55	-.0018	3.91	250.4	147.2

correction to this approximation). PWC chamber resolution depends on the wire spacing, 0.195 cm/wire, and the chamber voltage. Proper choice of chamber voltage increases the resolution. The PWC nominally detects particles crossing the chamber with a single wire; however particles crossing midway between two wires fire both wires, effectively increasing the resolution to 0.098 cm since the chamber distinguishes particle spacing at the half-wire level.

PWC chamber readout, performed sequentially over the three planes, combined any series of consecutive wires which recorded hits into a single group. The output record started with the total number

TABLE 2.4
Drift Chamber Physical Properties

	CHAMBER NAME	GAP SIZE SMALL/BIG (cm)	# of SMALL GAPS	# of CELLS	# of AMBG	Inactive region (cm)	DRIFT VEL. SMALL cm/ns	DRIFT VEL. BIG cm/ns	DELAY LINE VEL. cm/ns
1	PWC	.195cm/wire	0	86	1	1.2cm dot			
2	Drift	1.2/2.4	8	40	2	5.26	.00446	.00476	
3	Delay	1.2/2.4	8	42	4	4.05	.00387	.00536	.606
4	Drift	1.2/3.2	16	46	2	6.61	.00434	.00483	
5	Drift	1.2/3.2	16	48	2	6.01	.00447	.00478	
6	Drift	2.4/3.2	12	48	2	8.82	.00476	.00478	
7	Delay	2.4/3.2	12	50	4	5.98	.00491	.00513	.606
8	Drift	2.4/3.2	35	85	2		.00319	.00313	
9	Drift	2.4/3.2	34	86	2				
10	Drift	2.4/3.2	35	85	2		.00419	.00420	
11	Drift	2.4/3.2	34	86	2		.00426	.00418	
12	Drift	2.4/3.2	35	85	2		.00292	.00286	
13	Delay	2.4/3.2	34	86	4		.00320	.00333	.606

of groups (plus lone wire hits), followed by the mean half-wire number of each group and the number of wires within the group.

2.2.1.2 Drift and Delay Line Chambers -

The 3 pairs of drift chambers between the PWC and the momentum analysis magnet performed adequately, producing up to 6 X and 2 Y coordinates per track. Chambers downstream of the magnet were plagued with problems during the run (mainly resulting from the growth of carbon whiskers on the sense wires which eventually caused the chamber high voltage supplies to trip off because of current overloads). Only chamber 11 performed well enough to use in the track reconstruction,

adding another X coordinate. We collected field-free nuclear target data and mostly field-free hydrogen data; the algorithm excludes the rear chamber from track reconstruction whenever the tracks bent in the magnetic field.

Figure 2.2 shows the construction of cells from a drift chamber and from a delay line chamber; the wide cells lie at large θ and the narrow cells at smaller θ, roughly compensating for the change in Lorentz boost at different lab angles. Charged particles crossing a cell ionize the chamber gas and the resulting electrons drift in the high electric field and avalanche onto the sense wire. Drift chambers, working in a common stop mode, record the time difference between when the electrons strike the sense wire and when the delayed trigger signal stops the time-to-digital converters (TDCs). The minimum drift time, corresponding to a particle crossing a cell near the sense wire, results in the maximum measured TDC value, known as the T_0 value. To locate the distance from the sense wire, D, that a particle crossed a cell, one combines the recorded time T with the drift velocity V_x and the T_0 value, $D = V_x \cdot (T_0 - T)$. Recorded drift distances reflect the particle's true position within 0.05 cm. Drift chambers retain ambiguities as to which side of the sense wire the particle crossed the cell; track reconstruction determines whether the actual particle location is the wire location plus-or--minus the drift distance. LeCroy 4291 TDC's digitalized the difference between the signal arrival and the trigger signal in one nanosecond increments; these values were read by the computer using a CAMAC system.

Figure 2.2A: **Drift Cell construction**

Two sizes of drift chamber cells are shown in cross section. An incident particle would travel in the plane of the page creating ions in the region between the two planes of field shaping wires. The direction of the drift is limited by the 4.0 mm wire strips separating various cells. Particles at equal distances to the right and left of the sense wire produce identical drift times. Recorded information does not distinguish between these possibilities.

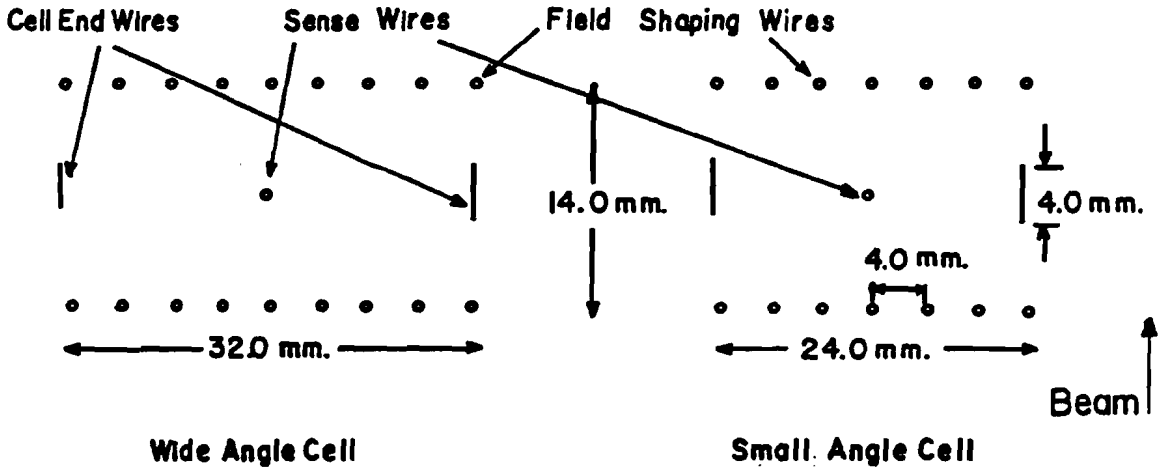

Figure 2.2: **Delay Line Cell construction**

Two sizes of delay line cells are shown in cross section. The delay line carries an induced pulse which is read at both ends. Particles passing within 2.0 mm of a sense wire produce 4 ambiguities.

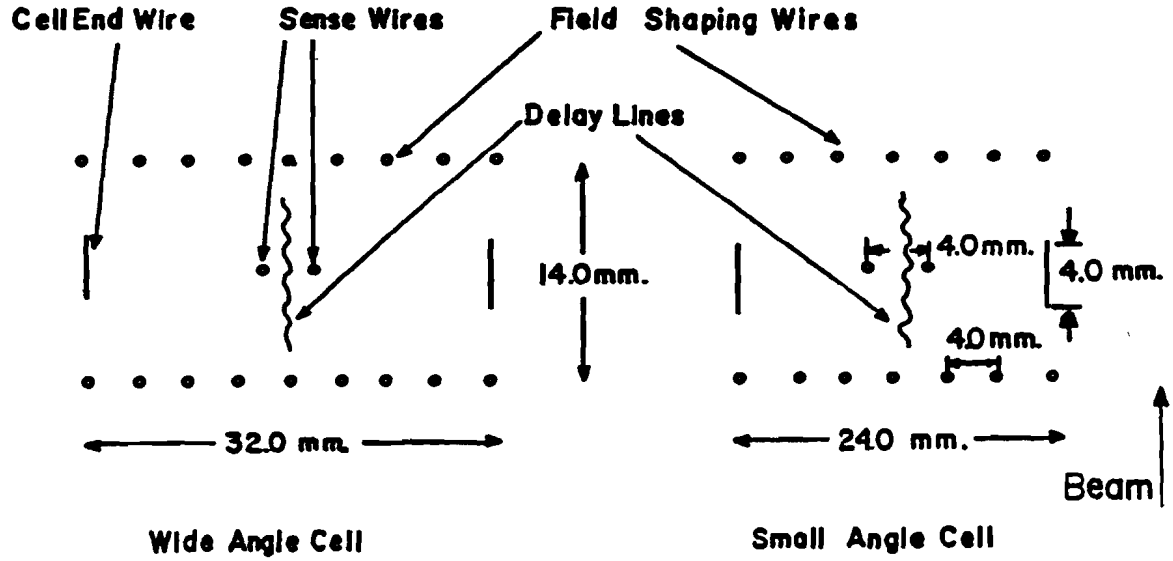

Drift chambers determine only the particles' X location, (and that with an ambiguity); determination of the particle's Y position by the delay line chambers depends on the time difference separating the signal arrival at the top and bottom of the sense wire. In practice, one adds a delay line to a drift chamber cell (with an effective thirty fold increase in length) to amplify the time difference. Electrons, resulting from a particle ionizing the chamber gas, drift toward the closest of the two sense wires sandwiched around the delay line and generate an electric pulse on the wire by avalanching. An image pulse, created in the delay line, propagates up and down the length of the line to where it is amplified, discriminated and recorded by a TDC, producing a pair of times for each particle. Averaging the time values gives the particle's X location (with up to 4 ambiguities) while the time difference unambiguously gives the particle's Y location. The one nanosecond TDC time increments set the Y resolution; the rapid signal speed along the delay line limits the Y determination to ±0.5 cm.

Parameters used to reconstruct hit locations (T_0 and V_x) depend strongly upon the applied chamber high voltage, which varied throughout the 1984 run depending upon beam intensity, incident particle flux, and chamber condition. Figure 2.3 displays a typical TDC time distribution for one of the drift chamber cells. Calculation of T_0 comes from the maximum recorded time (except for a background from chamber noise, see appendix B.2); a straight line fit to the right hand edge of the distribution gives a good T_0 estimate. Drift velocity is given by the difference between the maximum and minimum recorded times over the maximum drift distance. Fitting the left edge

Figure 2.3: **Raw Drift Chamber TDC Time Distribution**

The T_0 value is the shortest drift distance, (longest recorded TDC time) and the T_{max} value is the time required to drift from the edge of the cell to the sense wire at the cells center.

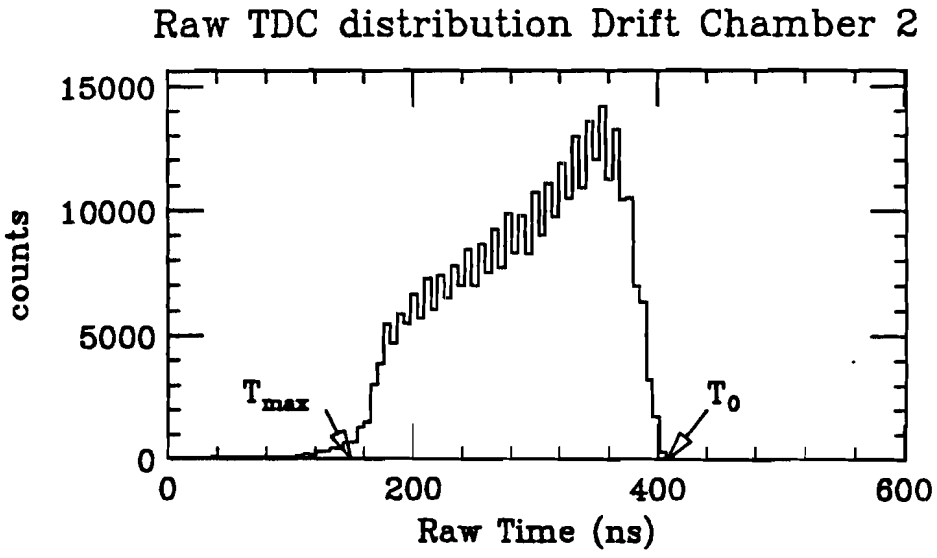

of the time distribution gives a reasonable value for the minimum recorded time, while the drift distance is half the cell size (less the sense wire-to-delay line distance for the chambers with delay lines). Averaged over 15 different time periods during the run, table 2.5 shows the cell drift velocities, T_0 values and their standard deviations; the size of the deviation gives an indication of the chamber stability over the run.

Estimation of chamber efficiency, not measured directly, requires use of the tracking algorithm (discussed in §2.2.4) to infer the chamber operation during the run. A set of isolated tracks were selected from the reconstructed data sample. Excluding the chamber in question during track reconstruction, the chamber's efficiency is

TABLE 2.5
Drift Chamber Drift Velocities and T_0's

CHAMBER NAME	DRIFT VELOCITY SMALL CELLS (cm/ms)	DRIFT VELOCITY BIG CELLS (cm/ms)	T_0 SMALL CELLS (ns)	T_0 BIG CELLS (ns)
2 Drift	4.48±.05	4.82±.03	402.1±0.7	301.1±0.7
3 Delay	3.84±.05	5.45±.03	419.7±0.5	290.3±1.6
4 Drift	4.32±.03	4.93±.03	481.0±0.4	299.8±1.7
5 Drift	4.45±.03	4.87±.03	481.4±0.3	300.0±1.4
6 Drift	4.75±.03	4.83±.04	475.9±0.4	400.9±2.0
7 Delay	4.91±.00	5.21±.00	587.7±1.8	525.9±3.5
8 Drift	4.33±.08	4.30±.04	474.6±0.5	399.2±1.0
9 Drift	dead	dead	dead	dead
10 Drift	4.15±.04	4.21±.08	476.1±1.3	394.9±2.9
11 Drift	4.22±.03	4.19±.04	473.0±0.3	397.5±0.4
12 Drift	4.35±.03	4.31±.08	469.4±1.2	393.2±1.0
13 Delay	4.79±.11	5.07±.05	640.8±2.6	571.6±4.3

given by the ratio of number of times the chamber detected a hit which would lie on the track over the total number of tracks through the chamber. Figure 2.4 contains the result of this calculation as a function of the isolated track slopes; dotted lines in this figure correspond to an upper estimate of the chamber efficiency while the solid lines represent the lower limit. (Details are presented in appendix B.1.)

Several features stand out in figure 2.4, showing detection efficiency for the eight utilized chambers. At small slopes a gap results from the non-instrumented portion of the chambers (the constant current drawn by noninteracting beam particles disables chambers in this region). Low efficiency regions appear in some of the

Figure 2.4: Chamber Detection Efficiency

Chamber efficiency, in bins of *X* slope values, is calculated from the number of isolated track hits recorded by the chamber over the number of tracks in the bin. The dotted lines show the number of chamber hits (regardless of their inclusion on the track) over the number of tracks in the bin; this gives a hardware efficiency estimate. Chambers 1-4 are shown.

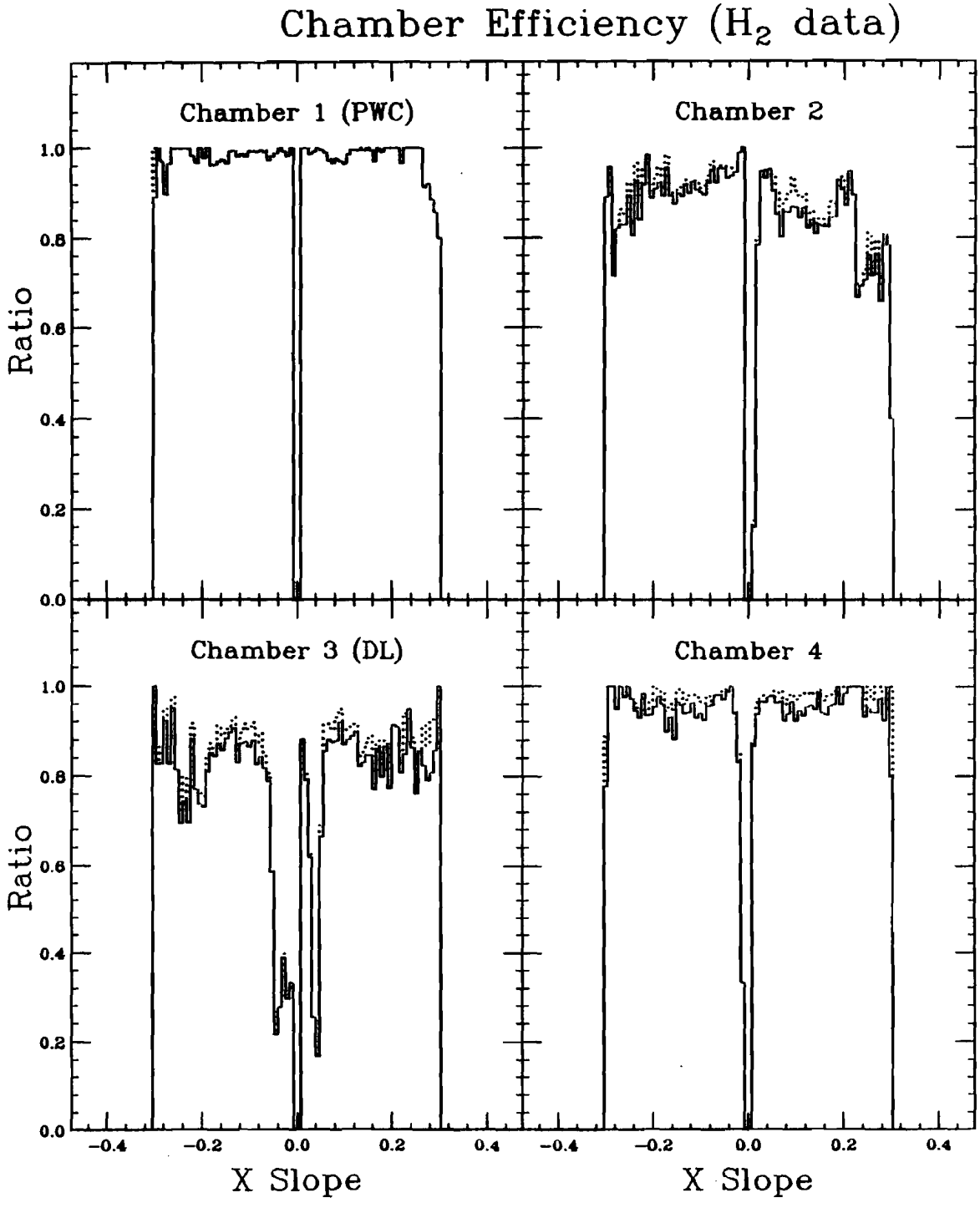

Figure 2.4: Chamber Detection Efficiency (Continued)

Efficiency of chambers 5-7 and 11 are shown. Notice the dramatic decrease in efficiency in chamber 11, the best of the chambers downstream of the momentum analysis magnet.

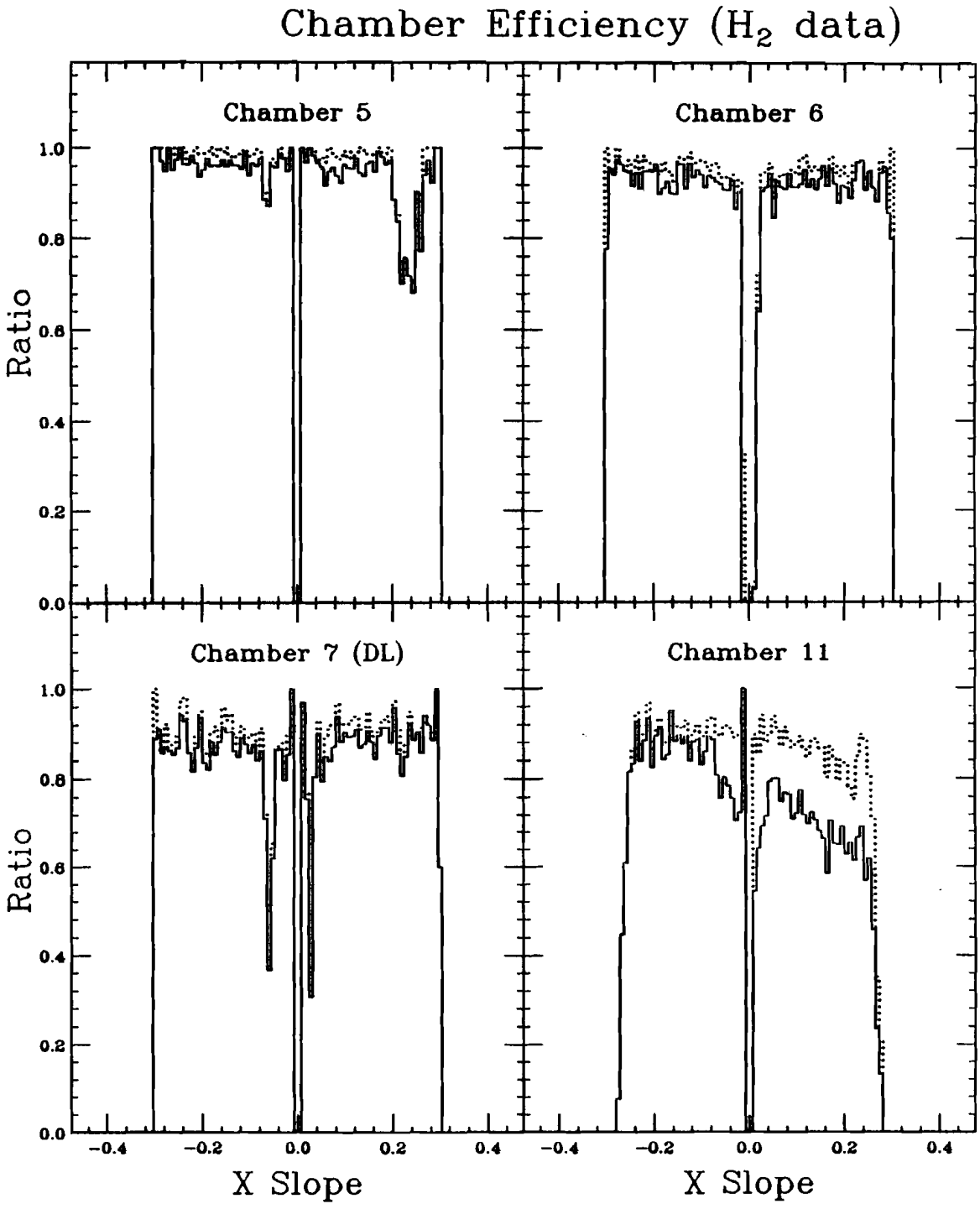

chambers, mostly occurring in delay line cells. An induced signal pulse is weaker than the direct signal pulse producing the reduced efficiency in the delay line chambers. The efficiency plot for chamber 11, the best of the downstream wire chambers, indicates how poorly these chambers operated.

2.2.2 PWC Detection Efficiency

The analysis assumes that the PWC gives a reasonable estimate of the charged multiplicity. We define charged multiplicity as the number of charged particles hitting the *drift chambers* in their active region, this excludes a central vertical gap (projecting to ~10 cm wide at the face of the calorimeter, for ϕ=0 a gap of $|\theta^*| \leq 25°$). Other than the gap and the edges above and below the calorimeter wings, the chambers match the calorimeter's acceptance.

Figure 2.4 shows the PWC detection efficiency to be nearly 100%. Inefficiencies arise from three sources: first, from a deadened area where the beam crosses the chamber's center; second, from the smaller solid angle coverage of the PWC than the other chambers; and third, the readout grouping of multiple hits on adjacent wires into an apparent single hit. Extra PWC acceptance in the gap region roughly balances these inefficiencies for typical event multiplicities of 10-15 charged particles. A Monte Carlo, simulating the chamber, indicated that the number of *hits* recorded (with the half-wire resolution) was the most accurate measure of the total event multiplicity for events recording 12 or fewer hits for the hydrogen target position and less than 15 hits for the nuclear target position (where the

Figure 2.5: **M.C. Correction to PWC Charged Particle Multiplicity**

A) Hydrogen, B)Nuclear target position: # of generated particles vs. # of recorded PWC 'hits' (+) and firing wires (*). Coefficients for the parabolic lines, solid for PWC 'hits' and dotted for firing wires, appear in table 2.5.

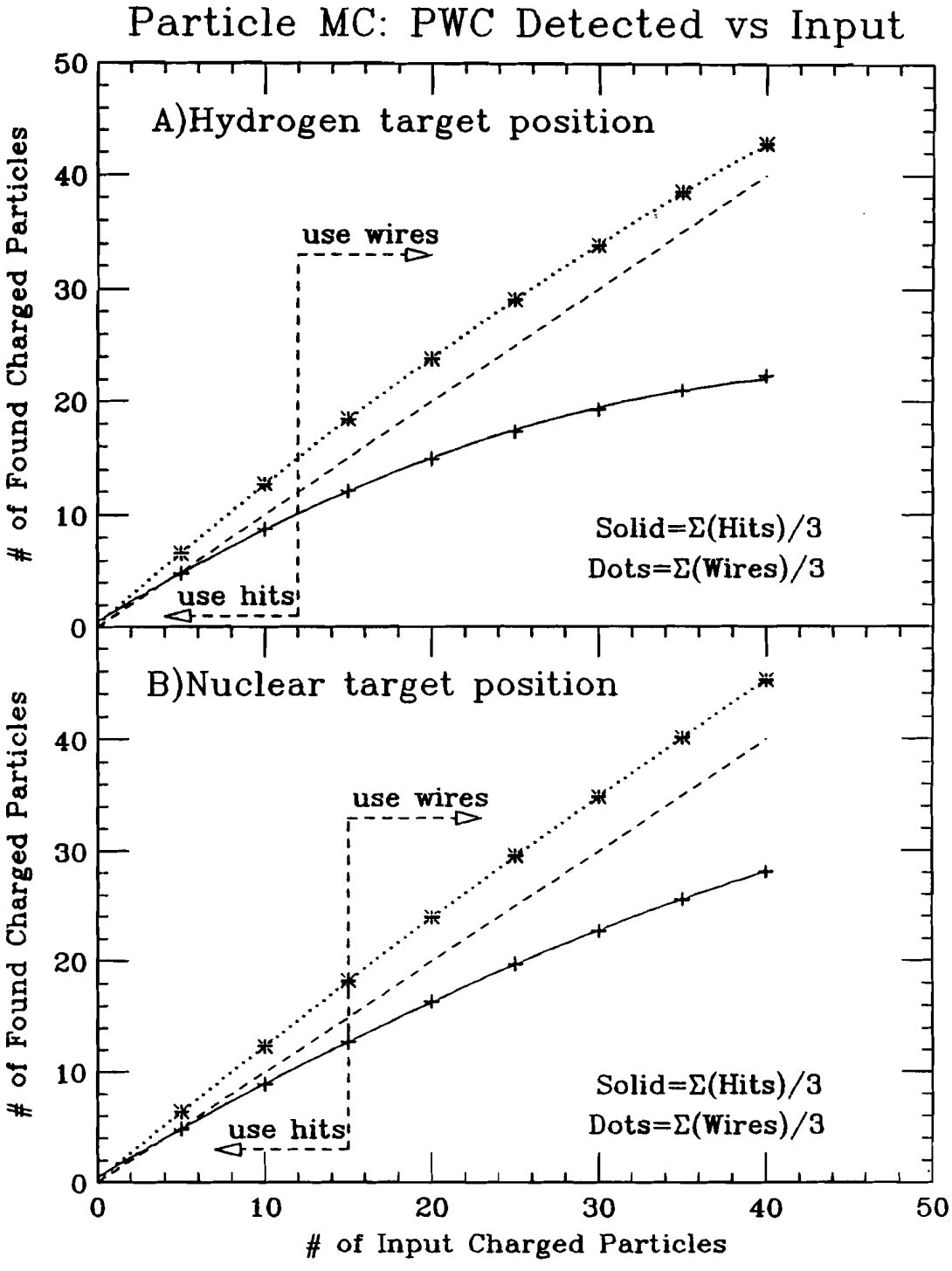

TABLE 2.6

Fit Coefficients for PWC vs. Input Hits

Fit as $A_0 \cdot + A_1 \cdot N_{recorded} + A_2 \cdot N_{recorded}^2$

If # of recorded hits is $\leq$ 12 for LH_2 (15 for nuclear targets) then:

Use $N_{recorded}$=# of recorded *hits*

If # of recorded hits is > 12 for LH_2 (15 for nuclear targets) then:

Use $N_{recorded}$=# of recorded *wires*

----------Z=0.0---------- ---------Z=-99.5----------

If # of recorded hits is $\leq$ 12 for LH_2 (15 for nuclear targets) then:

Term	Coefficients	Errors	Term	Coefficients	Errors
A_0	1.342	0.031	A_0	-0.143	0.026
A_1	0.517	0.072	A_1	1.000	0.005
A_2	0.051	0.0003	A_2	0.0015	0.0002

If # of recorded hits is > 12 for LH_2 (15 for nuclear targets) then:

Term	Coefficients	Errors	Term	Coefficients	Errors
A_0	-0.012	0.027	A_0	-0.127	0.031
A_1	0.726	0.004	A_1	0.789	0.004
A_2	0.0047	0.0001	A_2	0.0022	0.0001

particles had another meter to separate). Corrections from the observed number of hits to the generated number of hits is possible using $N_{corrected} = A_0 \cdot + A_1 \cdot N_{recorded} + A_2 \cdot N_{recorded}^2$, where A_0, A_1 and A_2 are given by fitting a polynomial to the $N_{corrected}$ versus $N_{recorded}$ plot in figures 2.5A&B. Above 12 hits for hydrogen (15 for the nuclear targets) the best measure of the total multiplicity was the number of *wires* recording hits in the PWC; displayed by the dotted lines in figures 2.5A&B. Coefficients of the 4 parabolic fits appear in table 2.6.

2.2.3 Tracking Algorithm

The tracking algorithm, extensively described in [M0085], utilizes a "search light" technique to select candidate tracks from the points recorded in the chambers. Our track reconstruction program sorts through the array of chamber hits at least six times, selecting out the best (remaining) track candidates and combining all tracks to give the most probable event vertex. Each pass through the array of hits starts with the first point in a specified (prime) chamber. The algorithm then checks the other chambers for additional points which create a line, (straight within an allowed error). Sweeping across the chambers, as a search light would, the program locates all collections of aligned hits which contain a minimum number of points and considers the collection as a candidate track. For each point in the prime chamber the sweeping search is repeated to obtain all other track candidates. Use of the linear correlation coefficient reduces the candidate tracks to the most probable set of true tracks.

Determination of the event vertex is done by considering intersections of each pair of tracks in the X-Z plane and calculating a least squares deviation for all the tracks to optimize this point. The trial vertex with the most tracks within 1.0 cm of its position and with the smallest least squares deviation is considered the true event vertex. All vertex locations with at least three tracks are used as additional points during subsequent iterations of the event track reconstruction. Due to the uncertainty in the Y hit positions, and resulting uncertainty in the Y slope, the Y information

distinguishes between tracks with similar properties in the X-Z plane but serves minimally in the track and vertex reconstruction.

Track reconstruction efficiency depends strongly on the track angle through the chambers. At low center-of-mass angles the track density saturates the chamber array, dropping the efficiency to 45 percent, while the chambers operate at 95 percent efficiency at wide angles. Corrections for reduced chamber efficiency are needed to estimate particle flows. Appendix A gives a complete description of these corrections based on a Monte Carlo simulation of the chambers. Appendix B details additional factors affecting the tracking efficiency including the chamber efficiencies, noise, delay line position errors and Monte Carlo resolution smearing.

2.2.4 Vertex Resolution

Vertex reconstruction for the hydrogen target position, best displayed using target-empty data, determines the event vertex to within ±1.5 centimeters, as is shown in figure 2.6A. A pair of target protection tent walls, two vacuum vessel walls and four target walls stand out as peaks in the Z vertex distribution of target-empty data; wall locations reconstruct to their physical locations. Vertex resolution at the helium and nuclear target positions, an additional meter upstream from the chambers, deteriorates to ±2.5 centimeters (figures 2.6D&F), arising from reduced angular separation between tracks. A two centimeter resolution in the target implies knowledge of track angles to 0.3 milliradians. Table 2.7 lists the vertex cuts

Figure 2.6: **Track Reconstructed Vertex Locations**
Events passed the 2-high hardware cut without further jet selection. **A)** lH_2 Empty Target, the beam line obstructions (in cm) are: -70 & 30=lH_2 target protection tent (dash), -35.6 & 21.5=lH_2 target vacuum windows (dot), -27.3 & 3.18 = 12" target edges, 4.45 & 19.7 = 6" target edges. **B)** Full Hydrogen target. **C)** He Empty Target, -116.3 & -82.2=He target vacuum windows (dash), -103 & -95.4=He target edges. **D)** Full Helium Target. **E)** Empty Nuclear Target wheel. **F)** Lead Target.

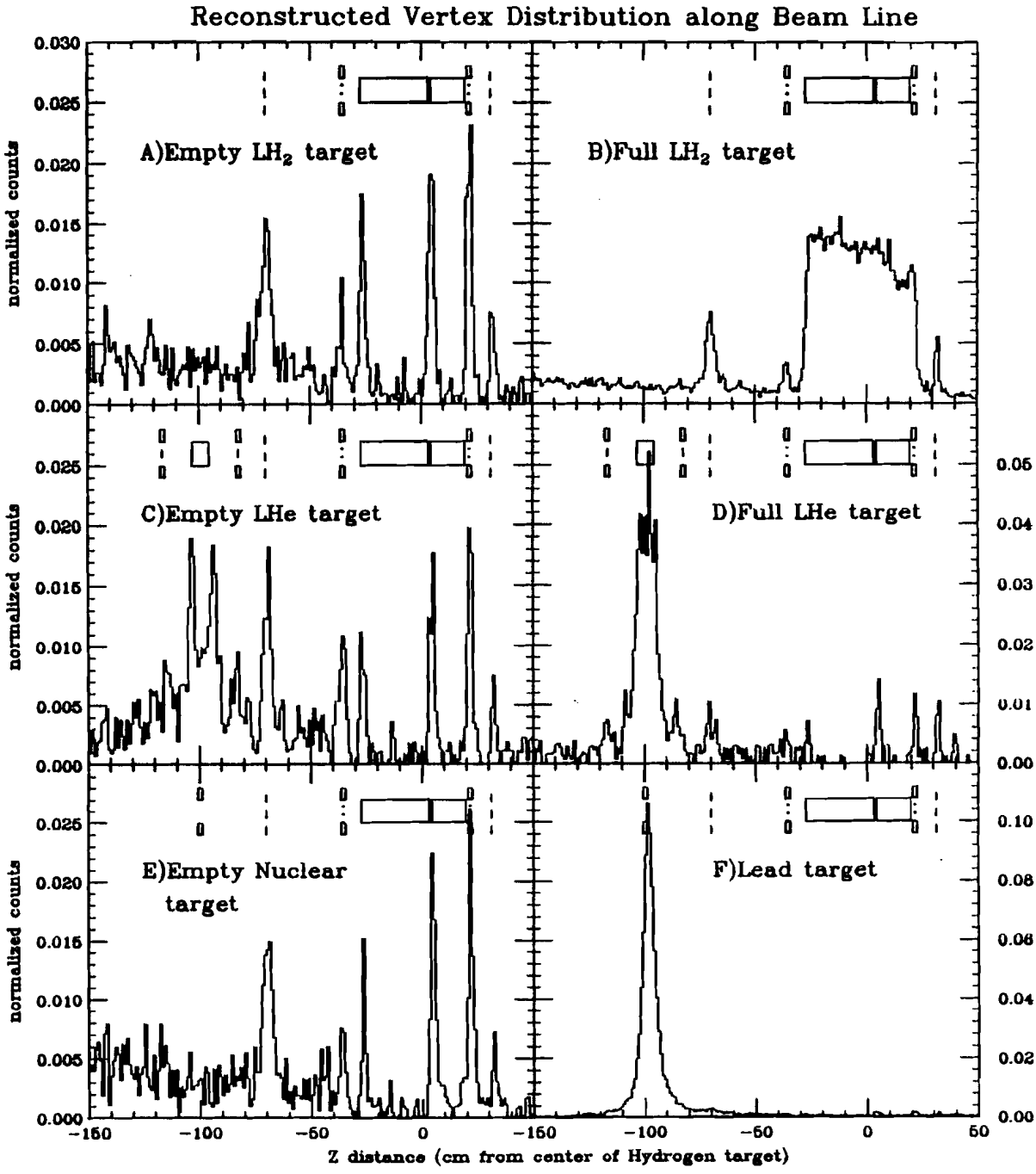

TABLE 2.7
Vertex Cuts for the Target Types

Target Type	$\|X\|$ cut (cm)	Z cut (cm)	Z cut (cm)	Z cut (cm)	Z cut (cm)
Hydrogen	2.5	-25	2	7	18
Helium	2.5	-106	-92		
Nuclear	2.5	-109	-89		

for the three target classes which reflect the decreased vertex resolution for the targets further from the chamber array.

2.2.5 Data Selection Cuts based on Tracking

Vertex information primary affects event selection; we exclude all events without a vertex in the target. Ideally our final event sample consists purely of interactions with the desired target. To measure the effectiveness of this selection one must know both the amount of impurities in the sample and fraction of useful data cut from the sample.

2.2.5.1 Background included in Event Sample -

Over the length of the hydrogen target vessel, the target-empty data contains 73 events coming from within the target container and 372 events coming from the walls giving a ratio of 19.6 ± 2.5 percent. Calculation of the ratio of the interaction length of H_2 gas over interaction length of both the H_2 gas and mylar target vessel walls gives 1.1%, implying that 6% of the events appearing in the target actually came from the gas within the target, while the other 94% come

from incorrectly vertexed events. Complete analysis on events from the empty hydrogen target runs gives an estimate of the the total background rate. Selection of events collected from empty hydrogen target data, requiring a vertex within the target and a pair of jets with <Jet P_T> of at least 4 GeV/c, leaves 7 events resulting from a corrected flux of $9.5X10^8$ beam particles. Full target runs produce 1700 pairs of high P_T jets from a corrected flux of $1.6X10^{10}$ beam particles. (See §4.1.2 for details on full target jet production). The ratio of the two production rates gives a background rate of 7.2 ± 2.6%.

Helium target background removal proves much more difficult, cutting tighter than the vertex resolution reduces the target length nearly to zero! (see figure 2.6C). Vertex cuts which include the entire target length contain 0.019 interaction lengths of helium and 0.0008 interaction lengths of the mylar walls giving an expected background rate of 4.2%. Using target-empty data to measure the number of events remaining after vertex selection gives a background rate of 11.1±4.6%.

Nuclear targets vertex cuts were chosen generously because of the low expected background rate. Figures 2.6E, showing the vertex distribution when the target wheel had its empty location in the beam, shows that 5.8% of the events lie within the 20 centimeter window for the empty tracking. Compared with the target full rates for the beryllium, the the target most likely to have significant background, the background with complete jet selection accounts for only 2.1±1.5% of the total events.

2.2.5.2 Event Fraction excluded by Tracking -

The fraction of events excluded by the vertex cuts but actually coming from hydrogen, calculated as the ratio of reduced target volume to the total volume, gives a 16.89% reduction in target length. Vertex smearing reduces this further since some events inside the target incorrectly reconstruct outside the cuts. Matching a variety of parameters, (track angles, track multiplicities, and chamber resolution) a Monte Carlo simulation of input data shows that the limited Z resolution increases the number of lost events to 17.8 ± 3.2%. (Appendix A discuss the details of this Monte Carlo). Reduction of the total target length to equal the fiducial target length corrects the cross section for the loss of hydrogen events; the loss of good events incorrectly vertexed outside the allowed fiducial target volume is balanced by the gain of hydrogen events outside the allowed target region which were incorrectly vertexed inside the allowed region. The systematic error on the hydrogen background reflects the uncertainty in the total number of *bona fide* events lost (3.2%).

Target empty subtraction at the helium target position, where both jet-finders find a pair of jets with P_T of at least 3 Gev/c (see chapter 3), shows that 19±5% of the events are reconstructed outside of the target cuts. Similarly, 10.1±1.5% of the nuclear target events lie beyond the ±10 cm cut. Figure 2.6F shows the vertex smear without the jet-finding requirements. Table 2.8 summarizes the allowed background and good event losses for the three target types.

TABLE 2.8
Target Background and Good Event losses

TARGET	BACKGROUND percent	EVENTS LOST percent
Hydrogen	7.2±2.6%	17.8±3.2% adjusted to 0.0±3.2%
Helium	11.1±4.5%	19 ±5%
Nuclear targets(Be)	2.1±1.5%	10.1±1.5%

2.3 CALORIMETER SPECIFICS

Event energy measurement utilized two calorimeters covering different regions of phase space. The main calorimeter, spanning 25°-138° in θ^* (-1.0 to +1.5 in pseudorapidity) for hydrogen and 22°-133° in θ^* (-0.8 to 1.6 in pseudorapidity for the nuclear targets, recorded particles with large transverse momentum and served as a trigger for this event type. The beam calorimeter, covering the small angle gap in the center of the main calorimeter, measured the forward energy after the collision. The two calorimeters measured most of the energy in an event, detecting all the energy except for the target jet fragments. The sum of the energy recorded by the calorimeters helps detect events with more than one proton within the ADC gate, which appear to have impossibly large lab energies.

The main calorimeter constitutes the heart of the E609 experiment. It is made of 132 towers arranged in 6 complete rings which are constructed to subtend similar center-of-mass solid angles. The calorimeter primarily measures energy; however it also distinguishes between electro-magnetic and hadronic particles. A

series of electronic modules interpret the signals from the calorimeter photomultiplier tubes and produce both a digitized energy pulse height and an analog signal corresponding to the measured transverse energy.

2.3.1 Main Calorimeter Construction

The main E609 calorimeter, shown in face view in figure 2.7, measures energy deposited in 528 modules (aligned 4 deep into 132 towers), and absorbs nearly all the energy incident upon it (containing over 5 absorbtion lengths and over 50 radiation lengths [MAR87]). Particles striking the calorimeter interact with alternating lead (or iron)-scintillator layers and emit light in proportion to their energy. Scintillation light, piped to a photomultiplier tube, creates a signal voltage which enters logic to determine an event trigger and integrating ADC's for off-line analysis.

Each tower, made of four layers, samples the shower as it develops. Showers from electro-magnetic particles [electrons, photons, π^0's, or their parents] develop quickly through bremsstrahlung and pair production; their energy deposits in the first layer (made of a lead-scintillator sandwich) and second layer (iron-scintillator sandwich). Hadronic particles, interacting with the iron nucleus, deposit a reasonable fraction of their energy in the third and fourth layers (iron-scintillator sandwiches) . Thus the ratio of energy in the first two layers over the total tower energy distinguishes between particles interacting electro-magnetically and hadronically. Enhanced calorimeter response to the numerous photons in an electro-magnetic

Figure 2.7A: **Front view of Main Calorimeter:Lab Frame**

The calorimeter consists of 3 layers in addition to the one shown. The layers grow in surface area to create towers with a roughly constant solid angle. There are 132 towers producing full center-of-mass azimuthal coverage from 30° to 120° for the hydrogen target position.

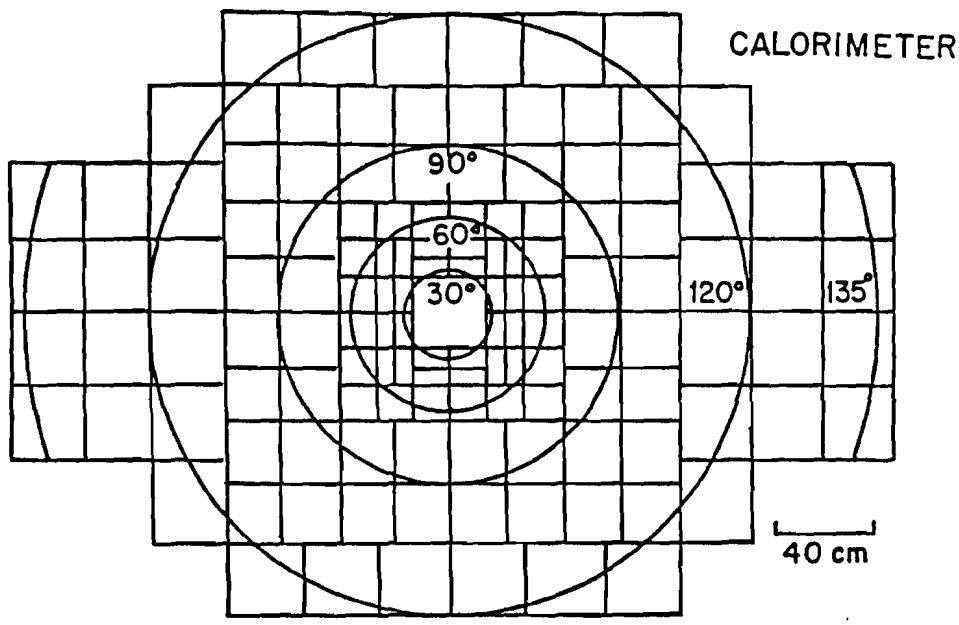

Second Layer of Segments

Figure 2.7B: **Front view of main calorimeter:Center-of-Mass Frame**

In the center-of-mass frame the calorimeter modules appear larger in the central region and smaller at wide angles, producing similar solid angle towers at all azimuths.

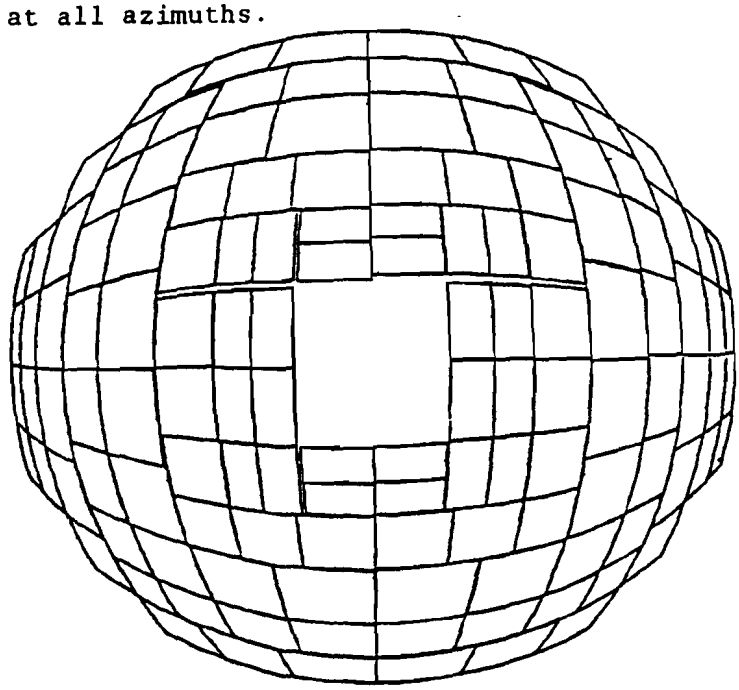

shower requires a weighting to normalize the transverse energy measurement between the shower types [FAB77]; the last two layers measure hadronic showers and are weighted 1.25 with respect to the first two layers.

Figure 2.8 illustrates the construction of one modules with its iron-scintillator sandwich structure. Sampling frequencies in the modules varied with θ^*, compensating for the reduction in energy of particles at large angles. The lead layer ranged from 5.4 to 8.8 radiation lengths while the iron layers contained 5.8 to 7.6 absorption lengths. Details of the calorimeter construction and performance appear in [YOS79,SEL79,CORM82,JOH83].

Each layer within a tower subtends a constant solid angle pointing toward the target; the modules increase in physical size with increasing distance from the target. Solid angles covered by the towers range from 0.014 sr to 0.150 sr, remaining approximately constant at a given θ^*. The limited variation in solid angle reflects an attempt to make each tower subtend the same solid angle in the proton-proton center-of-mass with a 400 GeV beam, requiring small modules (2"X4") near the beam line and larger modules (8"X8") at the edge of the calorimeter (see figure 2.7B). For the hydrogen target the towers sum to cover a total solid angle of 9.53 sr but only cover 9.16 sr for the nuclear targets which lie an additional meter from the calorimeter. The transverse energy within a tower at θ^* is given by $E_T = E_{lab} \cdot \sin \theta_{lab}$.

Figure 2.8: **Module Construction**
This figure shows the construction of an iron-scintillator calorimeter module. The notched corner accommodates the light pipe which is attached to a photomultiplier tube.

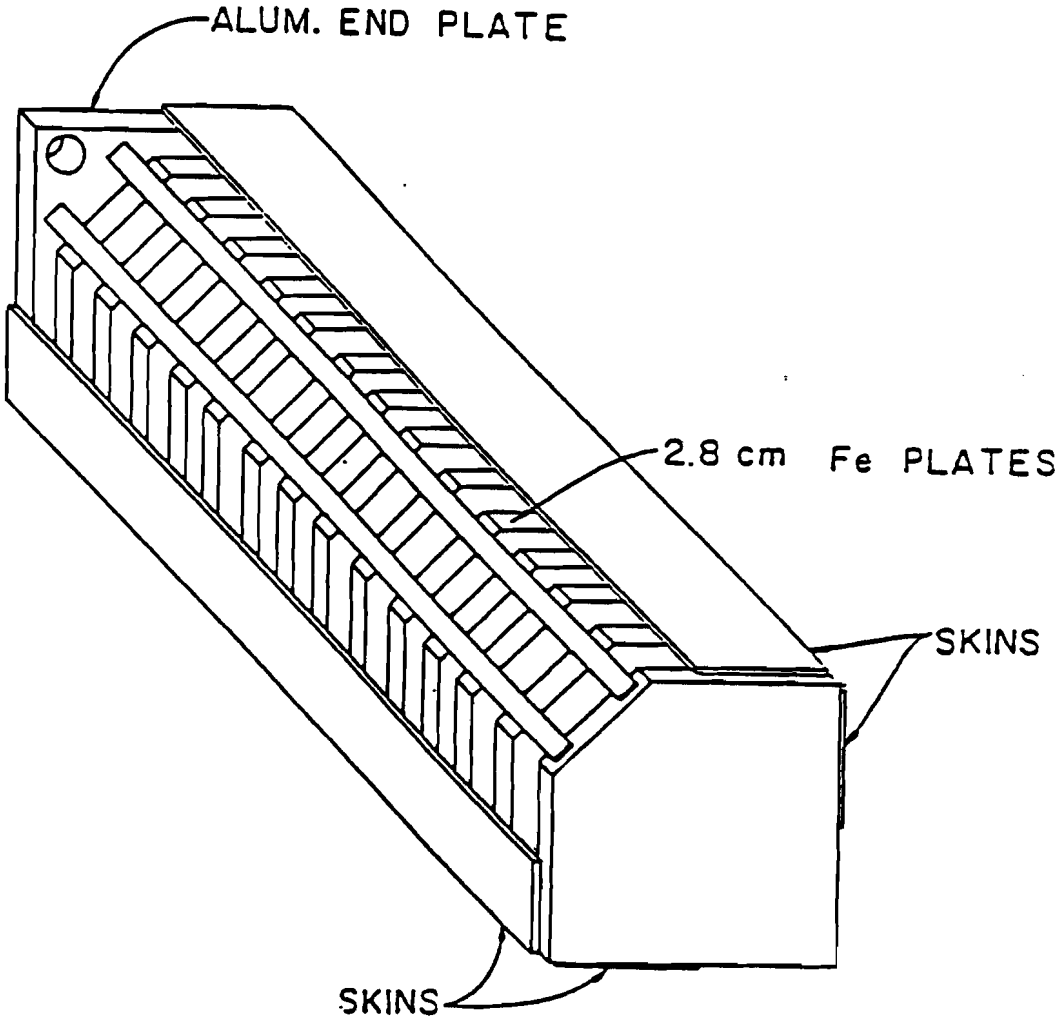

2.3.2 Main Calorimeter Electronics

For data collection, the output signal from each photomultiplier tube travels just outside the light-tight box containing the layers of segments to a two-stage calibration amplifier which increases the signal a factor of 5. (Signals recorded during muon calibration require an increase by a factor of 20). TWINAX cables carry the amplified signal to a SUMMING/WEIGHTING module where the signal branches, one branch passing unaltered to a LeCroy 2285a ADC while the other branch

joins with signals from the other modules making up a particular calorimeter tower. Before combining, the tower signals are weighted by layer, equalizing the calorimeter response to shower type, and then passed onto a fixed attenuator where the weighted tower energy is reduced by $\sin(\theta_{lab})$ to give the tower E_T. Finally the E_T signal passed into the trigger logic to identify desired events. The results of the trigger were passed to LRS ECL 4432 latching scalers which, if the trigger conditions were met, were then read by the E609 version of the FNAL standard program, MULTI, via a Jorway Parallel Branch Driver/Camac Unibus (JY411) into a PDP-11/45 for recording to 6250 BPI tape and preliminary data analysis. In addition to the latches, the computer read the digital signals from the LeCroy 2285a ADC's and the recorded drift times in LeCroy 4291 TDCs.

Two systems monitored the calorimeter's day-to-day fluctuations: LED's built into the front of each module tested the entire signal path, and a calibration pulser, simulating the expected voltage pulse, tested the electronics. Both systems interfaced with the online computer which controlled the size of the input pulse and recorded the calorimeter response. Figure 2.9 details the calorimeter electronics [ARE82].

2.3.3 Main Calorimeter Triggers

The calorimeter determines which events pass the trigger. Triggering on jet-like events often introduces undesired biases. In an attempt to minimize biases, we used three geometrically unbiased triggers, one of which is particularly rich in events reflecting the

Figure 2.9: **Electronics used for a calorimeter tower**

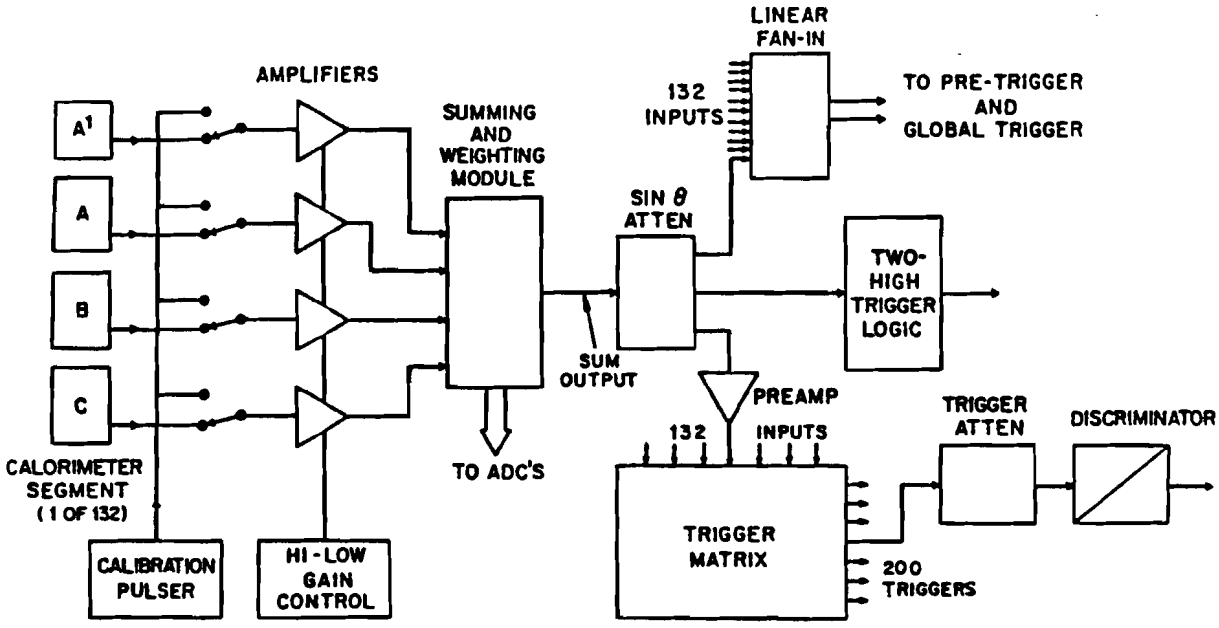

parton nature of the collisions. Global triggers, requiring the total transverse energy summed over all towers,

$$E_T = \sum_{i=1}^{132} E_i \sin(\theta_i),$$

to exceed a specific threshold, mostly produce events with high multiplicities and low planarity [DeM82]. We used two global trigger E_T thresholds, one at 17 GeV for hydrogen (16 GeV for the nuclear targets) and a pre-scaled global trigger at 12 GeV for hydrogen (10 GeV for nuclear targets). Pre-scaled data contains only one out of every 264 events passing the pre-scaled trigger, keeping the data collection from being swamped by this common event type.

The second geometrically unbiased trigger type, the "two-high" trigger, required two towers anywhere on the calorimeter to each contain E_T in excess of 1.5 GeV. The off-line analysis imposed

software thresholds of 1.9 GeV E_T on the hottest tower and 1.6 GeV on the second tower. Software E_T cuts allow comparison between all targets; the hardware trigger "turns on" much faster for the low atomic number targets than it does for the high atomic number targets. This trigger recorded events of higher planarity and lower multiplicities than the global trigger. This each portion of this trigger requires events with large concentrations of E_T in a single tower, most often satisfied by a pair of particles striking a single segment, see §4.2.3.1.

A third trigger, not designed for locating jets, required the deposition of 20 GeV of energy in the calorimeter. This "interaction" trigger accepted events without demanding high transverse energy and allowed reference to data with more typical interactions. Interaction data does not fall within the scope of this work (see [MAR89]).

The triggers introduce a variety of biases into the event sample. The two-high trigger preferentially selects particles with narrow showers, triggering more easily on particles interacting electromagnetically like the π^0, than particles with hadronic showers like the π^+ or π^-. Additionally the triggering segments have slightly different solid angles, creating symmetric regions of the calorimeter which are more likely to trigger than others. All the triggers skew the distribution near threshold requiring additional software cuts above the hardware values. The various trigger biases remain roughly constant as a function of atomic number; comparisons of cross section ratios cancel the trigger bias effects. The threshold bias requires the exclusion of all events with E_T's below the peak in the lead E_T spectrum; the spectrum with the greatest E_T peak value.

2.3.4 Main Calorimeter Calibration

Calibration of the calorimeter started with a muon beam which was steered into each module. Each photomultiplier tube voltage was adjusted until the tube gave a desired signal response. Ideal for calibration, minimum ionizing muons give a calculable signal in different types of matter, allowing standardization between module types. Further, with a nearly constant dE/dx energy loss, muons deposit energy equally in all 4 calorimeter layers, enabling calibration of modules beyond the range of other particles. Finishing touches balanced the calorimeter for the offline analysis by applying a series of gain factors, calculated from the muon data, which increase the average module energy by 2.5% with an average size ± 4% (maximum increase of 16% and a maximum decrease of 14%).

After the muon calibration, proton beams of various momenta were swept across the calorimeter face to determine the actual calorimeter energy resolution and shower size parameters. This study measured a hadron energy resolution of $70\%/\sqrt{E}$ and an electron energy resolution of $35\%/\sqrt{E}$. Because the protons deposit 10 to 20 times more energy in the towers than the muons (which deposit ~500 MeV), photomultiplier signals, amplified 10 times during data collection, were increased an additional factor of twenty during muon calibration. In spite of the care taken while balancing the calorimeter with muons, symmetric modules produce unbalanced E_T's when averaged over a run. Inaccurate gain ratios in the calibration amplifiers, giving ratios only *around* 20, provide a consistent explanation of this effect. Module rebalancing requires a second set of gain factors to adjust the

recorded ADC values. The additional gain factors do not change *total* average energy while the average *modules* energy changes by ±13%. The two worst "hot" modules require over a 100% decrease in energy (without correction these modules skew the energy distribution) while several modules require up to 76% more energy. Vector sums of the event transverse energy consistently point to the left of the calorimeter. Tower energies, resulting from the sum of four modules, typically change 7.9% while the extremes need multiplication by 1.79 and 0.72. The gain factors based on symmetry remove some of total event P_T unbalance, however a 30% energy unbalance still appears -- weighted toward the calorimeter's left side.

2.3.5 Beam Calorimeter

The beam calorimeter measured energy of particles passing through the 8"X8" hole in the center of the main calorimeter. This reasonably simple calorimeter, once in place, operated stably during the run. Taken in tandem with the main calorimeter, the calorimeters provide a measure of the total event energy; only a small fraction escapes to θ^* angles larger than 130°.

Consisting of 30 iron-scintillator layers, the beam calorimeter contains 6.7 interaction lengths. Four photomultiplier tubes measure the light produced in the array by means of Lucite light pipes. Energy resolution in the beam calorimeter was measured as $1.10/\sqrt{E}$, while the the beam calorimeter was calibrated so that $E_{measured}/E_{true} = 1$. See [JON74] for a complete description of this calorimeter.

Figure 2.10: Logic Diagram for data collection

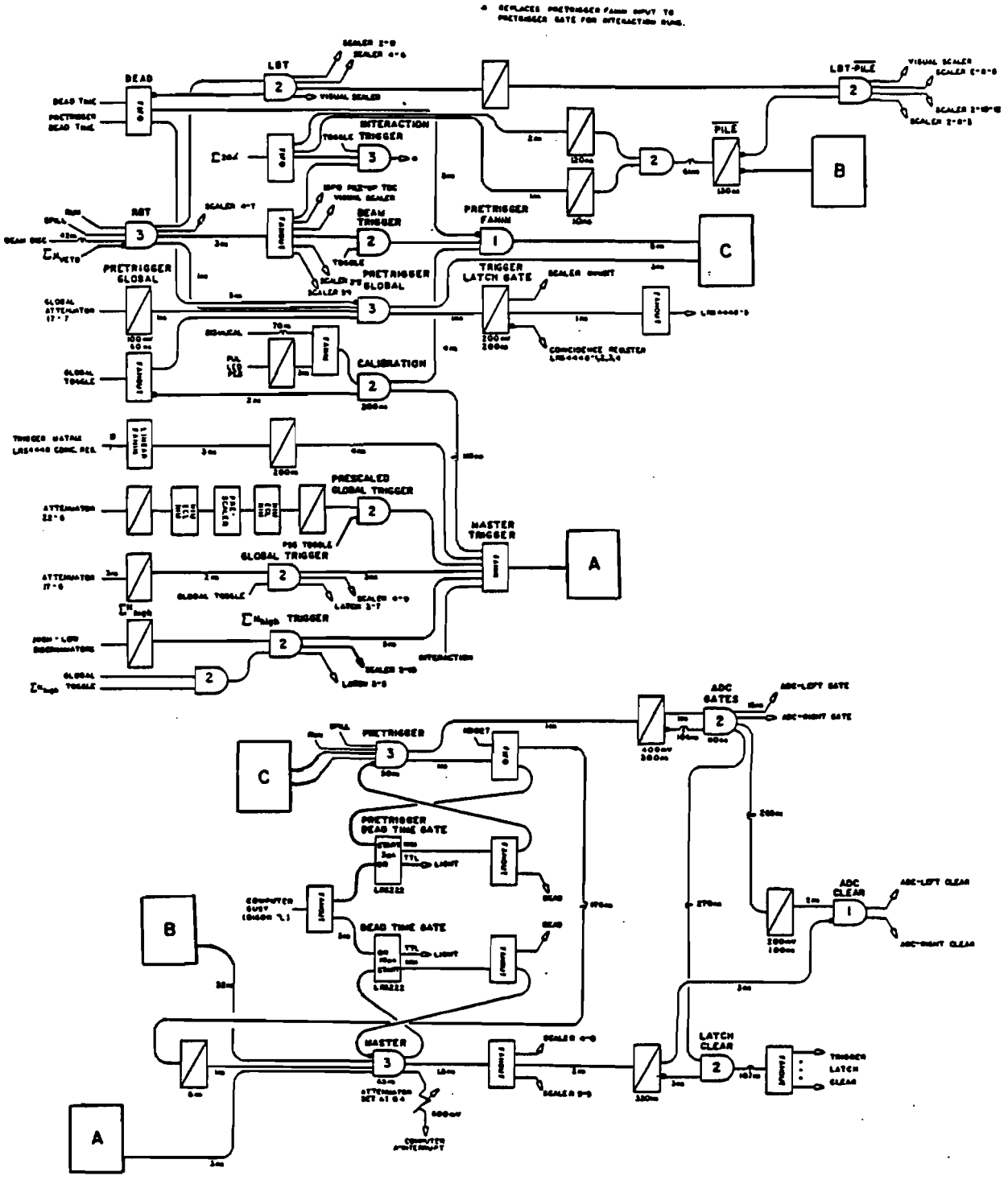

2.4 E609 LOGIC

Figure 2.10, courtesy of M. Marcin [MAR85], diagrams the main logic of the experiment. To record an event both a PRETRIGGER and a MASTER trigger must occur. The rapid PRETRIGGER comes from the combination of an RBT (resulting from the beam telescope) and a signal from the calorimeter that some kind of target interaction occurred. This signal disables the experiment for at least 3 microseconds for the calorimeter signals to integrate and filter through the trigger logic. A MASTER trigger requires a three-fold coincidence of the PRETRIGGER, a satisfied calorimeter trigger, and the absence of pile-up. Additional particles depositing energy during the ADC integration time created a pile-up signal and vetoed the whole event. MASTER gate signals disabled the experiment for at least 10 microseconds allowing the computer to readout the CAMAC registers, latches and scalers and write them to magnetic tape.

In an attempt to avoid events where a second beam particle deposited additional energy in the calorimeter before the previous event has been read from the data acquisition logic, an "interaction" veto was used for the hydrogen data. This veto measured additional energy deposited in the front layer of the calorimeter during the integration phase of the data collection. Nuclear data collection rates were reduced to a point where this veto was not necessary.

2.5 DATA ACQUISITION

After the generation of a MASTER gate, the data acquisition system recorded all measured parameters for the event. Using a version of MULTI, the computer created an event buffer starting with the event number and type. For a typical data event, the computer started by writing a series of flags, indicating the available hardware, and then a series latches which indicate the various triggers the event satisfied. Readout of the location of the nuclear target wheel and the wires hit in the PWC was followed by the drift chamber TDC values. Finally the computer wrote out all the ADC values from each of the calorimeter modules as well as the ADC values from the beam calorimeter and beam telescope counters. The computer also read event-by--event scalers recording the total beam flux as well as information to monitor beam pile-up.

Between spills, the spill-by-spill beam flux counters were read as well as the drift chamber high voltages. The TDC controller initiated an autotrim, which assured their one nanosecond resolution. Finally the computer read the SWIC information, recording the wires hit along with the position of the beam centroid.

Four other event types rounded out the data collection. A begin-run record was written at start of each run. Following this record, buffers containing the computer code which interfaced the computer with the CAMAC modules and a buffer recording four manually set counters, (used to input the current tape number) were written to tape. The final event type, written at the conclusion of each data run, was an end-run record containing comments about the run.

2.6 PRELIMINARY DATA ANALYSIS AND SELECTION

2.6.1 Data Selection

After data collection a variety of cuts removed events that failed to contain unambiguous information. Pile-up requirements demanded that only one interaction occurred while the calorimeter recorded the event, a 870 ns time window. Checking that only one particle generated the event, the beam telescope vetoed events with 2 particles in an RF bucket. TDC data was recorded to examine whether another beam particle occurred within -400 to +470 nanoseconds of an event trigger. Logic utilized 400 ns of internal delay in the master gate to look ahead in time for non-triggering interactions in the calorimeter and, using additional delays, monitored the time after the triggering event. Examination of beam telescope ADC's determined if the incident beam RF bucket carried a single incident proton or if more than one proton combined to create a trigger. Details of the pile-up logic are given in [MAR85,FLE87].

Physical limits constrain the values of recorded energy; physically impossible events outside these limits result from some kind of failure. Conservation of energy forbids the calorimeter to record more energy than available in the lab for pp events, $\sqrt{s}$ = 27.4 GeV. Conservation of momentum requires that any half of the calorimeter contain no more than half the center-of-mass energy. Finally, requiring a correct trigger, the total transverse energy must exceed the trigger threshold.

TABLE 2.9
Preliminary Analysis Data Selection Criteria

PILE-UP TDC's	No interaction for 400ns after master gate No interaction for 470ns before master gate
PILE-UP ADC's	Only 1 particle logic pulse during ±250ns 1 particle logic pulse in a 100ns window
BEAM TELESCOPE	(Events showing 3 out of next 4 are cut) B3 recorded 2 particles in 100ns ADC B3 recorded 2 particles in 110ns ADC B6 recorded 2 particles in 100ns ADC B6 recorded 2 particles in 110ns ADC
MAIN CAL ADC's	Modules must record values below saturation
KINEMATICS	0 GeV < Main calorimeter energy < 400 GeV
TRIGGER CUTS	Trigger threshold < Total P_T

Many of the selection criteria in table 2.9 explain themselves, however the BEAM TELESCOPE cuts, removing events with 2 particles in a single bucket requires an additional note. Events failing this cut appear similar to events passing all cuts, implying that, for a reasonable fraction of these events, the second particle did not interact with the target and the event should be considered in the cross section calculation. Rather than risk contamination of the event sample, we remove these events and correct our total particle flux down to account for the excluded events. Given the target interaction length, 10% for hydrogen [5% for the nuclear targets], the second particle in the bucket should interact 10 [5] percent of the time leaving 90 [95] percent of the excluded events as *bona fide* events. Assuming a uniform beam during the spill and over the run, the recorded flux should be reduced by R, where

$$R = 1 - G \times F$$

and G = 1.0 - target interaction length
= .90 for hydrogen
= .95 for nuclear targets

and F = Fraction of events with $\geq$ 2 beam particles.

The corrected beam flux, used in cross section calculations, comes from the RBT scaler times R, the flux correction. Typically this corrects the beam flux down by ~20%.

Further analysis shows the need for additional cuts. Summed energy from the main calorimeter and the beam calorimeter occasionally exceeds 400 GeV, due to either the calorimeter energy resolution or because two beam particles created the event. Avoiding the second situation, we applied a series of target-dependant total energy cuts. These cuts remove a long tail of high total energy events without affecting the bulk of the events. Cut windows come from examination of the total energy distributions; dropping energy with increasing atomic number reflects increased energy going into the target fragmentation region. Table 2.10 lists the total energy cuts for the various targets.

2.6.2 Clustering Towers into Particles

Event physics should reflect the true particles rather than the towers illuminated, however a one-to-one correspondence between towers and particles does not exist. Energy distribution from the tower array reflects the particle flow; however, particles in the calorimeter shower and deposit their energy in a variety of towers. Reconstruction of the location and energy of a single incident

TABLE 2.10
Main & Beam Calorimeter Energy Cut

TARGET	MINIMUM ENERGY (GeV)	MAXIMUM ENERGY (GeV)
Hydrogen	300.	500.
Helium	290.	470.
Beryllium	285.	460.
Carbon	280.	460.
Aluminum	275.	460.
Copper	260.	450.
Tin	250.	450.
Lead	240.	445.

particle uses the summed momentum vector from a cluster of towers. Multiple particles remain reconstructible while their showers remain distinct, but climbing multiplicity (especially for jets with low internal P_T) causes the showers to overlap and creating particles from tower clusters becomes difficult. Electro-magnetic or hadronic shower differences provide information to help reduce shower overlap, however showers eventually blend into the appearance of a single particle. Our analysis includes a careful clustering of showers into 'particles' (we use the term cluster to refer to these 'particles' [MAR87]). The average cluster distribution reflects the true particle distribution giving a handle on their multiplicities, energy per particle and particle flow. Care is advised when considering specific events recalling that the clusters are reconstructed particles inherent with the difficulties of recreating a point when the information available is the smeared and binned version of that point.

CHAPTER 3

JET-FINDERS

Jets at fixed target energies, once viewed with skepticism (because, in part, of global triggering [DeM82,BROW82]), now stand on firm experimental ground [CORM85,ARE85]. Confidence that jet signals exist amidst the sea of isotropic events stems, in part, from dominate jet cross section at collider energies [ÅKE85,BAG83a,ARN83a]. In spite of the acceptance of jets, their properties require careful extraction from the background. Predominate methods of studying jets rely on the tacit assumption that jets exist in the data sample and one simply needs to measure them.

Reasonable jet properties arise from selecting events with high E_T and high planarity and labeling them 'jet-like' [MIE88,GOM86b], allowing one to study the effects of jets in a strictly defined manner. Several short comings appear in this definition based on a measure of the total event; the most obvious being that 'real' jets do not suddenly appear at a specific planarity and E_T but the jet population within the event distribution should grow as these parameters increase; no matter what the planarity and E_T cuts are, the sample contains some 'non-jet' events and excludes 'true-jet' events. Additionally, the event based definition misses information specific to jets such as the jet E_T, as distinct from the total event E_T, a closer measure of the original parton E_T. Identification of specific

jets allows the study of jet parameters including: multiplicity of particles within the jet, internal jet energy flow, and the jet opening angle. Comparisons between the two large transverse momentum jets demand a specific jet definition, allowing consideration of the di-jet angle, momentum balance, and particle balance.

Jet identification becomes relatively simple at high energy and high E_T where jets dominate the cross section. Figure 3.1A demonstrates the clear nature of collider jets; nearly any definition should locate this type of jet. Figure 3.1B shows two high P_T events from our hydrogen data, one with high E_T and one with high planarity. Figure 3.1C shows similar events from protons on lead. Bjorken and Brodsky [B&B70] suggest three steps to finding jets:

> (a) Find for each event the axis which minimizes the sum of the squares of the transverse momentum to it. This axis defines the reconstructed jet axis.
> (b) Construct a quantitative measure of the amount of jet-like structure by comparing the relative amount of transverse momenta to orthogonal axes.
> (c) Perform Monte Carlo simulations to evaluate the significance of the results. [F&P77]

In practice the jet axis aligns with the direction of maximum local transverse momentum. Jet-finding algorithms first locate a jet axis and then assign particles in a limited region around the axis to represent the jet fragments; final particle assignment is based on criteria set by a jet Monte Carlo.

Specific examples of jet definitions come from the $p\bar{p}$ collider experiments at CERN. UA1 (where a cell corresponds to a tower in our

Figure 3.1A Jet Event from UA2

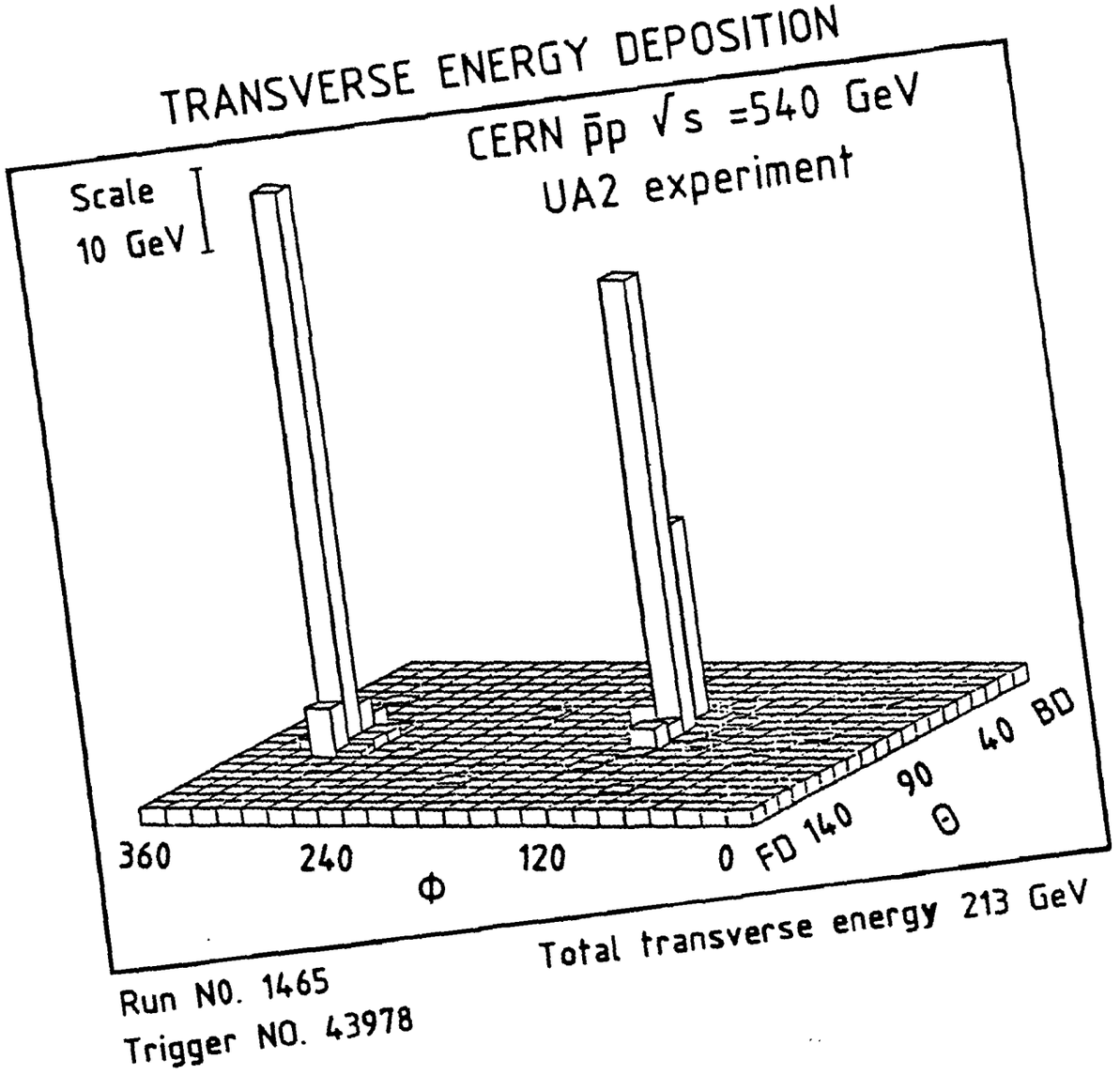

Figure 3.1B **Hydrogen Jet Events from E609**

The height of the blocks corresponds to the cluster P_T.

High E_T Hydrogen Two-Jet Event

Tape 3067 Run 6 Event 3534
Planarity=0.701
Event Et=23.93 GeV
Max Cluster=4.40 GeV E_T
Conical jet finder:
jets of 8.9 and 4.4 GeV/c P_T
Gaussain jet finder:
jets of 8.9 and 4.8 GeV/c P_T

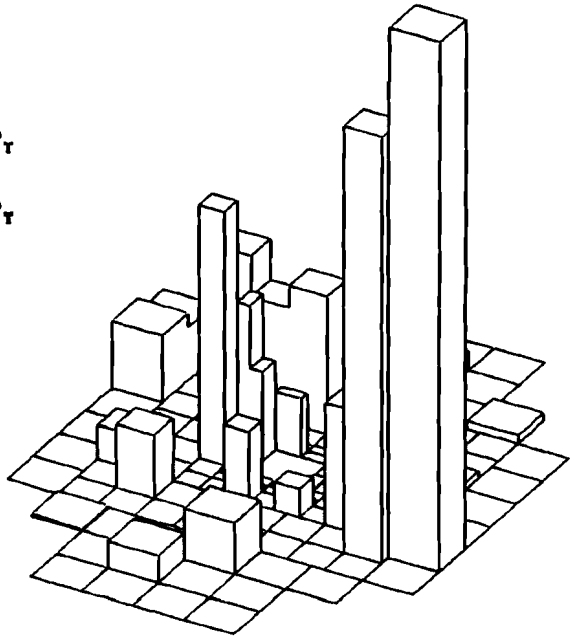

High Planarity Hydrogen Two-Jet Event

Tape 3062 Run 4 Event 387
Planarity=0.995
Event Et=18.8 GeV
Max Cluster=7.00 GeV E_T
Conical jet finder:
jets of 9.8 and 8.3 GeV/c P_T
Gaussain jet finder:
jets of 9.5 and 8.1 GeV/c P_T

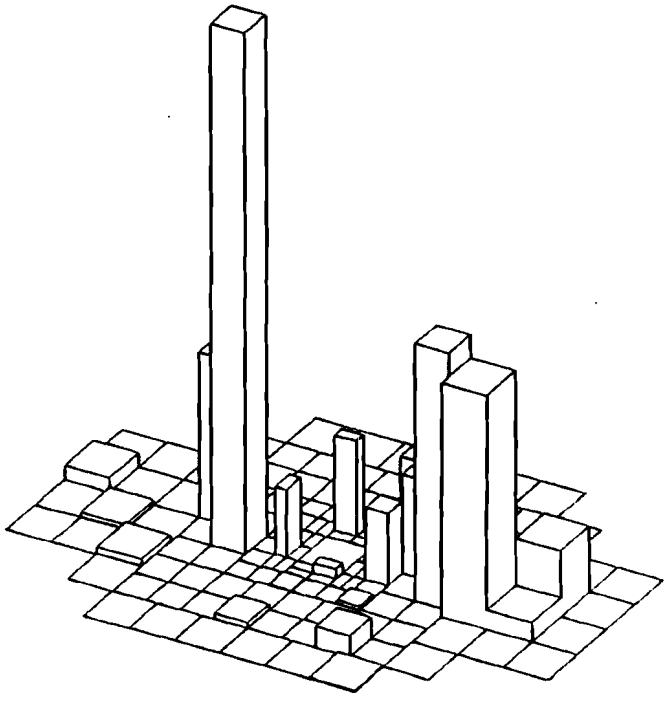

Figure 3.1C **Lead Jet Events from E609**

The height of the blocks corresponds to the cluster P_T.

High E_T Lead Two-Jet Event

Tape 3090 Run 5 Event 19941
Planarity=0.708
Event Et=22.9 GeV
Max Cluster=5.57 GeV E_T
Conical jet finder:
jets of 6.9 and 6.9 GeV/c P_T
Gaussain jet finder:
jets of 8.2 and 5.8 GeV/c P_T

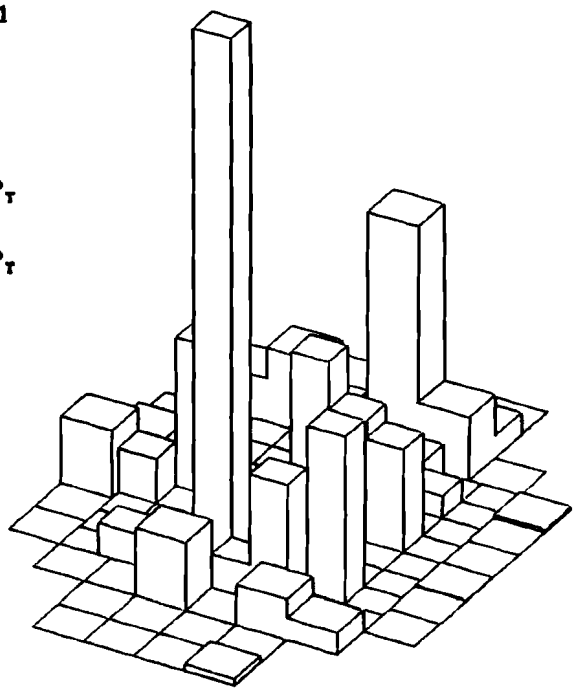

High Planarity Lead Two-Jet Event

Tape 3080 Run 5 Event 1146
Planarity=0.907
Event Et=18.5 GeV
Max Cluster=5.61 GeV E_T
Conical jet finder:
jets of 7.1 and 6.9 GeV/c P_T
Gaussain jet finder:
jets of 7.0 and 6.8 GeV/c P_T

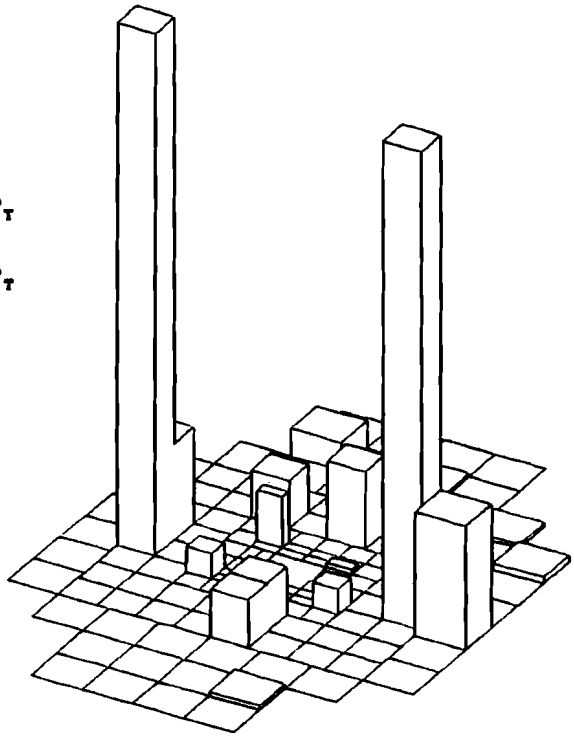

experiment) uses a conical jet-finding algorithm, defining jets with the following criteria:

> (In jet reconstruction), cells are treated differently depending on their E_T being above or below 2.5 GeV:
> - Among the cells with $E_T \geq 2.5$ GeV, the highest E_T cell initiates the first jet. Subsequent cells are considered in order of decreasing E_T. Each cell in turn is added vectorially to the jet closest in (η,ϕ) space, i.e. with the smallest $d \equiv \sqrt{(\Delta\eta^2+\Delta\phi^2)}$ (with ϕ in radians), if $d \leq 1.0$. If there is no jet with $d \leq 1.0$, the cell initiates a new jet.
> - Cells with $E_T \leq 2.5$ GeV are finally added vectorially to the jet nearest in (η,ϕ) if their transverse momentum relative to the jet axis is less than 1 GeV and if they are not further than 45° in direction from the jet axis. [ARN83a]

This technique corresponds to selecting the maximum local E_T vector, drawing a 45° half angle cone around the vector and summing all the energy within the cone to create a jet. Concentrations of energy separated by more space than 45° represent separate jets.

Approaching jet definition from a different direction, UA2, a second CERN experiment, located jets based on the event scalar transverse energy deposition.

> We join into a cluster all cells which have a common side and have a cell energy $E_{cell} > E_{cell}^{min}$ (= 400 MeV). Clusters having two or more local maxima separated by a valley deeper than 5 GeV are then split. In each event the clusters are ranked in order of decreasing transverse energies and denoted by $E_T^1 > E_T^2 > E_T^3 > \ldots$. [BAG83b]

In this definition, energy clusters with high enough E_T correspond to

jets. Many of the triggered UA2 events contain a pair of high P_T jets (E_T > 20 GeV) while 29% contain a third jet of E_T > 4 GeV, additional jets with large E_T are even less common. Energy in cells not identified with the high energy clusters are attributed to spectator jet fragments. This jet definition corresponds to considering the event E_T distribution as a smooth surface and identifying the peaks as jets.

Lower energy, fixed target, studies can apply these two definitions to extract jets from the data sample. Rigorous identification of each particle (a cluster in our analysis) as a fragment from the hard-scattering jet or a fragment from one of the spectator jets is impossible, even in theory. Particles from spectator jets overlap the hard-scattering jets. Particle assignment to jets then becomes a balancing between particles lost from the hard-scatter and those gained from the soft 'non-jet' spectators to reproduce expected jet properties. Monte Carlo jet simulations determine the parameters for the operation of jet-finders.

3.1 QUARK JET MONTE CARLO

This thesis focuses on the comparisons between the various nuclear data samples and less on direct comparisons with QCD predictions, (see [SHAT84,WEB83a,83b] for examples of comparisons). However, fine tuning of the jet-finders requires a QCD Monte Carlo simulation of jet physics. The Monte Carlo allows optimization of jet-finding parameters needed to accurately reproduce the physics of the input jets. Comparisons between events from different nuclei

allows substantial reduction in the systematic biases inadvertently introduced in the simulation; as long as the inconsistencies between data and Monte Carlo calculations remain constant with atomic number, comparisons *between* various nuclear targets factor out the errors.

In spite of the disclaimer in the previous paragraph, the Monte Carlo generating the jets used for jet-finder optimization agrees well with pp data. Originally written by R. A. Singer, M. D. Corcoran refined and polished the Monte Carlo used to simulate the jets in this analysis. Full details of the Monte Carlo appear in [CORC85]; the following paragraphs paraphrase this reference's general description of the Monte Carlo. Not including gluon bremsstrahlung, the Monte Carlo simulates high-transverse energy pp events using a Field-Feynman four-jet algorithm.

The Monte Carlo, operating in the scattered parton center-of-mass frame and considering all partons as massless, scattered only valance quarks and gluons. Produced x values (where x equals the parton momentum over the proton momentum) always exceeded 0.1. Structure functions excluded scale-breaking effects which are small at our energy [GLÜ82]. Consistent with Drell-Yan [YOH78] and di-jet experiments [CORC78,80a,80b], the scattered partons start with intrinsic transverse momentum k_T, such that

$$k_T \sim \exp\left[\frac{-k_T^2}{2\sigma^2}\right]$$

with σ=0.70, giving $\langle k_T^2 \rangle \sim 1.0(\mathrm{GeV/c})^2$ and $\langle k_T \rangle = 0.0$, (the scattered parton k_T balances the spectator parton k_T). Useful in setting Monte Carlo parameters, the Mandelstam variables, describing the

center-of-mass scatter of two particles with momentum p_1 and p_2 and resulting momentum p_3 and p_4, are

$$\hat{s} = (p_1+p_2)^2 = (p_3+p_4)^2$$

$$\hat{t} = (p_1-p_3)^2 = (p_2-p_4)^2$$

$$\text{and} \quad \hat{u} = (p_1-p_4)^2 = (p_2-p_3)^2.$$

Generating values of $\hat{t}$, the first order QCD cross sections diverge as $\hat{t} \to 0$, necessitating a cutoff, set in the Monte Carlo as $|\hat{t}| > (1.0\ \text{GeV/c})^2$, along with a symmetric cut in $\hat{u}$. The strong coupling constant a_s, was defined as

$$a_s = \frac{12\pi}{25 ln(Q^2/\lambda^2)},$$

with $\lambda^2=0.1\ \text{GeV}^2$ and $Q^2=2\hat{s}\hat{t}\hat{u}/(\hat{s}^2+\hat{t}^2+\hat{u}^2)$.

Feynman and Field [F&F77,FF&F77,78] suggested fragmentation functions, $D_q^h(z)$, to generate "the mean number of hadrons of type h and momentum fraction z (per dz) in a jet initiated by a quark of flavor q with high momentum" [F&F78]. Using the ansatz that every quark in a cascade decays in a manner dependent only on its momentum, four parameter classes determine the jet structure (fragmentation function): (1) the probability, $f(\eta)d\eta$, that the parent leaves a fraction of its momentum η to the remaining cascade, (2) three flavor parameters, (3) the spin of the meson produced in the decay chain, and (4) the internal jet transverse momentum, q_T. Fragmentation parameters, (again from Feynman and Field), were selected with (1) the fixed constant a, in $f(\eta)$, set equal to 0.77, (2) $s\bar{s}$ quark pair production

TABLE 3.1
Jet-Finders Definitions from previous Experiments

EXPERIMENT	REFERENCE	$\sqrt{s}$ (GeV)	TRIGGER	JET DEFINITION
FERMILAB WAS	[BROM78]	19.4	limited Ω	$\Delta\phi<20°$, $\lvert\eta\rvert<0.2 \equiv$ Trig
CERN NA5	[DeM82]	23.8	global	no jets found
CERN NA5	[DeM84]	23.8	limited Ω	40° half-angle
FERMILAB E609	[ARE85]	27.4	two-high	55° half-angle
FERMILAB E609	[CORM85]	27.4	global/lim Ω	45° half-angle
FERMILAB E557	[GOM86b]	38.8	global/lim Ω	planarity cut
FERMILAB E672	[STE88]	38.8	lim Ω	$\sqrt{(\Delta\eta^2+\Delta\phi^2)} \leq 1.0$
CERN ISR BFS	[ALB79a]	52.6	1 hi-P_T hadron$^{\pm}$	Gaussian Surface
CERN ISR AFS	[ÅKE85]	63	"two-jet"	$\Delta\phi<30°$, $\lvert\eta\rvert<0.7$
CERN UA1	[GLÜ82]	540	"two-jet"	45° calorimeter slice 35° charged pls
CERN UA2	[BAG83a]		540	"two-jet"
	energy surface peaks			

half as likely as $u\bar{u}$ and $d\bar{d}$ quark pair production, (3) equal production of vector and pseudoscalar mesons and (4) internal q_T according to

$$q_T \sim \exp\left[\frac{-q_T^2}{2\sigma^2}\right]$$

with σ=0.35, to agree with e^+e^- data [HAN82,WOL80,TASSO80]. No baryons were produced. Additional details on the Monte Carlo, including the choice for momentum and energy conservation appear in [CORC85]

The conical jet-finding technique, reasonably straight forward, has been used successfully to measure jet cross sections [ARE85]. A single parameter, the cone half-angle, dominates the physics results. For $\sqrt{s}$ = 27.4 GeV the choice of cone size affects the cross section

30% for every 5° change in cone half angle. Proper selection of the cone angle relies on Monte Carlo simulation of event physics and optimization of the cone parameters to reproduce the simulated event. Two of our collaborators selected cone sizes, one used 45° to describe jets from solid angle triggers [CORM85], the other used 55° [ARE85] to describe jets from the two-high trigger. Similar analysis for $\sqrt{s}$ = 63.0 GeV [ÅKE85] used a conical box for the jet definition spanning $|\eta^{jet}| < 0.4$ (~45° slice in θ) and $\phi = \pm 30°$; here the cross section changed less than 15% for a 10° decrease in the selected ϕ angle. Another CERN experiment, at a lower $\sqrt{s}$, used a 45° region in ϕ and included their entire calorimeter θ^* coverage, 45° to 135° [DeM82]. In later analysis they utilized a 40° cone around the leading particle to study jet properties. Table 3.1 displays jet-finder parameters for a variety of collaborations.

3.1.1 Conical Jet-Finder Flow Chart

In this analysis the conical jet-finder operates as shown in figure 3.2. Free parameters, appearing in bold face, control the construction of jets. They determine the availability of particles to start a new jet and the addition of particles after initial jet identification.

Figure 3.2 Conical Jet-Finding Flow Chart

A) Select Leading Particle to Start New Jet

Leading Particle Requirements:

1) Select unused cluster with the largest P_T
   a) The cluster must have $P_T > P_T$**CUTOFF**
   b) The cluster is at least **OPEN_ANGLE** from all other jets (otherwise it would be part of that jet)

2) Set initial jet axis along cluster momentum vector

B) Determine Jet Axis and Particles Belonging to Jet

The Additional Particles Must Satisfy:

1) Unused in any other jet

2) Lie within a cone angle of **OPEN_ANGLE**

3) Exclude clusters from the beam jet by requiring $\theta^* >$ **MIN_ANGLE**

4) Avoid soft clusters belonging to the beam jet
   a) Require $\theta^* > 30^\circ$ or
   b) Cluster $P_T > 0.3$ GeV/c

5) Calculate jet axis as vector sum of all cluster momentum

C) Check All Particles within OPEN_ANGLE of the Jet Axis are in Jet

1) No change => try to find next jet (GOTO A)

2) Change => Calculate new jet axis with current cluster set
   a) If the change in jet P_T is $> P_T$**SHIFT** or we have tried < 5 times

      REPEAT THIS STEP (GOTO C)

   b) Else if the change is $< P_T$**SHIFT** or we have tried ≥ 5 times, then take the jet axis as calculated and then try to find the next jet (GOTO A)

D) After All the Jets are Found

1) Release all particles from jets with $P_T < 1.0$ GeV/c (not enough transverse momentum to consider this a jet)

2) Check each cluster is assigned to the closest jet

3) Calculate the final jet axis and the physical quantities.

3.1.2 Conical Jet-Finder Parameters

Parameter determination for the optimum jet-finding utilizes Monte Carlo events which were generated according to the sharply dropping P_T spectrum observed in real data. Events were included in the simulated data sample when the simulated event energy distribution satisfied the two-high trigger. The distribution of Monte Carlo events passing the trigger contains events with jet P_T's as low as 1.0 GeV/c while most events lie near 4.5 GeV/c and with a few events in the high P_T tail extending to 8.0 GeV/c. Figure 3.3 displays mean jet P_T of the Monte Carlo events passing the two-high trigger along with the P_T of events which have 2 reconstructed jets containing at least 3 GeV/c. Some of the lower P_T jets (1-3 GeV/c) are incorrectly reconstructed in the 3-4 GeV/c range by the conical jet-finder. This effect is reduced if jets located by the jet-finders are required to have at least 4 GeV/c P_T. A 50% non-jet background in the jet P_T range below 5 GeV/c is reported on in [ARE85].

P_TCUTOFF determines the total number of jets by setting the minimum P_T threshold to begin a jet. Hard scattering jet physics depends weakly on this parameter provided it allows two jets to routinely appear. However, **P_TCUTOFF** strongly affects the study of three or more central jets since changing the threshold determines the frequency of these events. The Monte Carlo only includes a pair of hard scattered jets, ignoring a possible third jet from gluon bremsstrahlung or from the spectator jets. Without guidance from the Monte Carlo ([ARE85] used 0.5 GeV/c), we selected this parameter so the number of number of 3 jet events found by the conical jet-finder technique roughly corresponds to the number found by the Gaussian jet-

Figure 3.3 **Monte Carlo Jet P_T**

The P_T distribution of the Monte Carlo Jets which pass the two-high trigger corresponds to the solid curve; (shown twice). The dashed line in figure **A** results from Monte Carlo events where the optimized conical jet-finder located 2 jets with at least 3 GeV/c. The optimized Gaussian jet-finder produces the dotted curve in figure **B**.

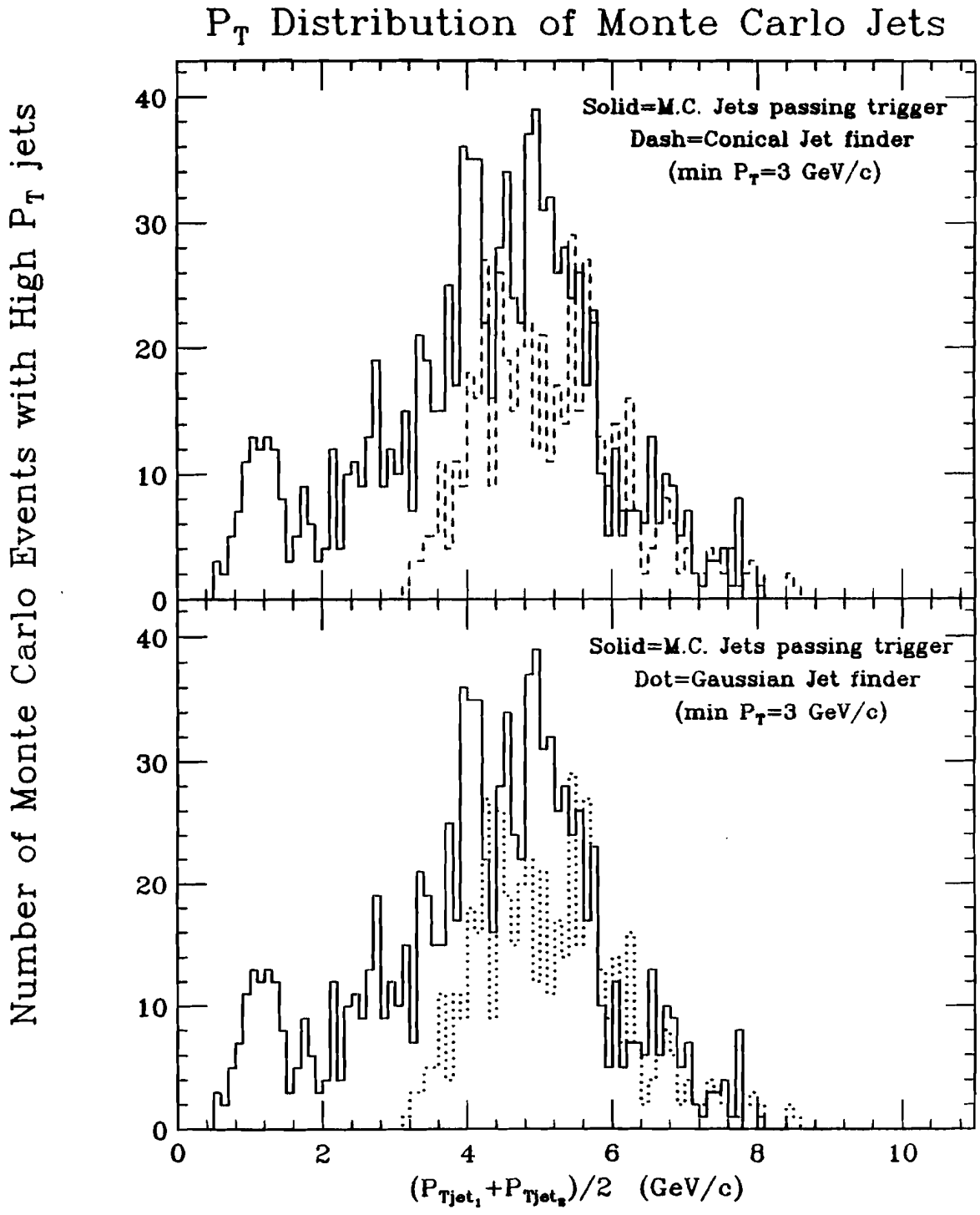

-finder (described later), requiring P_T**CUTOFF** > 0.8 GeV/c for clusters starting new jets.

Selection of **OPEN_ANGLE** requires the cone angle best reproducing the true jet P_T, as generated in the Monte Carlo. Figure 3.4 shows, as a function of cone angle, the difference between the Monte Carlo jet P_T and the reconstructed jet P_T. Shifting as the average P_T in the jet pairs increases, the optimum cone angle reflects the balance between the hard-scatter jet particles and the spectator particles. As the cone angle increases, two effects occur: (1) each jet gains additional particles, thus increasing its P_T, and (2) more jets pass the minimal P_T cut, therefore increasing the total found jet sample. Figure 3.5 shows the increase in the number of jets passing a 3 GeV/c threshold for a 30° half-angle cone and a 60° half-angle cone. For the small angle cone, jets just above threshold dominate the sample while the large angle cone promotes these jets to higher P_T's, moving the distribution away from the 3 GeV/c cut. Because of the difficulty in distinguishing low energy jets from background fluctuations we study only the events with average jet P_T > 4 GeV/c. Disregarding the 3-4 GeV/c P_T bin, jets found with a cone half-angle between 40° and 45° most closely reproduce the Monte Carlo jet P_T.

In addition to the jet P_T, several other parameters vary with the cone angle. Summing the cluster momentum vector magnitudes gives the jet E_T, a larger value than the vector momentum sum, P_T. Figure 3.6 shows the Monte Carlo E_T minus the found E_T versus the cone half-angle. Correct jet E_T measurement requires a slightly larger cone angle than indicated by P_T considerations. The total number of expected found jets over the number generated, shown in figure 3.7,

Figure 3.4 P_T(Monte Carlo)-P_T(found) vs. Cone Angle

For four bins of found jet P_T's, the relationship between cone angle and ΔP_T shows that the optimum cone angle is near 45°. Monte Carlo input events come from all triggering two-high events.

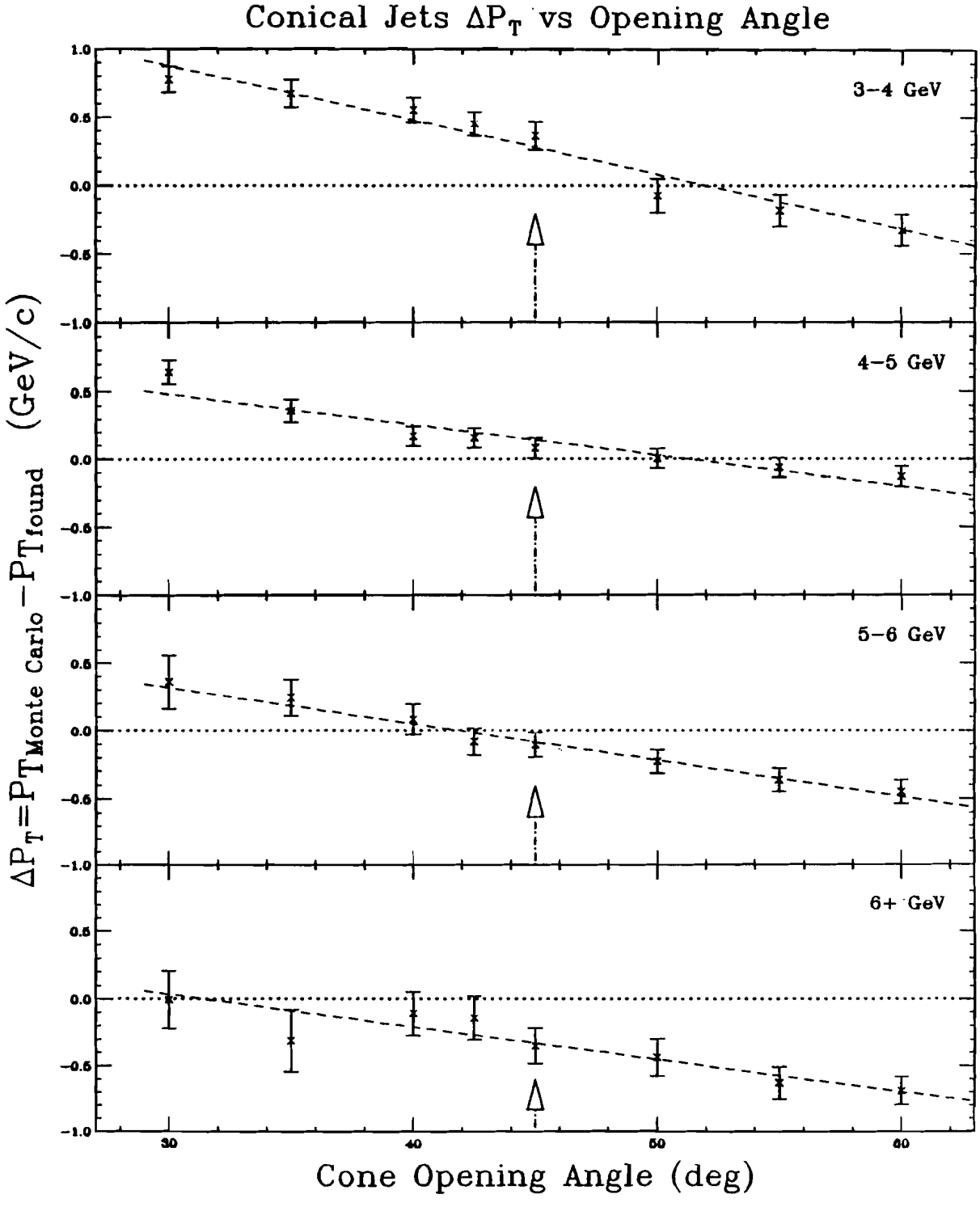

Figure 3.5 Jet P_T for 30° and 60° Cones

The resulting P_T distributions for located jets using a 30° cone angle (dotted line) and a 60° cone angle, (solid line).

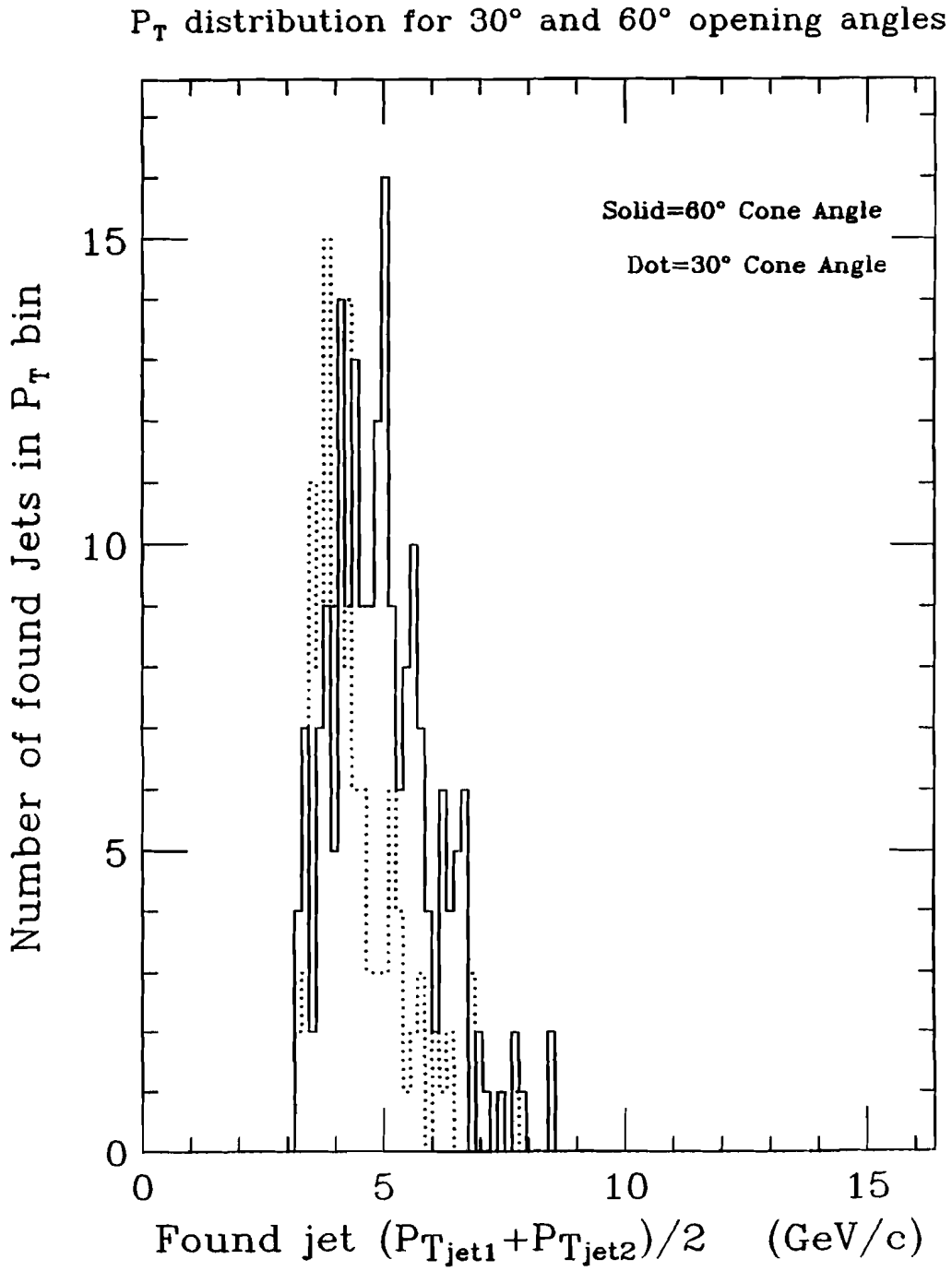

Figure 3.6 E_T(Monte Carlo)-E_T(found) vs. Cone Angle

For four bins of found jet P_T's, the relationship between cone angle and ΔE_T shows that the optimum cone angle is near 45°. Monte Carlo input events come from all triggering two-high events.

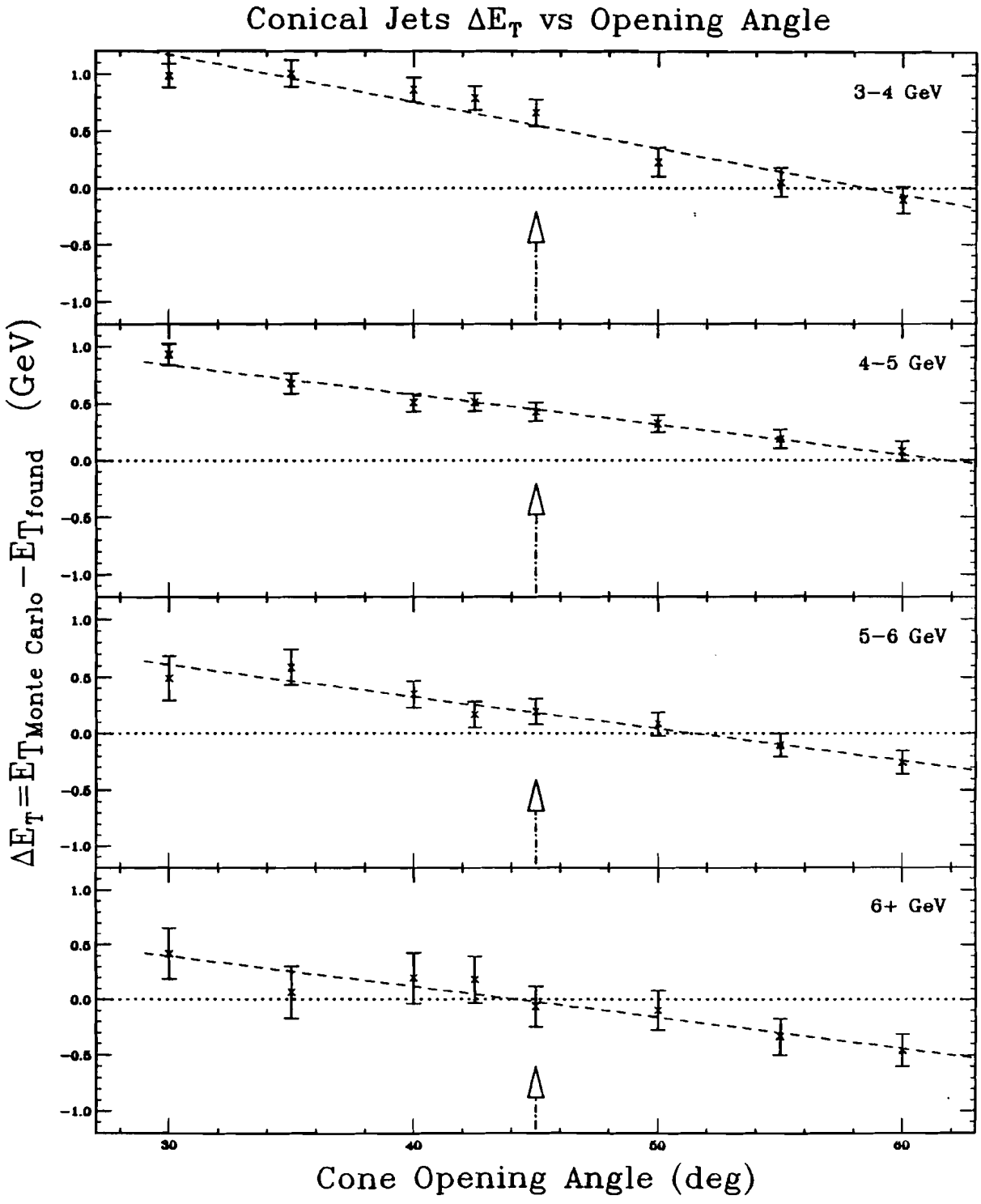

Figure 3.7 **# Conical Jets Found/# Jets M.C. vs. Cone Angle**

For four bins of found jet P_T's, the ratio of the total number of conical jets found over the total number generated is shown as a function of the jet cone angle. Again the optimum cone angle is near 45°.

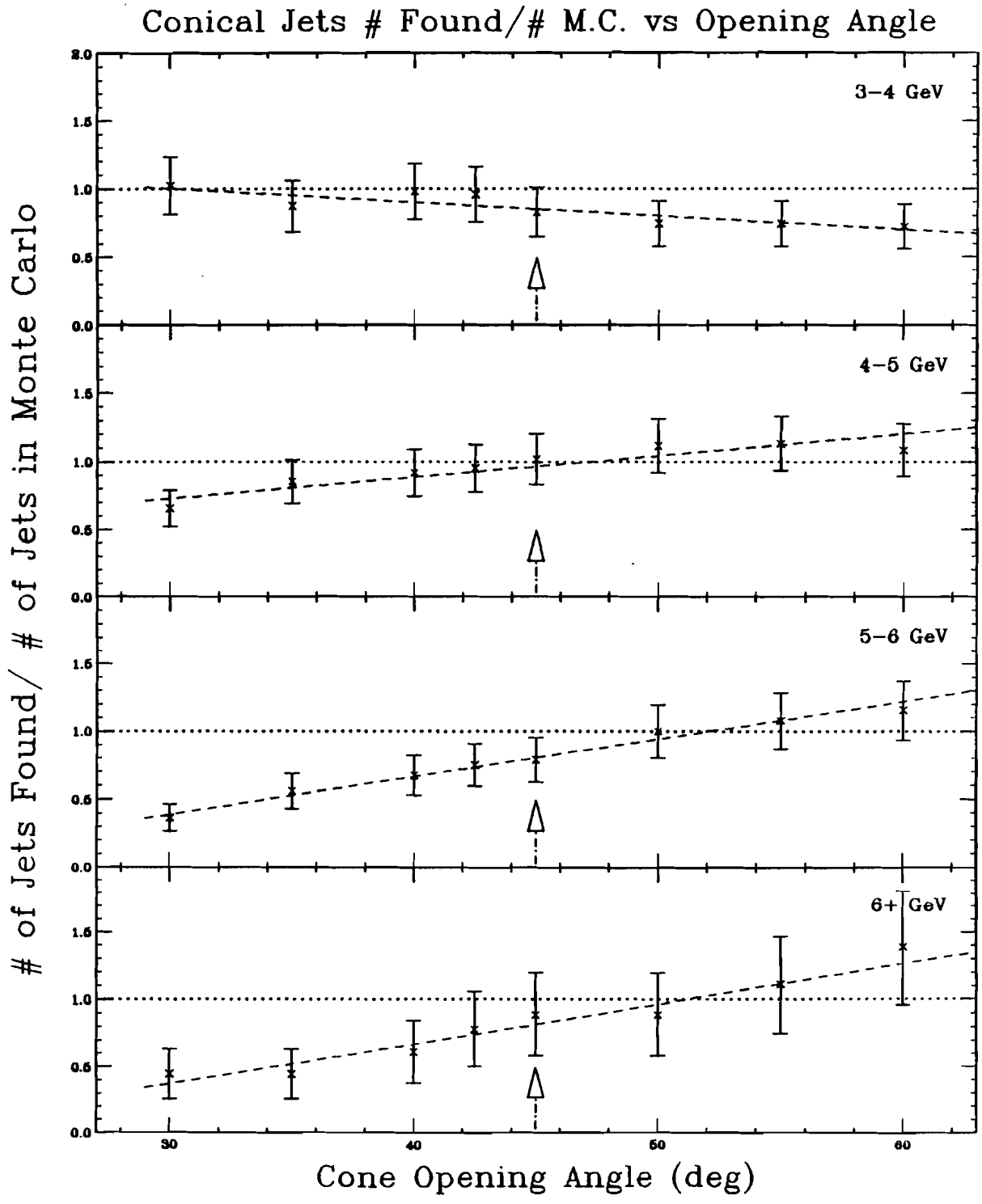

also implies the need of a cone angle slightly below 50°. As a compromise, we select a cone half angle of 45° for this analysis. Increasing the cone angle causes the located jet P_Ts to increase; jets from the 3-4 GeV/c bin feed up into the higher P_T bins, explaining the drop in the ratio with increasing cone angles seen in 3-4 GeV/c bin of figure 3.7 while the higher P_T bins display an increased ratio with increasing cone angle.

A 45° cone angle matches the value selected by several other researchers; the disagreement between the cone size used in [ARE85] and this study probably reflects the different methods used in generating Monte Carlo jet distributions. We generated our jet sample starting from 1.0 GeV/c P_T and modeled the steeply falling P_T spectrum, while [ARE85] generated P_T spectrum starting with P_T greater or equal to 3.0 GeV/c and then weighted the results to simulate the true distribution. As seen in the 3-4 GeV/c bin of figure 3.4, the jets just passing threshold require a wide cone angle to completely contain their energy, however as the jet P_T increases the required cone size decreases. The full spectrum from 1.0 GeV/c and above is required to fully simulate the fluctuation of lower P_T events into narrow cones and appearing at high P_T's. A flat P_T distribution contains primarily wide jets just above threshold rather than the much rarer case where the hard scattering parton fragmented into a small region of space.

Two other, less important, parameters contribute to the conical jet reconstruction. Excluding beam (spectator jet) particles from the event, **MIN_ANGLE**, the minimum allowed θ^* for a cluster to qualify as a member of a central jet, nearly matches the center-of-mass radius of

the beam hole, 30°. Without affecting the energy distribution available for jet-finding, the **MIN_ANGLE** cut eliminates only a few clusters from consideration. A final variable, P_T**SHIFT**, helps limit the number of iterations the algorithm attempts in selection of the optimum jet axis. P_T**SHIFT** limits oscillations due to the inclusion of particles at the edge of the cone angle by stopping the search if the P_T for the new cone axis is within P_T**SHIFT** of the old jet P_T value. A P_T**SHIFT** equal to 0.1 GeV/c causes the algorithm to converge without affecting the jet physics. Table 3.2 summarizes the parameters for conical jet--finding and their values used in this study.

The HERA collaboration at DESY, studying electron-proton collisions, points out that "jets in different regions of the laboratory phase space corresponding to the forward, central and backward parts of the detector will typically correspond to different kinematics, i.e. different (Lorentz) boosts, and thus have different widths in terms of lab angle [BUR87]." They draw the conclusion that a fixed cone angle is improper to use and support the method where the cone width changes with angle based on $\Delta R = \sqrt{(\Delta\eta^2+\Delta\phi^2)} \leq$ a constant. Their observations are valid, however the effect is small for our final θ^* selection of jets, set by the requirement of full jet containment in the main calorimeter. We limit each jet axis to the θ^* region of 60°-110°. Additional support of the validity of our conical jet--finder results is its close agreement with the Gaussian jet-finder, to be discussed next. Interested persons might further pursue this reference [BUR87] since they present a new jet-finding method based on the invariant mass-squared of the individual particles.

TABLE 3.2
Conical Jet-Finder Parameters

PARAMETER	VALUE	DETERMINATION
MIN_ANGLE	30°	Beam hole in Calorimeter
OPEN_ANGLE	45°	P_T(Monte Carlo)-P_T(Jet-Finder)
P_TCUTOFF	0.8 GeV/c	Match Gaussian 3 jet production
P_TSHIFT	0.1 GeV/c	Value below Jet P_T uncertainty

3.2 GAUSSIAN JET-FINDER

Our analysis gains credence when we define jets using a second technique, which operates on either isotropic or jet-like events, especially if the results agree. In a method similar to that used by UA2, we consider the event as an E_T surface and look for isolated peaks above the background. Unlike the outstanding jets of UA2, a simple algorithm (combining adjoining energy towers and setting a valley criteria to distinguish jets) fails since the angular spread of the particles within a jet allows zero-energy valleys between particles. The British-French-Scandinavian ISR collaboration at CERN [ALB79a,79b] smoothed the energy distribution to remove this effect. Using a Gaussian function to weight the transverse energy of each cluster by its distance from any point, Gaussians from each cluster sum to produce a smooth transverse energy surface. Figure 3.8 shows a plot of the cluster P_T (= E_T assuming a zero cluster mass) as a function of X and Y position; overlaying the P_T's is a smoothed Gaussian P_T surface where the height, G, at any point (η,ϕ) results from,

Figure 3.8 **Cluster P_T's with Gaussian surface overlay**

The X and Y axes correspond to the surface of the calorimeter in the lab frame, showing the segments. The height of the surface at each point corresponds to the transverse energy at that point. The overlaying (half Z scale) surface results from a Gaussian P_T sum of all the segments based on the optimum parameters.

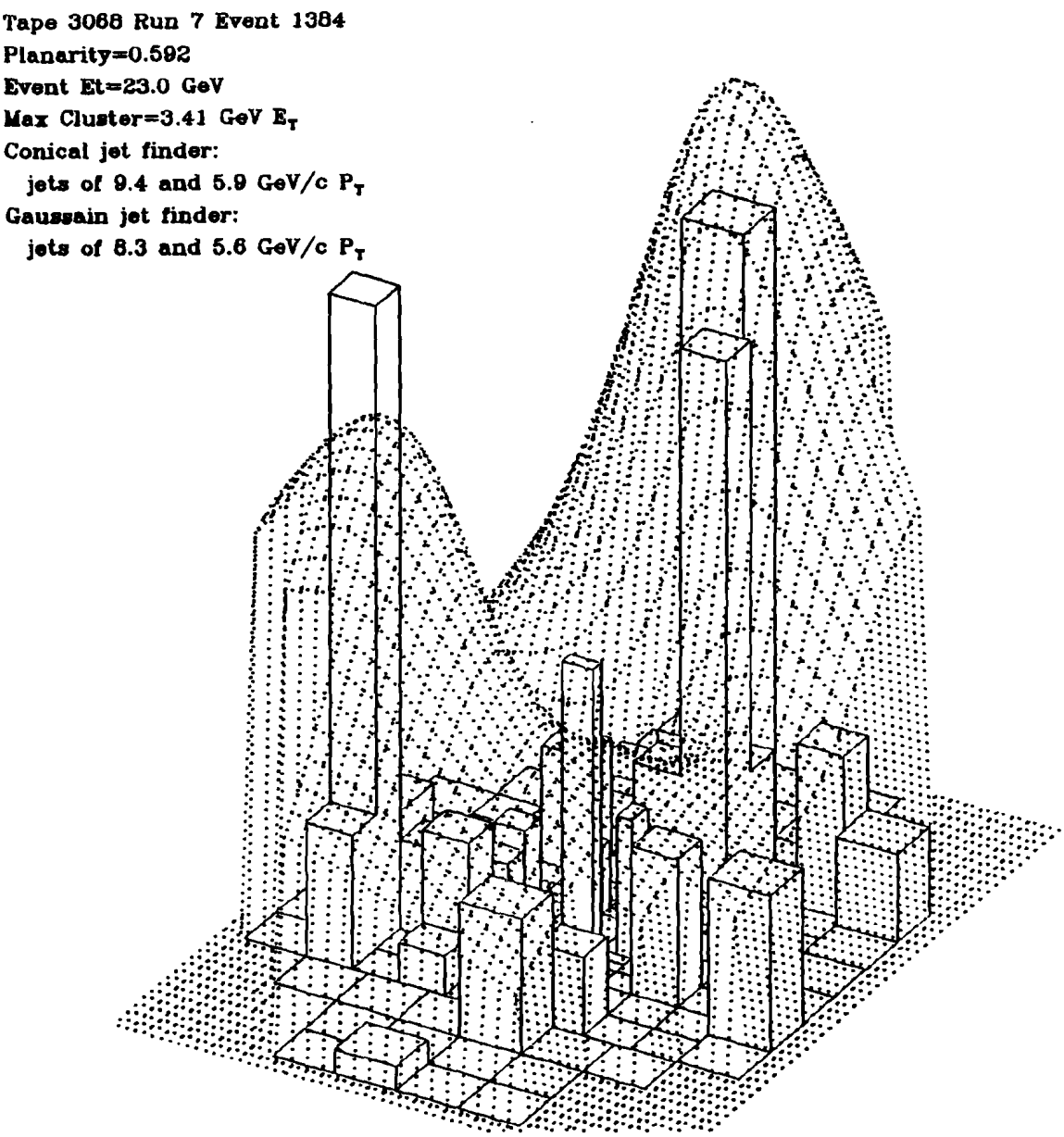

$$G = \sum_{i=1}^{n\ \text{clusters}} P_{T_i} \exp\left[- \frac{(\phi-\phi_i)^2}{2\sigma_\phi^2} - \frac{(\eta-\eta_i)^2}{2\sigma_\eta^2} \right].$$

New variables here, σ_η and σ_ϕ, set the width of the Gaussian, determining, like the cone angle size, many features of the jets.

3.2.1 Gaussian Jet-Finder Flow Chart

Figure 3.9 describes the application of the Gaussian surface in locating jets. Again the free parameters, appearing in bold face, control the construction of jets, determining the availability of particles to start a new jet, a satisfactory first guess P_T, a minimum jet P_T, number of jets found, and the identification of specific particles with each jet.

3.2.2 Gaussian Jet-Finder Parameters

Of the ten parameters in the Gaussian jet-finder, σ_η and σ_ϕ, the Gaussian widths, determine most of the physics. Reporting on two pairs of values, [ALB79b] selected $\sigma_\eta = 0.5$ and $\sigma_\phi = 30°$ after studying these values along with $\sigma_\eta = 0.75$ and $\sigma_\phi = 45°$. Their conclusions, based on a simple Monte Carlo including jet events and a background of events from the minimum bias sample (later studies indicate jet background approaches twice the minimum bias background), state that "where the methods are applicable, for $P_T > 1.5$ GeV/c, there are no compelling differences between (the two sets of parameter values). The Gaussian smearing method with the narrow set of widths, being more restrictive, is, however, marginally better in representing the input [ALB79b]." The improved representation of the data appears

Figure 3.9 Gaussian Jet-Finding Flow Chart

A) Locate Local Peaks on the Gaussian P_T Surface

Loop over Clusters to Serve as Trial Peak Locations

1) Select cluster with the next largest P_T
   The cluster must have $P_T \geq$ G1 **(If not GOTO B)**

2) Use this (η, ϕ) position to start search for peak

3) Value of Gaussian surface at cluster location
   must have $P_T \geq$ G2 **(If not GOTO B)**

4) Locate the peak with a Gradient search using
   variable step sizes starting with DELϕ and DELη

5) Value of Gaussian surface at Peak location
   must have $P_T \geq$ G0 **(If not GOTO B)**

6) Compare this peak location with other jets
   a) If the peak differs from all other jets
      in pseudo-rapidity by > DIFη and in ϕ by > DIFϕ
      Record this Location as a New Jet
   b) If not
      Compare Peak and Nearby Jet
      If Surface P_T is higher for jet location
         skip this location
      Else if Surface P_T is higher for peak location
         overwrite jet with new location

7) This jet is located so look for next jet **(GOTO A)**

B) For Each Cluster Locate the Jet it Belongs with

1) Loop over jets and calculate cluster to jet distance

2) Include a cluster in a jet (closest jet first) if:
   a) FWHM·Cluster $P_T \leq$ Jet $P_T \leq$ Cluster P_T
   b) $|$Jet ϕ - Cluster $\phi| \leq \pi/2$
   c) The Gaussian surface continually increases from the
      cluster to the jet maximum. (Checked in 5 steps)

3) Loop over all free clusters. Clusters failing tests in
   step B2 are not included in any jet

C) Calculate the Jet Physics

1) loop over each jet
   Jet P_T = Gaussian peak height, @(η, ϕ)

2) Calculate physics based on pair of highest P_T jets

Figure 3.10 **P_T(Monte Carlo)-P_T(found) vs. Gaussian Width Parameters**

For four bins of found jet P_T's, the relationship between Gaussian width parameters and ΔP_T shows that the optimum width equals 0.579. Monte Carlo input events come from all triggering two-high events.

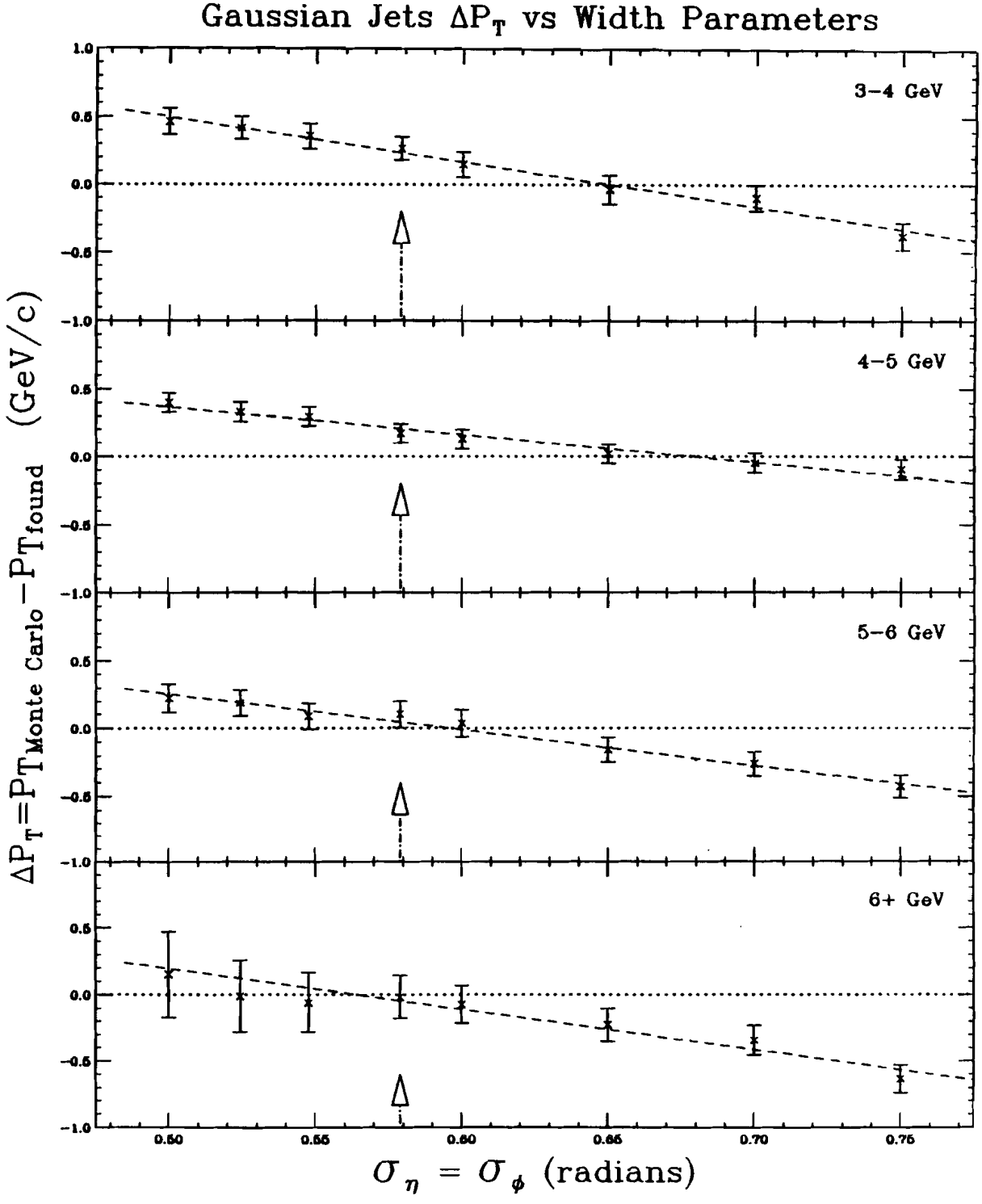

Figure 3.11 E_T(Monte Carlo)-E_T(found) vs. Gaussian Width Parameters

Four bins of found jet P_T show the relationship between Gaussian width parameters and ΔE_T.

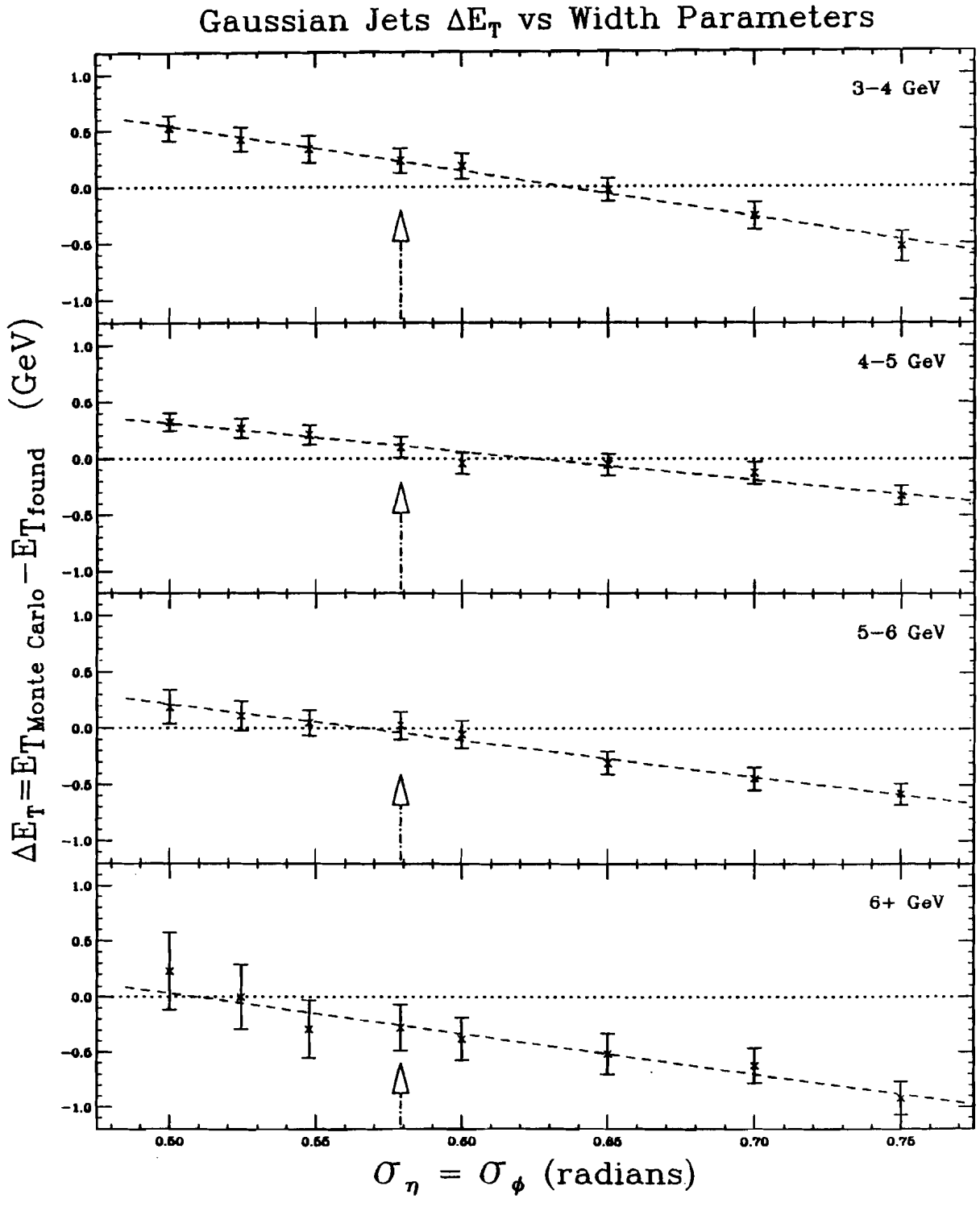

Figure 3.12 **# Jets Found/# Jets in M.C. vs. Gaussian Width Parameters**

For four bins of found jet P_T's, the ratio of the total number of jets found over the total number generated is shown as a function of the width parameters.

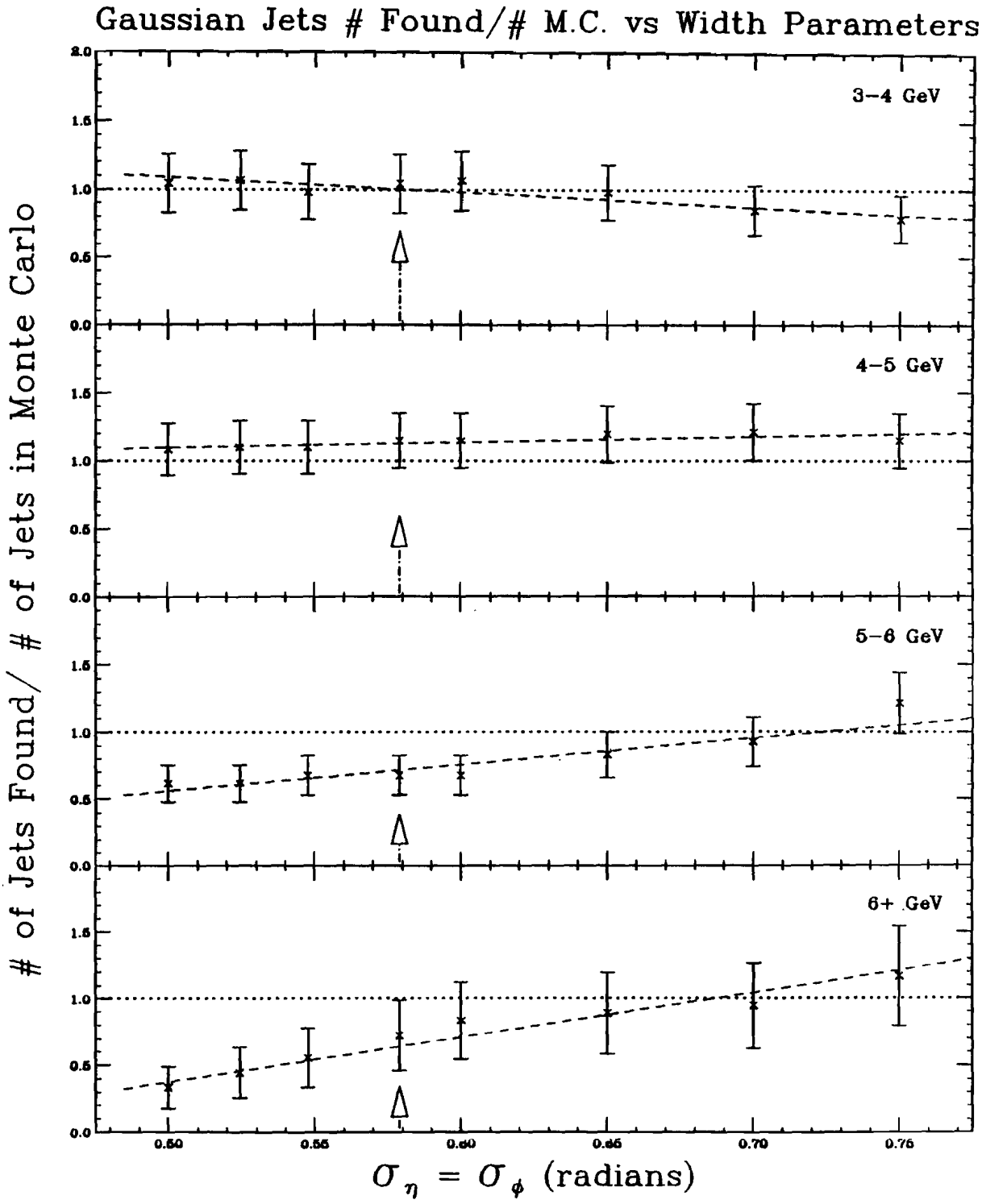

mostly in a plot comparing the number of jets found by each jet-finder with the number of jets available in the Monte Carlo sample. Jet--finders can locate more jets at a given P_T than the number present in the Monte Carlo by joining background particles with real jet particles to synthetically elevate the jet P_T; narrow Gaussian parameters reduce this effect. For our purposes the number of jets found at each P_T is important, but more important is the correct estimation jet P_T. Figure 3.10 plots the difference in mean Monte Carlo jet P_T minus the mean jet P_T for the Gaussian jet-finder over a range of σ_η and σ_ϕ values. Excluding the uncertain 3-4 GeV/c bin, as was done with the conical jet-finder, the optimum values for the Gaussian smear parameters are 0.579 for σ_η and 33.2° (0.579 rad) for σ_ϕ. Again, jet E_T and the number of found jets over the number of Monte Carlo jets in each P_T bin (figures 3.11 and 3.12) help determine the optimum values.

Three parameters determine the the P_T jet thresholds, G1, G2 and G0. G1 (0.8 GeV/c) sets the P_T threshold for the initial cluster to start a jet. G2 (0.9 GeV/c) sets the minimum height of the Gaussian surface for the search to continue and G0 (1.0 GeV/c) determines whether a peak qualifies as a jet. The final jet sample depends only slightly on the first two parameters since most jets of interest contain a triggering particle already passing a high P_T threshold while the third parameter, akin to P_TCUTOFF, determines the number of three and four jet events located by this jet-finder. Below 1.0 GeV/c the Gaussian jet-finder fails to distinguish jets from the background, therefore [ALB79b] set G0 to 1.0 GeV/c, while [JOH85] and [TON85] set this value to 3.0 GeV/c (with G1 = 0.6 GeV/c and G2 = 1.2 GeV/c). To match the number of jets found by both the conical and Gaussian jet

-finders, we set **G0** equal to 1.0 GeV/c, however we effectively increase it to 4.0 GeV/c since we study only these higher P_T jets.

Location of the maximum peak utilizes a gradient search which follows the steepest delta P_T along η and ϕ to reach a local peak. Step sizes along the 2 directions vary with the slope magnitude; initially **DEL**η and **DEL**ϕ equal 0.04 and 0.04 radians, increasing or decreasing by factors of two until the trial peak location changes by less than 0.01 GeV/c. After identifying a possible jet axis, we require a separation of new jets by **DIF**η (0.579) in η and by **DIF**ϕ (33.2° = 0.579 rad) in ϕ from all other located jets, avoiding overlapping jets within the Gaussian width parameters.

Determining the particles within a jet, **FWHM** defines a contour delineating the clusters qualifying as jet members. Setting this parameter to 0.5, the ISR choice, creates jets which average two particles smaller that the Monte Carlo jets (see figure 3.13B), primarily due to missing wide-angle low-P_T Monte Carlo jet fragments. As shown in figure 3.13A, the 45° cone angle misses a similar number of particles; we therefore leave this parameter at 0.5. Table 3.3 lists the Gaussian jet-finder parameter values used in this study.

Figure 3.13A # M.C. Jet "Particles" - # Conical Jet "Particles"

The difference in the number of clusters (≃ particles) generated in the jet minus the number found by the conical jet-finder in four bins of mean jet P_T.

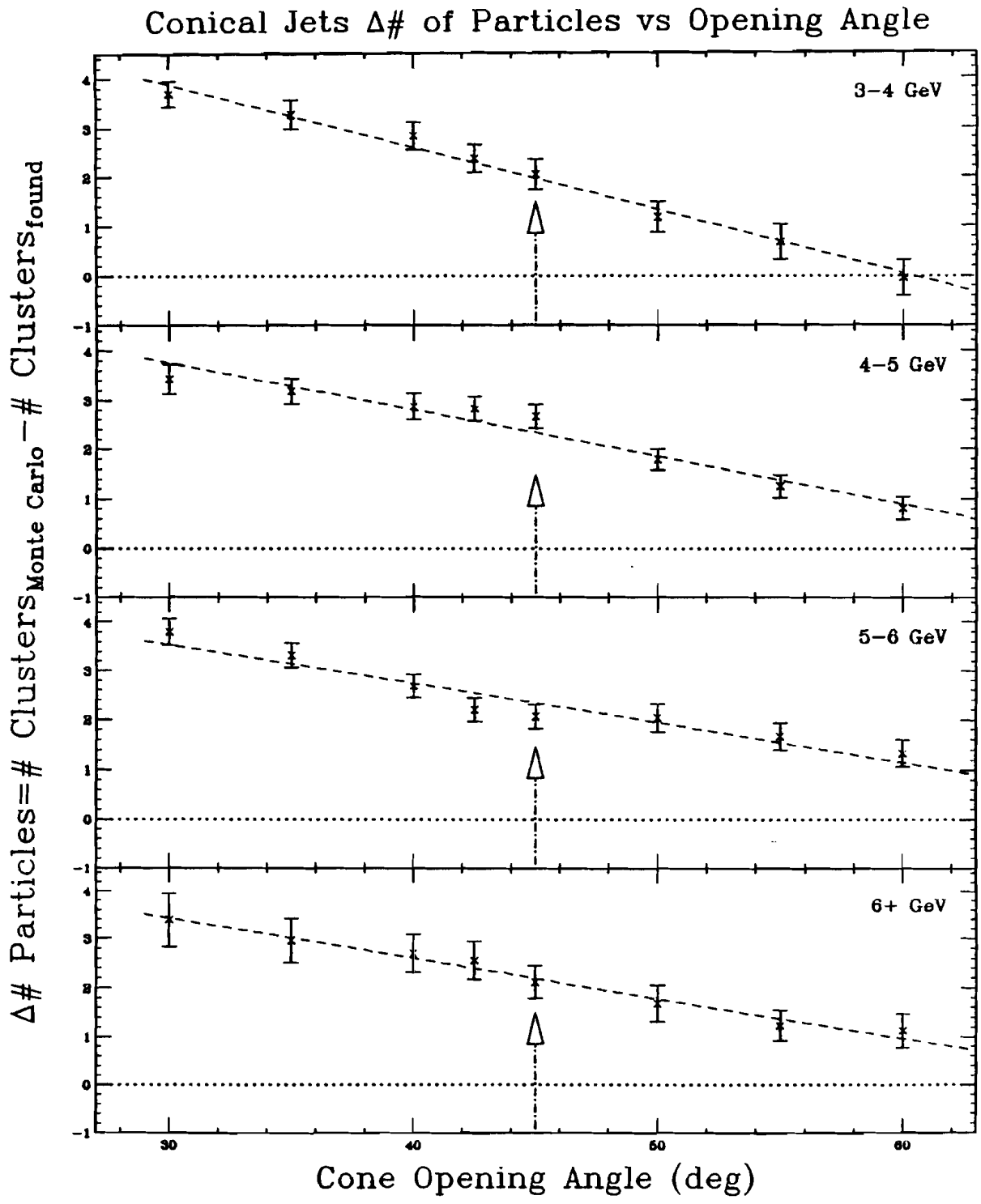

Figure 3.13B # M.C. Jet "Particles" - # Gaussian Jet "Particles"

The difference in the number of clusters (≃ particles) generated in the jet minus the number found by the Gaussian jet-finder in four bins of mean jet P_T.

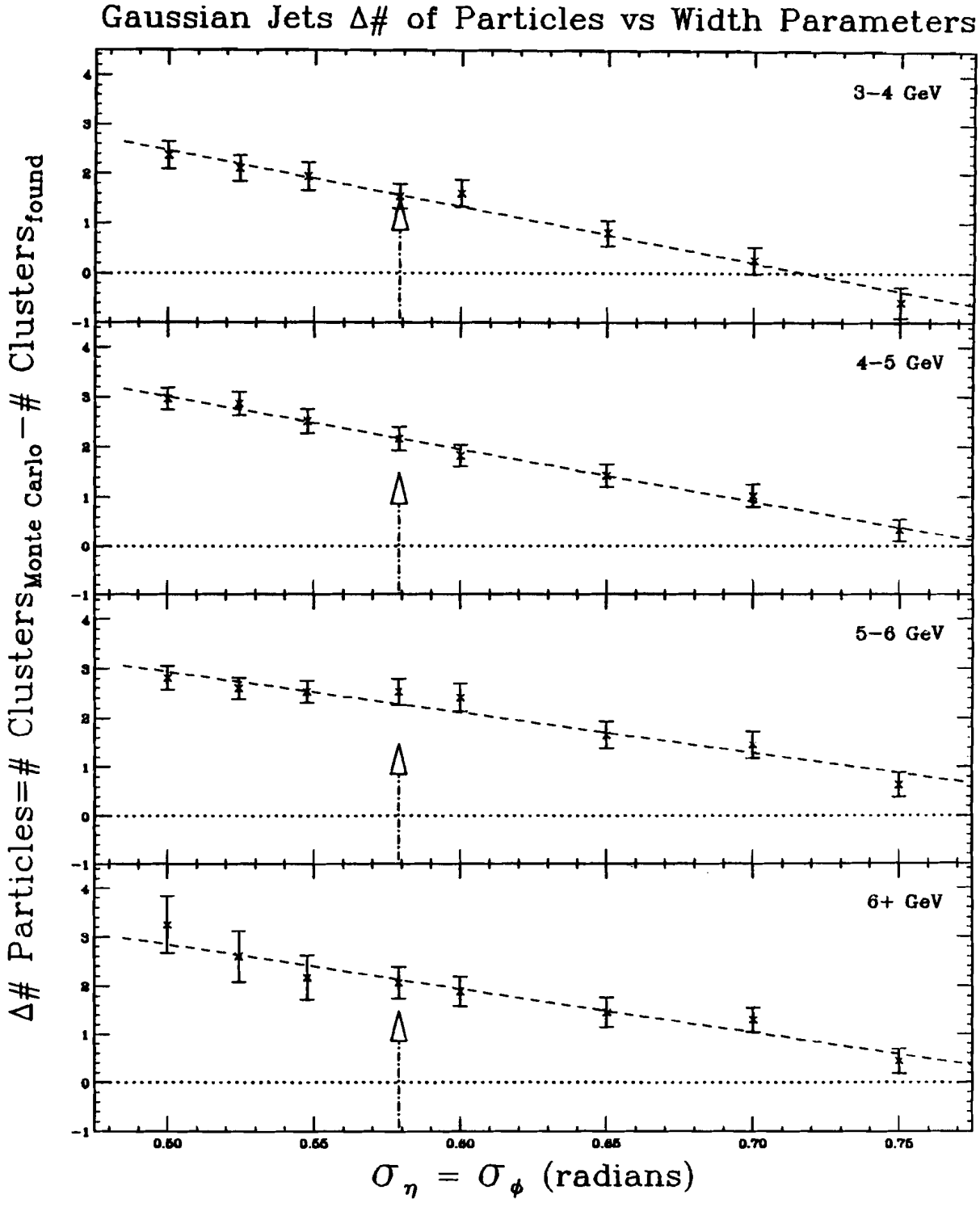

TABLE 3.3
Gaussian Jet-Finder Parameters

PARAMETER	VALUE	DETERMINATION
σ_η	0.579	P_T(Monte Carlo)-P_T(Jet-Finder)
σ_ϕ	33.2°	P_T(Monte Carlo)-P_T(Jet-Finder)
G1	0.8 GeV	Minimum Cluster P_T
G2	0.9 GeV	Minimum Gaussian height at Cluster (η,ϕ)
G0	1.0 GeV	Minimum Jet P_T (4.0 GeV effective)
DELη	0.04	size to start variable search
DELϕ	0.04 rad	size to start variable search
DIFFη	33.2°	Match width of Gaussian smear
DIFFϕ	0.579	Match width of Gaussian smear
FWHM	0.5	Half Maximum value

CHAPTER 4

RESULTS

Our results from data analysis lie in five classes: the general properties of events containing jets, the internal jet structure, the di-jet structure, the properties of the beam jet and target jet (target jet strictly by inference), and an examination of the region near 90° in the center-of-mass but away from the triggering jets, the "rotated" jet region. For each property studied one must examine the basic property and then observe how it changes as a function of mean jet P_T and atomic number. The general event structure, discussed in [MIE88,MAR88], requires a brief mention here, while the jet structure study requires in-depth analysis.

The uncertainties presented in the data are statistical only; the systematic errors between the nuclear targets (Be...Pb) should be no more than a few percent; regular target changing removes biases due to detector drift, while similar analysis for all the targets removes model dependencies. The major systematic uncertainty in our data results from different target-to-calorimeter distances for the hydrogen target and the nuclear targets (~1 meter). This effect has been accounted for in the analysis; however the slightly different solid angle and its effect on the event trigger may introduce an inherent bias in the events collected. We estimate the uncertainty in our correction of this effect as 15-20% for comparisons between the

hydrogen cross section and the nuclear target cross sections [MIE88]. One should note that our hydrogen point tends to agree with an A^{α} fit much better than the fit observed in the early E557 data [BROW83], however E557/E672's recently reported data [STE88] concurs with our current fits. Tracks from all events were reconstructed and the event vertex was required to correspond to the target position. Our helium data contains ~10% background due to events from the target vessel walls with verticies which reconstruct in the fiducial volume, which, in turn causes an over estimate of the helium cross section. The results presented here do not contain a correction for this effect.

Calculation of the center-of-mass variables from the lab frame also introduces a slight reference bias; in every case we assume a proton-nucleon collision producing massless products. The proton--nucleon center-of-mass frame serves as a convenient compromise between the various frames one might choose including the jet-jet frame and the pA frame. The massless product assumption is necessary since particle identification was impossible for this experiment. The assumption of massless products becomes important in the calculation of the center-of-mass momentum of the soft particles; discussions involving the momentum of these particles is limited by our unphysical but internally consistent assumption of zero mass particles. Our estimates of the number of soft particles also reflect this assumption since the clustering algorithm contains thresholds which would change if the mass of the particles were known or all particles were given a pion mass.

Raw E_T-spectra corrections, arising from the calorimeter resolution effects, were estimated from the pp Monte Carlo. Generated

events were put through a calorimeter simulation and then analyzed in the same manner as the real data. The uniform correction (**ESCALE**=1.36) should be the same for all targets since the shape of the E_T-spectra is nearly independent of **A** [MIE88].

4.1 EVENT STRUCTURE OF HIGH P_T JETS

This thesis presents a study of events triggered on high transverse energy as a function of several variables such as jet P_T, E_T and planarity. Jet E_T is defined as the scalar sum of particle E_{T_i} over all particles identified as belonging to the the jet. Conical jet P_T is defined as the vector transverse momentum sum of particles comprising the jet, while Gaussian jet P_T equals the height of the P_T surface for the Gaussian jet-finder. In every case jet E_T is greater than jet P_T. In our data we cluster adjacent segments and assume the clusters represent physical particles, therefore P_T and E_T also include this additional assumption.

Planarity, a ratio described fully in §4.1.4, measures the the energy flow along the axes of an ellipse in the X-Y plane. Energy vectors from an isotropic event project onto the P_T plane uniformly and produce nearly equal major and minor elliptical axes. A di-jet event projects as a long narrow ellipse with unequal axes. Planarity, defined as the ratio of the length difference of the major and minor axes over the sum of their lengths, ranges from 0 for spherical events to 1 for two coplanar particles.

Limitations on the jet-finding algorithm require two selective cuts on the jets shown in the distributions. Loss of energy off the

calorimeter edges limits the allowed θ^* jet angle to $60° \leq \theta^*_{jet_1} \leq 110°$, as compared to the full azimuthal calorimeter coverage of 30° to 120° for hydrogen and 25° to 115° for the nuclear target position. To ensure proper jet-finding the mean P_T of the jet pair must be above 4.0 GeV/c. The 3.0-4.0 GeV/c bin is included in plots of various variables as a function of <Jet P_T>, the P_T of the jet pair; however the systematic errors on this point are large. Similar cuts were utilized by [ARE84] who observed that over half the events with jets in the 3-4 GeV/c bin resulted from background sources.

4.1.1 Jet E_T and P_T Distributions

Cross sections, the most throughly studied event property of our data [CORM85, ARE85, FLE88], represent the production rate of jets as a function of their transverse momentum. Jet production drops rapidly as the required transverse momentum increases. This trend is clearly seen in the hydrogen and lead jet P_T and E_T distributions, figures 4.1A-D. The sharp edge at low P_T and E_T reflects the threshold, set initially by the trigger and eventually re-set by the jet--finding parameters. Production of jets with P_T values below 3.0 GeV/c increases exponentially, however the jet-finders can no longer resolve between the individual jets and the non-jet background, which dominates for P_T's below 4 GeV/c. In general the two jet-finders agree, showing enhanced production of high P_T jets from lead over the production from hydrogen.

One of the major differences between the conical and Gaussian jet-finder definitions appears in comparing P_T and E_T. At large P_T

Figure 4.1 Average Jet P_T and E_T

A) Hydrogen & B) Lead:<Jet P_T> distribution is shown for the conical and Gaussian jet-finders.
C) Hydrogen & D) Lead:<Jet E_T> distribution is shown for the conical and Gaussian jet-finders.
All events contain at least two jets with P_T>3.0 Gev/c.
Recall that <Jet P_T>=($P_{T_{jet_1}}$+$P_{T_{jet_2}}$)/2 and <Jet E_T>=($E_{T_{jet_1}}$+$E_{T_{jet_2}}$)/2.

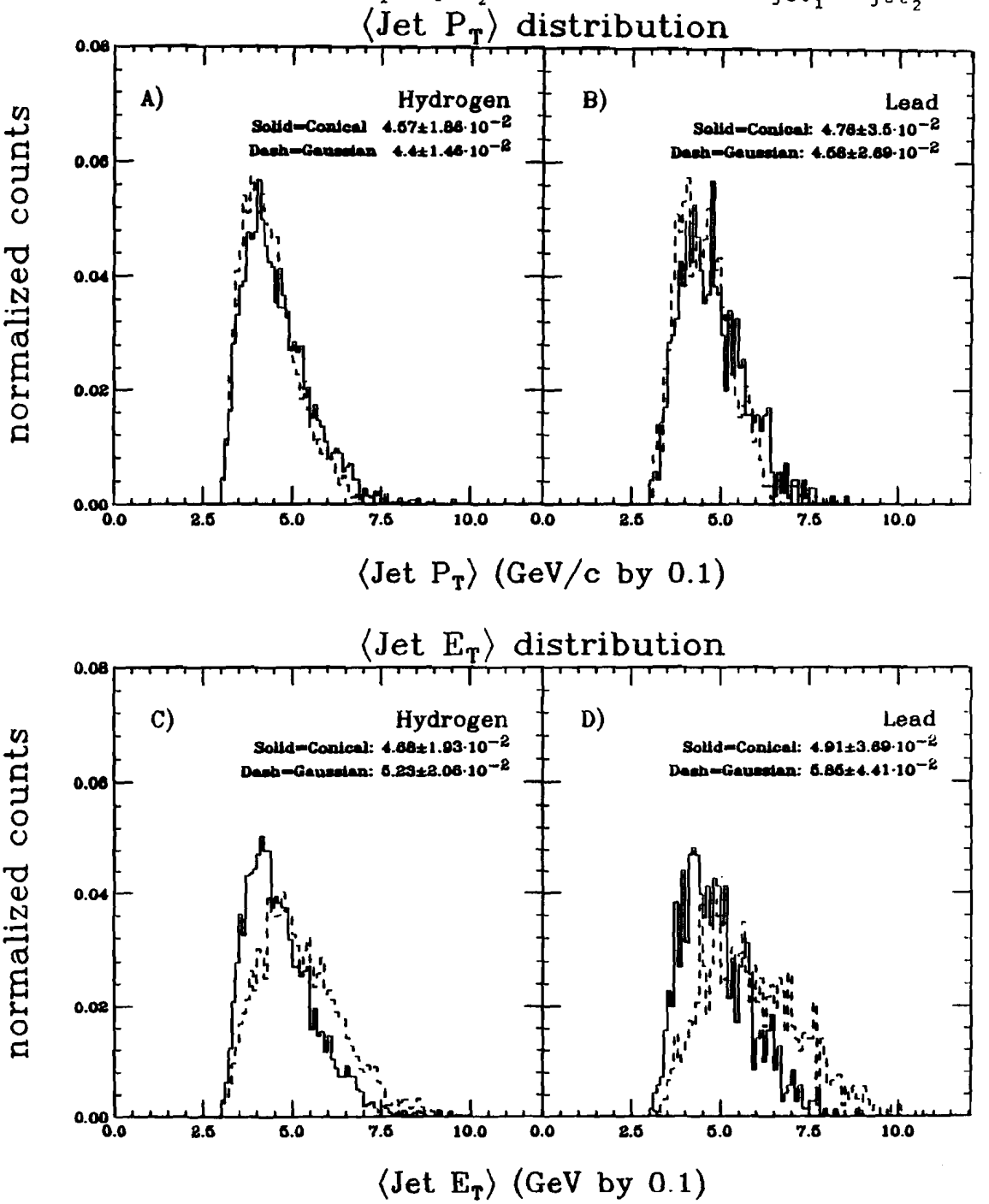

the conical jet-finder locates slightly more events than located by the Gaussian jet-finder; E_T distributions show the opposite trend. Summed over all targets, the conical jet-finder $<P_T>$ exceeds the Gaussian jet-finder $<P_T>$ by 0.15±0.05 GeV/c but the conical jet $<E_T>$ is lower than the Gaussian jet E_T by 0.77±0.05 GeV. The Gaussian jet-finder P_T definition requires more clusters to produce the same P_T as measured by the conical jet-finder definition; the additional clusters produce a higher E_T.

4.1.2 Raw Cross Section vs. <Jet P_T>

Figures 4.2A&B show the raw <Jet P_T> cross sections of our eight nuclear targets for the two jet-finders. Here <Jet P_T> equals $(P_{T_{jet_1}} + P_{T_{jet_2}})/2$ and the cross section is calculated from:

$$\sigma = N^* \left[\frac{A}{N_0 \rho L F} \right] = N/N_d$$

where N = The number of selected events
A = Molecular weight of the target material
N_0 = Avogadro's number (6.022×10^{23} particles/mole)
ρ = Density of Target (see table 2.1)
L = Target Length (see table 2.1)
F = Beam Flux, the corrected # of live beam particles
N_d = Number Density (see table 2.1)

Figure 4.2C compares the two jet-finder's raw cross sections. The conical jet-finder locates fewer jets with <Jet P_T> near threshold and more jets in the highest P_T bins than the Gaussian jet-finder. Figure 4.2D shows that the difference between jet-finders becomes

Figure 4.2A **Raw Conical Jet Cross Section**

A) The conical cross section for the 8 nuclear targets is shown without further corrections for triggering efficiency, jet reconstruction efficiency or adjustments to jet P_T. The jets satisfy $60° \leq \theta^*_{jet_1} \leq 110°$. The lines are exponential fits for data $\geq$ 4.5 GeV/c.

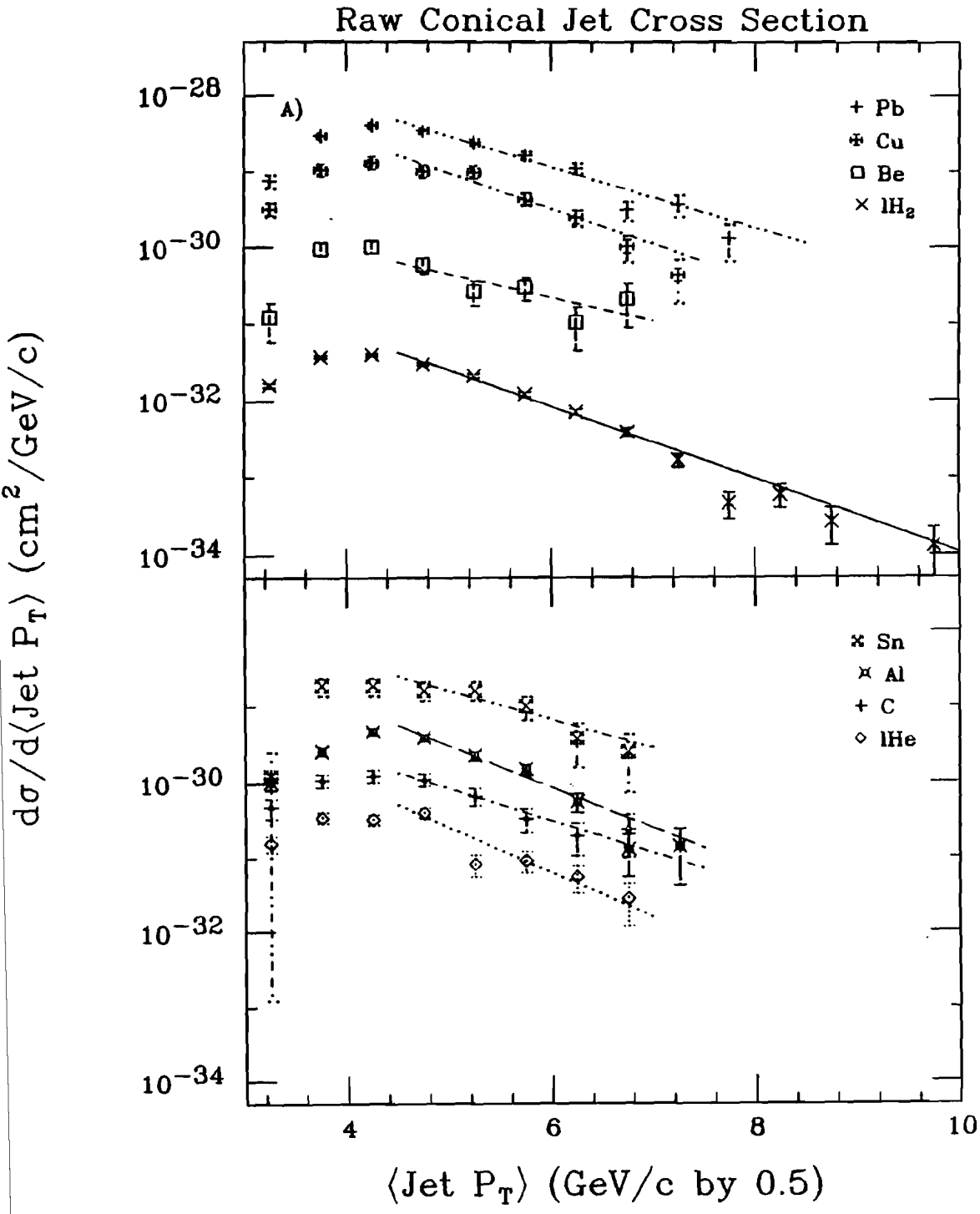

Figure 4.2B Raw Gaussian Jet Cross Section

B) The Gaussian cross section for the 8 nuclear targets is shown without further corrections for triggering efficiency, jet reconstruction efficiency or adjustments to jet P_T. Jets are selected to have $60° \leq \theta^*_{jet_1} \leq 110°$.

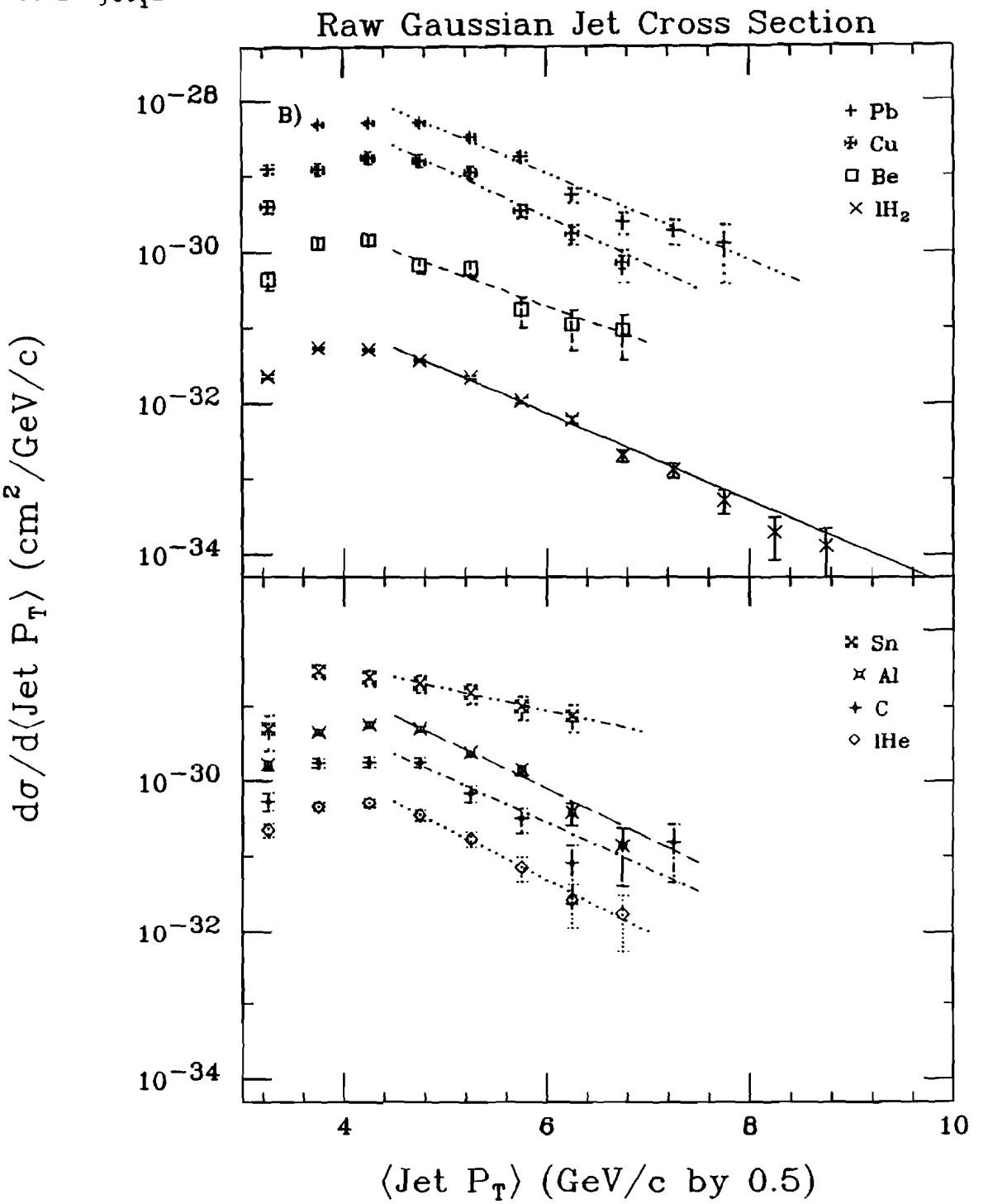

Figure 4.2C **Comparison of Raw Conical and Gaussian Jet Cross Sections**

C) Fits to the raw **conical** and Gaussian cross sections are compared for the 8 of the nuclear targets; two points per line are repeated from figures 4.2A&B. No corrections for triggering efficiency, jet reconstruction efficiency or adjustments to jet P_T have been included.

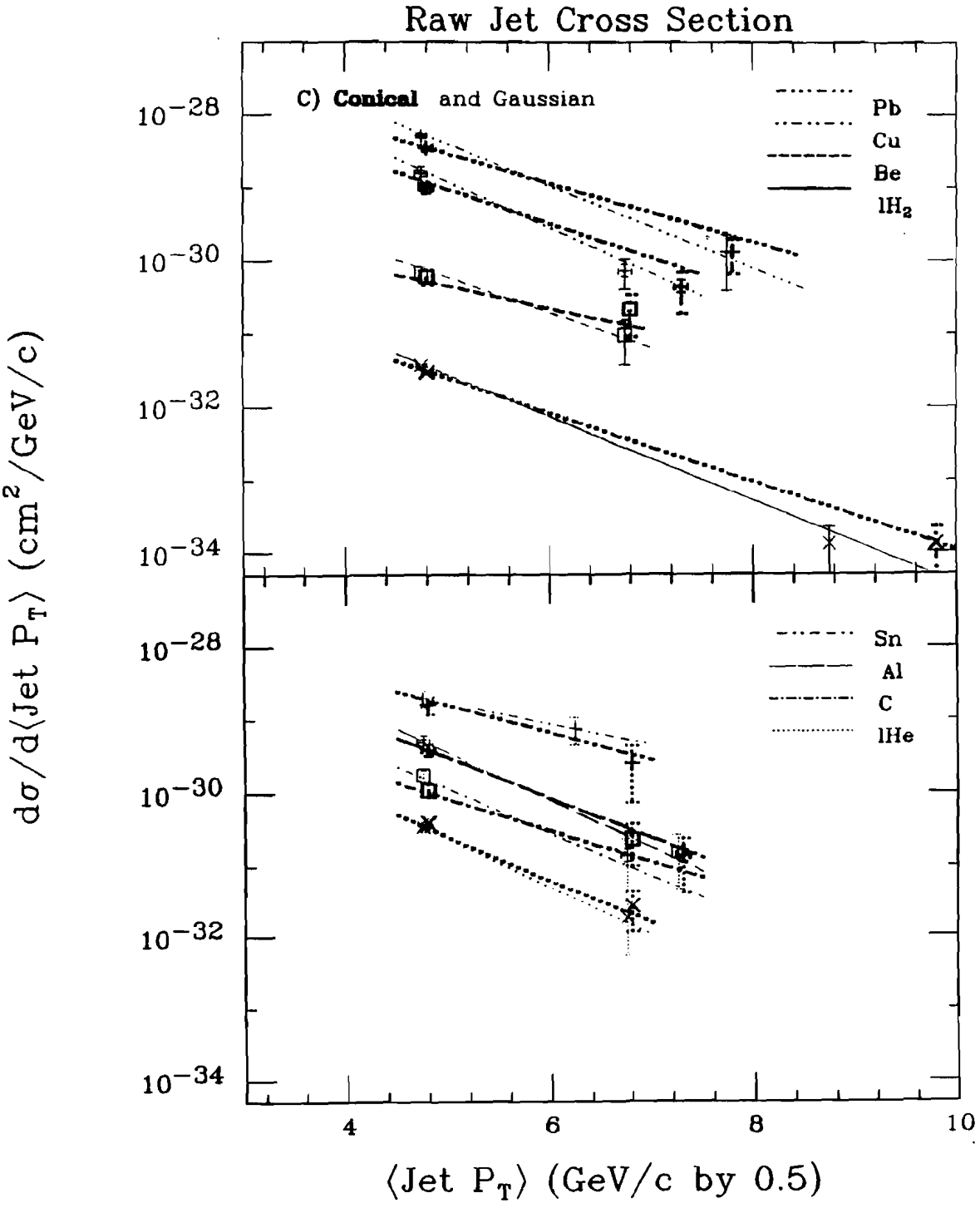

Figure 4.2D **Raw Jet Cross Sections corrected for P_T shift**

D) Fits to the raw conical and Gaussian cross sections have been shifted by the ΔP_T observed in the Monte Carlo. The shifts from figure 3.13 are approximated by the functions below. No corrections for triggering efficiency or jet reconstruction efficiency have been included.

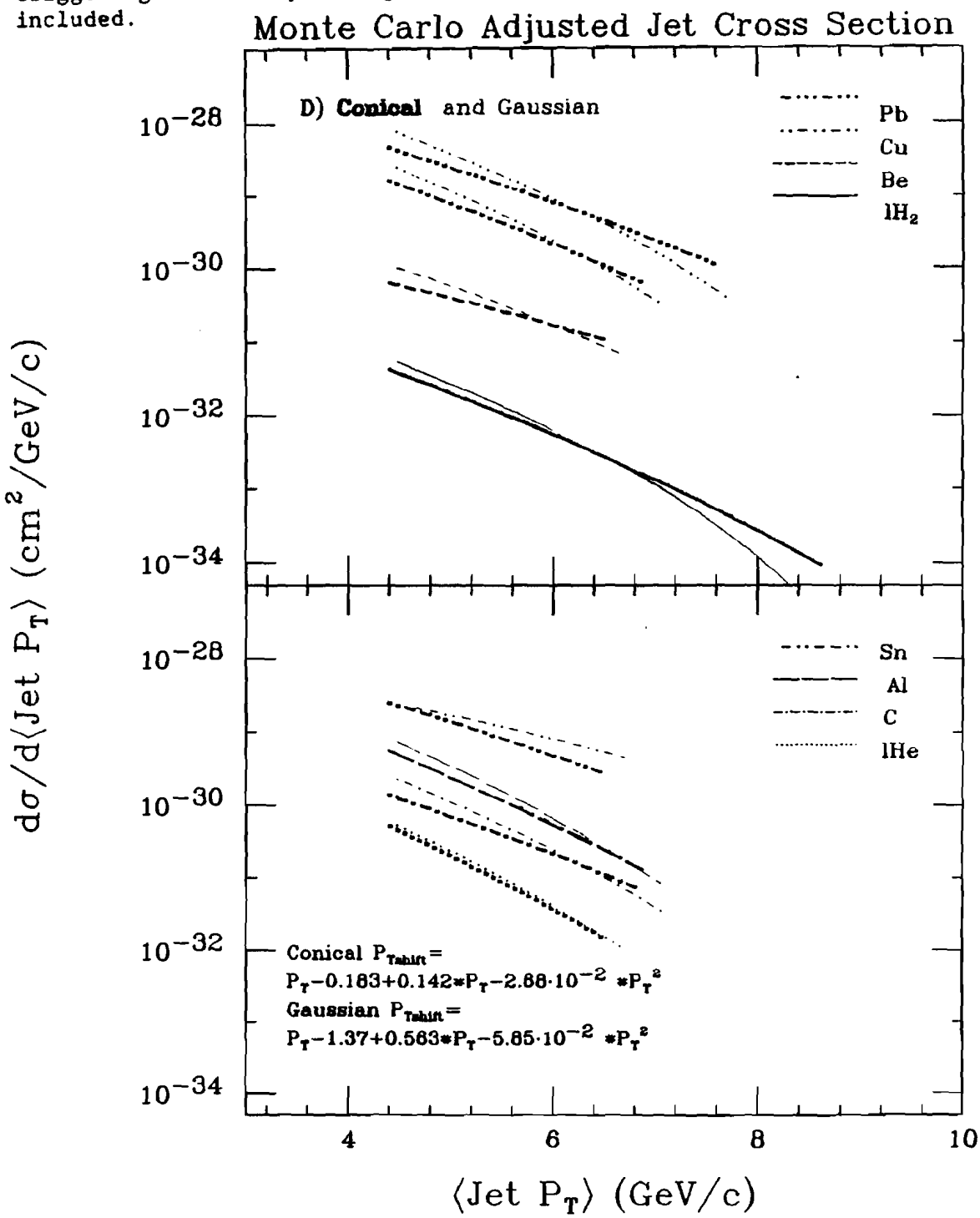

smaller when the found jet P_T's are shifted down to the "true" value as indicated by the ΔP_T Monte Carlo calculations (figure 3.13). Extracting the actual cross section for jet production from these raw cross sections requires another pair of corrections: a correction for the trigger efficiency (ranging from ~2% at small jet P_T's to nearly 100% at large jet P_T's) and an estimate of the jet-finder's ability to locate jets (ranging from ~2.5 times too high for $P_T \simeq 3.5$ GeV to ~50% too low for $P_T \simeq 7.5$ GeV). The focus of this thesis is not on the extraction of the full cross section (partially since it has been studied in the previously sited references and partially since these corrections cancel out when one considers the ratio of nuclear to hydrogen cross sections), however both jet-finders give basic agreement with the previous authors results after estimation of the various corrections [MOO88].

Table 4.1 lists the beam flux for the data used to collect our data. Chapter 2 give the cuts applied to reduce the raw events to the sample of usable events, (see also [MAR85]). Recall that the final sample of jets represents events having two jets with at least 3 GeV/c of P_T and having the average P_T of the jet pair $\geq$ 4 GeV/c. The jets also must have a θ^* angle with respect to the beam line of $60° \leq \theta^*_{jet_1} \leq 110°$. The angle cut assures that the jet lies well within the calorimeter.

TABLE 4.1

Numbers of: Beam Particles, Integrated Luminosity and Jets

TARGET CODE	TARGET LENGTH (cm)	# of BEAM PARTICLES	INTEGRATED LUMINOSITY (cm^{-2})	RAW 2-HI TRIGGERS
20 LH2	38.00	$1.59X10^{10}$	$2.54X10^{34}$	412912.
30 LHE	8.527	$1.14X10^{9}$	$1.83X10^{32}$	17760.
40 BE1	1.179	$1.62X10^{8}$	$2.35X10^{31}$	4496.
41 BE2	1.190	$1.71X10^{8}$	$2.51X10^{31}$	4602.
50 C2	1.275	$1.91X10^{8}$	$2.12X10^{31}$	5898.
51 C1	1.276	$1.69X10^{8}$	$1.89X10^{31}$	4943.
60 AL1	0.963	$4.08X10^{8}$	$2.37X10^{31}$	20610.
61 AL2	1.947	$1.24X10^{8}$	$1.45X10^{31}$	11425.
70 CU	0.358	$3.76X10^{8}$	$1.14X10^{31}$	25562.
80 SN	0.301	$1.19X10^{8}$	$1.33X10^{30}$	6809.
90 PB1B	0.178	$8.83X10^{7}$	$5.18X10^{29}$	5170.
91 PB1A	0.192	$2.19X10^{8}$	$1.38X10^{30}$	13320.
95 PB2B	0.366	$9.70X10^{7}$	$1.17X10^{30}$	9664.
96 PB2C	0.366	$8.20X10^{7}$	$9.89X10^{29}$	8229.
97 PB2A	0.368	$2.09X10^{8}$	$2.54X10^{30}$	21612.

Number of Events with Jets of <Jet P_T> $\geq$ 4 GeV/c & $60° \leq \theta^*_{jet_1} \leq 110°$

Target	Gaussian	Conical
$^1H_2$	2021	1781
^1He	128	109
Be	98	76
C	119	91
Al	346	305
Cu	349	286
Sn	63	56
Pb	670	550

4.1.3 A Dependence of Jet Cross Section

The typical method to compare cross sections as a function of atomic number, A, is to take the ratio of σ(pA), the proton-nucleus collision cross section, over σ(pp), the proton-proton collision cross section. If the probability of producing the desired jet type is related only to the number of nucleons in the target nucleus then this

Figure 4.3 α Calculation and α vs. <Jet P_T>

A) R = σ(pA)/Aσ(pp) vs. atomic number is shown for the conical and Gaussian jet-finders (Gaussian offset 5%). Lines fit through the log-log curve produce the reported α values.
B) α vs. <Jet P_T> is shown for both jet-finders; Gaussian points are offset 0.1 GeV/c. The dotted line results from events with E_T>18 GeV, spanning the indicated range of <Jet P_T> with a mean at 5.16 GeV/c and a mean planarity of 0.6.

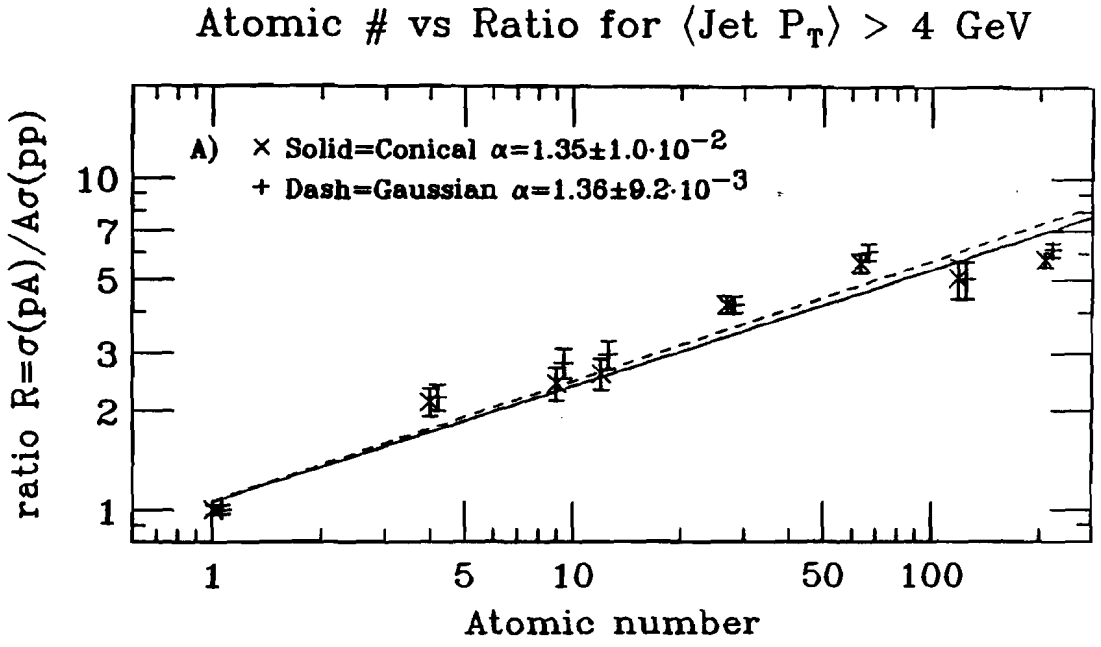

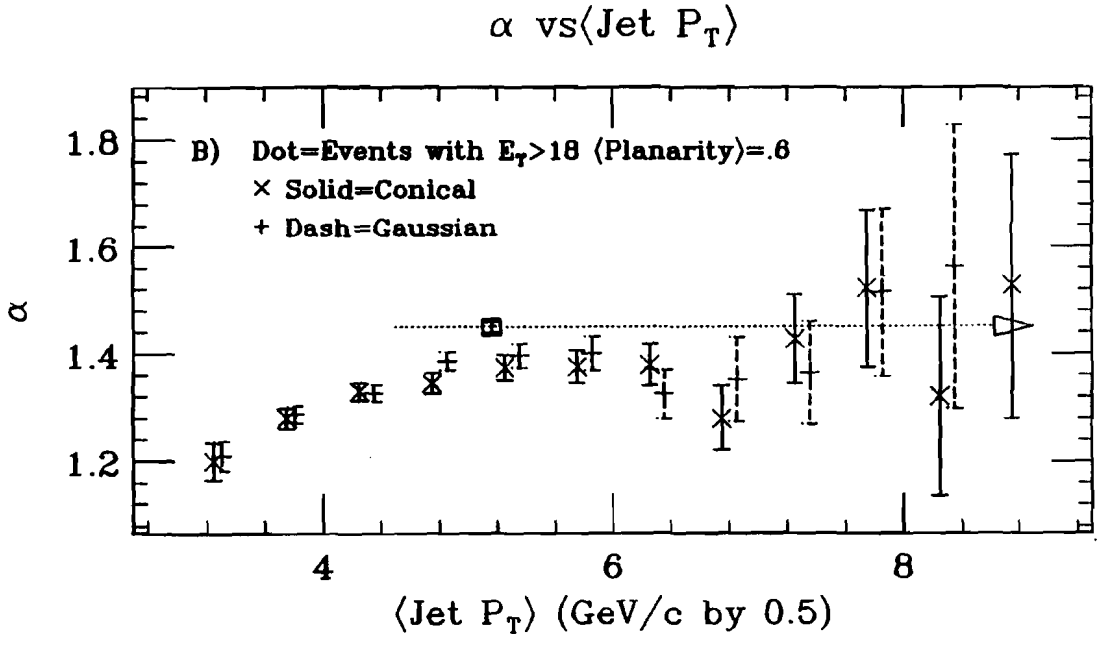

ratio will be equal to the atomic number, $A^{1.0}$. If the front surface is active in the collision, (occurring if the front nucleon surface "screens" the nuclear bulk), then the ratio would go as the area of the front face, or (using the observation that the nuclear radius, r, is proportional to the atomic number to the one third) the ratio $\sigma(pA)/\sigma(pp)$ would go as $A^{2/3}$. One should note that "nuclear screening", the name attached to $A^{2/3}$ processes, does not imply that the bulk of the nucleus is shielded during the collision; it implies that every proton incident on the nucleus interacts -- regardless of where it strikes the front face of the nucleus. Division by an additional factor of A gives the ratio $R = \sigma(pA)/A\sigma(pp)$; plots of $log(R)$ against the $log(A)$ have zero slope if the cross section increases in proportion to the number of available nucleons and a slope of -1/3 when screening is in effect. Figure 4.3A shows however, that for production of jets with <Jet P_T>'s greater than 4 GeV/c and $60° \leq \theta^*_{jet_1} \leq 110°$, additional nucleons increase the jet production probability *faster* than the number of scatters increases! Increased production of events with high P_T's, know as nuclear enhancement or as the Cronin effect, was first observed by Cronin in 1973 [CRO73]. Fitting a straight line through the various targets produces a slope with a value of 0.36, or (replacing the factor of A^{-1}) an α value of 1.35±0.01 for the conical jet-finder and 1.36±0.009 for the Gaussian jet-finder.

Figure 4.3B shows how α changes as a function of <Jet P_T>. As the jet-finder becomes more reliable (values of <Jet P_T> greater than 4.0 GeV/c) α rises to 1.35 and remains reasonably constant, perhaps climbing slightly again at the highest <Jet P_T> values. Selection of high planarity events with E_T values greater than 15 GeV produces an α

value somewhat smaller, around 1.14±0.02 [MIE88] (additional analysis by [MAR89] may indicate this value is 1.24±0.02). The lower α follows from the sharp planarity cut (see §4.1.4). Removing the planarity cut, events with 18 GeV of E_T contain jets ranging over a variety of <Jet P_T> values and produce a higher α value of 1.45, as indicated by the dotted line in figure 4.3B. The highest <Jet P_T> found by the jet-finders also produce α values near 1.45 however the statistics are to poor to distinguish between a rising value of α and a flat α value of 1.35.

Zmushko's explanation of nuclear enhancement [ZMU80B], based on simultaneous scatters contributing to the enhancement, predicts that the enhancement will grow sharply after the jet P_T exceeds the pp $\sqrt{s}/2$ since the single scatter is prevented while a dual scatter is still allowed. Our data runs out well before the <Jet P_T> of 13.7 GeV/c required to test this prediction.

4.1.4 Planarity

To circumvent the model dependency inherent in using a jet-finder, several variables exist which quantify an event's jet-like nature, measuring how closely an event resembles two coplanar particles, the "ideal" jet pair. Planarity, our standard variable for measuring the "jettyness" of an event, (sphericity and thrust are the other commonly used variables), operates in the transverse energy plane and describes energy deposition in this plane as an ellipse, comparing the lengths of the major and minor axes, λ_+ and λ_-. Specifically,

$$P = \left| \frac{\lambda_+ - \lambda_-}{\lambda_+ + \lambda_-} \right|$$

where

$$2\lambda_\pm = \Sigma p_x^2 + \Sigma p_y^2 \pm \left[\left[\Sigma p_x^2 - \Sigma p_y^2 \right]^2 + 4 \left[\Sigma p_x p_y \right]^2 \right]^{\frac{1}{2}}.$$

Isotropic events, with nearly equal major and minor axes, have planarities near zero. "Jet-like" events, where most of the transverse energy lies in two regions separated by 180°, have a long major axes and a short minor axes and produce planarities near 1. In general all events with planarities over 0.8 appear "jet-like" to the eye.

An algorithm-independent sample of reasonably jet-like events can be obtained by setting planarity and event E_T thresholds and calling events passing these thresholds jet-like. Figures 4.4A&B show the hydrogen and lead planarity distributions for events selected using three different triggers: the global trigger (resulting in a planarity distribution with a mean below 0.5), all events passing the two-high trigger, and events with E_T greater than 15 GeV passing the two-high trigger. The two-high trigger selects a sample of events considerably richer in jet-like events than the global E_T trigger. Figures 4.5A&B show the mean planarity as a function of E_T for hydrogen and lead events satisfying the two-high trigger. The high planarity at low event E_T reflects the two-high trigger; nearly all the E_T in the event comes from the two triggering clusters and conservation of momentum requires that they balance, producing a high planarity. The <planarity> drops as E_T increases, resulting from the addition of clusters beyond the triggering pair. This trend reverses

Figure 4.4 Planarity Distributions

A) Hydrogen & B) Lead: Normalized planarity distributions are shown for events passing the 2-hi trigger(solid), 2-hi trigger events with E_T>15 GeV(dots), and events passing the global E_T trigger(dash). C) Hydrogen & D) Lead: Normalized planarity distributions are shown for events with <Jet P_T>24.0 GeV/c & $60° \leq \theta^*_{jet_1} \leq 110°$ for the conical(solid) and Gaussian(dash) jet-finders. FF Monte Carlo(dotdash, area reduced 50%) and 2-hi trigger events with E_T>15 GeV & planarity>0.8(dots) are also shown. [# of events in (), means in <>].

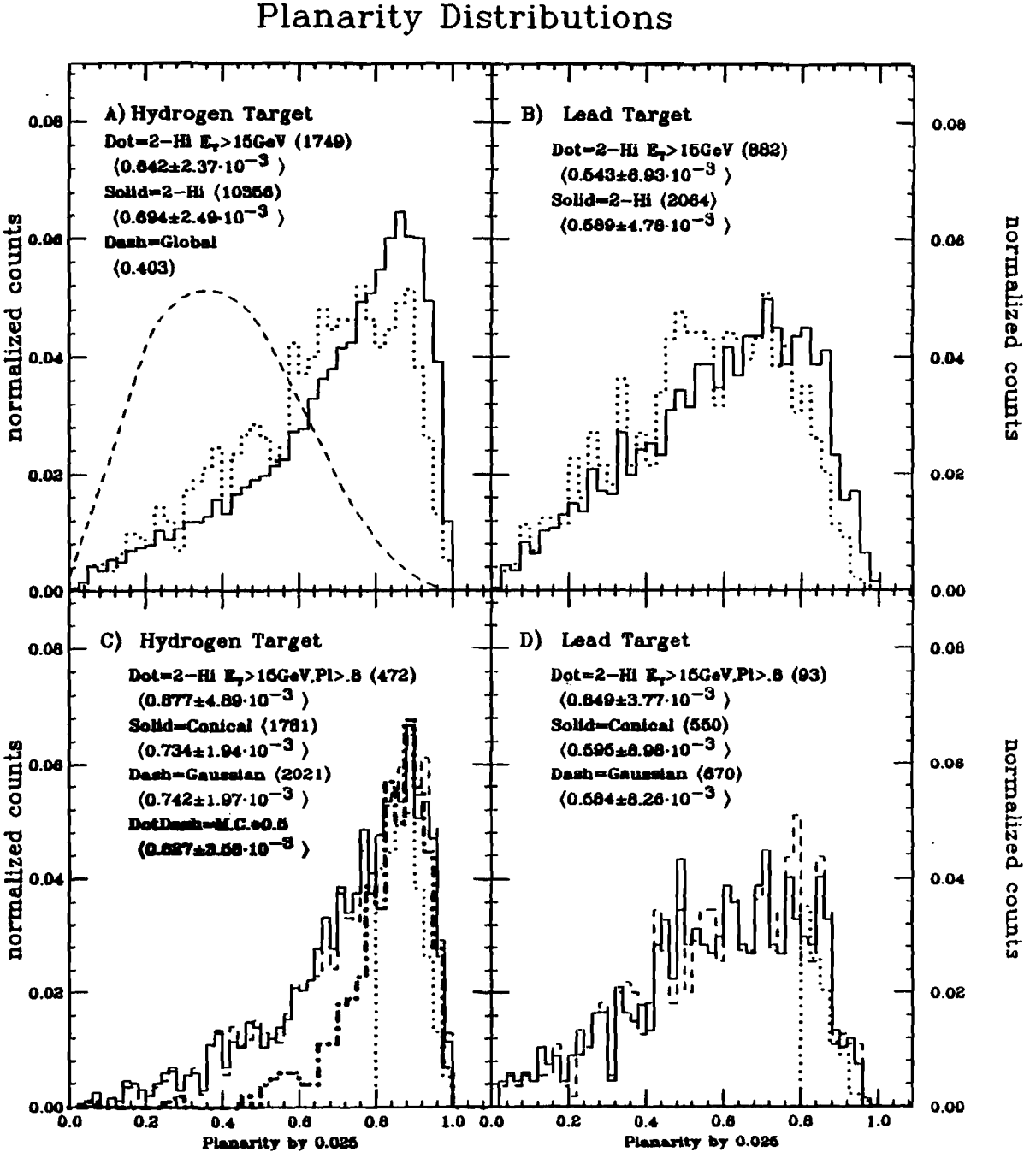

Figure 4.5 <Planarity> vs. Event E_T

A) Hydrogen & B) Lead: The mean planarity is shown, in 1.0 GeV bins of event E_T, for events passing the 2-hi trigger (solid) and for events where both jet-finders located at least two jets with <Jet P_T> greater than 3.0 GeV/c (dash).

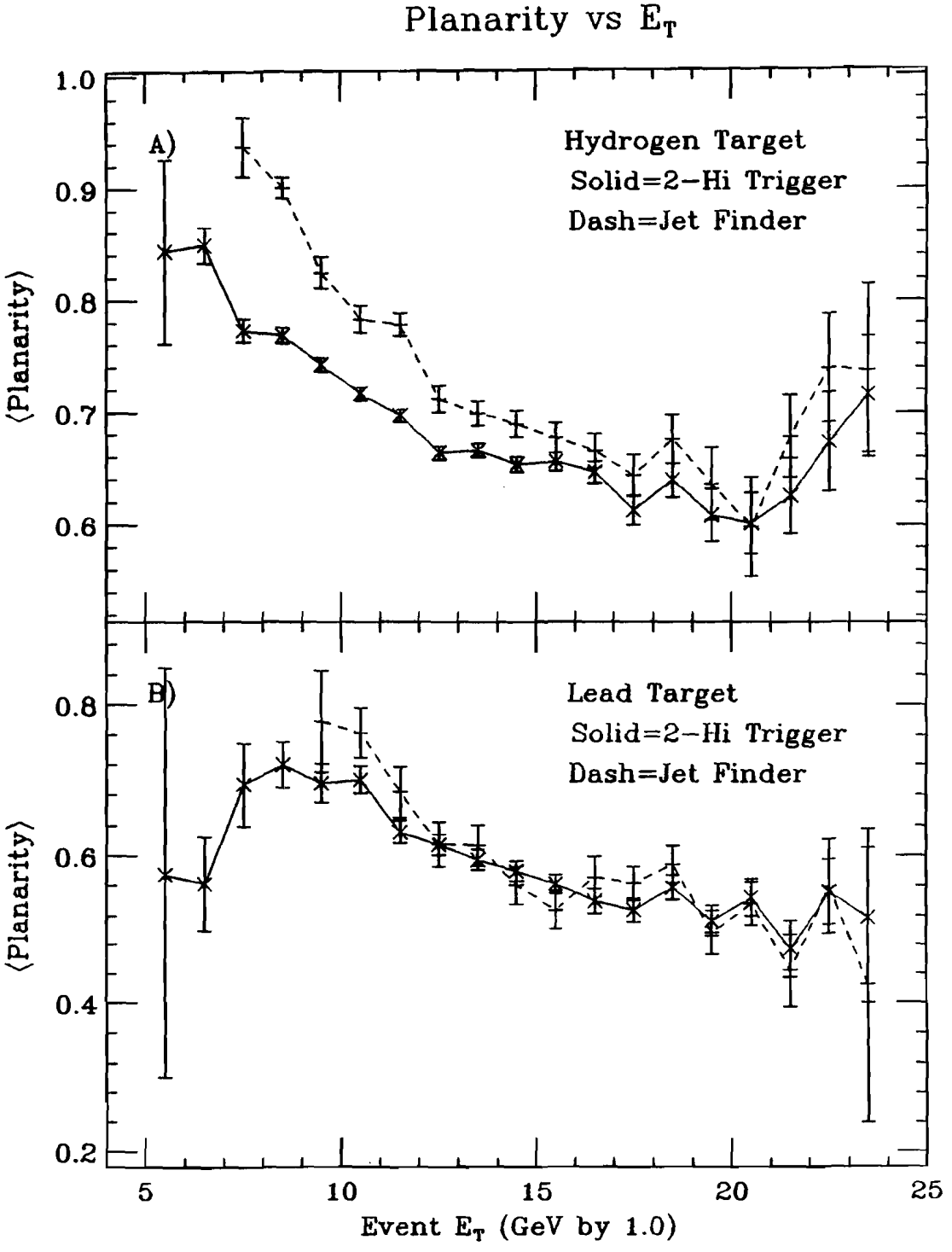

Figure 4.6 **<Planarity> vs. <Jet P_T> and Atomic Number**

A) Hydrogen and **Lead** <Planarity> is shown as a function of <Jet P_T> for the conical (solid,**dotdash**) and Gaussian (dash,**dot**) jet-finders. The **lead target** produces uniformly lower planarities.
B) Conical (solid) and Gaussian (dash) <Planarity> is shown as a function of atomic number.

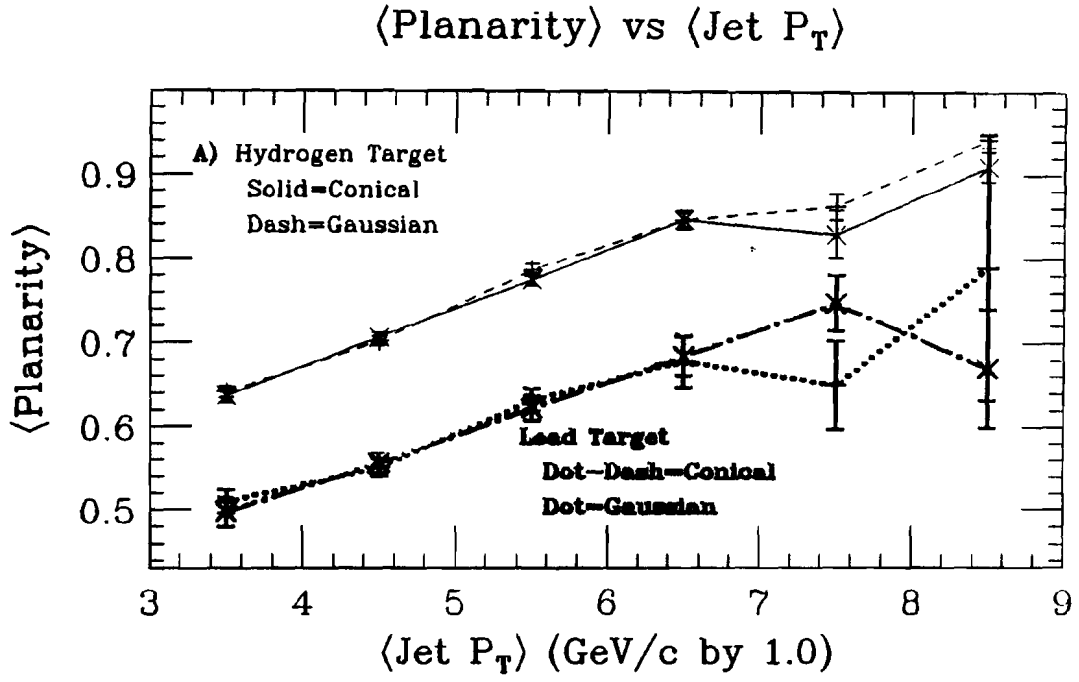

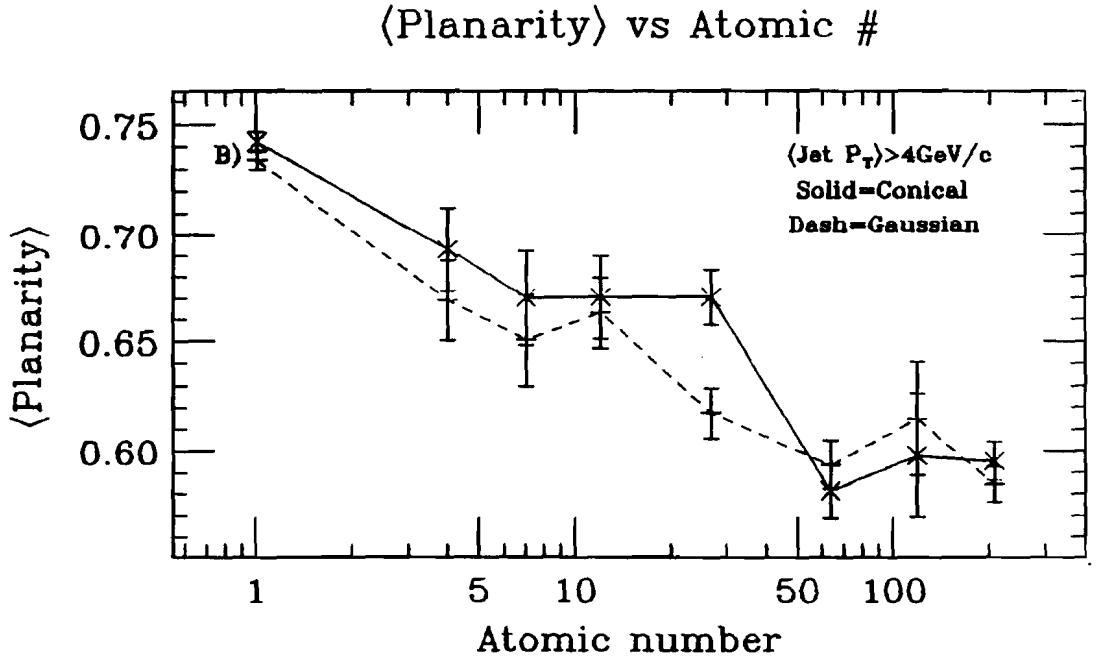

and the <planarity> rises again at the highest E_T's since the jet-like event cross section begins to dominate trigger-clusters-plus-spectator cross section. The lead <planarity> versus E_T curve reproduces the shape of the hydrogen curve at a lower <planarity> and without the rise at highest E_T's. The jet-like event cross section never dominates the increased cluster multiplicity found in 400 GeV p-Pb collisions. Selecting events with a pair of jets with P_T over 4 GeV/c (and passing the fiducial cut), increases the mean planarity above the values obtained with applying a 15 GeV E_T threshold selection, as shown in figures 4.4C&D. Very little change in mean planarity occurs when lead events with jets are selected from the larger sample of events passing the two-high trigger, figures 4.4B&D.

In figures 4.4C&D, one also sees how the jet-finder planarity distributions compare with events selected for high event E_T. The jet-finders agree reasonably well with the claim that jet-like events can be selected by requiring planarity greater than 0.8 and event E_T greater than 15 GeV (as was done in [MIE88]). This selection criteria however retains only 25% of the hydrogen events identified as having two jets with more than 4.0 GeV/c P_T, biasing the sample against the lower planarity events which nevertheless have two jets of P_T greater than 4 GeV/c using the jet-finder to define jets.

Event planarity increases as the <Jet P_T> increases (demonstrated in figure 4.6A); however, increasing the atomic number of the target decreases the planarity (figure 4.6B). Planarity is strongly coupled with event multiplicity; as the atomic number of the nuclear target increases the total number of clusters in the event increases accompanied by a decrease in mean planarity.

Plots of the ratio $\sigma(pA)/A\sigma(pp)$ in bins of planarity also produce nearly linear increases with the *log* of the atomic number, figure 4.7. As the planarity increases the slope of the ratio-versus-*log*(A) drops dramatically, starting with an α value as high as 1.7±0.2 for event planarities between 0.0 and 0.1 and dropping to 1.06±.04 for planarities between 0.9 and 1.0. The drop in α implies a reduction in the nuclear enhancement mechanism for events that contain a hard parton scatter and a fragmentation mode which retains the properties of the original scatter. Figure 4.8 shows the decrease in the value of α as the planarity increases. For reference, the α for two-high trigger events selected with E_T greater than 15 GeV and planarity greater than 0.8 or less than 0.5 appear as dotted lines in figure 4.8. Similar values are reported by the E672 experiment.

Figure 4.7 **α Generation:** $\sigma(pA)/A\sigma(pp)$ vs. A in bins of Planarity

Figure 4.7 demonstrates the lines with slope α resulting from linear fits to $log[\sigma(pA)/A\sigma(pp)]$ vs. $log(A)$ in planarity bins 0.1 units wide for conical jets with <Jet P_T> greater than 4.0 GeV/c and $60° \lesssim \theta^{*}_{jet_1} \lesssim 110°$. α is the slope of the dotted line.

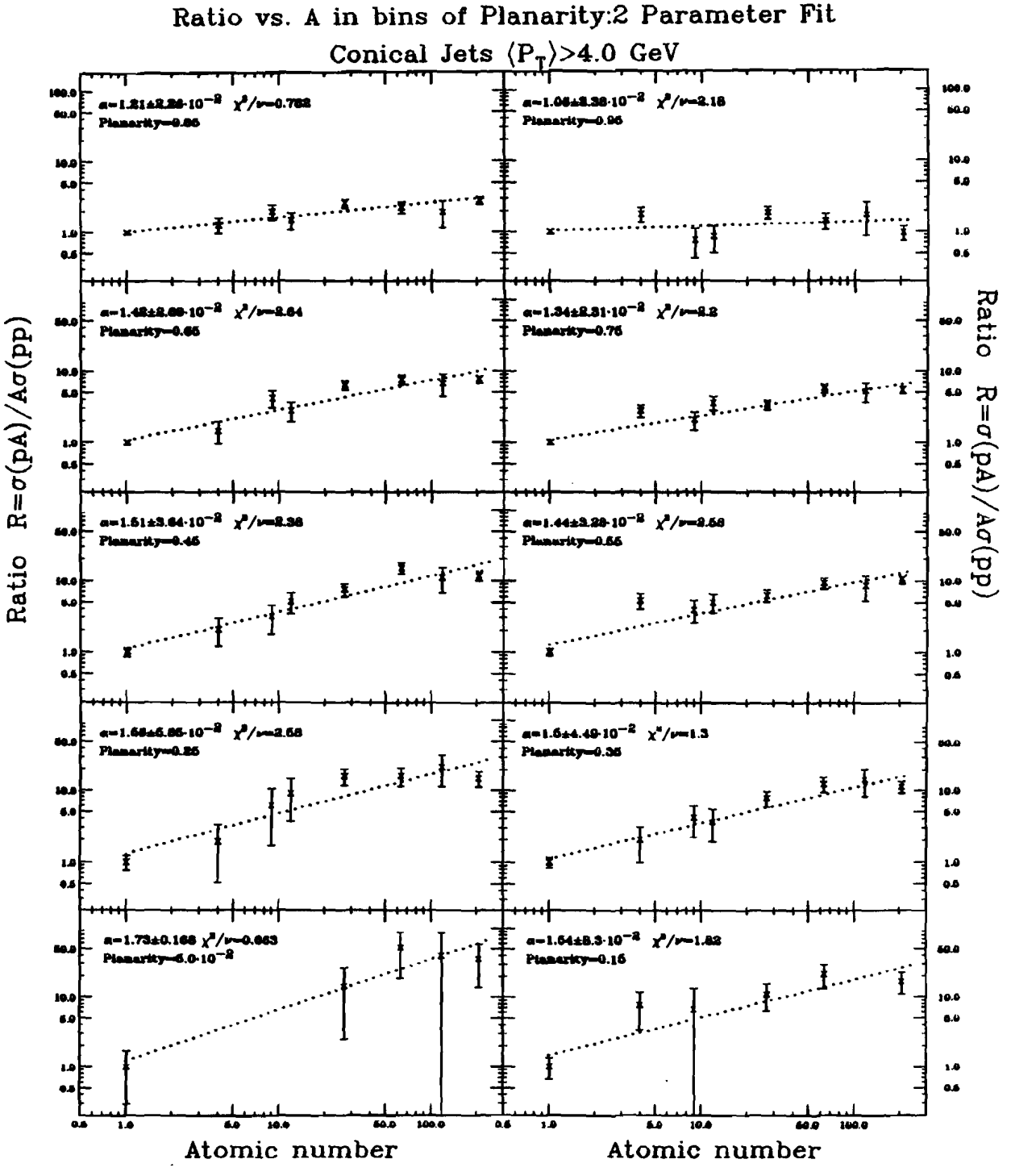

Figure 4.8 α vs. Planarity

Figure 4.8 shows planarity vs. α in 0.05 bins for the jet-finders averaged together (the stars); both jet-finders produce α values consistent within errors in each planarity bin. The squares result from events selected for E_T > 15 Gev and planarity below 0.5 or above 0.8 [MIE88] (dots). E672 α values for events collected with a global trigger [GOM86c] are shown as circles (dash).

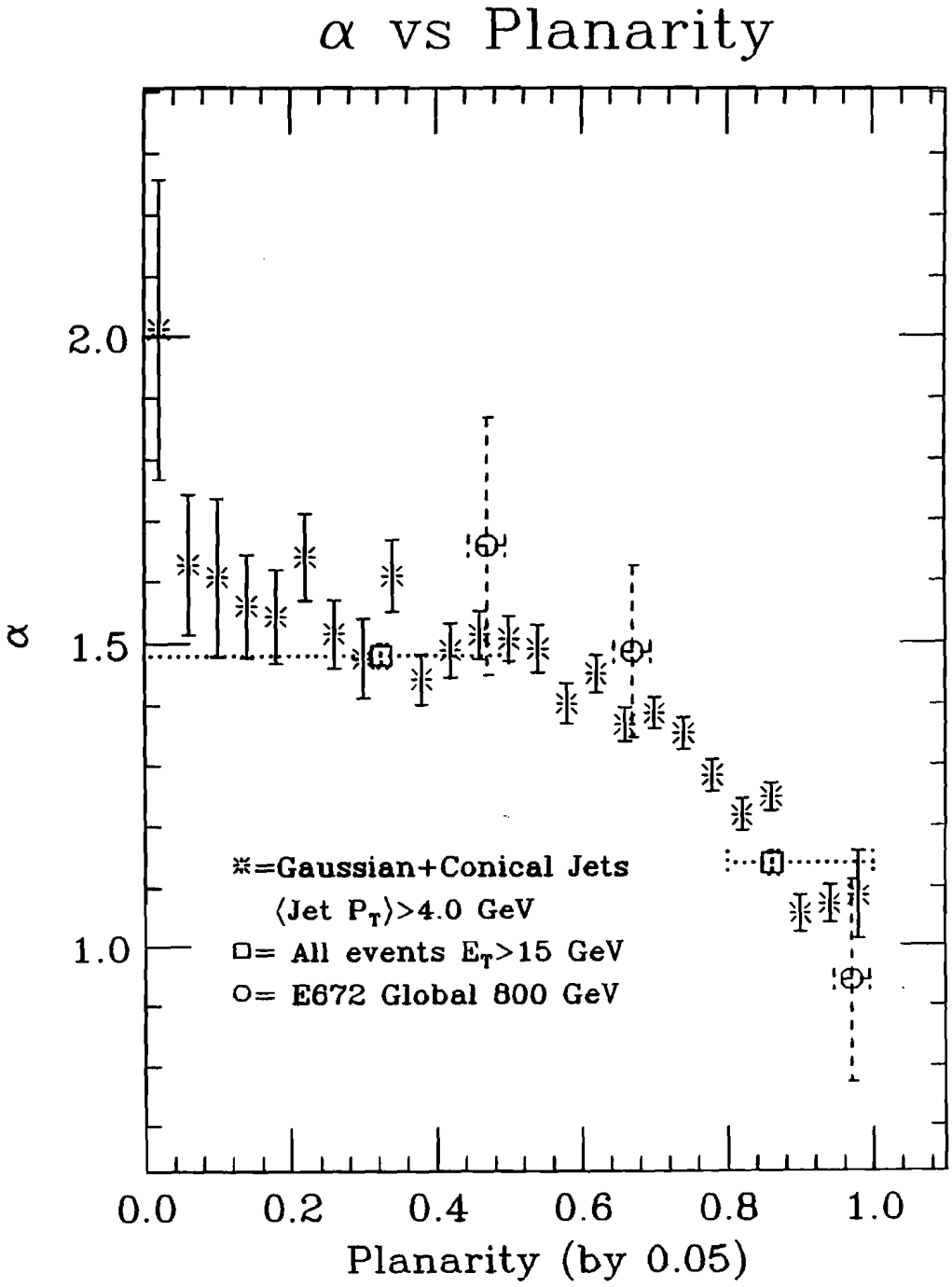

Figure 4.9A Fit 2 Lines: $\sigma(pA)/A\sigma(pp)$ vs. A in Planarity Bins

Figure 4.9A shows a pair of lines(dots) fit through $log[\sigma(pA)/A\sigma(pp)]$ vs. $log(A)$ for $1 \leq A \leq 27$ and $27 \leq A \leq 207$ in planarity bins 0.1 units wide for conical jets with <Jet P_T>$\geq$4.0 GeV/c & $60° \leq \theta^*_{jet_1} \leq 110°$. The resulting α slopes are given in the figure. Experimental results for E672's pA collisions, collected with a global trigger, are shown by dashed lines [GOM86c,GOM87].

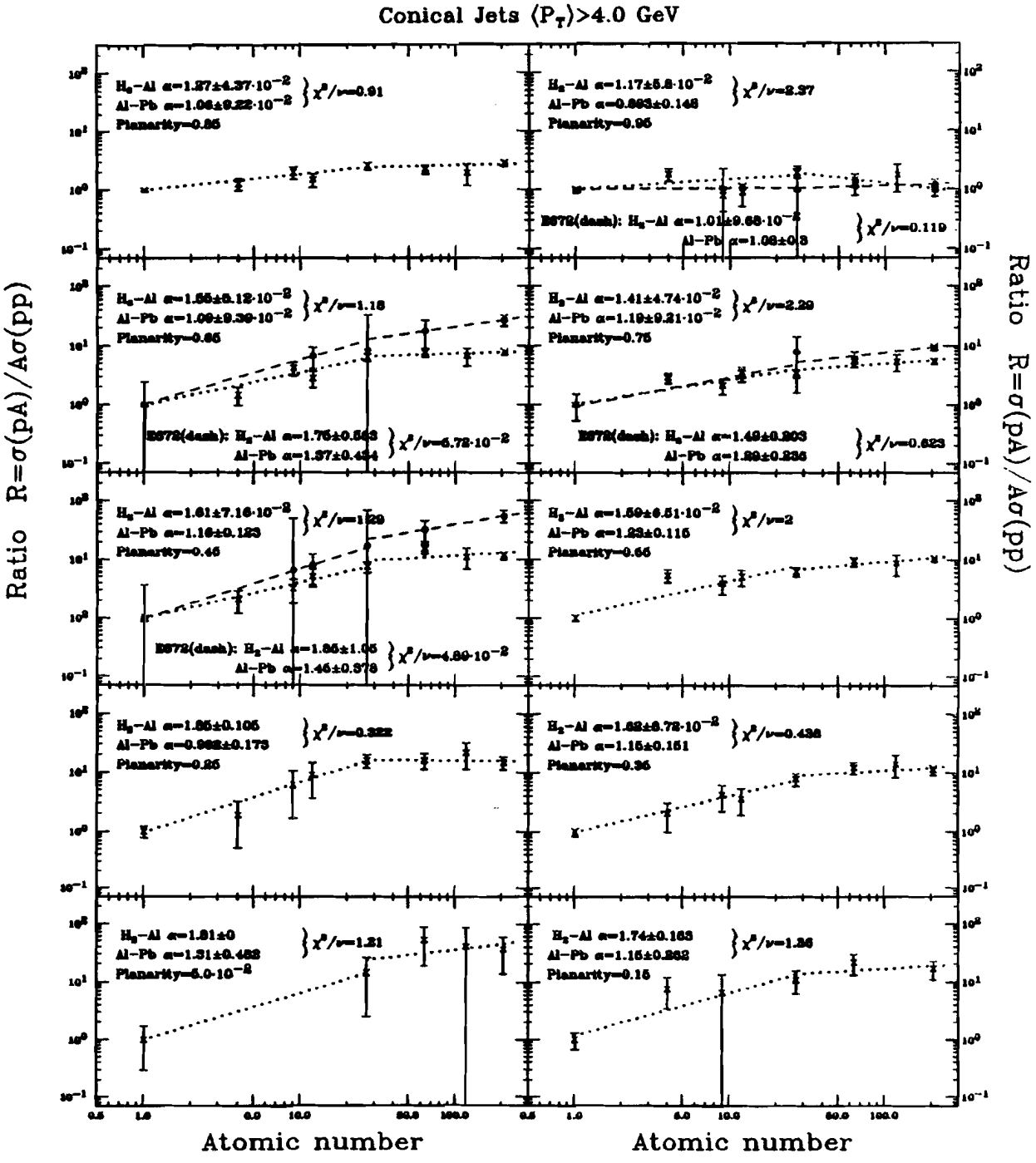

Figure 4.9B Fit $a+bA^{1/3}+cA^{2/3}$: $\sigma(pA)/A\sigma(pp)$ vs. A in Planarity Bins

The plots in figure 4.9B contain a 3 parameter fit giving $\sigma(pA)/A\sigma(pp)$ vs. $a+bA^{1/3}+cA^{2/3}$ in planarity bins 0.1 units wide for conical jets with <Jet P_T> greater than 4.0 GeV/c and $60° \lesssim \theta^*_{jet_1} \lesssim 110°$. Numerical values of a, b and c are also given in table 4.2.

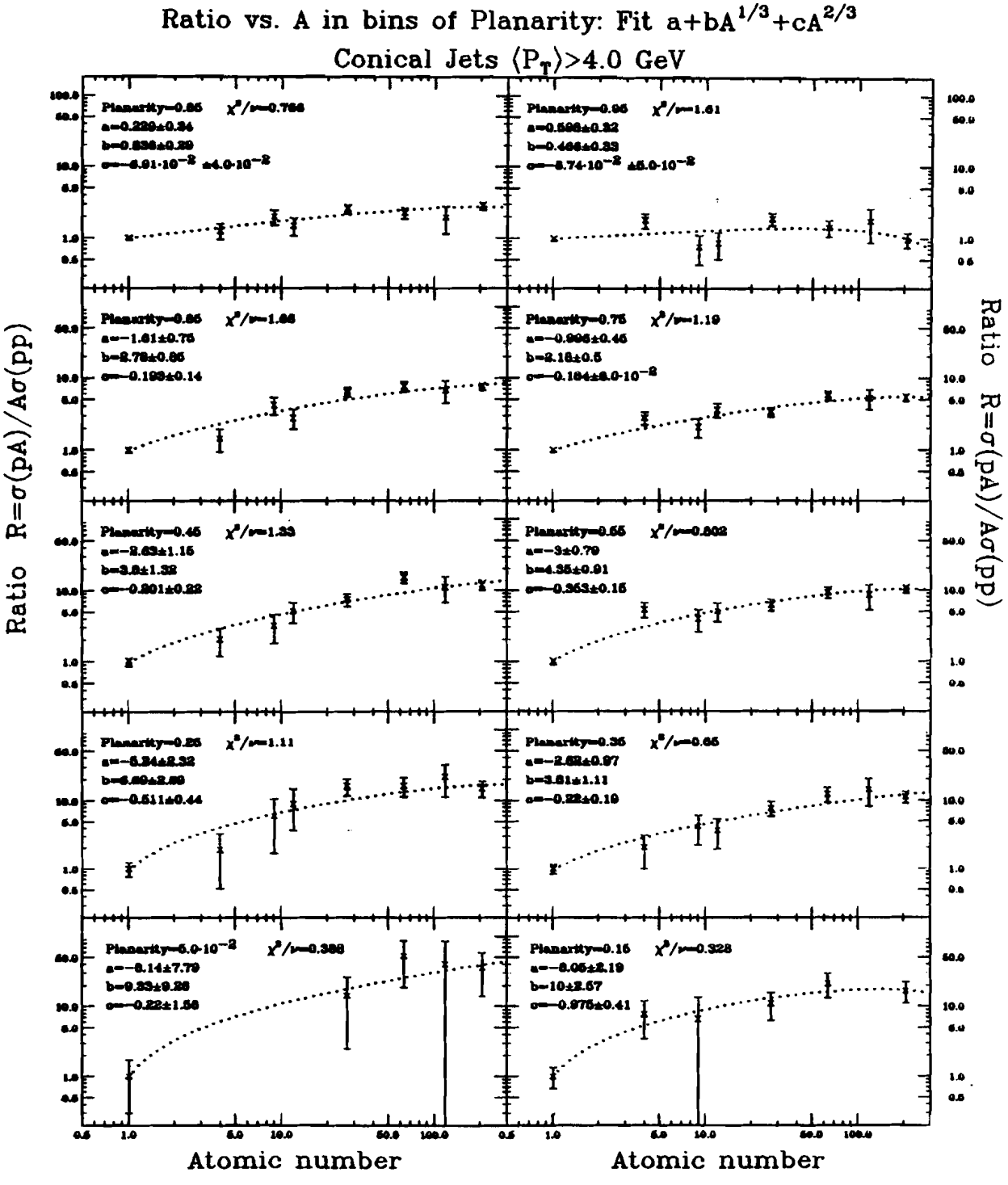

Figure 4.9C Fit $a+bA^{2/3}+cA^{1}$: $\sigma(pA)/A\sigma(pp)$ vs. A in Planarity Bins

The plots in figure 4.9C contain a 3 parameter fit giving $\sigma(pA)/A\sigma(pp)$ vs. $a+bA^{2/3}+cA^{1}$ in planarity bins 0.1 units wide for conical jets with <Jet P_T> greater than 4.0 GeV/c and $60° \leq \theta^{*}_{jet_1} \leq 110°$.

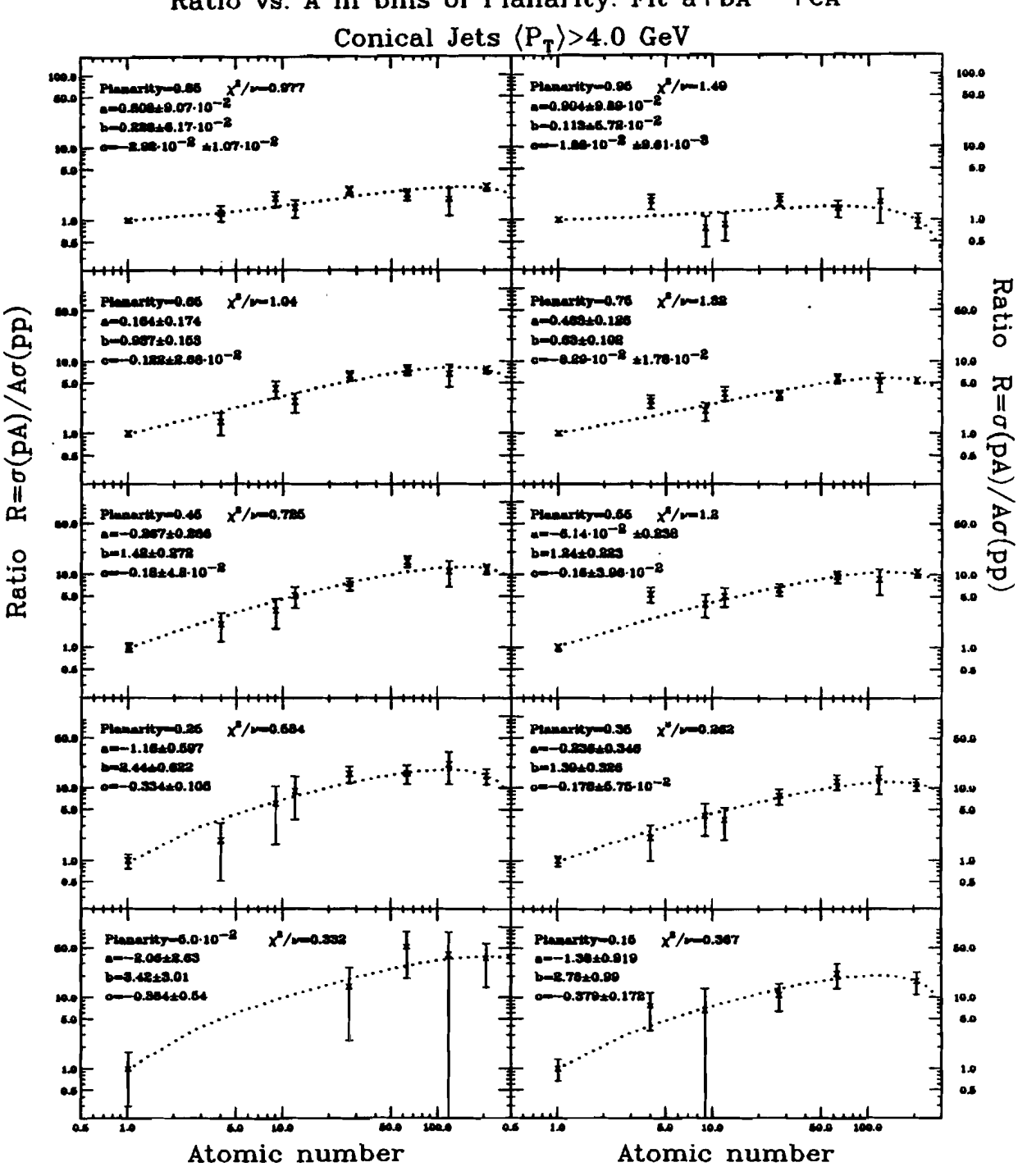

Figure 4.10 Cronin Data: Original Nuclear Enhancement Data

Figure 4.10 shows the first single particle high P_T triggers from nuclear targets [CRO73,75]. The curves show cross section ratios for incident 400 GeV protons on five targets (lH_2,d,Be,Ti and W) that produced single particles with P_T between 4.96 GeV/c and 5.72 GeV. The rise in R with A is nuclear enhancement; no break at A=27 is observed.

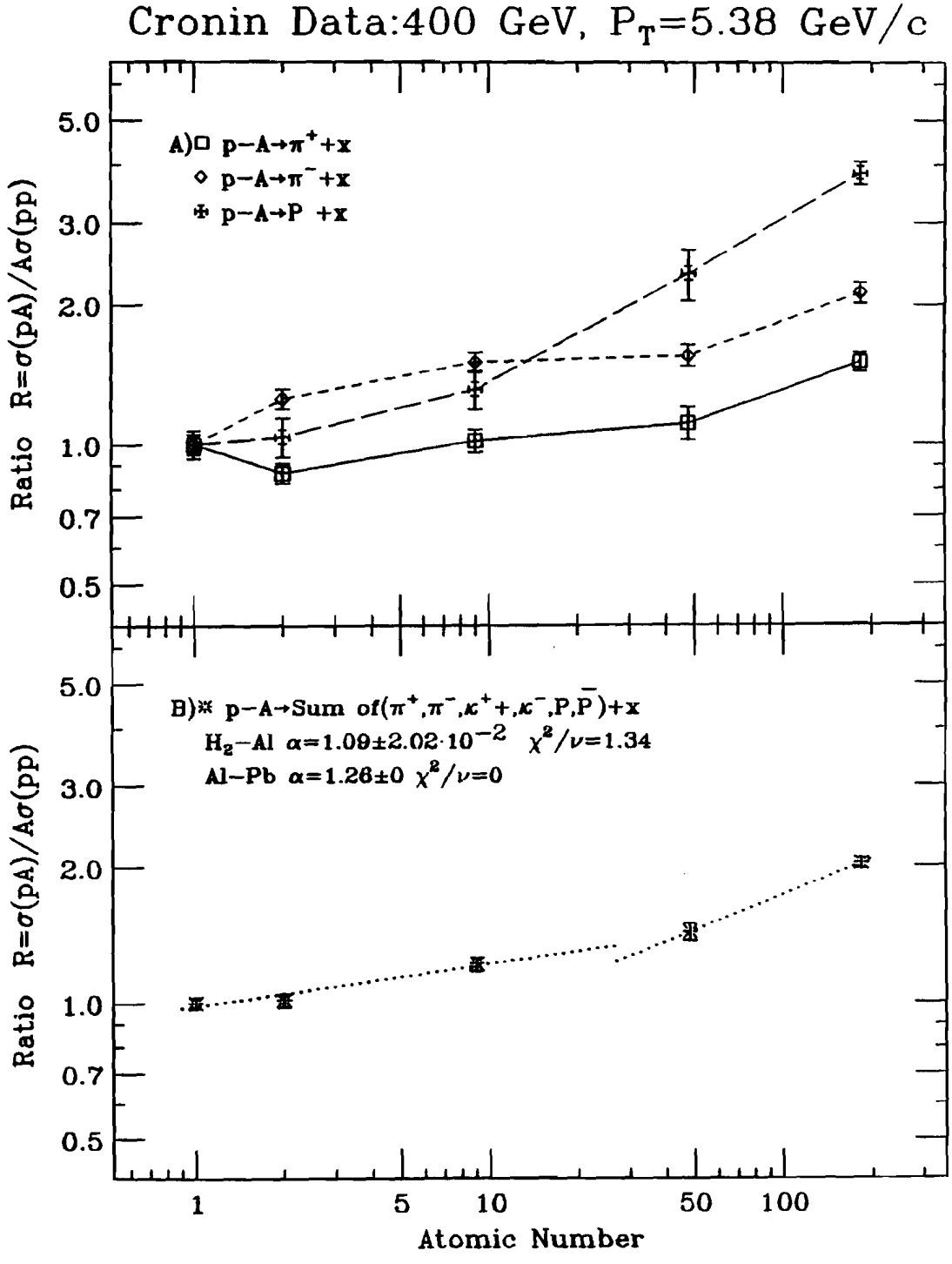

Figure 4.11 Abramov Data: Cronin's experiment repeated

Figure 4.10 shows Serpukhov $\pi^{\pm}$ data [ABR83] which displays the flattening trend at high A values. The incident 70 GeV proton beam struck C,Al,Cu,Sn or Pb to produce $\pi^{\pm}$,$K^{\pm}$,p,$\bar{p}$. Hydrogen points were inferred from earlier experiments.

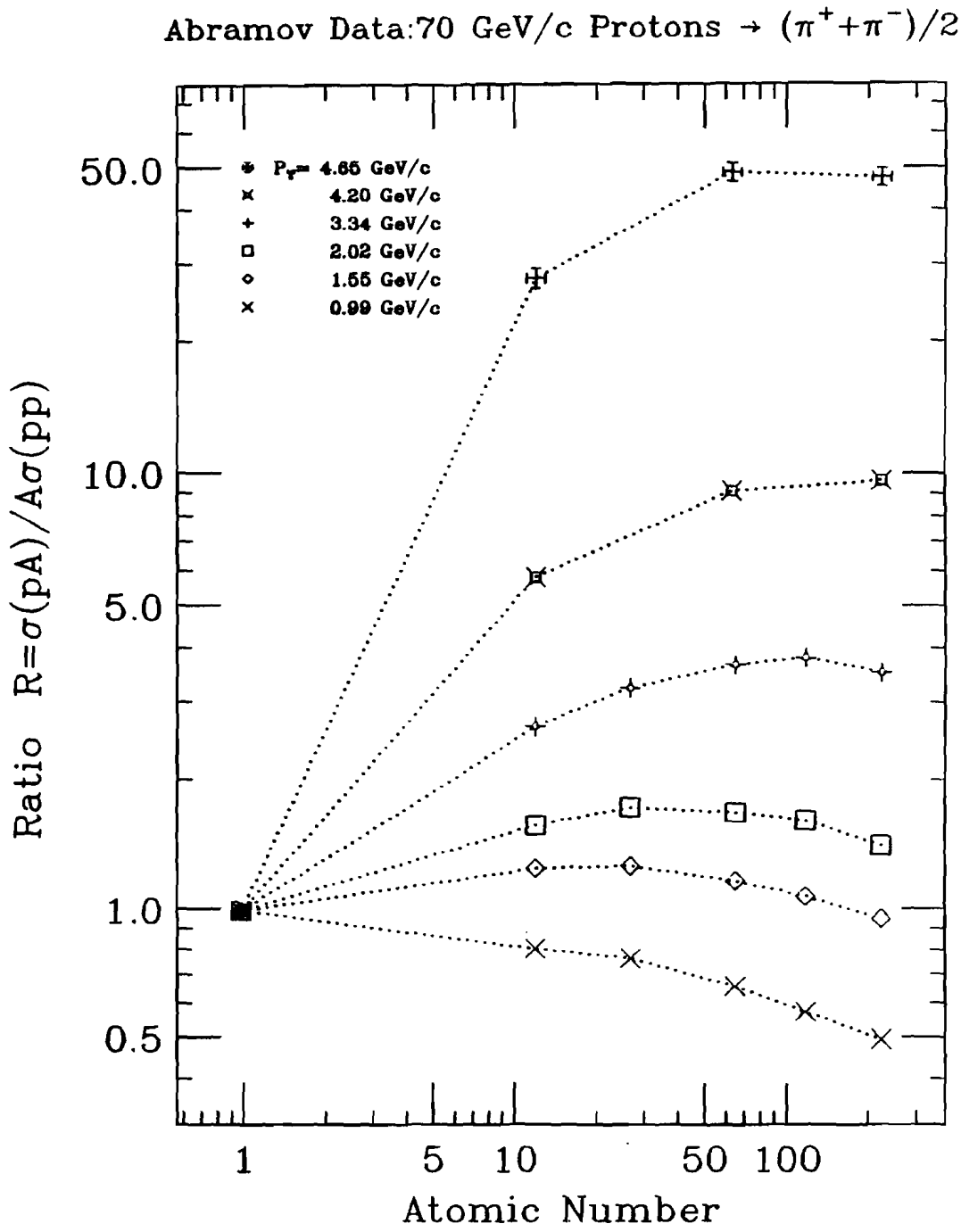

4.1.5 Fits of $log[\sigma(pA)/A\sigma(pp)]$ vs. $log(A)$

It is commonly accepted to fit a straight line through the $log[\sigma(pA)/A\sigma(pp)]$ versus $log(A)$ plot [CRO73,BROM79,BROW83,GOM86c], however careful examination of our data may indicate that there is a general flattening trend after the atomic number reaches aluminum. Figure 4.9A explores this observation further by showing a pair of lines, one fit through the A=1.0 (hydrogen) to A=27 (aluminum) ratio values and the other fit from A=27 to A=207 (lead). This flattening trend is observed in nearly every version of the ratio versus atomic number plot, regardless of the binning scheme (figure 4.3A shows a similar trend). The χ^2/ν improves in most planarity bins for the pair of fits, in spite of the required 4 degrees of freedom. Four bins of figure 4.7B show data from a similar calorimeter experiment, E557/E672 [GOM86c,GOM87] collected with a global trigger for events with more than 23 GeV/c E_T. This independent data also hints at a two curve hypothesis; the E557/E672 collaboration excluded the hydrogen cross section from their α calculations, to produce reasonable fits, without further comment. The original Cronin data [CRO73,CRO75] does not appear to support the two slope picture; however this data used a single particle trigger rather than a di-jet trigger. Figure 4.10A shows the π^+ and proton Cronin data (note that the atomic number has been factored out) while figure 4.10B contains the ratio-versus-A curve for the cross section sum of the 6 detected particles. A similar p+(C,Al,Cu,Sn or Pb)$\rightarrow$ ($\pi^\pm$,$K^\pm$,p or $\bar{p}$) experiment at Serpukhov does observe a flattening trend and concludes "the power law A^α is not valid" [ABR83, see also ABR84]. Figure 4.11 displays their p+A$\rightarrow\pi^\pm$

data, showing the change in the ratio value for several values of single particle P_T's.

It is worth noting that other jet-from-nuclei experiments used many fewer nuclear targets, ([BROM79] used lH_2 and Al, [GOM86c] used 6 targets but report results only on 5 and one of those has large error bars, [ABR83] fits 3 nuclear targets and a previously measured hydrogen cross sections for their highest P_T bin). Our experiment's unique advantage lies in our systematic collection of data from multiple targets.

The flattening trend observed in our data presents a major challenge to all models utilizing multiple scattering [PUM75] and extensions to this model [FAR75,LAN75,KÜH76,SUK82]. The prediction of $A(a+bA^{1/3}+cA^{2/3}+...)$, (see figure 4.9B), describes the scattering using the assumption that a, b, and c are all positive numbers each representing 1, 2, 3, ... collisions. Table 4.2 presents the coefficients of two and three term fits for our data in bins of planarity. The higher order terms are negative! Figure 4.9C contains a similar set of curves where the fit is through $A(a+bA^{2/3}+cA^{1}+...)$. Both parameterizations produce reasonable fits with small χ^2/ν values.

4.1.6 Event Multiplicity

Increasing the A of the target produces an increase in the number of particles produced in the collision, the event multiplicity. Our measurement of the total number of charged particles in an event is imprecise due to difficulties in identifying individual particles. Figure 4.12 shows three separate measures of the total event "charged"

TABLE 4.2
Fit Coefficients of *log(R)* vs. *log(A)*

Fit $\sigma(pA)/\sigma(pp) = e^{a} \cdot A^{1+b} = e^{a} \cdot A^{\alpha}$

PLANARITY	χ^2/ν	a	$1+b = \alpha$
0.-.1	0.663	0.20±0.67	1.73±0.17
.1-.2	1.82	0.38±0.29	1.54±0.08
.2-.3	2.58	0.26±0.21	1.56±0.06
.3-.4	1.30	0.10±0.16	1.50±0.04
.4-.5	2.38	0.10±0.13	1.51±0.04
.5-.6	2.58	0.23±0.11	1.44±0.03
.6-.7	2.64	0.08±0.09	1.42±0.03
.7-.8	2.20	0.08±0.07	1.34±0.02
.8-.9	0.78	0.01±0.06	1.21±0.02
.9-1.	2.18	0.04±0.07	1.06±0.03

Fit $\sigma(pA)/A\sigma(pp) = a + bA^{1/3} + cA^{2/3}$

PLANARITY	χ^2/ν	a	b	c
0.-.1	0.388	-8.14±7.79	9.33±9.26	-0.220±1.56
.1-.2	0.328	-8.06±2.19	10.01±2.57	-0.985±0.41
.2-.3	1.11	-5.24±2.32	6.69±2.69	-0.511±0.44
.3-.4	0.650	-2.62±0.97	3.81±1.11	-0.220±0.19
.4-.5	1.33	-2.63±1.15	3.80±1.32	-0.201±0.22
.5-.6	0.802	-3.00±0.79	4.35±0.91	-0.353±0.15
.6-.7	1.66	-1.61±0.75	2.78±0.85	-0.193±0.14
.7-.8	1.19	-1.00±0.45	2.18±0.50	-0.184±0.08
.8-.9	0.766	0.21±0.34	0.85±0.29	-0.079±0.04
.9-1.	1.61	0.60±0.32	0.47±0.33	-0.077±0.05

multiplicity as a function of atomic number. The solid line displays the number of charged particles recorded in the MWPC as a function of atomic number (with an efficiency correction applied, see appendix A). The nearly flat dashed curve results from total number of clusters (reduced by a third to account for neutral particles). The steeper

Figure 4.12 Total Event "Charged" Multiplicity

Figure 4.12 shows 3 separate "charged" multiplicity measures as a function of A for events where the Gaussian jet-finder located 2 jets with <Jet P_T> $\geq$ 4.0 GeV/c and passing the θ^* cuts; the conical jet-finder produces similar curves. The corrected number of hits in the MWPC (solid), the reconstructed tracks (dotdash) and the tracks with full angular information pointing to the calorimeter (dots) utilize the chamber information, while 2/3 times the number of clusters in the calorimeter produces an independent multiplicity estimate (dash).

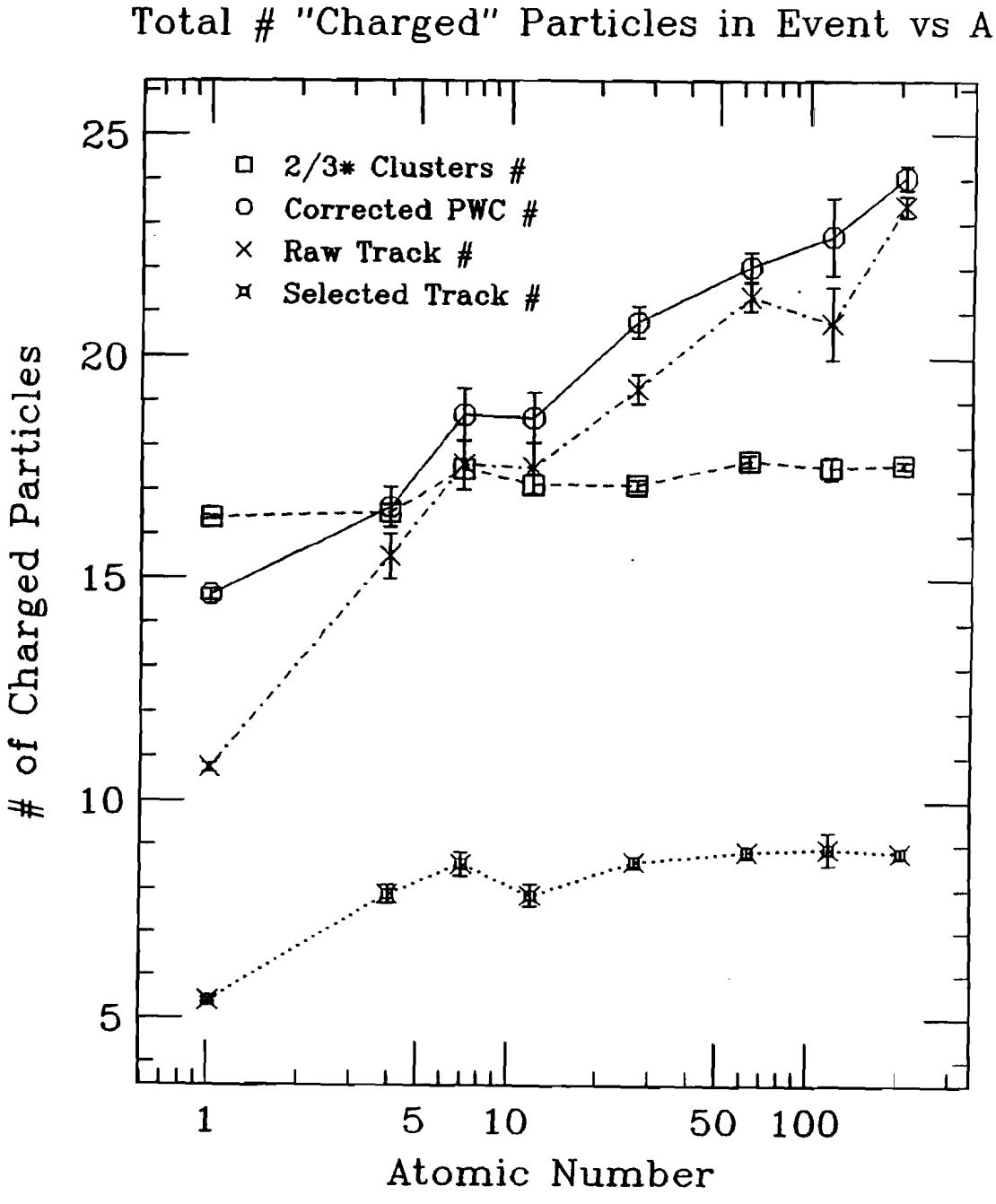

slope in the MWPC measurement results, in part, from the increased coverage of the wire chamber and its sensitivity to softer particles; (the calorimeter can not identify particles below ~1 GeV). The slightly lower dotdash curve is the number of raw tracks reconstructed; as expected the slopes resulting from wire chamber measurements are nearly parallel. The lowest, dotted curve corresponds to the number of vertexed tracks with reasonable X and Y slopes (at least 5 points in X, 2 points in Y and pointing to the calorimeter). Studies of the tracking efficiency in high track density regions imply that slightly less than half the tracks are reconstructed (again see appendix A). The hydrogen requires a 55% correction and the nuclear targets require a 45% correction, (different because of the different solid angles). The size of the correction should also scale with multiplicity, however we have not estimated the magnitude of this effect. Charged multiplicity within individual jets requires full angular information; charge multiplicity must therefore be inferred from either the number of tracks that pass selection and lie within the jet cone, or 2/3 times the number of clusters included by the jet-finder.

4.2 INTERNAL JET PROPERTIES

Internal jet properties, including particle content and particle distribution, arise from the parton fragmentation of events satisfying our specific trigger. Estimates of particle content depend on the assumption we can approximate real particles with either clusters of segments, limited by the calorimeter resolution, or by reconstructed

tracks, with the difficulties of track reconstruction. Study of how the various properties change as a function of P_T and atomic number reveal physical properties even though the specific values depend on our experimental apparatus.

Various internal jet properties describe how the jets change as a function of <Jet P_T> and atomic number. For each property studied, (ie. the number of particles in the jets, the angular distribution of the particles, the particle momentum along the jet axis, the particle momentum transverse to the jet axis, and the ratio of the particles interacting electromagnetically to hadronically), the changes behave as expected; as <Jet P_T> increases the distributions reflect the increased energy, and as the atomic number increase the properties change to reflect the increase in total number of particles.

4.2.1 Particle Content of Jets

4.2.1.1 Mean number of clusters in the jets -

Counting the number of clusters, which approximate particles, in each jet depends heavily on the jet definition. The Gaussian jet--finder, allowing a greater fluctuation in the jet structure, tends to include more clusters than the conical jet definition. We define a cluster as a member of Gaussian jet when it is within the Full-Width--at-Half-Maximum (FWHM) contour of the E_T peak, while a cluster belongs to a conical jet if it lies within the 45° cone half-angle. Plotting the number of clusters within the jet for a variety of selection criteria (Gaussian jets -or- conical jets, individual jets

-or- the average for the jet pair, and the number of clusters making up various fractions of the total jet transverse energy) indicates that the number of clusters in a jet increases with both jet P_T and atomic number.

Comparison with the world data requires use of M_{jj} rather than our more common variable <Jet P_T>. (See figure 4.53E for the number of clusters as a function of <Jet P_T>). Recall that M_{jj}^2 equals $(E_{jet_1}+E_{jet_2})^2-(\vec{P}_{jet_1}+\vec{P}_{jet_2})^2$. Both M_{jj} and <Jet P_T> produce similarly shaped curves since the <Jet P_T> versus M_{jj} relation is nearly linear, as is seen in figure 4.13. Figures 4.14A&B show typical plots demonstrating how the "particle" content of the jets tracks the jet P_T and target A. These figures display the average number of clusters in a jet pair (which equals the average value of $(\#_{jet_1}+\#_{jet_2})/2$) over a range of di-jet invariant masses, M_{jj}. Both the Gaussian and conical jet-finders are shown as a function of atomic number for events having <Jet P_T> greater than 4.0 GeV/c and $60°\leq\theta^*_{jet_1}\leq 110°$. Changing the atomic number increases the number of particles in the jets, perhaps expected since the total event multiplicity climbs with atomic number. The curves verify the reported trends and also demonstrate a difference in the jet definitions; both jet-finders show a clear increase in the number of clusters per jet with increasing M_{jj}. The Gaussian jet-finder repeats this trend as A increases, while the conical jet-finder demonstrates only a slight rise in the number of particles per jet with increasing atomic number.

The relative P_T of the jet containing the most clusters depends on the jet-finder. The clusters divide roughly into two classes; a quarter of the clusters have over 2.0 GeV of E_T and represent the

Figure 4.13 M_{jj} vs. <Jet P_T> for Hydrogen

Figure 4.13 shows a scatter plot of M_{jj} vs. <Jet P_T> for hydrogen events located by the Gaussian jet-finder containing at least 3.0 GeV/c P_T. The size of the square corresponds to the number of entries in the bin.

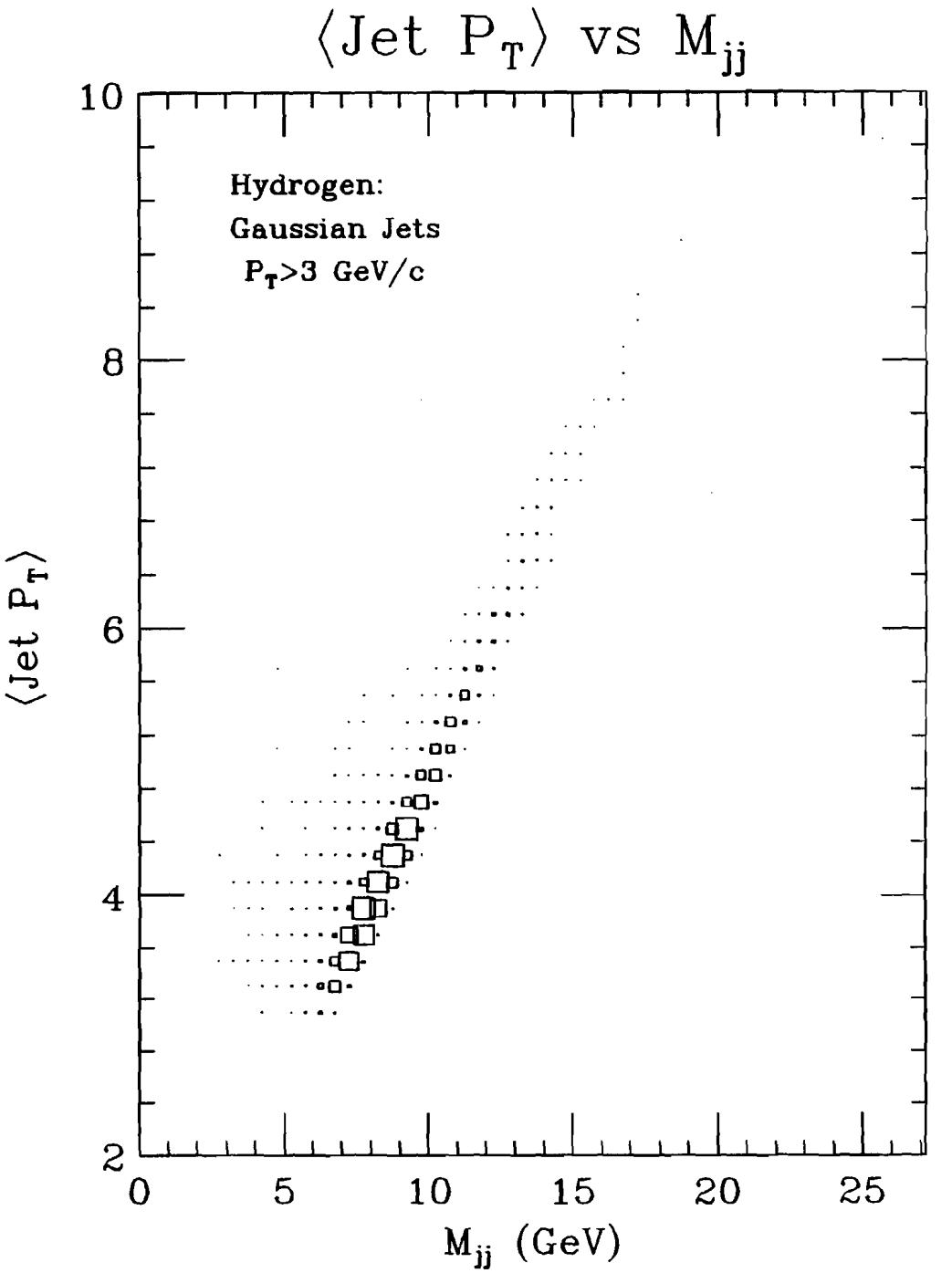

Figure 4.14 <# of Clusters>/Jet vs. M_{jj} and Atomic Number

A) Hydrogen & Lead: The <number of clusters> in the jet pair, the mean of $(\#_{jet_1}+\#_{jet_2})/2$, is shown for the conical (solid,dot) and Gaussian (dash,dotdash) jet-finders as a function of M_{jj}.
B) The <number of clusters> in the jet pair is shown for the conical (solid) and Gaussian (dash) jet-finders as a function of target atomic number.

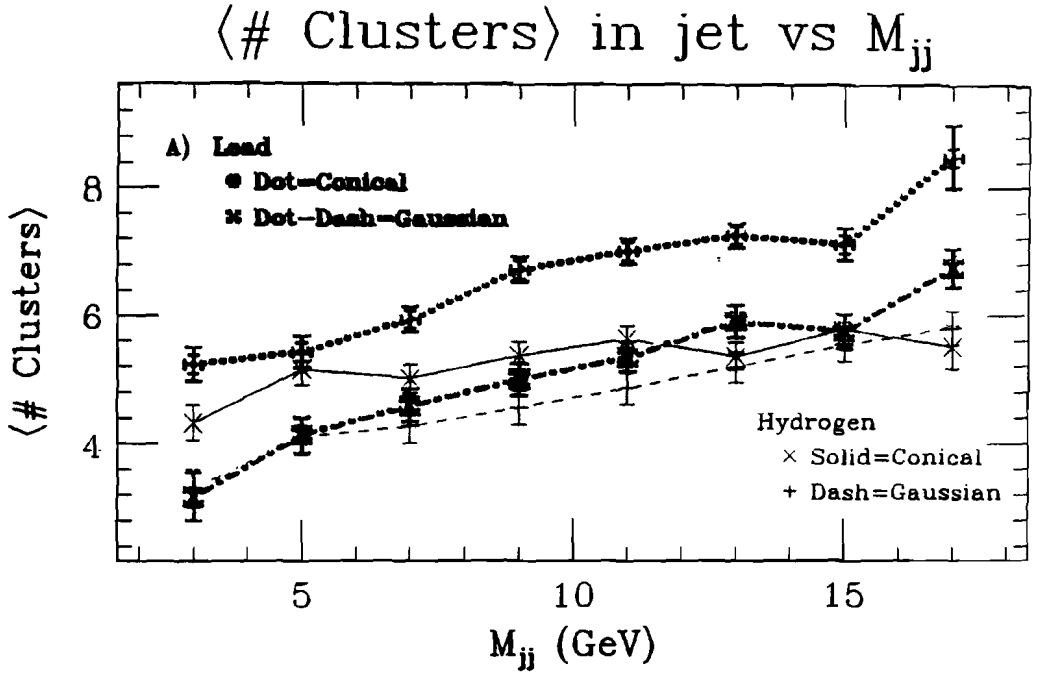

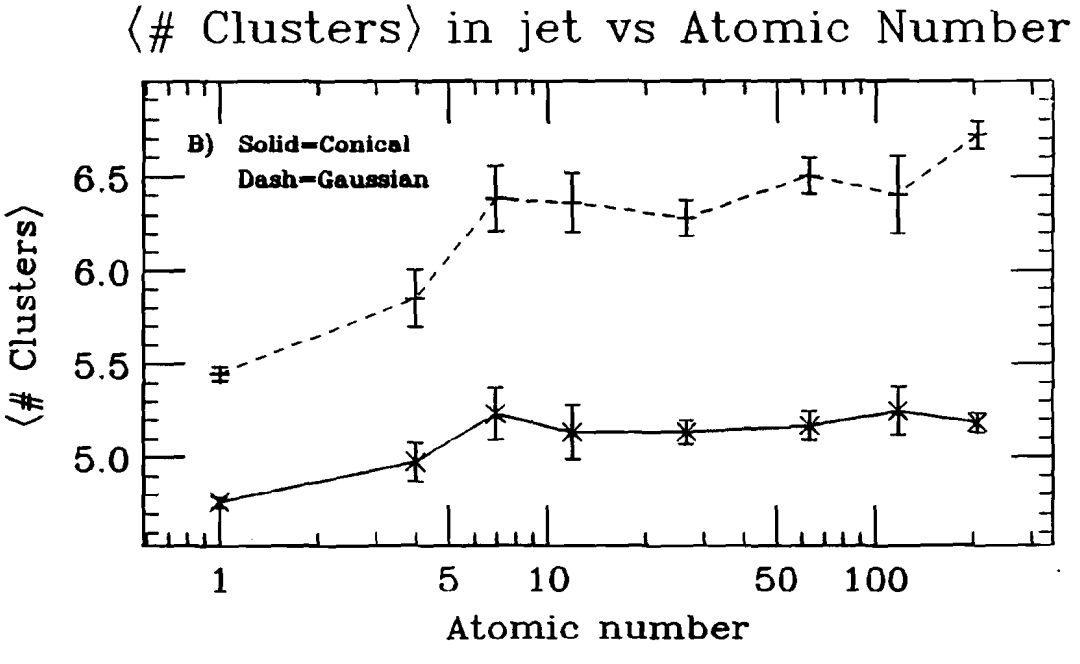

Figure 4.15 # Clusters in top 2 Jets as a function of A

A) Conical & B) Gaussian: The number of clusters jet with the highest P_T (jet_1,solid) compared with the number of clusters in the jet with the second highest P_T (jet_2,dots) as a function of A. The events contain <Jet P_T> at least 4.0 GeV/c and $60° \leq \theta^*_{jet_1} \leq 110°$.

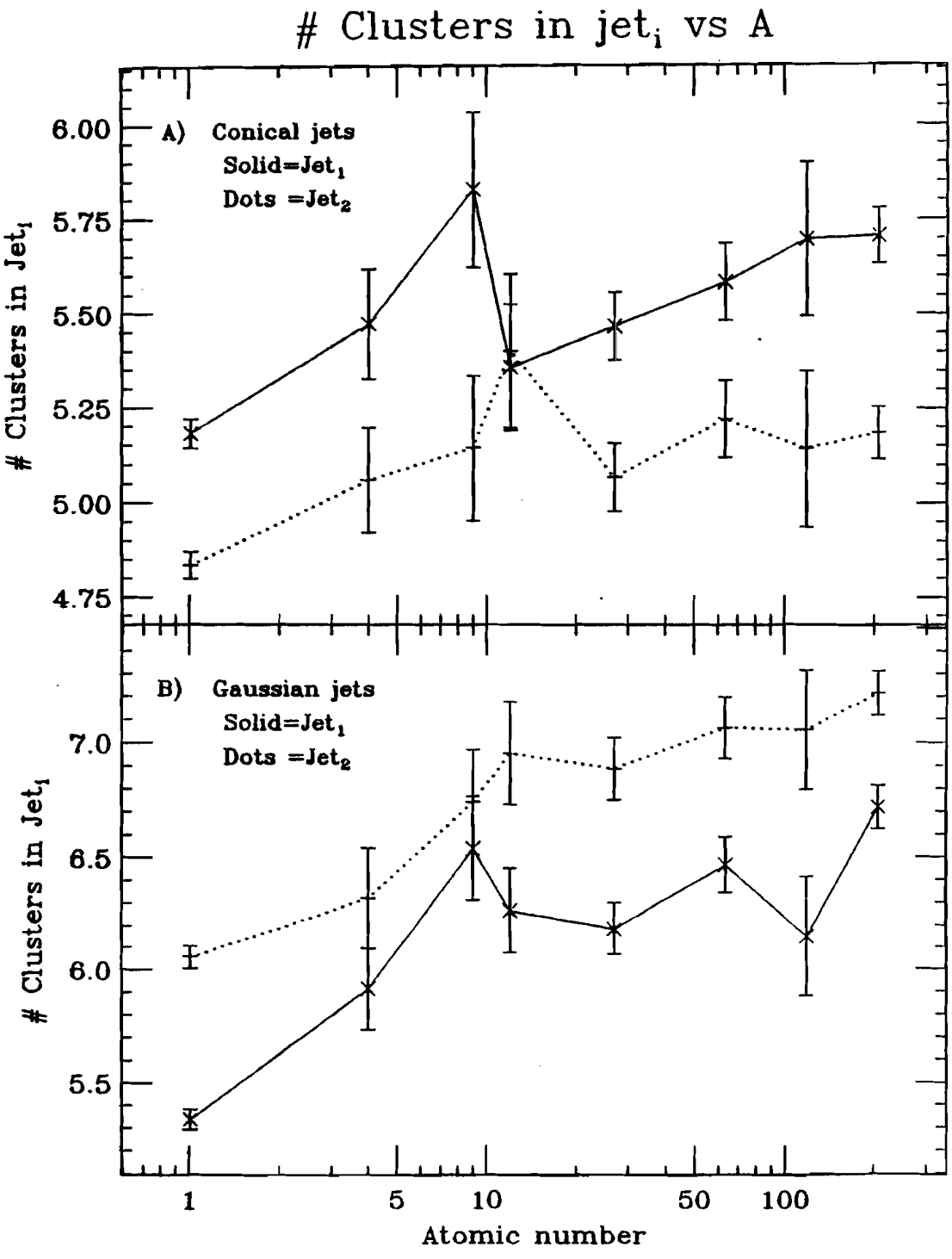

leading "particles" in the jets, while the remaining three-quarters of the clusters are soft, with a mean E_T near 0.5 GeV (see §4.2.3.1, and figure 4.32). Both jet-finders include the same leading clusters; differences in definition occur with the inclusion of the lower energy clusters. The P_T of a jet located by the conical jet-finder results from the P_T sum of the clusters in the jet; the jet with the most clusters usually has the highest P_T, as shown by the two curves in figure 4.15A. For the Gaussian jet-finder, figure 4.15B, the second highest P_T jet contains the most clusters. This results from the <Jet P_T> threshold cut. The trigger is most easily satisfied by the addition of extra clusters to the wings of the Gaussian distribution.

Field-Feynman 4-jet Monte Carlo events satisfying the two-high trigger display this same trend; the softer jet of the high P_T pair has 10% more particles than the highest P_T jet. After the Monte Carlo data passes through the calorimeter simulation and the resulting clusters are analyzed by the Gaussian jet-finder, the reconstructed pair of jets contain 30% fewer "particles" than were originally produced in the Monte Carlo jets. (Particle loss can occur at several stages in this process for example: by missing the main calorimeter, by creating overlapping showers which are clustered into a single "particle", or by spreading out beyond the calculated jet volume). The Gaussian jet-finder, operating on simulated clusters, does however show that the second jet contains 9% more clusters than the first jet, nearly matching the ratio observed for the original Monte Carlo particles and in agreement with the data. The conical jet-finder reports fewer simulated clusters in the second jet. The rate of increase in cluster content for both jet-finders slows at the higher A values.

4.2.1.2 <# Tracks> within 45°s of the jet axis -

A second measure of the particle flow, shown in figure 4.16, results from the charged particle tracking (without adjustment other than track selection). This measure no longer depends on the approximation that a cluster of calorimeter segments represent a real particle, but instead depends on the chamber efficiency and track reconstruction algorithm. This introduces the possibility of missed tracks and spurious tracks from accidental matches. Given a Gaussian or conical jet axis, we count the charged particles (transformed to the center of mass assuming zero mass particles) that lie in a 45° half-angle cone around the jet axis. The nearly identical jet axes located by the two jet-finders produce similar charged particle multiplicity curves. Particle tracking, as detailed in appendix A, misses a substantial fraction of the charged particle tracks, especially for those with limited spacial separation. Monte Carlo studies indicate the number of charged particles needs to be increased by fifty percent for high density tracks. The hydrogen target position, allowing less spread before the particles strike the chambers, requires a larger correction than the rest of the nuclear targets, which were a meter further from the chambers. Additionally, the total number of particles observed by the calorimeter includes neutral particles; if a third of the particles are neutral, the calorimeter should detect 1.5 times more particles than a perfect chamber array. The results shown in figure 4.16B have the hydrogen point increased by 55 percent and then multiplied by 1.5, while the nuclear data contains a 45 percent increase due to tracking inefficiency and the 1.5 charged to neutral ratio. Error bars shown on the plot are statistical, however the

Figure 4.16 <# Tracks>/Jet vs. M_{jj} and Atomic Number

A) lH_2 **& Pb: The <# Tracks within 45° of jet axis> for the conical (solid,dot) and Gaussian (dash,dotdash) jet-finders is shown vs.** M_{jj} **without efficiency corrections.**
B) Jet_1 **&** Jet_2**: <Adjusted Track #>*1.5, the "effective" particle number, is shown vs. A.** lH_2 **has been increased 55% and the nuclear targets increased 45% to adjust the tracking efficiency; an over all factor of 1.5 accounts for the unobserved neutrals. The Gaussian jet--finder produces similar results.**

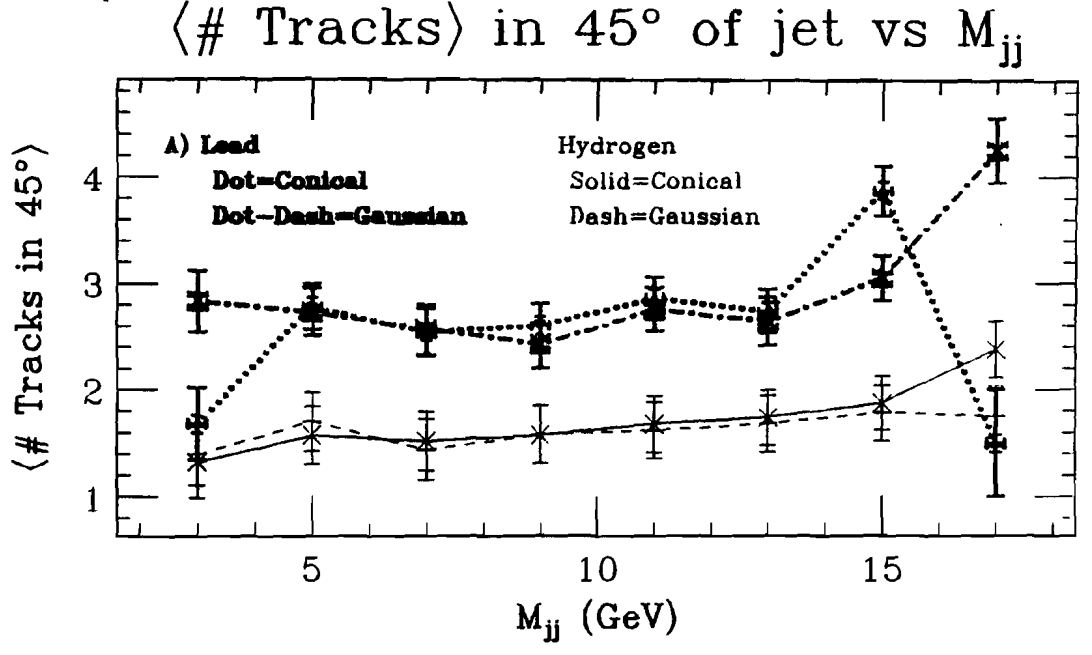

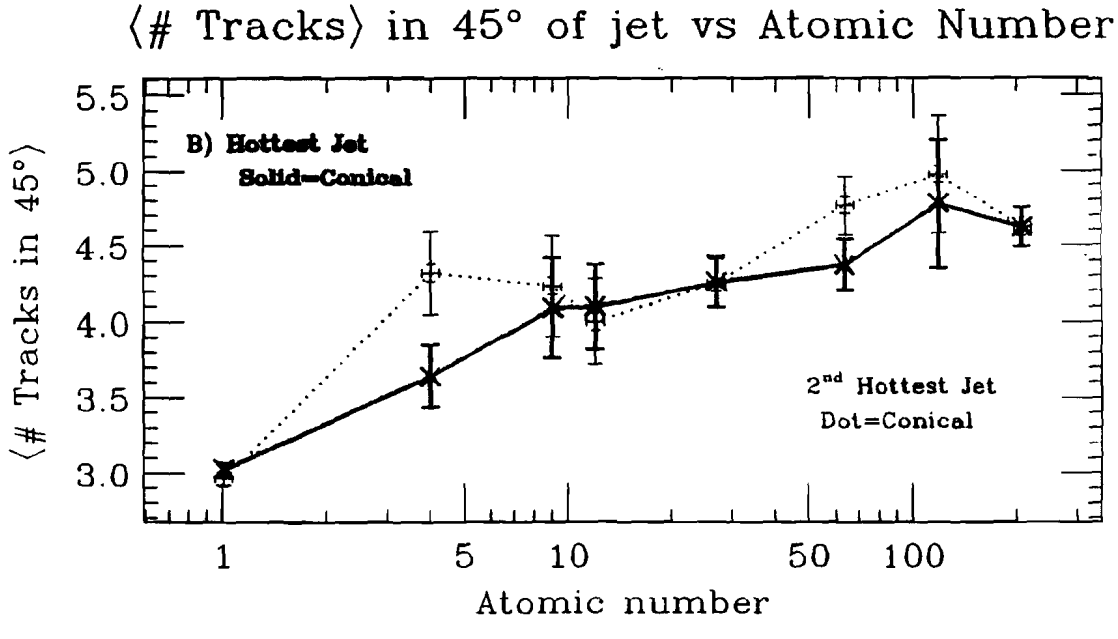

uncertainty from the tracking corrections could increase the errors another twenty percent. The 17% offset from a line fit through the A>2 targets and the <# Tracks>/Jet seen in hydrogen can be attributed to differences in target location and its effect on tracking efficiency. Both the highest P_T jet and the second highest P_T jet contain similar numbers of tracks, the second jet perhaps having slightly more.

4.2.1.3 Jet particle content by $dN_{clusters}/d(\Delta\phi)$ -

A third method to measure the jet particle multiplicity utilizes the cluster density, ρ, as a function of the azimuthal angle between jet clusters and the jet axes, $\Delta\phi$. Shown in figure 4.17A, the cluster density, $\rho(\Delta\phi) = dN_{clusters}/d(\Delta\phi)$, drops sharply as the $\Delta\phi$ with respect to (w.r.t.) the highest P_T jet axis increases, maintains a flat region between the jets and rises again in the backward direction due to the second jet. The cluster density is nearly independent of the jet-finder used since both locate the same jet axes. The conical jet-finder does however show a systematic ripple in the distribution near 45°; the Gaussian jet-finder is free of this artifact. The asymmetric distribution results from the two jets not being exactly coplanar. Acoplanarity could arise from various sources, for example: k_T effects (where k_T is the parton's internal transverse momentum), uncertainty in the jet reconstruction, energy leakage off the calorimeter, or three jet event contamination. Figure 4.17B displays the same curve except that the angle is measured from the second jet axis, allowing an estimate of this jet's width. Figure 4.17C shows an overlay of the hydrogen ρ distributions measured with respect to both

Figure 4.17 Cluster Density: ρ vs. $\Delta\phi$

A) $\Delta\phi$ w.r.t. Jet_1 & B) $\Delta\phi$ w.r.t. Jet_2: $dN_{clusters}/d(\Delta\phi)$ (cluster density, ρ) vs. $\Delta\phi$ (4° steps) is measured from the jet axis. Gaussian jet ρ, for lH_2(solid) and Pb(dots) is plotted; The Conical jet-finder produces similar curves.
C) $\Delta\phi$ w.r.t. Jet_1 & $\Delta\phi$ w.r.t. Jet_2: The widths of the 2 jets are compared for hydrogen Gaussian jet data.
D) $\Delta\phi$ w.r.t. Jet_1: The Monte Carlo cluster density(dash) is compared to the lH_2 cluster density(solid). Events have <Jet P_T>≥4.0 & $60° \leq \theta^*_{jet_1} \leq 110°$.

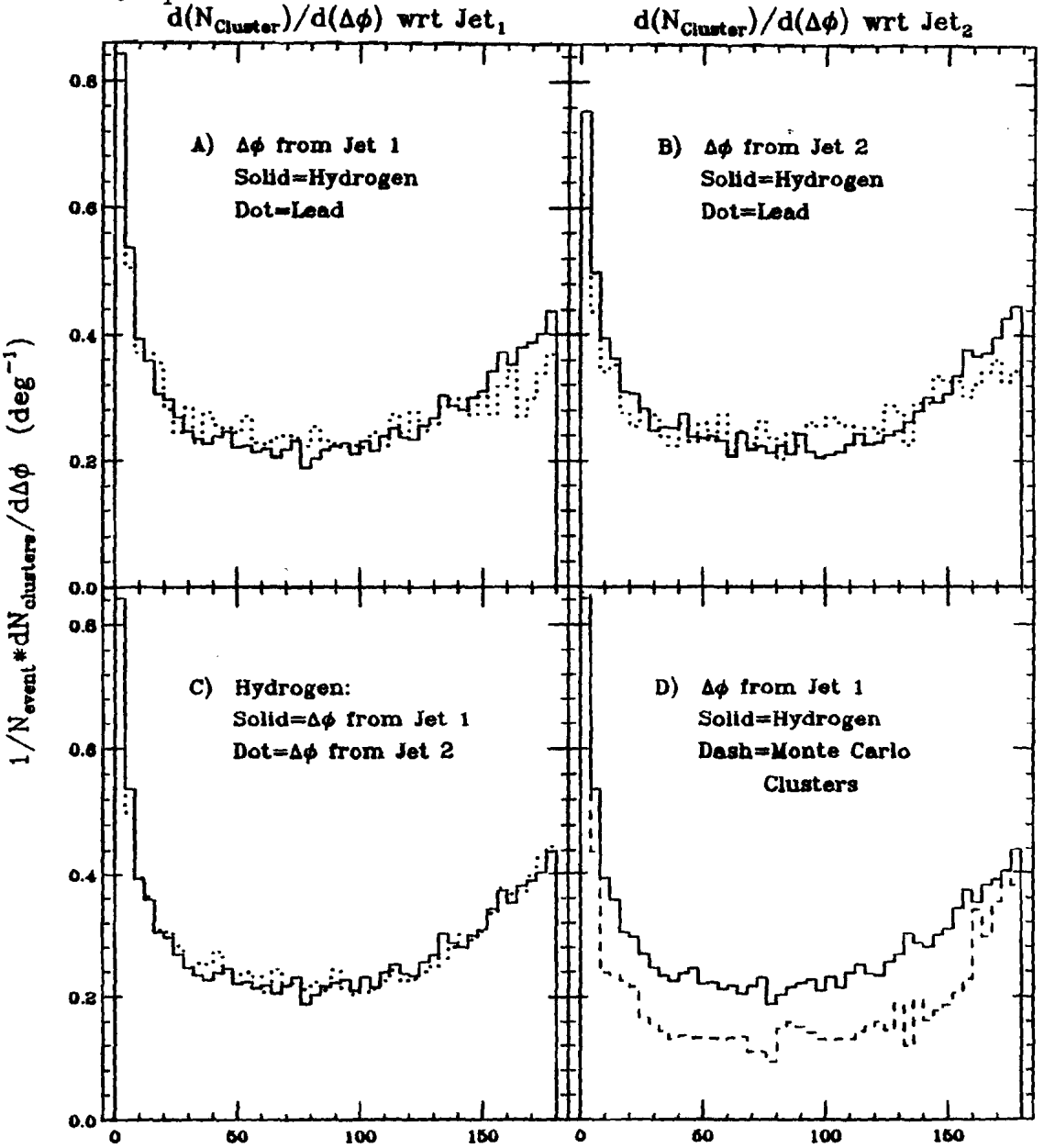

jet axes. The hot jet contains a slightly greater cluster density; however, the two jets are very similar. Figure 4.17D compares the hydrogen data with the results of the Field-Feynman Monte Carlo after the calorimeter simulation. The peaks for the Monte Carlo jets are much sharper, reflecting the higher event planarities. The reduced cluster multiplicity shows up as a lower level between the jets.

Population in the region $\Delta\phi = 90°$ results mostly from particles not associated with either jet (they come from the spread in the beam and target jets or gluon bremsstrahlung). Assigning the non-jet particle density as ρ_0, these particles are assumed to be uncorrelated with the jet distribution [BAG83a] and to contribute a uniform distribution $\lambda\rho_0$ to $\rho(\Delta\phi)$. The jet particle density is $dN/d(\Delta\phi) = (1-\lambda)\rho_0$, where λ depends on the parton fragmentation and the rapidity distribution (which changes with θ). λ can take any value ranging from 1 (all particles between jets are background) to 0 (no particles at $\Delta\phi = 90°$ belong to the jets). Knowing λ, the average jet multiplicity is given by

$$N_{particles} = \tfrac{1}{2}\int_0^{\pi} [\rho(\Delta\phi)-\lambda\rho_0]\, d(\Delta\phi)$$

Here we can avoid the bias of the asymmetric $\Delta\phi$ distribution by defining the jet multiplicity as the average multiplicity of the two jets. Not knowing λ explicitly, we calculate a lower bound of $N_{particles}$ by setting $\lambda = 1$. This clearly underestimates the number of particles in the jets (particles for the Monte Carlo high P_T jets spread to $\Delta\phi$ values even larger than 90°) but provides a minimum reference value.

4.2.1.4 Jet particle content summary -

Figures 4.18A&B compare various estimates of the particle multiplicity as a function of M_{jj}. The lower bound multiplicity calculation from the $\rho(\Delta\phi)$ distribution, λ=1.0, subtracts off a uniform background, $\rho(\Delta\phi)|_{\Delta\phi=90^\circ}$, from the total particle density. The spread in values give an estimate of the systematic uncertainty of the number of particles in the jets. The tracks have been crudely corrected for tracking efficiency: the clusters are assumed to represent particles.

The number of particles in each jet from hydrogen compares favorably with similar information from other experiments, given the experimental uncertainties. Figure 4.19, adapted from [BAG83a,BAG84b] and [WEB83b], shows the number of charged particles per jet for a variety of experiments. UA2 measures jet particle content using the $dN_{charged}/d(\Delta\phi)$ estimate method with λ based on a QCD calculations [WEB83c]. The colliding beams experiments (where the lab corresponds to the center of mass) use many planes of wire chambers and record the charged particles number and momenta with a much greater efficiency than the E609 chambers. Our charged particle data requires sizeable corrections due to tracking inefficiencies (noted in figure 4.18). To compare with the world data we therefore use the cluster jet multiplicities and remove the neutral contribution by multiplying by 2/3.

The number of particles per jet, as observed earlier, increases with atomic number. Figure 4.20 shows the jet particle content as a function of atomic number for jets with $\langle P_T \rangle$ larger than 4.0 GeV/c and passing the fiducial cuts. Again, the number of tracks has been corrected upward 55% to account for the tracking efficiency for the hydrogen target position and 45% for the nuclear target position.

Figure 4.18 **Estimates of Jet Particle Multiplicity vs. M_{jj}**

A) Hydrogen & B) Lead: Estimates of the number of particles/Jet
1) Cluster # under FWHM of peak in Gaussian P_T surface (dash,+)
2) Cluster # in the 45° cone (solid,x)
3) Track # in 45° cone, adjusted by lH_2:*1.55(eff) or Pb:*1.45(eff) times 1.5(neutrals) (dot,*)
4) $d\rho/d\Delta\phi$ area above background, λ=1.0 (dotdash,diamond)

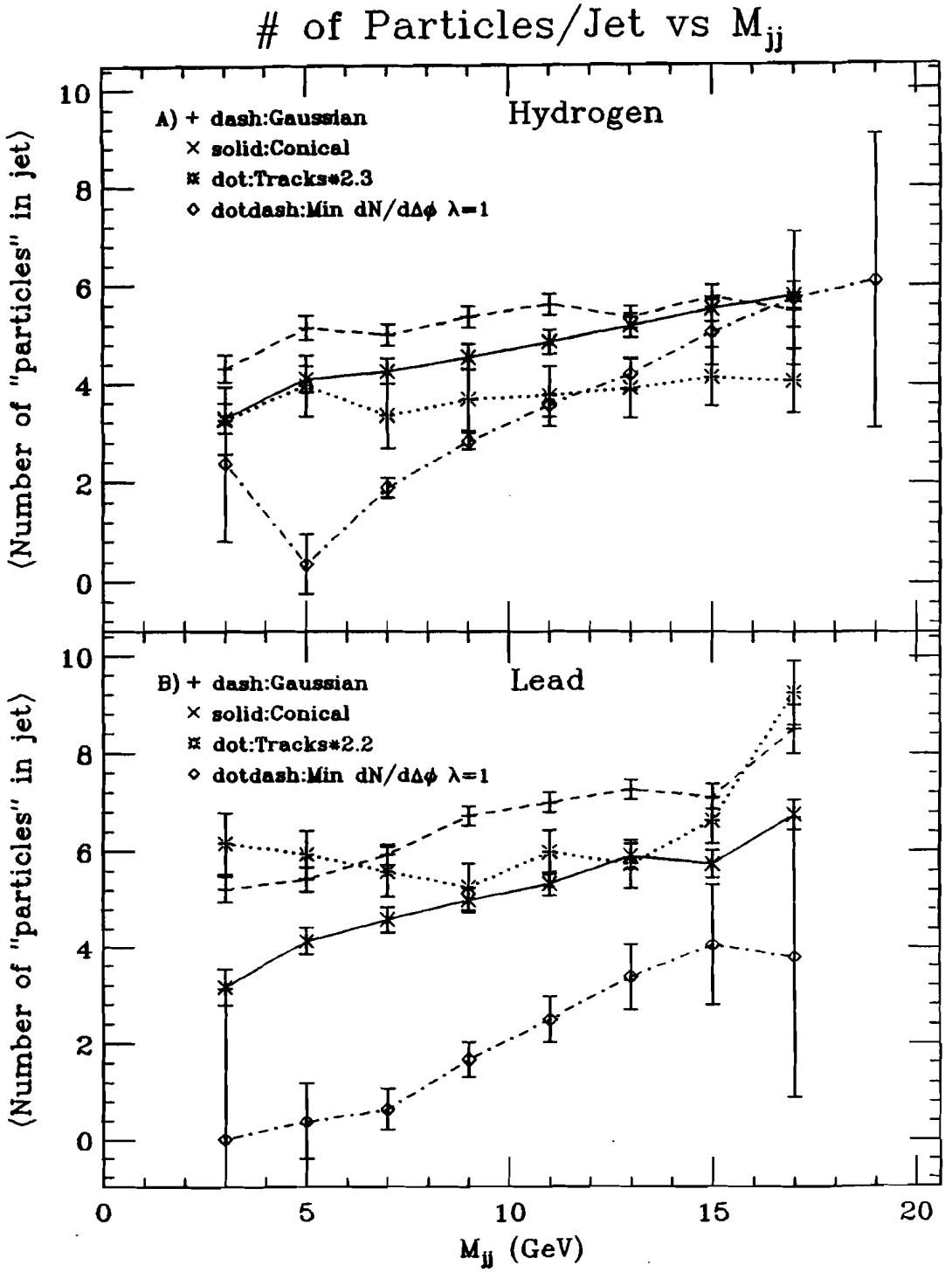

Figure 4.19 Number of "particles"/jet: World data

Figure 4.19 compares of the number of clusters, times 2/3, in the Gaussian jets (squares) with the world's charged particle multiplicity data for pp, $\bar{p}p$, and e^+e^- taken from [BAG83a,BAG84b] who references [BRA79,BRA80,WEB83a,WOL81].

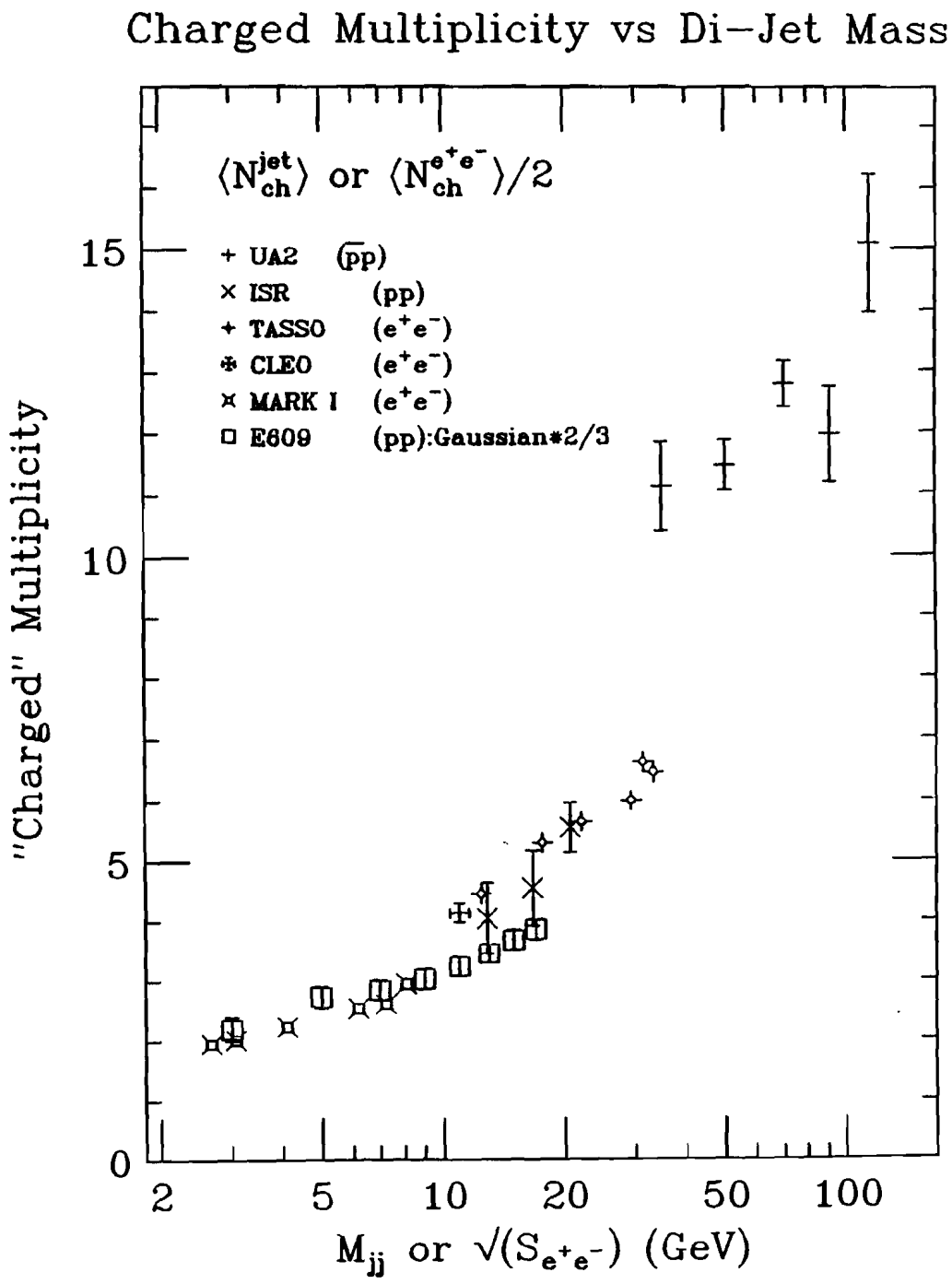

Figure 4.20 Estimates of Jet Particle Multiplicity vs. A

Estimates of the number of particles/Jet
1) Cluster # under FWHM of peak in Gaussian P_T surface (dash,+)
2) Cluster # in the 45° cone (solid,x)
3) Track # in 45° cone, lH_2:*1.55(eff)*1.5(neutrals),
Nuclear:*1.45(eff)*1.5(neutrals) (dot,*)
4) $d\rho$(clusters)/$d\Delta\phi$ area above background, λ=1.0 (dotdash,diamond)

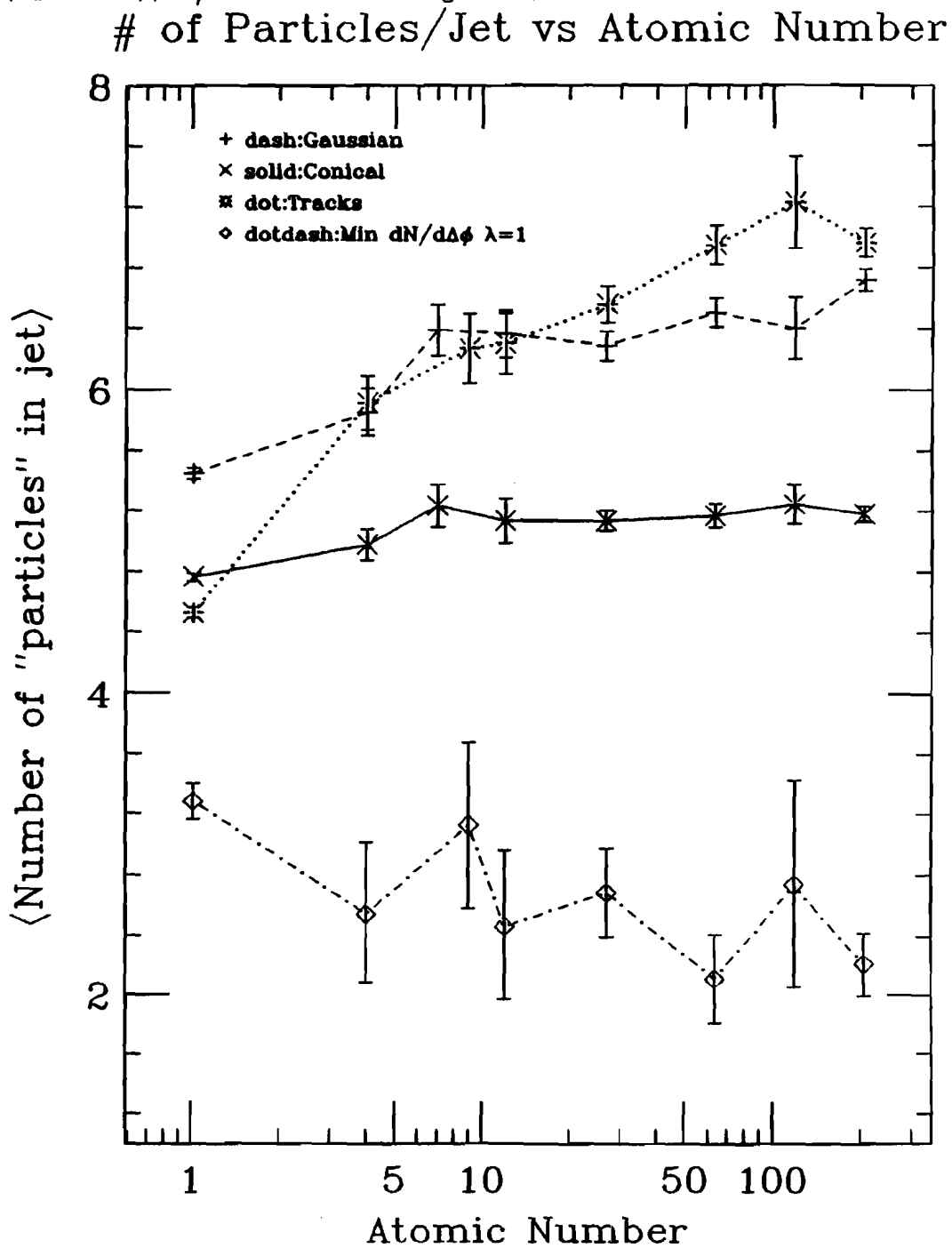

Figure 4.21 α vs. Number of "Particles" per Jet

A) α vs. <Number of clusters> per jet is shown for events with more than 4.0 GeV/c <Jet P_T> and passing the fiducial cuts as found by the conical jet-finder (solid) and the Gaussian jet-finder (dash).
B) α vs. <Number of Tracks> within 45° of jet axis is shown for the highest P_T jet (solid) and the second jet (dots). The results from the 2 jet-finders have been averaged together.

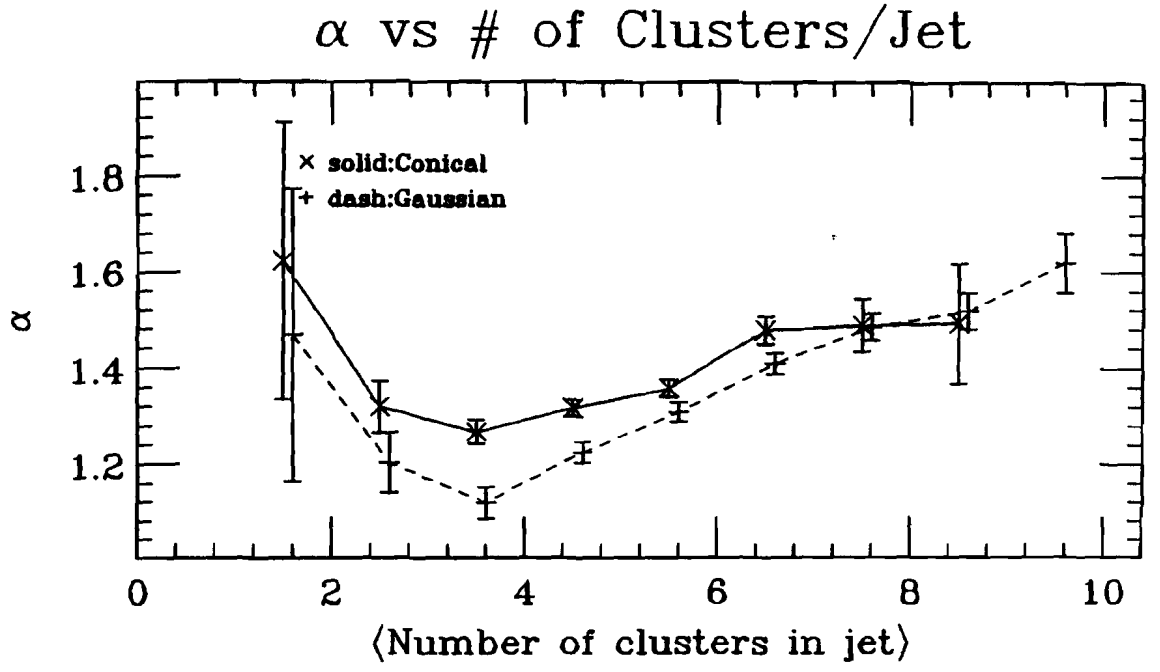

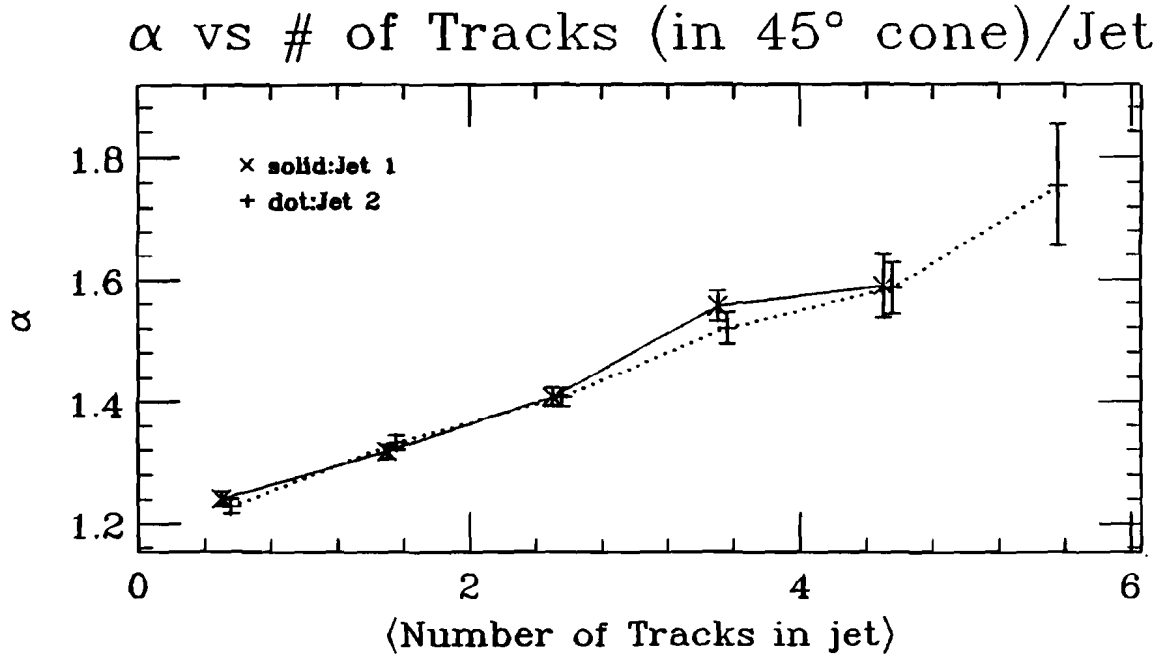

Accounting for neutral particles increases the track particle estimate an additional factor of 1.5. The minimum cluster per jet estimate from the $dN/d\Delta\phi$ calculation with λ=1.0 appears to decreases with increasing atomic number.

Plotting α verses the number of particles in the jet, figure 4.21, shows that the nuclear enhancement diminishes as the number of particles in the jets drop. This effect reflects the trend observed for planarity.

4.2.2 Cluster Angular Distribution within the Jets

4.2.2.1 Jet Aperture -

Study of the angular spread of the clusters within the jets is better done with the Gaussian jet-finder since the conical definition places a sharp cut on possible cluster-to-jet angles. Figures 4.22A&B show the cluster-to-jet angle, w_i, for hydrogen and lead jets. Similar trends are observed for both jet-finders up to the conical jet-finder's 45° cut off. This follows since the bulk of the jet clusters are identical for both jet-finders. As explained earlier, the hottest jet is narrower, almost by definition, for the Gaussian jet-finder.

Quantification of the angular spread of the ensemble of jet clusters as a single number includes the cluster-to-jet angle, w_i, weighted by the center-of-mass energy each cluster carries E_i. UA2 defines the jet aperture as $\Omega = (\Sigma E_i w_i^2 / \Sigma E_i)^{\frac{1}{2}}$ [BAG83a]. Figures 4.23A&B display distributions for our hydrogen and lead

Figure 4.22 **Angular Distribution of Jet Clusters**

A) Highest P_T Jet: The cluster-to-jet axis angles, ω_i, are shown for hydrogen using the conical (solid) and Gaussian (dash) jet-finders and for the **lead** target using the Gaussian (**daash**=**long dash**) jet-finder. **B)** Second Highest P_T Jet: ω_i from Gaussian jets are shown for the for hydrogen (dotdash) and for **lead** (**dotdaash**). Events have more than 4.0 GeV/c <Jet P_T> and $60° \leq \theta^*_{jet_1} \leq 110°$. The distributions have been normalized to the same number of events.

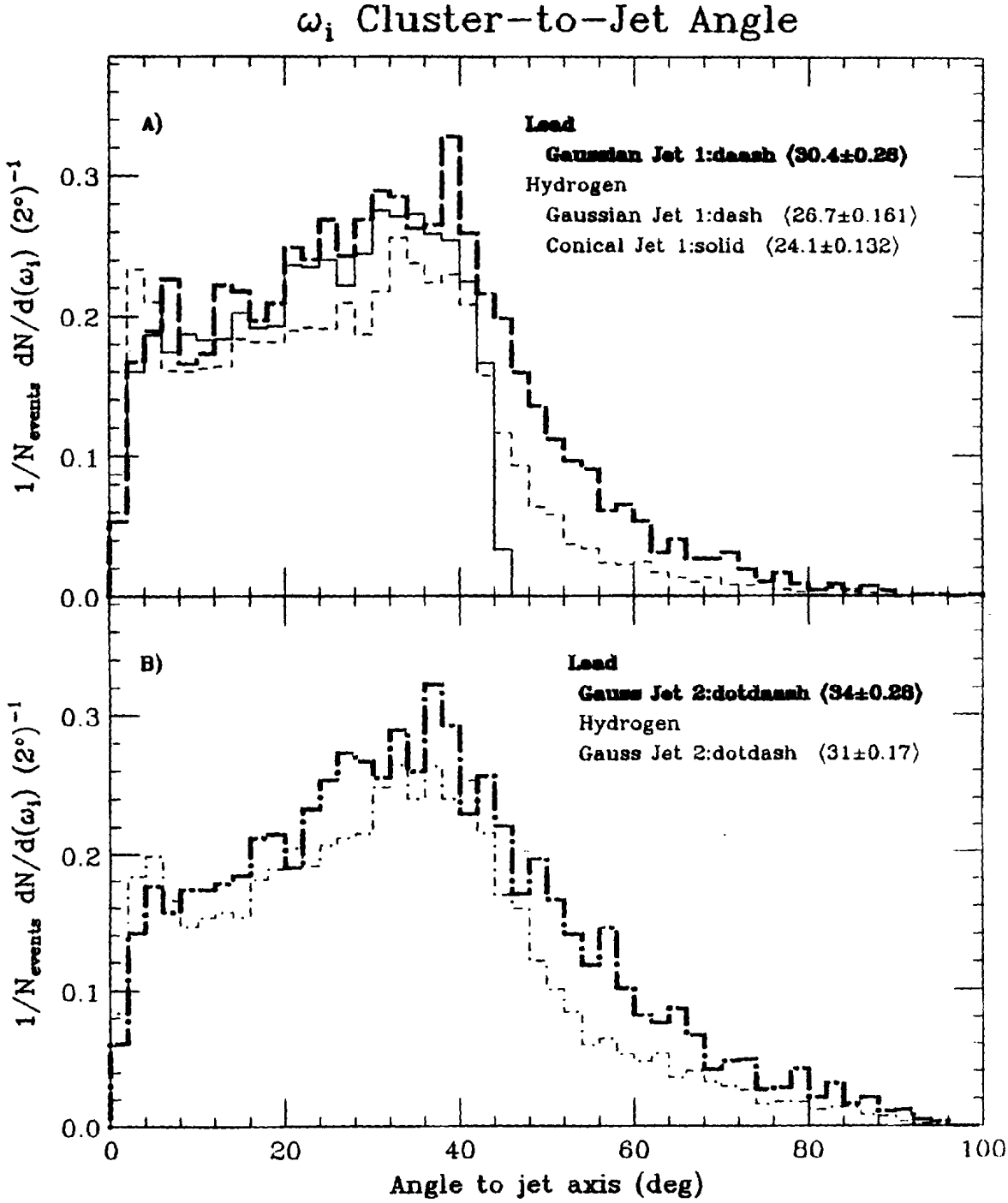

Figure 4.23 Gaussian Jet Aperture, Ω

A) Highest P_T Jet: The distribution of jet aperture, Ω, is shown for the Gaussian jet-finders for hydrogen (dash) and the for **lead (daash)**. The solid curve is from UA2 data with a minimum <Jet E_T> of 20 GeV, $\sqrt{s}$ = 540 GeV [BAG83a,BAG84b].
B) Second Highest P_T Jet: The Ω distribution is shown for the Gaussian jet-finder for hydrogen (dotdash) and for **lead (dotdaash)**. Events have more than 4.0 GeV/c <Jet P_T> and $60° \lesssim \theta^*_{jet_1} \lesssim 110°$.

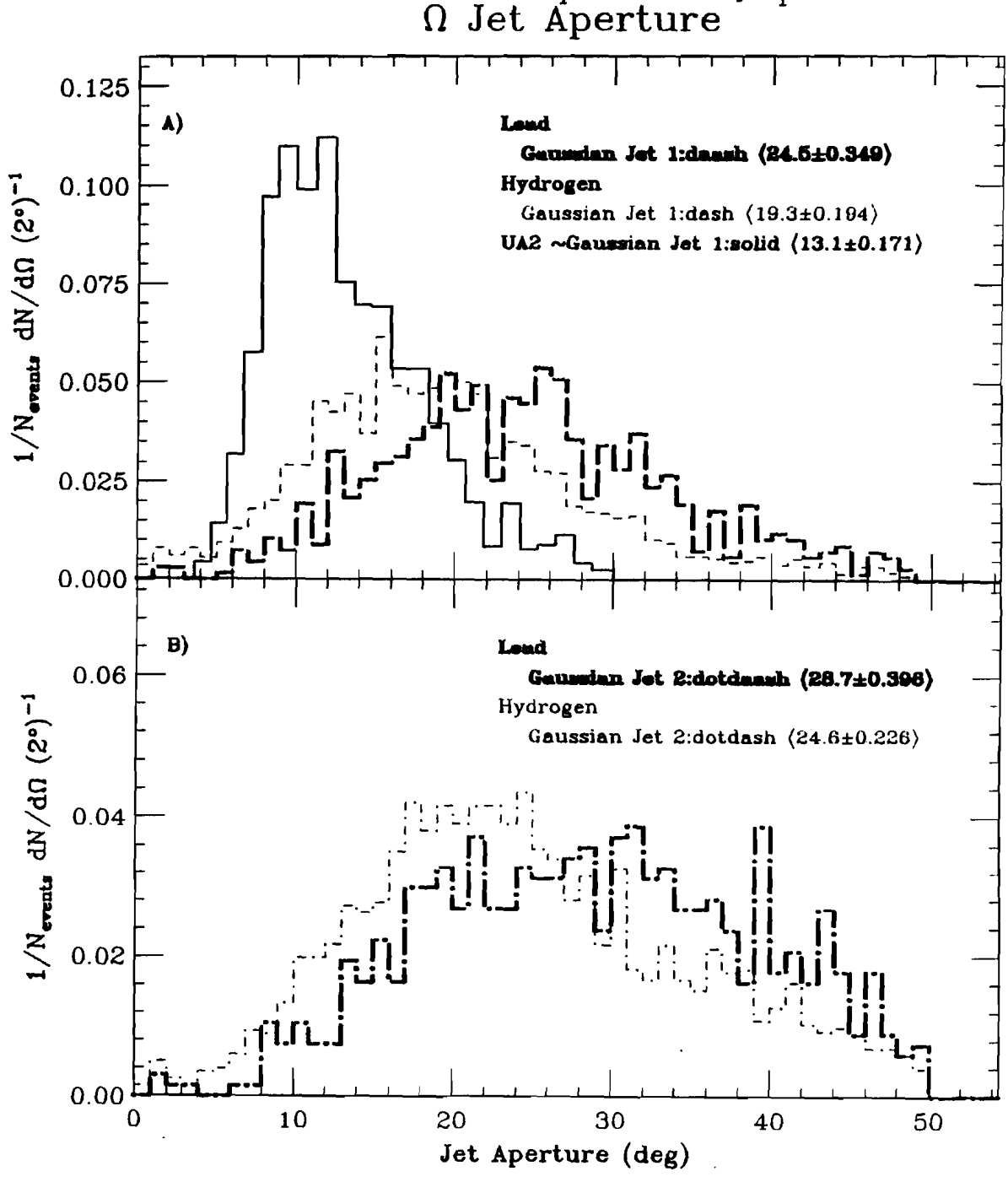

Gaussian jet apertures along with data from UA2. The UA2 jets, with a minimum of 20 GeV <Jet E_T>, contain tightly bunched particles compared to our jets with a minimum P_T of 4.0 GeV/c. Our data shows a tail reminiscent of the one seen in the UA2 data.

The trend of decreasing aperture with increasing <Jet P_T> is shown in figure 4.24A. The data from lead shows only slight narrowing of the jets with increased <Jet P_T>; however, given the large error bars, the slopes of the hydrogen and lead data could even match. When plotted as a function of atomic number the jet aperture increases, figure 4.24B. This increase is similar to that observed in the number of clusters versus A plot (figure 4.14B). Again the rate of increase may slow for high atomic numbers.

4.2.2.2 Jet $d(E_T)/d(\Delta\eta)$, $d(E_T)/d(\Delta\phi)$ -

Data from UA1 is reported as a function of E_T instead of P_T, the scaler (instead of the vector) sum of the jet particles momentum. Jet properties depend on P_T and E_T similarly, with the E_T scale slightly larger than the P_T scale. The UA1 detector's resolution was much finer in polar angle than in azimuth; while UA2 was more highly segmented in azimuthal angle. E609 has better segmentation in azimuth angle than in the polar angle; however the polar resolution is still fine enough for comparisons with the UA1 data. Recall that η, pseudo-rapidity, is related to polar angle, θ, (with the assumption that the particles have zero mass) by $\eta = \frac{1}{2}ln[(1+\cos\theta)/(1-\cos\theta)]$. Following a trend similar to that observed for the jet aperture, the mean cluster P_T distribution, considered in steps of $\Delta\eta$ (the difference between the jet axis pseudo-rapidity and the cluster

Figure 4.24 Jet Aperture <Ω> vs. <Jet P_T> and A

A) The mean jet aperture, $(\Omega_{jet_1}+\Omega_{jet_2})/2$, for Gaussian jets vs. <Jet P_T> is shown for hydrogen (dash) and for **lead (daash)**.
B) The mean jet aperture vs A for the Gaussian jet-finder. Events have two jets ≥ 4.0 GeV/c <Jet P_T> and $60° \leq \theta^*_{jet_1} \leq 110°$.

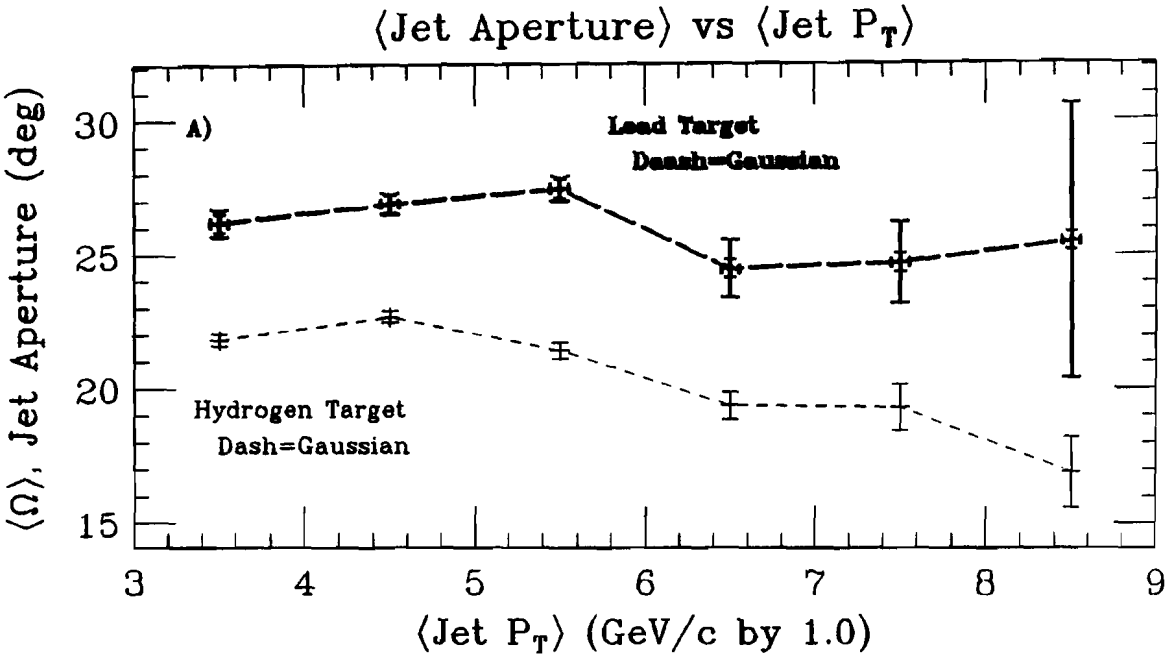

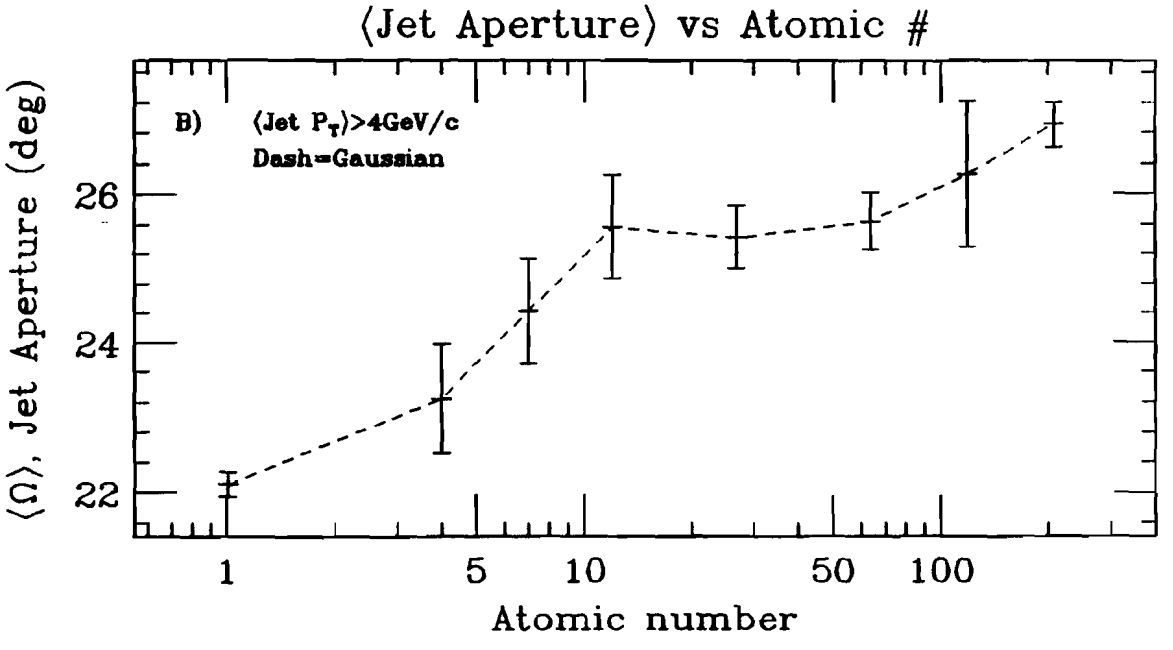

Figure 4.25 $d(E_T)/d(\Delta\eta)$ in <Jet P_T> bins

A) 4-5 **B)** 5-6 **C)** 6+ GeV/c: The Gaussian jet-finder $d(E_T)/d(\Delta\eta)$ distribution (η step=0.05) for 3 <Jet P_T> bins. Jet pairs, including clusters within 90° of the jet axes, are averaged for lH_2(solid) and Pb(dots).
D) 20-30 **E)** 30-40 **F)** 40+ GeV: The UA1 $d(E_T)/d(\Delta\eta)$ distribution [ARN83a](½ scale). Events in low acceptance areas were excluded.

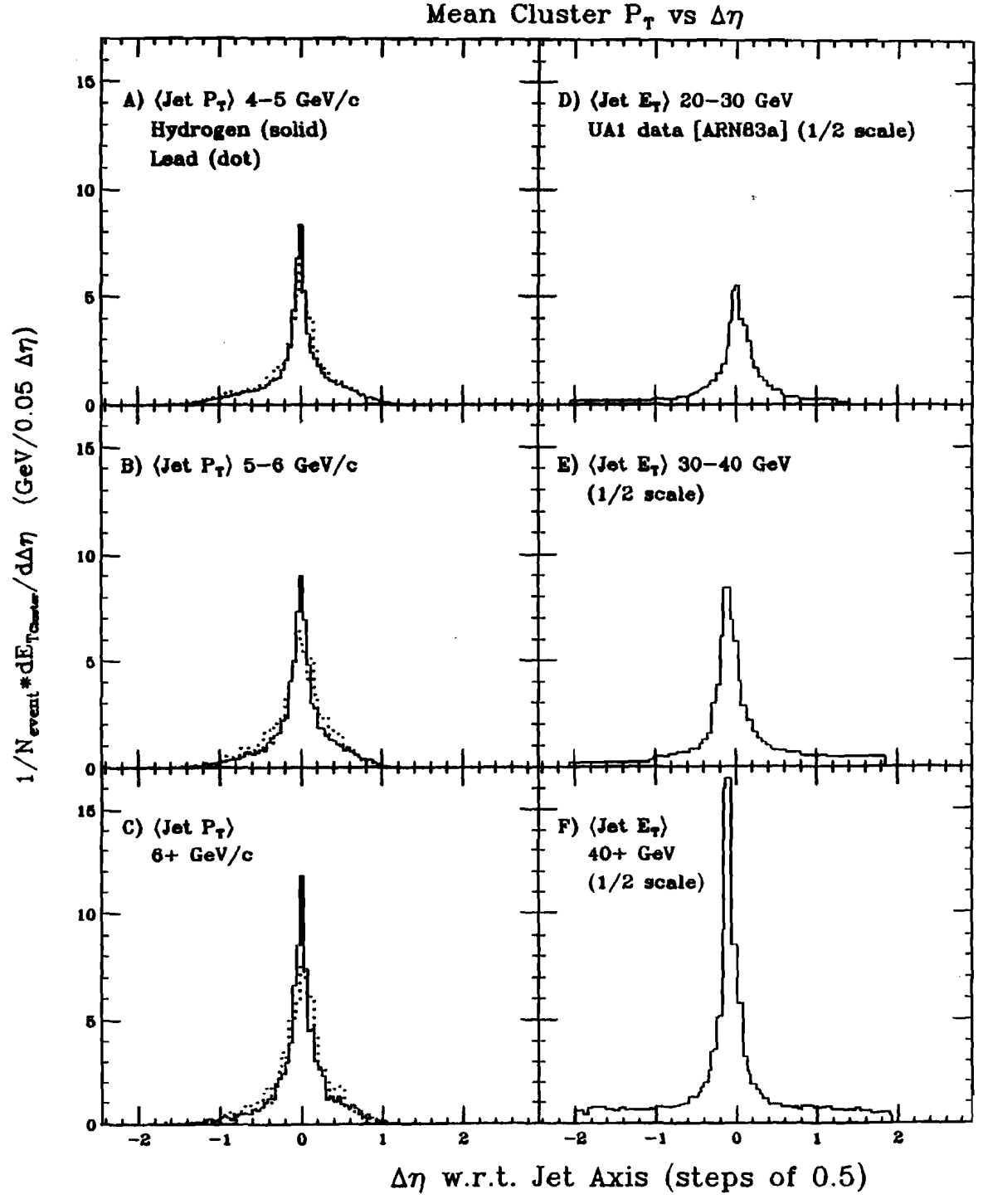

pseudo-rapidity), grows sharper with increasing <Jet P_T> and spreads as the atomic number increases. Figures 4.25A-C show the distributions for Gaussian jets from hydrogen and lead with <Jet P_T> starting from 4 GeV while figures 4.25D-F display similar curves from the UA1 data for $\bar{p}p$ jets with E_T's starting at 20 GeV [ARN83a]. Clusters included in this figure lie within 90° of one of the jet axes. Our calorimeter coverage and fiducial cut on the jet angles limits $\Delta\eta$ between -1.66 and 1.31; the flat background seen in the UA2 data is missing in our data because of our experiment's smaller acceptance.

Similarly, $dE_{T\text{clusters}}/d(\Delta\phi)$ displays E_T behavior in concert to $dE_{T\text{clusters}}/d(\Delta\eta)$. Figure 4.26 shows 4 plots similar to those previously studied in figure 4.17. Here the di-jet nature stands out distinctly. Again the Monte Carlo simulated clusters show a sharper peak for the away jet. Figure 4.27 shows that the distribution grows shaper with increased <Jet P_T>.

4.2.2.3 Jet $d(N)/d(\Delta\eta)$, $d(N)/d(\Delta\phi)$ -

The $dN_{clusters}/d(\Delta\phi)$ plots of figure 4.17 demonstrate the calorimeter resolution in ϕ. The number of clusters in the Gaussian jets, as a function of $\Delta\eta = \eta_{jet}-\eta_{cluster}$, show the limited θ^* resolution of the calorimeter. Figure 4.28A displays $dN_{cluster}/d(\Delta\eta)$ for the jets and the resulting asymmetric distribution. Some of the shoulder on the distribution is explained by figure 4.28B, showing the η distribution of the Gaussian jet axes. The sharp distribution edges in figure 4.28B correspond to the jet axis θ^* cut of 60°-100°; most of the jet centers are closer to the beam hole than the outer edge of the calorimeter; therefore the particle distribution making up these

Figure 4.26 $dE_{T\text{clusters}}/d(\Delta\phi)$, vs. $\Delta\phi$

A) $\Delta\phi$ w.r.t. Jet_1 & B) $\Delta\phi$ w.r.t. Jet_2: $dE_{T\text{clusters}}/d(\Delta\phi)$, vs. $\Delta\phi$ (4° steps) is measured from the jet axis. Gaussian jet E_T distribution, for lH_2(solid) and Pb(dots) is plotted; similar jet axes produce nearly identical curves for the conical jet-finder.
C) $\Delta\phi$ w.r.t. Jet_1 & $\Delta\phi$ w.r.t. Jet_2 for lH_2 conical jet data.
D) $\Delta\phi$ w.r.t. Jet_1: the Monte Carlo generated E_T distribution (dash) is compared to the hydrogen E_T distribution (solid). Events have <Jet P_T> greater than 4.0 GeV/c and $60° \lesssim \theta^*_{jet_1} \lesssim 110°$.

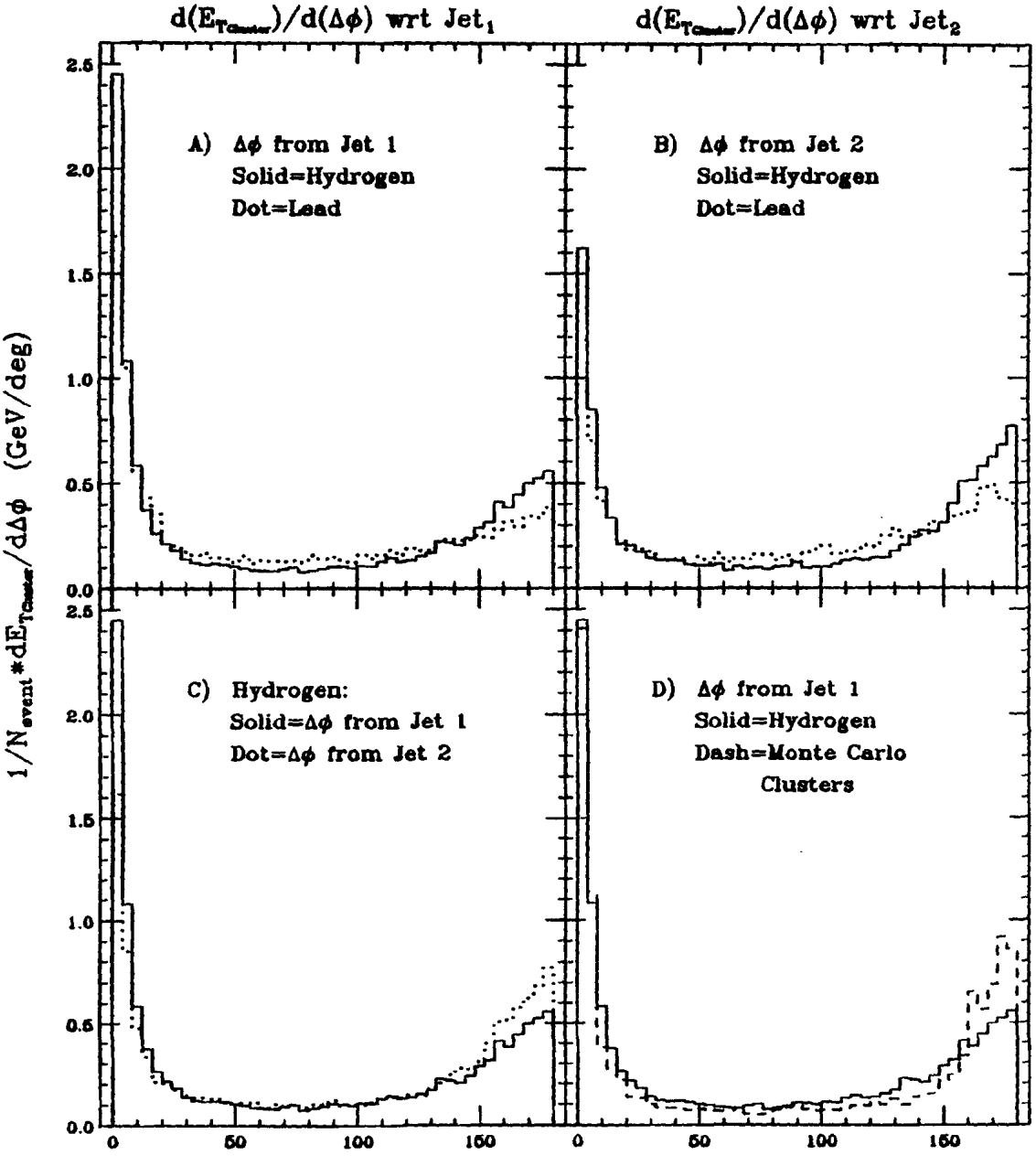

Figure 4.27 $d(E_T)/d(\Delta\phi)$ in <Jet P_T> bins

A) 4-5 GeV/c B) 5-6 GeV/c C) 6+ GeV/c: The $d(E_T)/d(\Delta\phi)$ distribution (ϕ step size of 4°) for 3 <Jet P_T> bins as found by the Gaussian jet--finder, hydrogen (solid) and lead (dots). $\Delta\phi$ is measured with respect to the highest P_T jet axis. Events passed the fiducial cut. E_T of all clusters are included the distribution

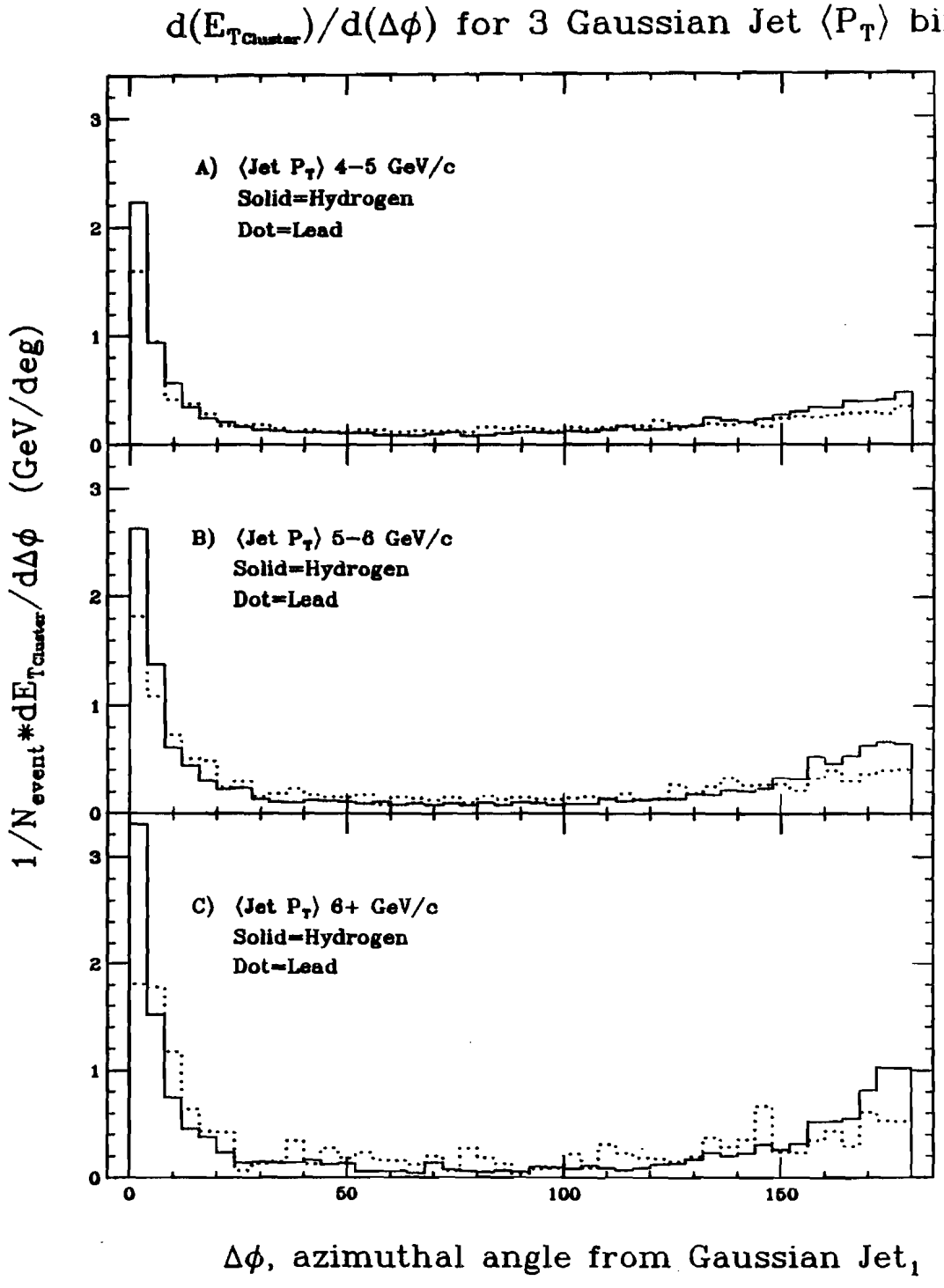

Figure 4.28 $d(N_{clusters})/d(\Delta\eta)$, η and θ^* Distributions

$^1H_2$(dash), Pb(dots):Gaussian Jet P_T> over 4.0 GeV/c & $60° \leq \theta^*_{jet_i} \leq 110°$.
Arrows point to the ring centers, top:Hydrogen, bottom:Nuclear.
A) $<N_{clusters}>$ vs. $\Delta\eta$ is shown in bins 0.05 wide. Solid line is from Pb events with no clusters below 0.75 GeV/c P_T.
B) η_{jet} distribution; the jet axis η limits reflect the $\theta^*_{jet_i}$ cuts.
C) The cluster θ* distribution.

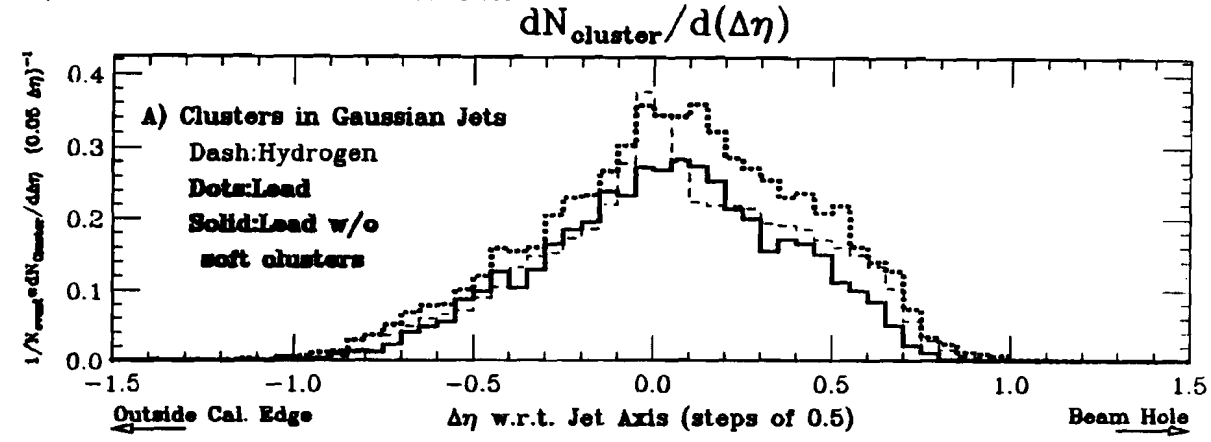

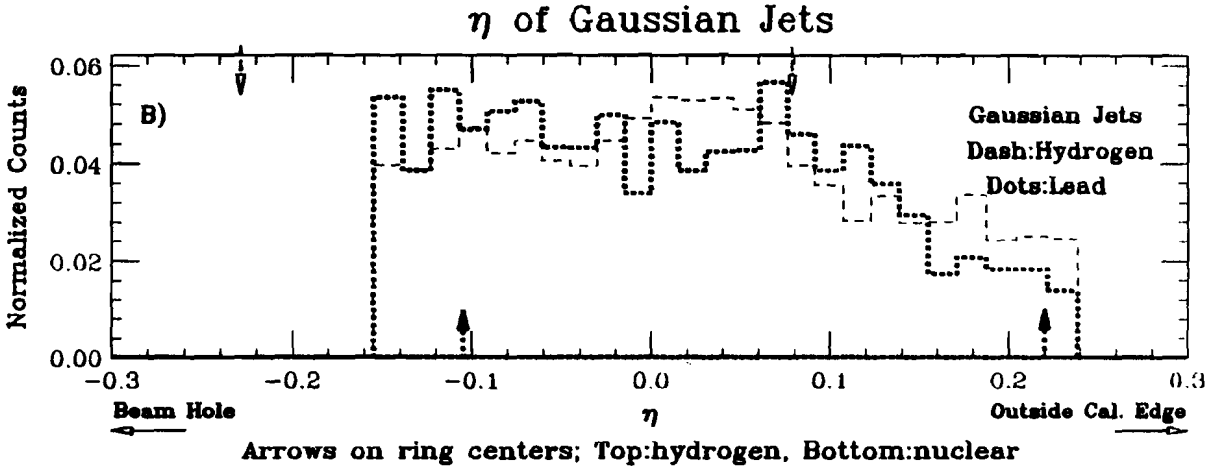

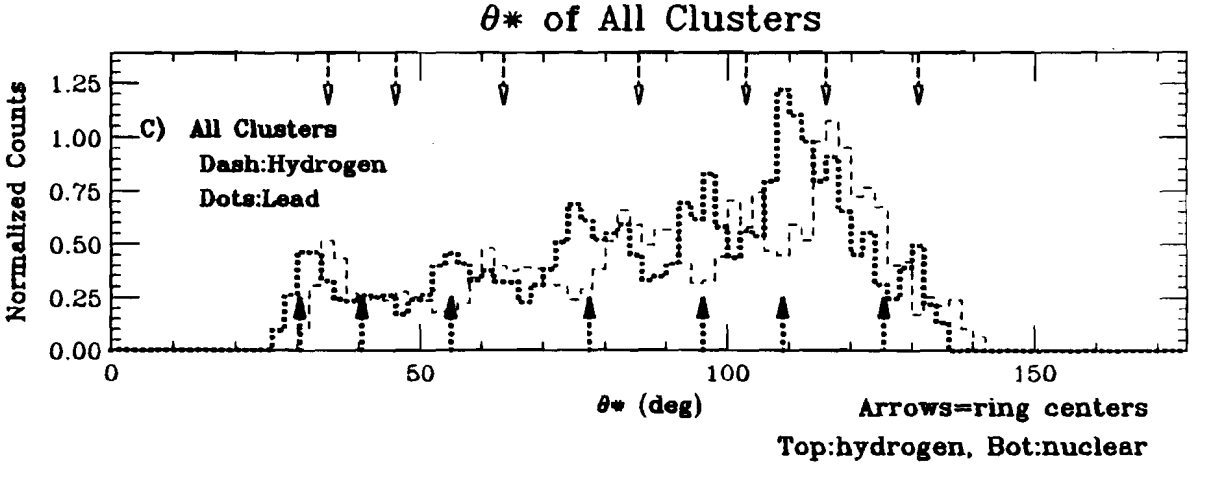

jets must also be asymmetric. Recall that our θ^*_{jet} cut reflects the calorimeter's lack of symmetry around 90°. The size of the distribution's shoulder near the beam hole is reduced when clusters below 0.75 GeV/c E_T are combined to produce "more energetic particles", the solid line in figure 4.28A. Removal of these particles suggests that part of the shoulder results from soft particles spilling into the calorimeter from the beam jet. The clustering algorithm may also produce some of this shoulder as an artifact. The slightly different acceptances of each ring of segments also affects this distribution.

Figure 4.28C shows the distribution of all clusters in the events as a function of θ^*. The multi-peak structure in the curves correspond to the calorimeter segment rings. Calorimeter rings, indicated by arrows for the hydrogen and nuclear target positions, appear as peaks in the θ^* distributions. Monte Carlo events indicate that the two-high trigger influences the particle distribution to match the ring structure, but that the bulk of the peak structure results when the highly structured segment energy is clustered into "particles". Similar peaks do not appear in the ϕ distribution, contrasting the calorimeter's resolution in ϕ and η.

Figure 4.29A further examines $dN/d(\Delta\phi)$ (previously discussed in figure 4.17 to estimate the total number of particles in the jets). As with the $\Delta\eta$ distribution, the peak $dN/d(\Delta\phi)$ value grows with increasing <Jet P_T> and as A increases. Figure 4.29A shows how the FWHM width behaves as a function of <Jet P_T> for hydrogen and lead jets found by the Gaussian jet-finder. The width of the hottest hydrogen jet stays nearly constant as the <Jet P_T> increases; however

Figure 4.29 **FWHM value of $dN_{clusters}/d(\Delta\phi)$ vs. <Jet P_T> and A**

A) The FWHM[$dN_{clusters}/d(\Delta\phi)$] for Gaussian jet_1 vs. <Jet P_T> is shown for lH_2(dash) & Pb(daash) and for jet_2 (w/dots, offset 0.1 GeV/c). B) The FWHM value of $dN_{clusters}/d(\Delta\phi)$ vs. A is shown for the Gaussian jet-finder, (jet_1,dash & jet_2,dot,offset 10%). Events have more than 4.0 GeV/c <Jet P_T> and $60° \lesssim \theta^*_{jet_1} \lesssim 110°$.

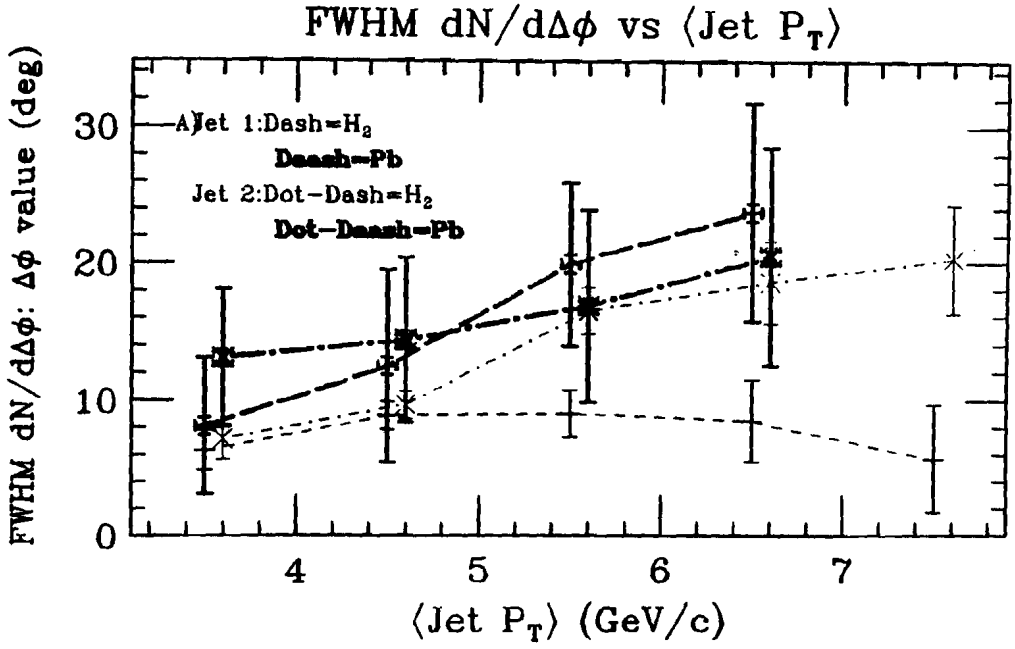

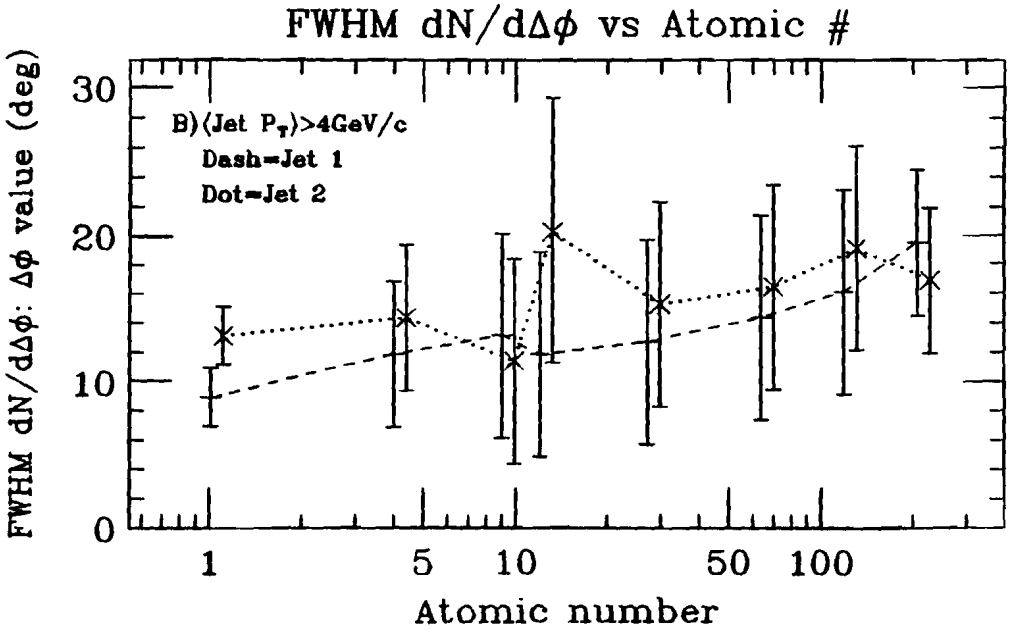

the second hottest jet clearly increases in width. The Monte Carlo particles show a similar trend. This measure of the jet width also increases for the nuclear targets, implying that the addition of particles at wide angles provides some of the increased <Jet P_T>. Figure 4.29B shows the increasing FWHM of the two jets as a function of atomic number. We expect a smaller width of the hotter jet from the Gaussian jet definition; operating on a hypothetical jet pair made from two sets of particles with identical transverse energies, the Gaussian jet-finder assigns the larger jet P_T to the jet with the least spread in the energy density, since the P_T contribution is weighted by its angle from the jet axis.

4.2.2.4 Jet Leading Cluster Angle -

The angle the leading cluster makes with the jet axis, $w_{\text{leading cluster}}$, is similar to FWHM $dN/d(\Delta\phi)$ in its dependence on <Jet P_T> and atomic number, as seen in figures 4.30A&B. Hydrogen produces a flat or slightly falling $w_{\text{leading cluster}}$ distribution with rising <Jet P_T> in the hot jet while the angle increases for the second jet; the other nuclei produce larger angles as the <Jet P_T> increases for both jets. This effect is consistent with an overall increase in the cluster multiplicity within the jet; additional clusters shift the jet axis away from the momentum vector of the leading cluster. Considering all jet pairs with <Jet P_T> above 4 GeV, increasing the target atomic number increases $w_{\text{leading cluster}}$. Both the jet-finders produce similar leading cluster curves.

α is a function of each of these angular measures, with α increasing with the jet width. Figures 4.31A&B show this trend for

Figure 4.30 Leading Cluster Angle with Jet vs. <Jet P_T> and A

A) The mean $\omega_{\text{leading cluster}}$ for Gaussian jet_1 vs. <Jet P_T> is shown for lH_2(dash)&Pb(daash) and for jet_2 (w/dots, offset .1 GeV/c).
B) The mean $\omega_{\text{leading cluster}}$ is shown as a function of atomic number for the Gaussian jet-finder jet_1 (dash) and jet_2 (dots, offset 10%). Events have more than 4.0 GeV/c <Jet P_T> and $60^\circ \lesssim \theta^*_{\text{jet}_1} \lesssim 110^\circ$.

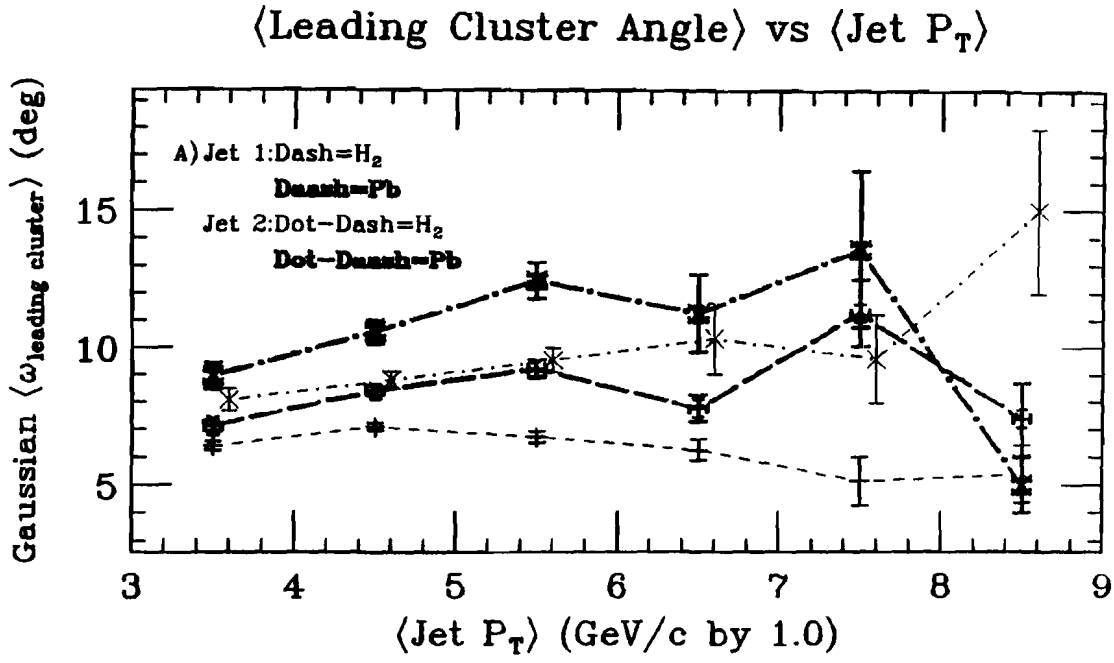

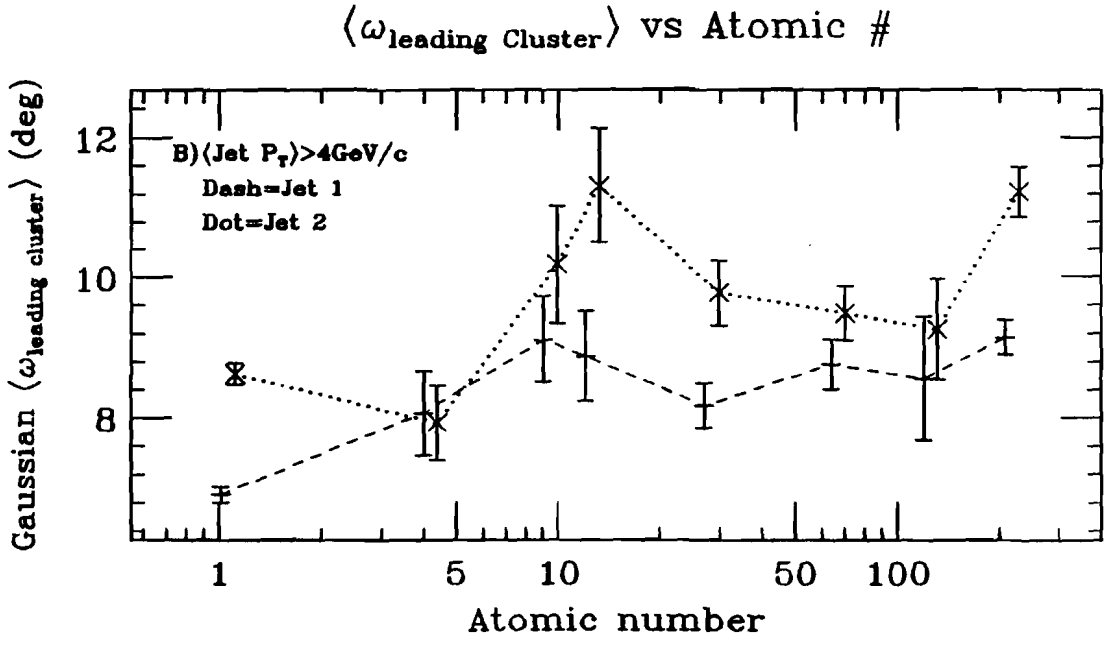

Figure 4.31 α vs. Cluster Angular Distribution

A) The α value decreases as Ω decreases for the conical(solid) and Gaussian (dash, offset 0.45°) jet-finders.
B) The α value decreases as $\omega_{\text{leading cluster}}$ decreases for the hot Gaussian jet(dash) and the second hottest (dotdash, offset 0.3°) jet.

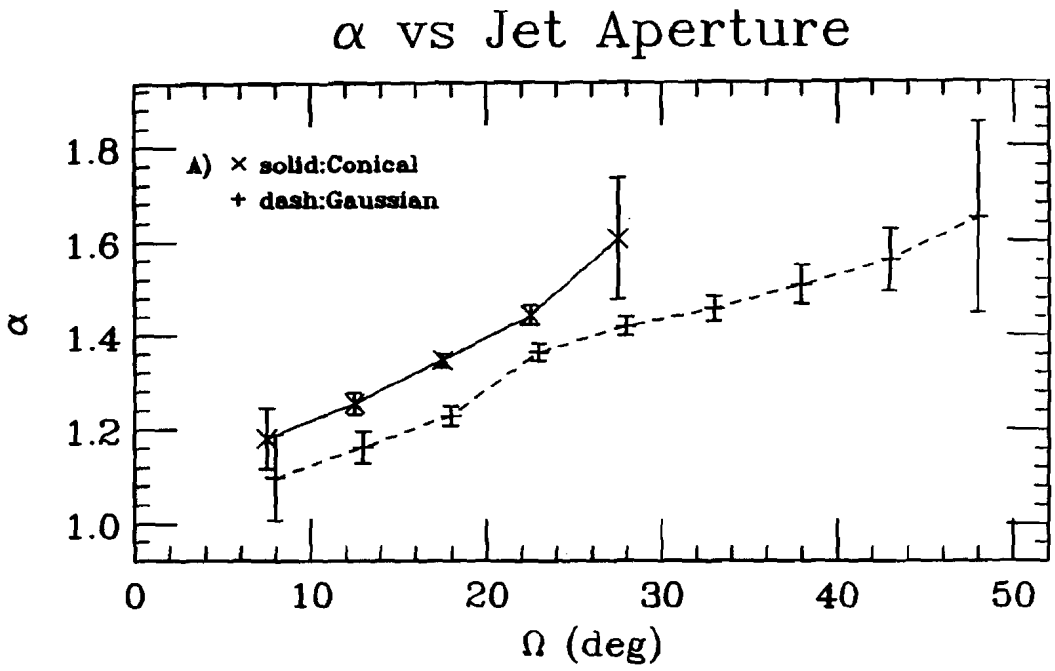

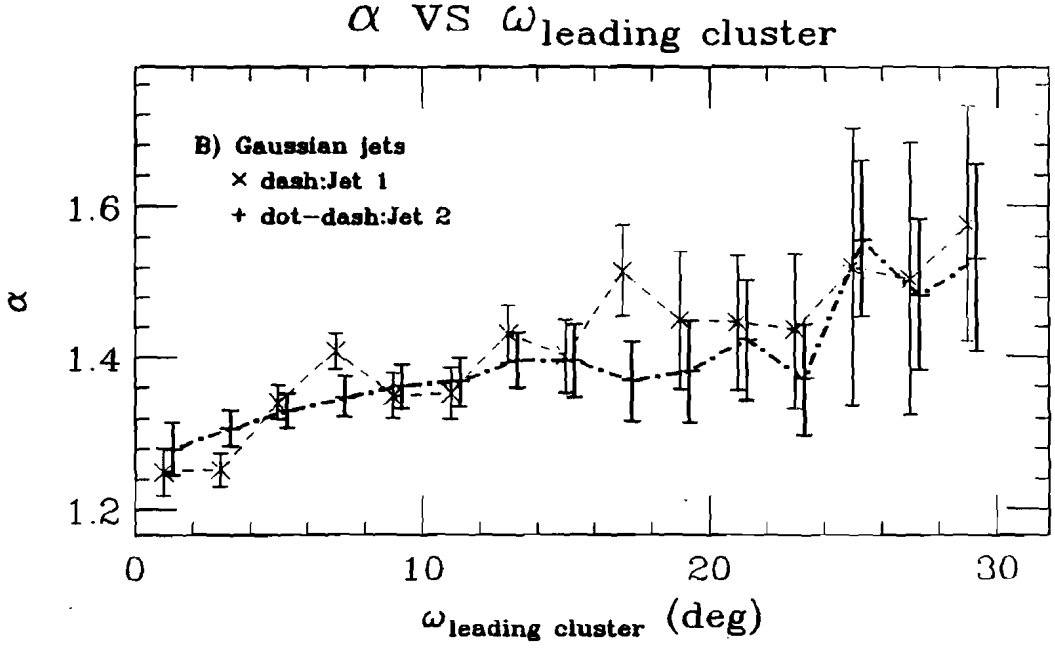

two of the angular measures studied above. As with planarity, the more "jet-like" events are least affected by the nuclear target.

4.2.3 Cluster Momentum along the Jets

4.2.3.1 E_T of jet clusters -

Before discussing the momentum of the clusters with respect to the jet axis it is interesting to observe the E_T distribution of the jet clusters, figure 4.32A. Two peaks appear, a result of the two-high trigger convolved with the clustering algorithm. The higher E_T peak comes from the leading clusters, which trigger the event, while the bulk of the clusters produce a peak at lower E_T. The source of this structure appears upon comparison of the Monte Carlo particle E_T spectrum with the E_T spectrum of the simulated clusters reconstructed in the calorimeter, figure 4.32B. The particle E_T distribution smoothly decreases with increasing E_T while the reconstructed E_T distribution of the clusters builds into a second peak around 4 GeV. This structure indicates that the trigger is sometimes satisfied, not by a single hot particle, but by two softer particles striking the same segment in the calorimeter. The two-high trigger selects a special class of events which have transverse energy concentrated into a small area; events may satisfy this requirement by putting two particles in the same cluster. The clustering algorithm, as well as the triggering logic, can not distinguish between one particle or several closely-spaced particles; it always produces a single cluster. Actual particle identification would be

Figure 4.32 Jet Cluster E_T Distribution

A)The jet cluster E_T distribution for Gaussian jet_1 from lH_2(solid) and Pb(dots) shows the effect of the two-high trigger convolved with the clustering, displaying two peaks in the distribution.
B)The Monte Carlo demonstrates the source of the dual peaks. The Monte Carlo particles produce a smooth spectrum(solid) while the simulated clusters(dash) show two peaks.

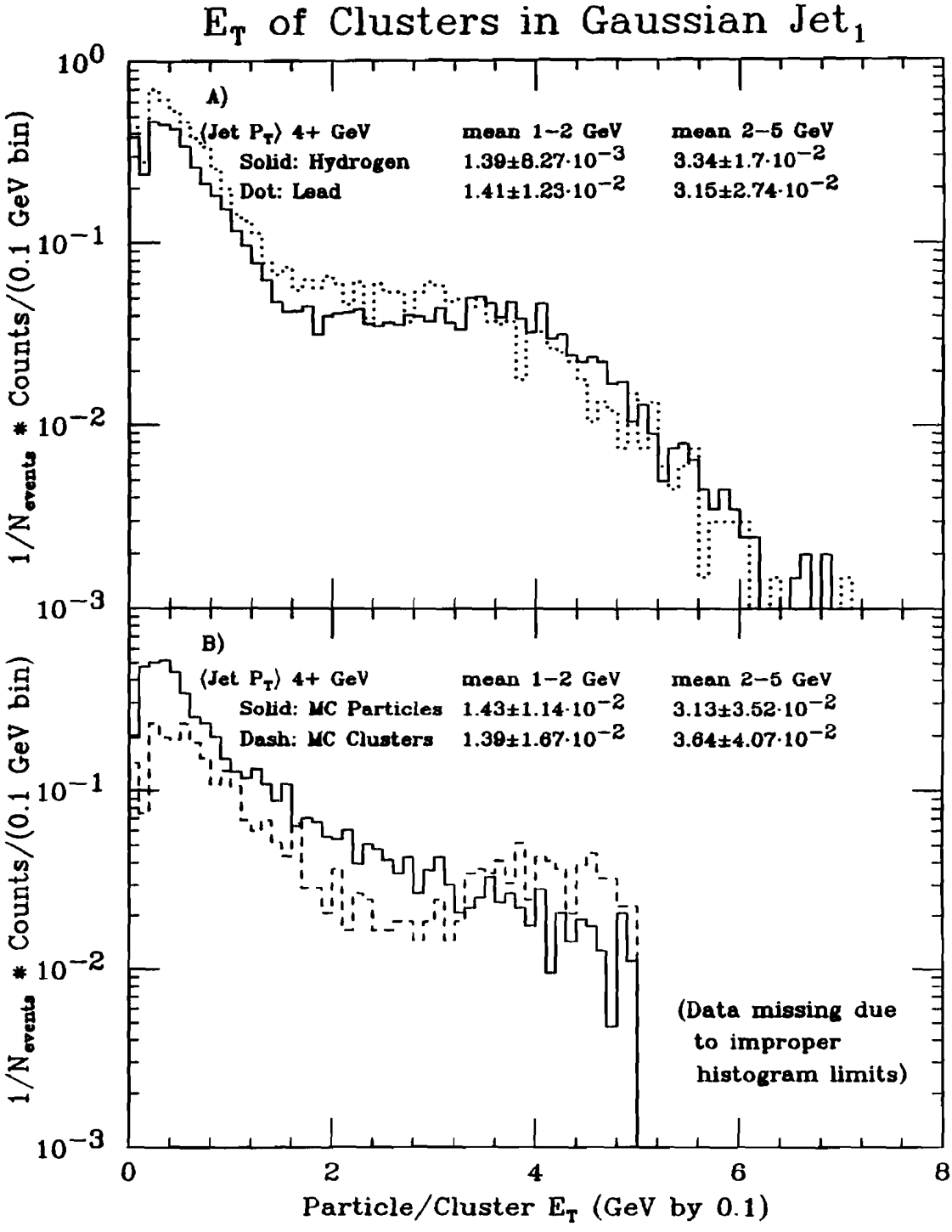

required to reproduce the smooth E_T spectrum. The clustering further affects this distribution since low P_T particles may be improperly combined into a single higher P_T cluster, or a high P_T particle may loose energy off the calorimeter. Thus, particle momentum along the jet axis must be studied in terms of the leading cluster and the other jet clusters, with the caveat that the clusters only roughly correspond to particles and that the leading cluster may result from the combination of several particles.

4.2.3.2 Momentum along the Jet Axis: Z -

A pair of variables, Z, the cluster momentum along the jet axis, and q_T, the cluster momentum perpendicular to the jet axis, quantify the energy flow within the jet. Typical D(Z) distributions, the density of particles within a jet as a function of their momentum along the jet, from other proton-on-proton experiments fall exponentially as Z increases (the dotted curve in figure 4.33A shows the ISR data [ÅKE85]). Our hydrogen data is shown on the same figure for comparison and agrees reasonably well up to Z values near 0.35. The curves can roughly be broken into three regions, Z <0.1 , 0.1 < Z <0.35, and Z >0.35. The steeply falling region for Z values below 0.1 consists mostly of low energy clusters and clusters at angles near 90° to the jet axis. The sharp rise in the data from the ISR experiment results from their inclusion of all particles within 90° of the jet without identifying specific jet particles. The dotdash curve in figure 4.33A shows D(Z) for our lH_2 data including all clusters within 90° of the jet. Identification of conical jet clusters produces the solid curve, lower at small Z values and identical at higher Z values to the curve

Figure 4.33 *Z* Distribution

A)Hydrogen & B) Lead:The Z distribution is shown for the conical jets for the 2-hi trigger including all clusters in 90° of the jet (dotdash) and the ISR data [ÅKE85] (dots). The D(Z) of the jet clusters produces a curve (solid) which differs from the inclusion of all clusters only at low Z. Exclusion of the leading cluster (dash) causes the distribution to drop to zero at 0.5. Events have <Jet P_T>'s over 4.0 GeV/c and $60° \lesssim \theta^*_{jet_1} \lesssim 110°$.

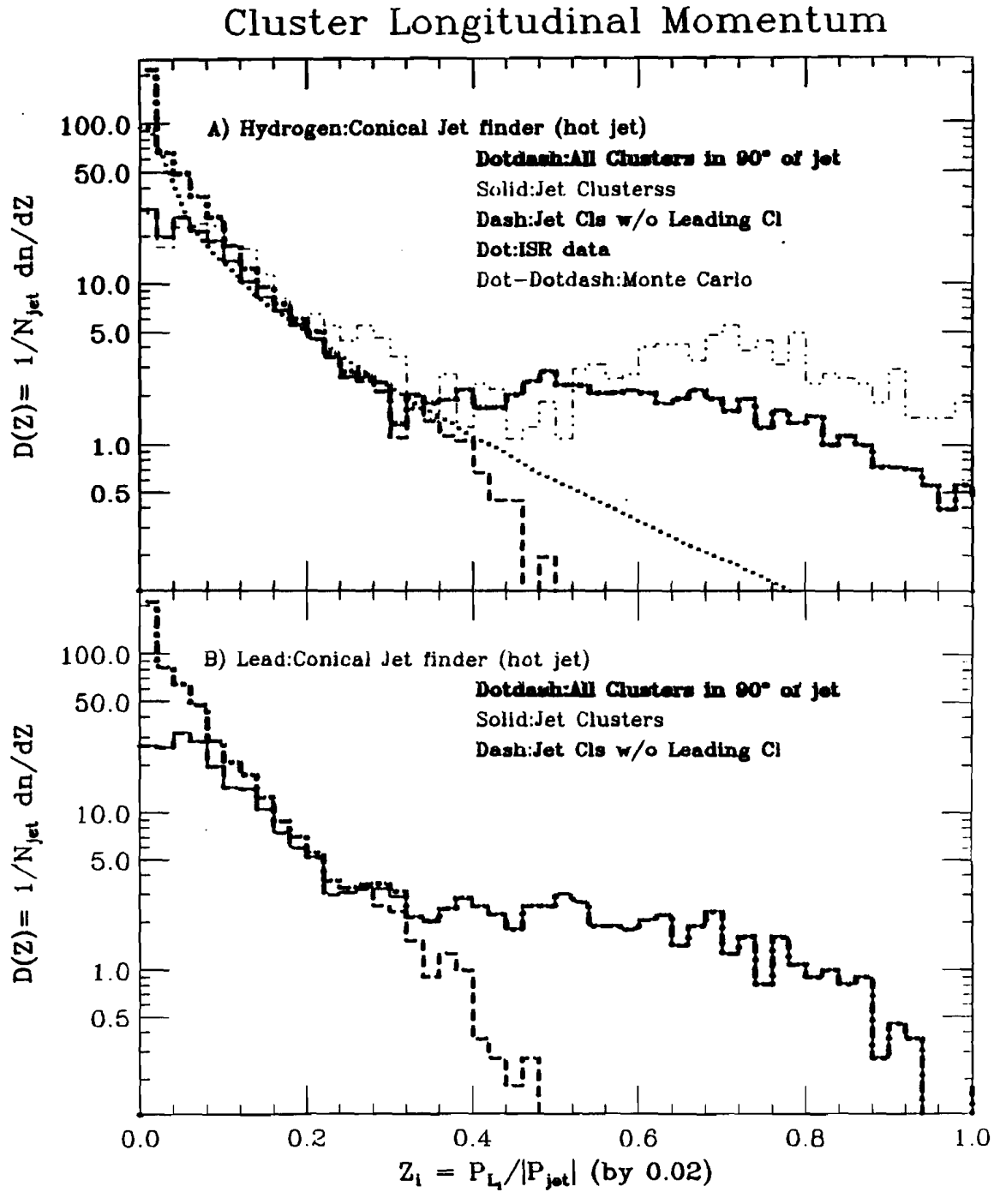

Figure 4.33 *Z* Distribution (continued)

C) The Gaussian jet lH_2 *Z* distributions for 3 bins of <Jet P_T>.
D) The lH_2 & Pb *Z* distributions are compared for the hot Gaussian jets. Jets have P_T between 4 and 8 GeV/c.
E) lH_2 & Pb: The *Z* distributions for Gaussian jet_2.
F) lH_2 & Pb jet *Z* distributions from experiment E672 [STE88].

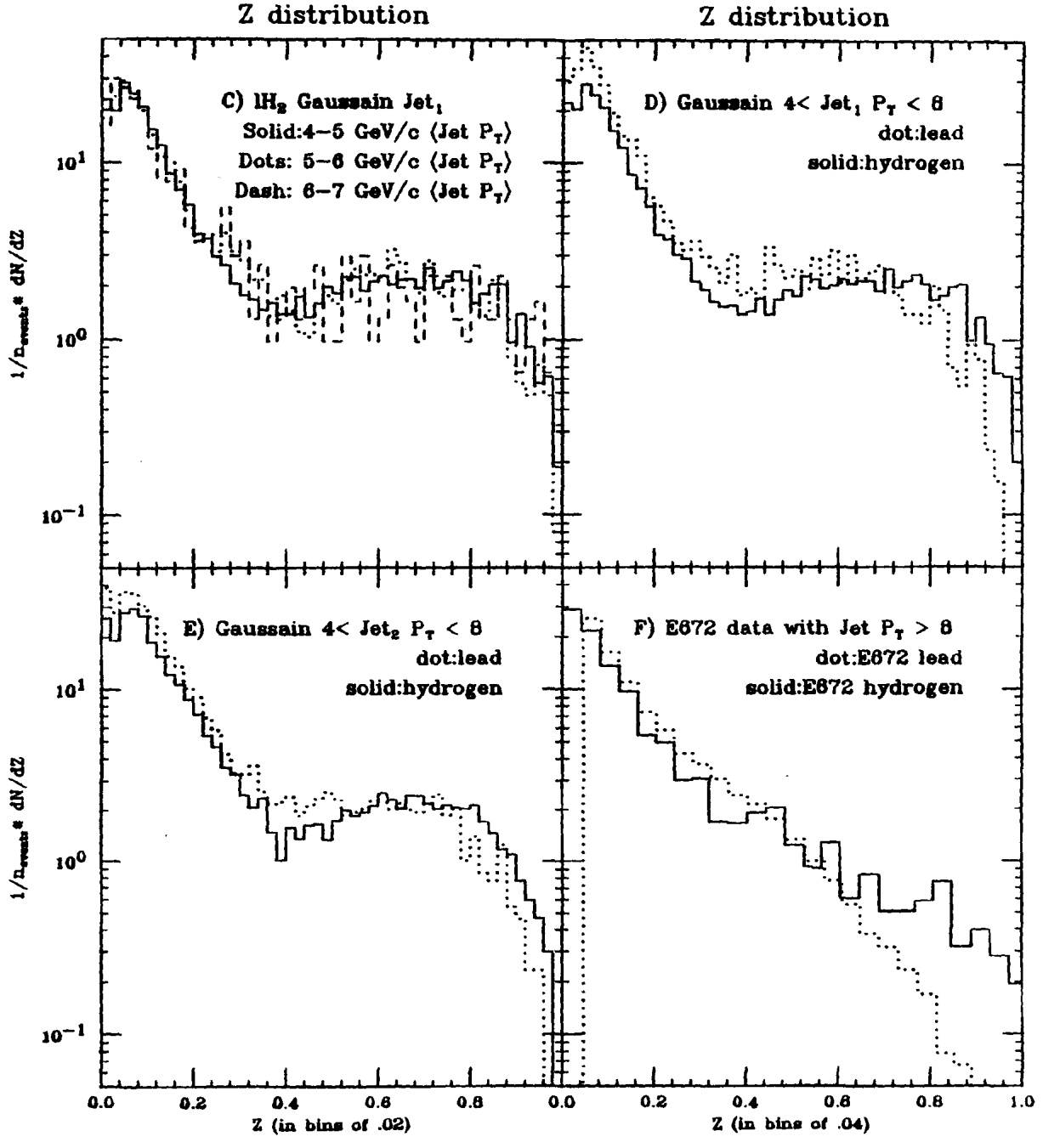

containing the hemisphere of clusters. NA5 sees a similar effect when they select clusters within 40° of the leading cluster [deM84]. The middle section of the curve, $0.1<Z<0.35$, where both samples agree, corresponds to the bulk of the jet clusters.

Above $Z = 0.35$ the density distributions differ radically between the ISR data and our data; the two-high trigger selects fragmentation modes in which a single cluster carries a large fraction of the total jet momentum (partly resulting from the combination of a pair of particles into a single cluster) while the ISR utilized a "two-jet" trigger which selected events with E_T above a threshold in phase space spanning 45° in $\Delta\phi$ and $45° < \theta^* < 135°$. Because of the slightly different fragmentation modes and the collection of two particles into a single cluster, our cluster density builds into a shallow peak around $Z = 0.6$, (the solid/dotdash line in figure 4.33A) while the ISR data continues to drop. The Monte Carlo jets, reconstructed with the conical jet-finder, exhibit a similar behavior (the dot-dotdash curve), with the peak at large Z values enhanced even over our data. The source of the discrepancy between the Monte Carlo and the data may be the sensitivity of the trigger to hot segments and the trigger thresholds. Excluding the leading cluster from the Z distribution leaves only the steeply falling portion of the curve (the dashed line). As the jet P_T increases, figure 4.33C, the dip between the peak and the falling spectrum fills slightly. For Z between 0.0 and 0.2 and for Z equal 0.6, $D(Z)$ stays roughly constant for all P_T values, while the $D(Z)$ slightly drops for the largest Z as the jet P_T increases. The ISR collaboration saw similar low and high Z effects as a function of jet P_T, however they do not observe an increased

density around Z equal 0.4 or the roughly constant value around Z equal 0.6. These differences are a result of the two-high trigger and the clustering algorithm.

When examined as a function of <Jet P_T> and atomic number, $\langle Z_{\text{leading cluster}} \rangle$ and $\langle Z_{\text{w/o leading cluster}} \rangle$ show differing trends, figures 4.34A-D. $\langle Z_{\text{leading cluster}} \rangle$ results when Z of the leading cluster is averaged over many events. $\langle Z_{\text{w/o leading cluster}} \rangle$ comes from averaging the Z of all the clusters in each jet except for that of the leading cluster, and then taking the average of this value over the entire sample of events. The requirement of increased transverse momentum in the jet comes primarily from the addition of more clusters rather than more energy in the leading cluster. Supporting this claim, the mean leading-cluster momentum fraction drops with increasing P_T (figure 4.34A) while the momentum fraction of the remaining clusters increases slightly, (the second hydrogen jet may drop slightly, see figure 4.34B; notice the difference in Z scales).

The drop in $\langle Z_{\text{leading cluster}} \rangle$ with increasing target A is consistent with the energy in the leading cluster remaining roughly fixed while the total jet momentum increases due to the presence of additional clusters. Recall that figure 4.32 shows nearly identical E_T densities for both hydrogen and lead when $E_T \geq 4.0$ GeV. Casual inspection of figures 4.33D-F might cause concern about this statement; a similar plot in [STE88], figure 4.33F, prompted the statement that "drastic changes in the properties of our jets are observed for the heavy target data, (in) which the 'core' of the jet completely disappears." However, figure 4.32 supports the claim that the energy in the leading cluster remains constant with A; the

Figure 4.34 <Z> vs. <Jet P_T> and A

A)Leading Cluster & B)Without Leading Cluster: <Z> from Gaussian jets vs. <Jet P_T> is show for lH_2(Jet$_1$:dash, Jet$_2$:dotdash) and for Pb(Jet$_1$:daash, Jet$_2$:dotdaash).
C)Leading Cluster & D)Without Leading Cluster: <Z> vs. A is shown for the Gaussian jet-finder. Events have more than 4.0 GeV/c <Jet P_T> and $60° \lesssim \theta^*_{jet_1} \lesssim 110°$.

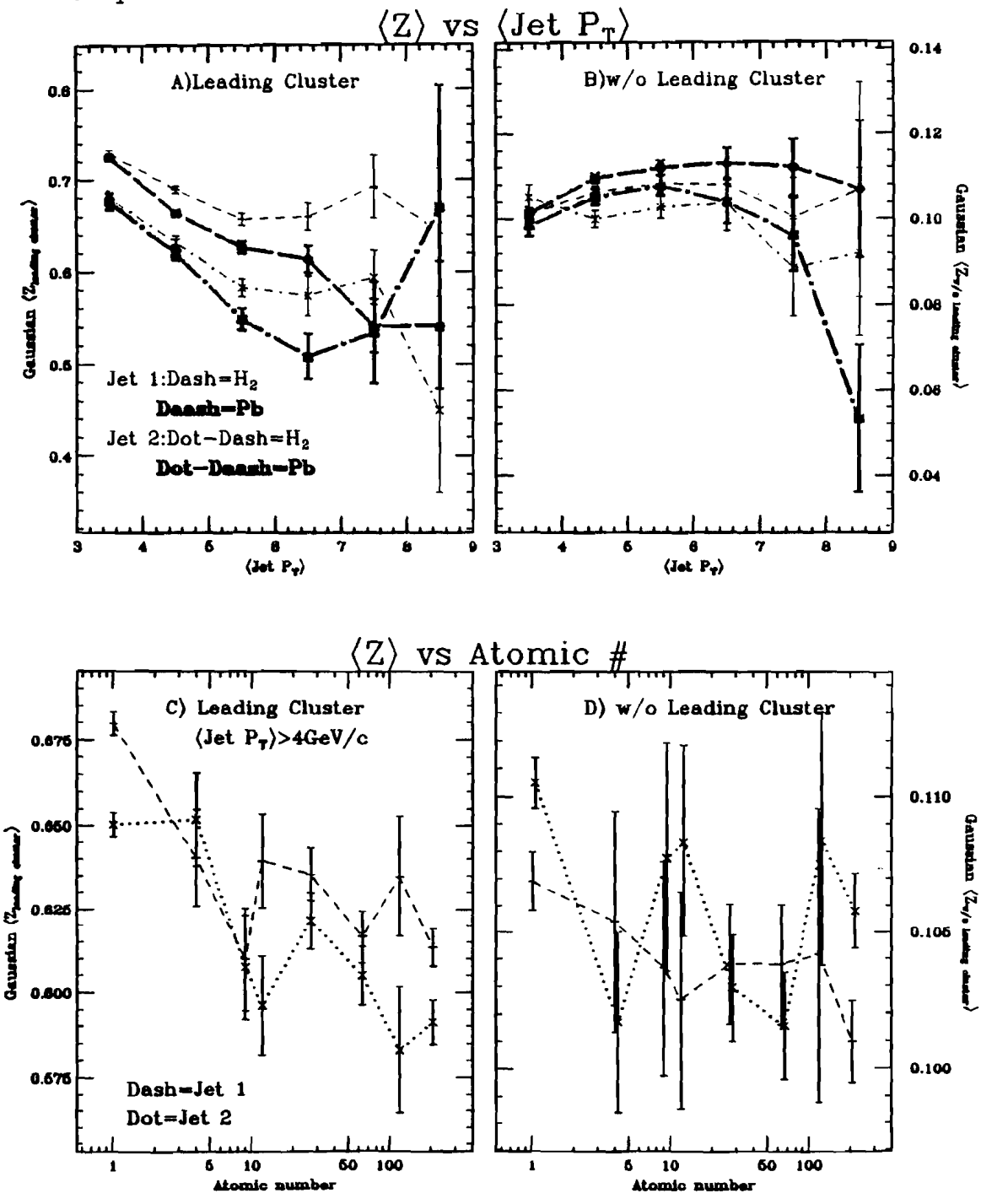

cluster density as a function cluster E_T shows no decrease of high E_T clusters when lead is compared to hydrogen. The "missing core" interpretation fails to recognize that Z is the *momentum fraction* of the clusters. Production of clusters with Z near one requires a jet with all the momentum in a single cluster; the increased multiplicity produced by high A targets reduces the chance for any jet to contain only a single cluster. The drop in D(Z) at the highest Z values reflects the increased event multiplicity, not a change in the E_T of the leading clusters. The remaining cluster's $\langle Z_{\text{w/o leading cluster}} \rangle$ density shows a slight drop with atomic number, implying that part of the change in jet structure results from the addition of more clusters. It is also interesting to note that the difference in the Z distribution between hydrogen and lead in our data, figure 4.33E, is much smaller than the difference observed in experiment E672, figure 4.33F. This difference may reflect the different triggers used in the two experiments.

Figure 4.35A demonstrates the decrease in nuclear enhancement for events where the leading cluster accounts for a larger fraction of the jet momentum; α drops as $\langle Z_{\text{leading cluster}} \rangle$ approaches 1.0. Figure 4.35B shows that this trend also appears, but to a much small extent, for $\langle Z_{\text{w/o leading cluster}} \rangle$, displaying a 4% drop in α. The second highest P_T jet shows a similar pattern except at lower Z values.

Figure 4.35 α vs. $\langle Z \rangle$

A) Leading Cluster & B) Without Leading Cluster: α is shown for Gaussian jets as a function of changing $\langle Z \rangle$ values. Events have more than 4.0 GeV/c <Jet P_T> and $60° \leq \theta^*_{jet_i} \leq 110°$.

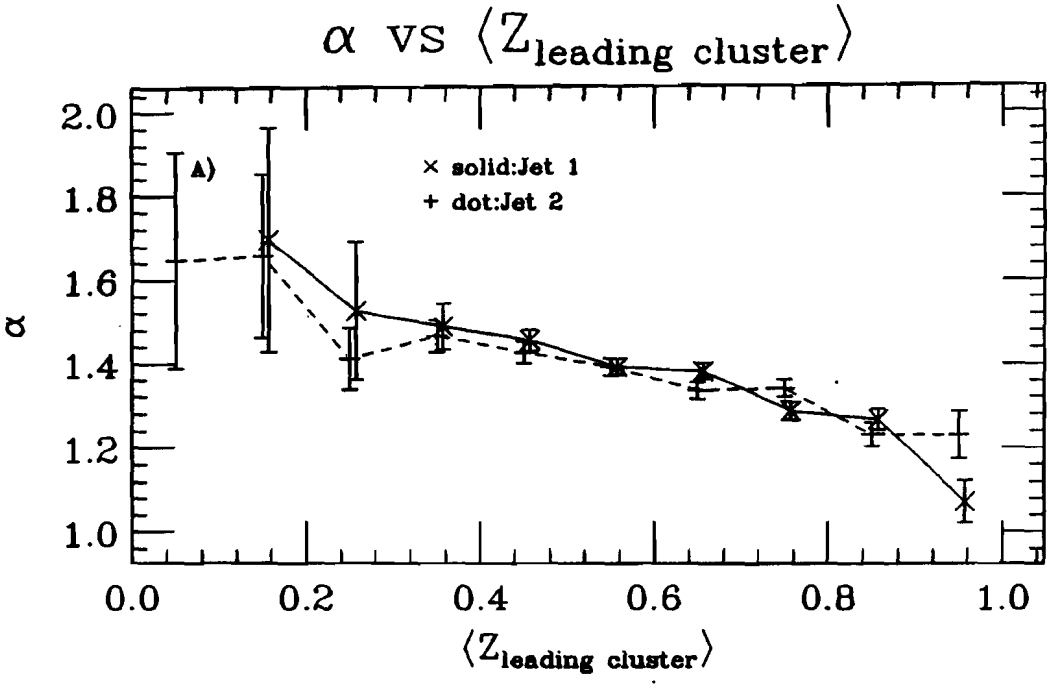

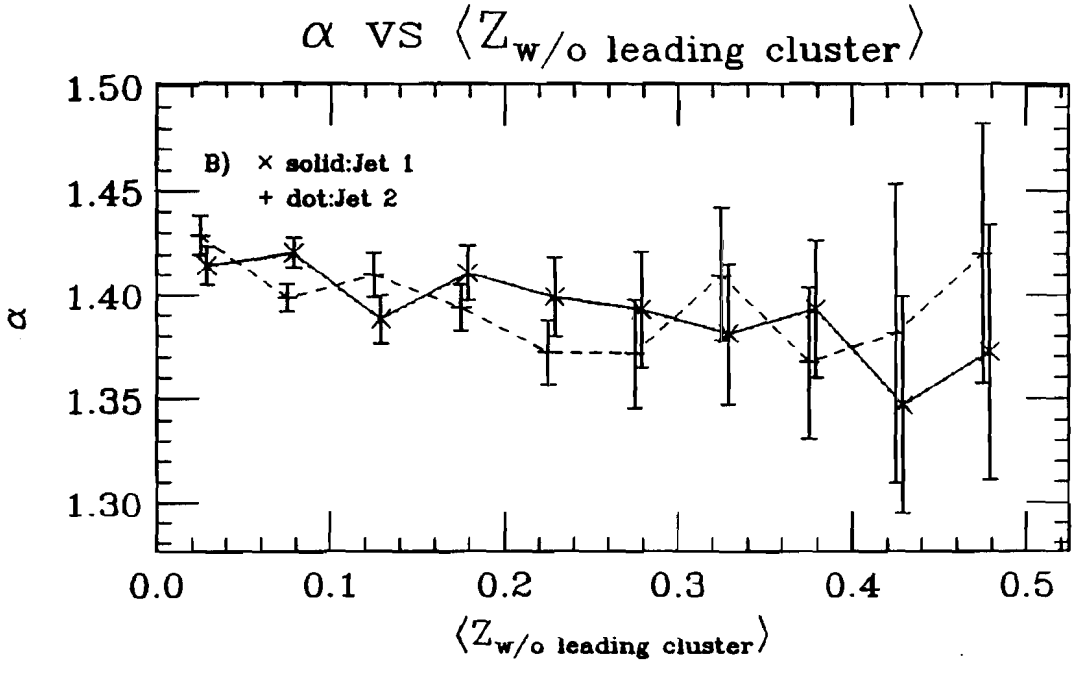

4.2.3.3 Momentum transverse to the Jet Axis: q_T -

The q_T is less sensitive to the inclusion of the leading cluster than the Z distribution, (the leading cluster still tends to carry more transverse momentum than the mean cluster q_T value). Figures 4.36A&B show the q_T distribution for all clusters assigned to the jet as well as the leading cluster q_T distribution. Energy flows for lead and hydrogen produce similarly shaped distributions.

Our distribution below q_T of 0.25 GeV/c is atypical. Other experiments observed curves like the dotdashed curve produced by the Monte Carlo. Our high density of clusters at very small q_T values results from the treatment of soft particles in the clustering algorithm. The q_T density, $D(q_T)$, drops a factor of three in the smallest q_T bins when clusters with less than 0.75 GeV of lab energy are combined to create events free of "soft particles". A cut on the remaining clusters, requiring them to have energy along the jet axis above 0.1 GeV, reduces $D(q_T)$ another factor of 8 for q_T values below 0.1 GeV/c. The dashed curves in figures 4.36A&B show the jet cluster $D(q_T)$ distribution when a Z cut of 0.1 is applied to the q_T distribution; most of the low q_T clusters are eliminated. These eliminated "particles" may have had no physical reality since the algorithm which clusters segments into particles fails near the detection threshold, (see [MAR87]). The number of clusters at small q_T decreases as the <Jet P_T> increases and is 15% smaller for the Gaussian jet-finder than the conical jet-finder. The conical jet-finder includes all clusters within the cone angle; however, the Gaussian jet-finder only includes clusters with enough P_T to raise the Gaussian P_T surface above ½ the peak value. A large angle cluster with a small

Figure 4.36 q_T Distributions

A)Hydrogen & B) Lead:The q_T distribution is shown for the conical jets for the 2-hi trigger including all clusters in the jets (solid). Leading clusters(dots) or clusters with Z>0.1(dash) produce smaller cluster densities at low q_T while not affecting the high q_T distribution. The full 4-jet Monte Carlo, without relying on the clustering algorithm, predicts fewer clusters in the lowest q_T bins and an enhancement at moderate q_T values (dotdash).

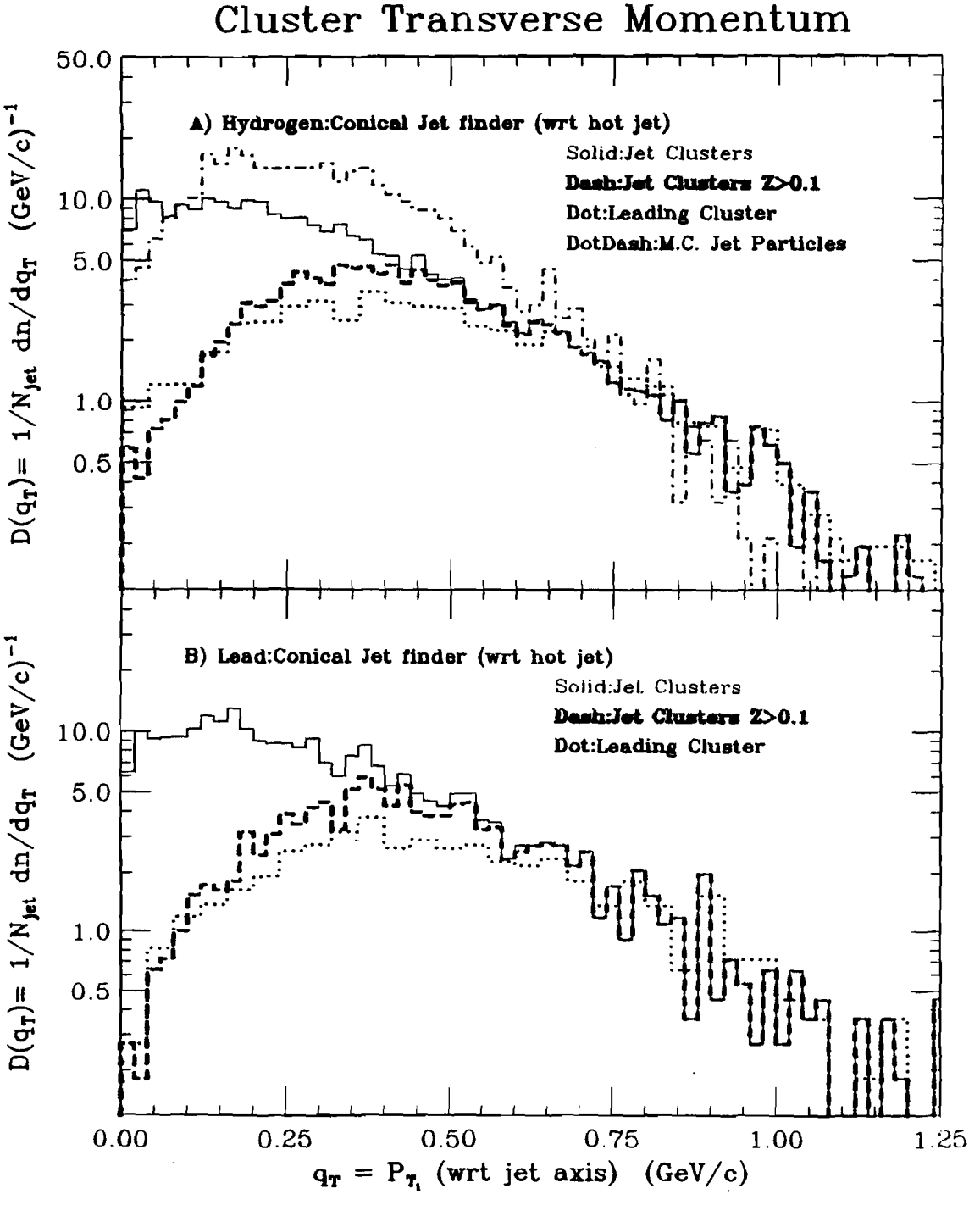

Figure 4.37 $<q_T>$ Distributions

A) The $<q_T>$ distribution for hydrogen (solid) and Lead (dots) produces mean values of 0.317±.004 GeV/c and 0.335±.006 GeV/c respectively.
B) The Monte Carlo high P_T jet particles produce a mean value of 0.313±.002 GeV/c (solid), while the conical jet-finder working on Monte Carlo clusters (dots) produces 0.364±.002 GeV/c.

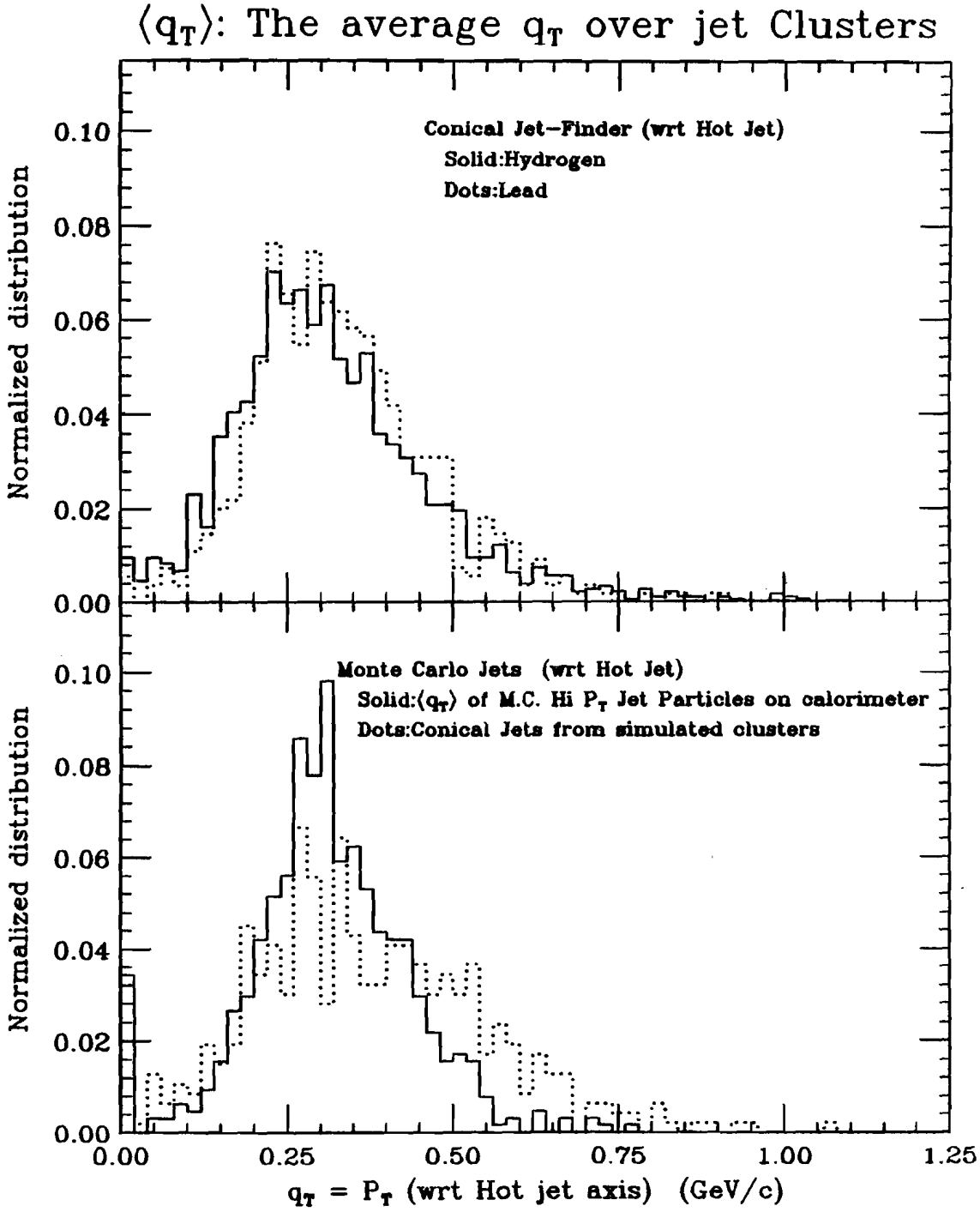

P_T will not be included as part of a Gaussian jet while a large P_T cluster at the same angle will be included; the conical jet-finder includes both clusters.

The average $<q_T>$ for a jet, calculated as the sum of the jet clusters' q_T divided by the number of clusters in the jet, is about 0.30 GeV/c. The Monte Carlo produces similar distributions, see figure 4.37. Figure 4.38A shows the growth of $<q_T>$ with <Jet P_T>. As the jet's total transverse energy grows, the energy available to flow transverse to the jet axis also grows. Figure 4.38B shows that $<q_T>$ also grows slowly with atomic number and figure 4.38C shows that α rises slightly with $<q_T>$.

Correlations between Z and q_T, seen in hadronic and leptoproduction physics [BAR66,HAN82,ALT83,ARN83b], have been labeled the "seagull-effect" to describe the increase of q_T with increasing Z for low Z values, the approach to a q_T near 0.5 GeV/c for Z values near 0.5 and the drop again in q_T values for large Z values. The circles in figure 4.39A show the results from UA1 [ARN83b] and the dotted line results from TASSO e^+e^- data [ALT83]. Our data at $\sqrt{s}$=27.4 GeV agrees reasonably well, given the different triggers, with the e^+e^- data acquired at 22.0 GeV and lies 0.25 GeV below the UA1 data, taken at $\sqrt{s}$=540 GeV. The highest P_T jet and the second highest P_T jet, figure 4.39B, produce similarly shaped curves but the second jet lies at slightly lower q_T values. Exclusion of the leading cluster from the q_T distribution produces a curve which climbs until the data runs out at Z values above 0.6. The leading cluster dominates events with the highest Z values (UA1 appears to have limited data in this region); above Z of 0.4 the q_T for the highest P_T cluster in the jet

Figure 4.38 <q_T> vs. <Jet P_T> and A

A) The mean <q_T> for the Gaussian jets is shown as a function of <Jet P_T> for hydrogen (solid) and for lead (dots).
B) For the 2 jets with highest P_T, <q_T> vs. A is shown for events with <Jet P_T> over 4.0 GeV/c and $60° \leq \theta^*_{jet_1} \leq 110°$.
C) α vs. <q_T> for the conical (solid) and Gaussian (dash) jet-finders.

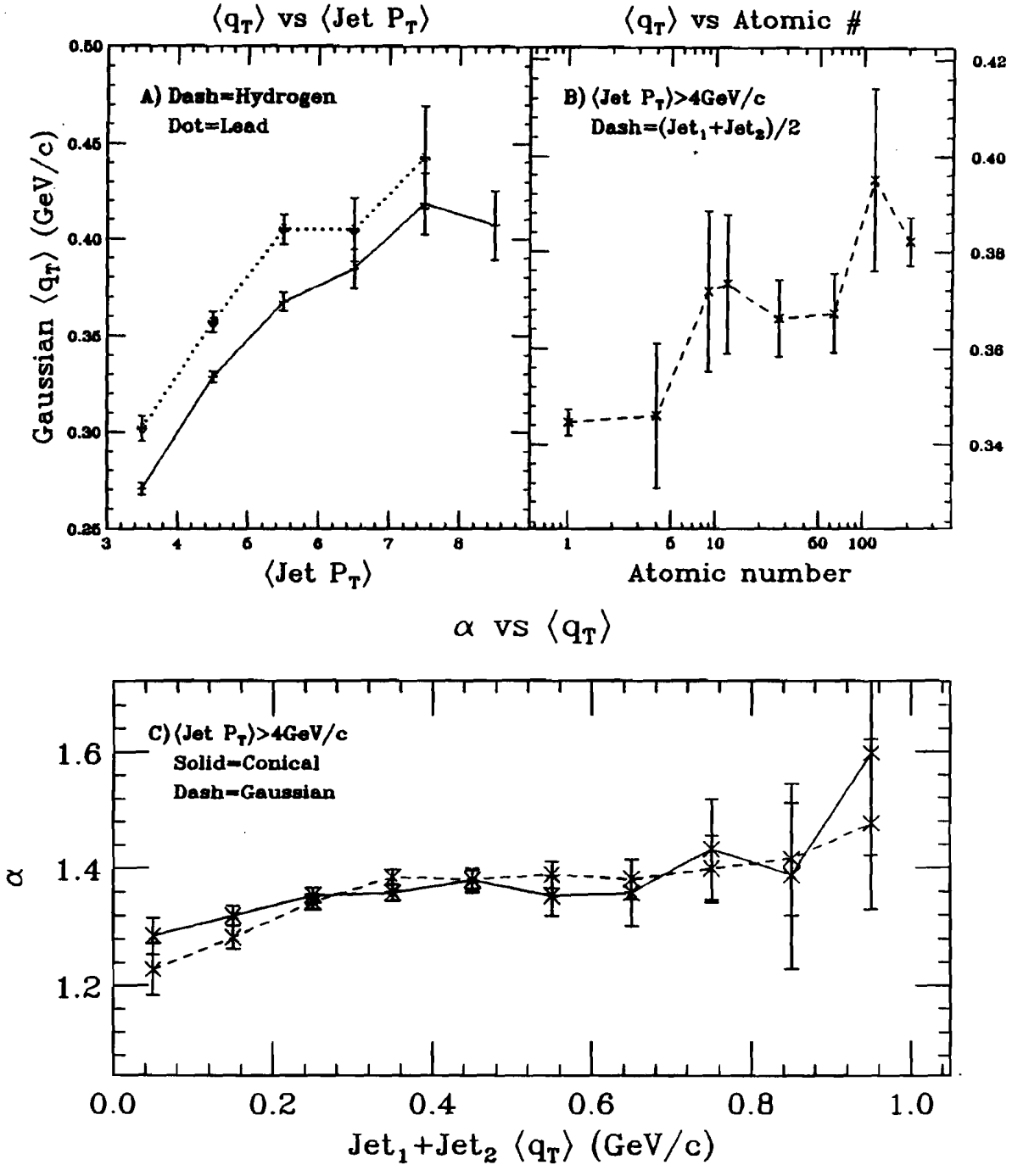

Figure 4.39 q_T vs. Z (The "seagull effect")

A) q_T vs. Z is shown for E609 2-hi trigger events with conical jets (solid). The UA1 [ARN83b] data, at 540 GeV center of mass energy, (circles) lies well above our data. The e^+e^- data from TASSO [ALT83], at 22 GeV, (dots) produces a curve similar to our data at 27 GeV.
B) IH_2: q_T vs. Z is shown for the conical jet_1(solid) and the jet_2(dots). The leading cluster(**dotdash**) and the other clusters (dash) separate for $0.4<Z<0.7$.
C) Pb: q_T vs. Z is shown for the jet_1(solid), the leading cluster(**dotdash**) and the non-leading clusters(dash). The IH_2 distribution is repeated(dots). Errors are statistical only.

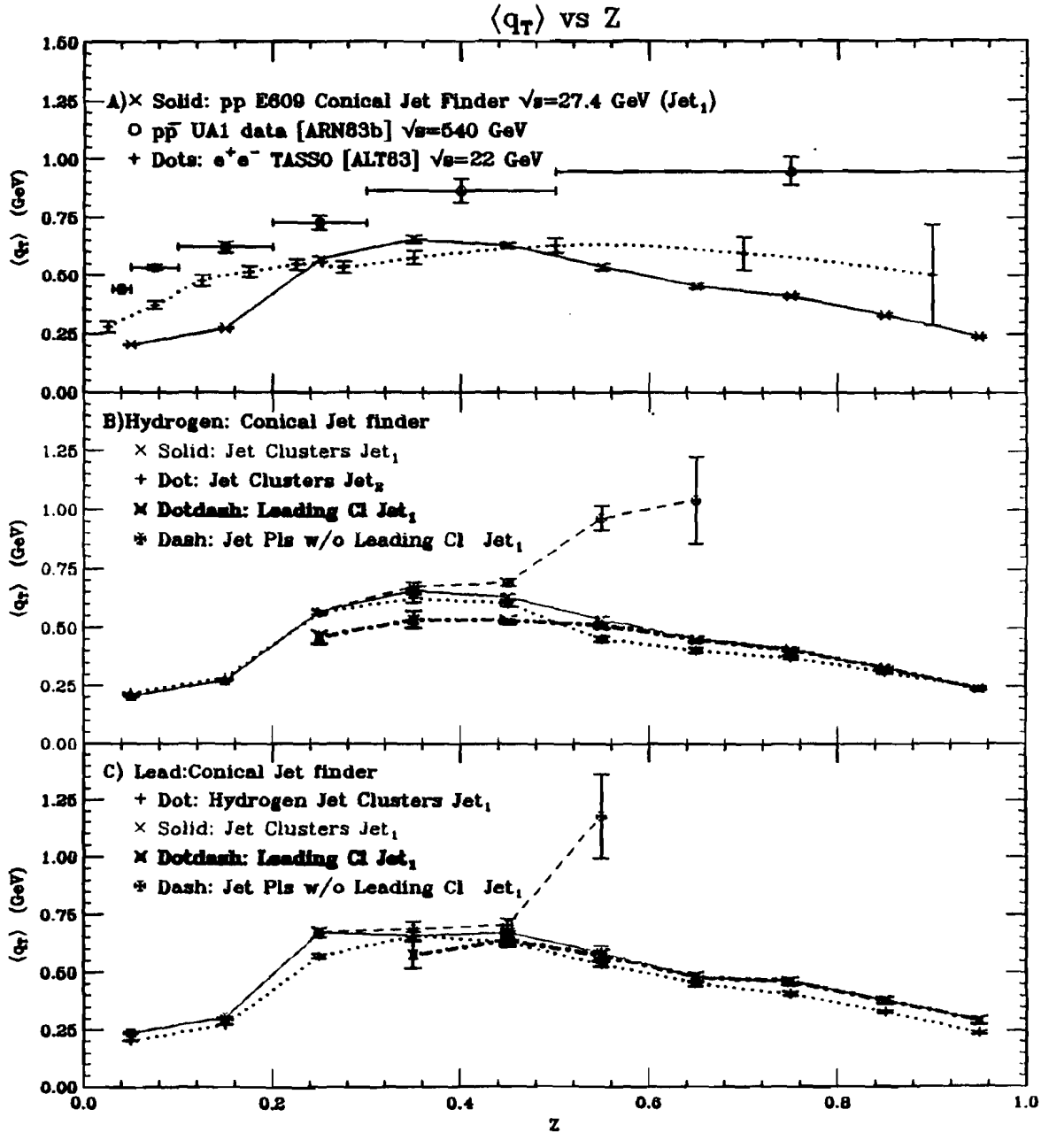

slowly drops toward zero. The decrease of q_T for the highest Z values is expected since Z represents the cluster momentum fraction along the jet axis; any cluster with Z equal to one represents a single cluster jet, and by definition a single cluster jet must have a q_T of zero. The lead data, (figure 4.39C) shows a slight increase in q_T over the hydrogen values, indicating that the jets from lead are not quite as well collimated as the ones from hydrogen.

4.2.3.4 Electromagnetic/Hadronic ratio: X_{jet} -

The calorimeter distinguishes between clusters interacting electromagnetically (π^0, γ, e^+, e^- ...) from those interacting hadronically (π^+, π^-, protons ...) by utilizing the different rates at which the showers develop. An electromagnetic shower deposits over 99% of its energy in the first two layers of the calorimeter while a hadronic shower deposits a significant fraction of its energy in the deeper layers. Taking the ratio of the cluster energy found in the first two calorimeter layers over the total cluster energy helps identify the type of cluster. Figure 4.40A shows the distribution of the X_{jet} ratio for our hydrogen and lead targets as found by the conical jet-finder. X_{jet} is the sum of the electromagnetic/hadronic ratio of each cluster in the jet divided by the total number of clusters in the jet. The Gaussian jet-finder produces a similar pair of curves. Figures 4.40C&D display the independence of the mean as a function of atomic number; similarly the X_{jet} ratio versus α remains relatively flat at 1.35, figure 4.40B. The drop in X_{jet} as a function of <Jet P_T>, figure 4.40E, may be related to the known trigger bias in the two-high trigger, which triggers more easily on lower energy

electromagnetic clusters (with well collimated showers which stay in the triggering segment) than clusters interacting hadronically (with larger showers which leak out of the triggering segment). One concludes that both classes of clusters behave similarly within the jets.

4.3 DI-JET STRUCTURE

Additional information beyond the internal structure of the jets can be obtained by studying how well the di-jet pair balances. Jet balance can be quantified in a variety of ways. $\Delta\phi_{jj}$ describes the ϕ angle between the jets, indicating their coplanar nature. UA2 used a pair of ratios, involving the total E_T in an event, E_{Tsum}, to quantify the transverse energy balance between the jets. The ratios, $H_1 = E_{Tjet_1}/E_{Tsum}$ and $H_2 = (E_{Tjet_1}+E_{Tjet_2})/E_{Tsum}$ (which equal 0.5 and 1.0 in the ideal scatter) measure how the jets share the transverse energy with the rest of the event. A third variable, $\Delta P_T = |P_{Tjet_1}|-|P_{Tjet_2}|$ measures the balance of P_T between the two jets. M_{jj}, the di-jet mass described above, reports the "mass" of the effective cluster creating the jet pair. The ratio $R_{21} = E_{Tjet_2}/E_{Tjet_1}$ describes the balance independent of the <Jet P_T>. Many other variables also describe properties about the jet pair; ω_{jj}, the angle between the jets; $\Delta\theta^*_{jj}$, the theta-center-of-mass angle between the jets; $P_{T_{jj}}$, the vector sum of the individual jet P_T vectors; $P_{L_{jj}}$, the sum of the jet momenta along the jet axis; and Δ(cluster #), the difference in the number of clusters in the highest P_T jet and the the second highest P_T jet. However, the angular information matches that described in $\Delta\phi_{jj}$ and the momentum

Figure 4.40 X_{jet}: Electromagnetic/Hadronic ratio

A) X_{jet} distribution. These curves are shown for $(X_{jet_1}+X_{jet_2})/2$ for the conical jet-finder on lH_2(solid) and Pb(dots).
---Cone(solid), Gauss(dash)---
B) α vs. $\langle X_{jet}\rangle$ $\langle$Jet $P_T\rangle$'s over 4.0 GeV/c & $60°\leq\theta^*_{jet_1}\leq 110°$.
C) $\langle X_{jet}\rangle$(nuclear)/$\langle X_{jet}\rangle$(lH_2) vs. A D) $\langle X_{jet}\rangle$ vs. A
E) $\langle X_{jet}\rangle$ vs. $\langle$Jet $P_T\rangle$ Cone:H_2=solid,Pb=dot Gauss:H_2=dash,Pb=dotdash

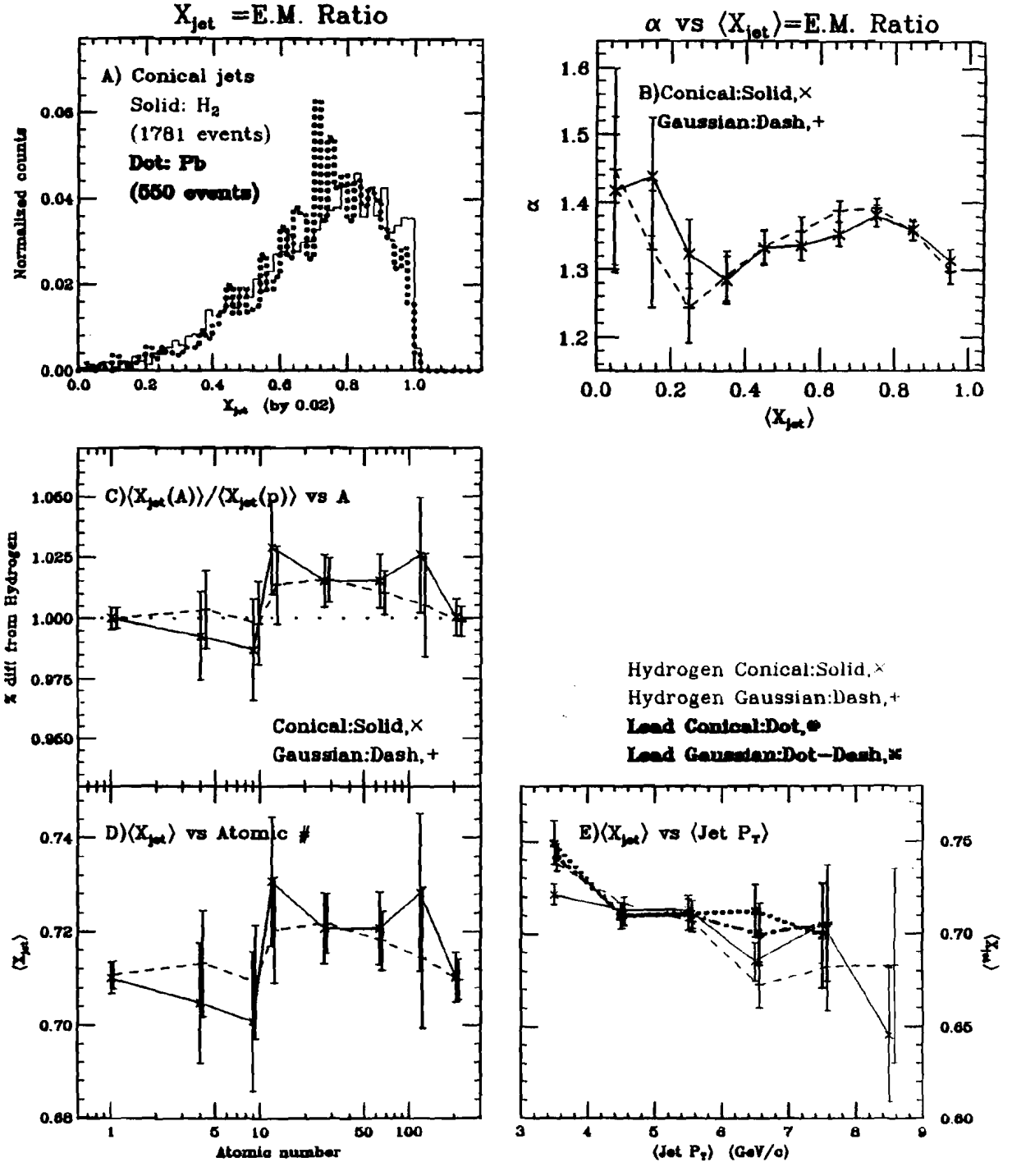

information can be inferred from ΔP_T, H_1 and H_2. The Δ(cluster #) closely tracks ΔP_T.

The $\Delta\phi_{jj}$ distribution, displayed in figures 4.41A-E, peaks for back-to-back jets 180° apart. Indicative of di-jet structure, the mean of the $\Delta\phi_{jj}$ distribution increases toward 180° as the <Jet P_T> increases, figure 4.41E. The hydrogen data shows the greatest degree of balance; as the atomic number of the nuclear target increases the $<\Delta\phi_{jj}>$ drops an additional 10% from direct balancing (figures 4.41C&D). Once again α follows the trend observed before -- the least amount of enhancement is observed for the most "jet-like" events. α drops from 1.55 to 1.25 as $\Delta\phi$ approaches 180°, figure 4.41B.

Figures 4.42-4.44 each contain a similar set of plots for the various jet energy comparisons. In each case the trends follow the expected pattern; as <Jet P_T> increases the fraction of the total event E_T in the hottest jet increases (H_1, figure 4.42E) and the total fraction in the jet pair increases (H_2, figure 4.43E). As the <Jet P_T> grows, 15% more of the energy appears in the hotter jet while the second jet grows more slowly, increasing the P_T imbalance between the two jets, figure 4.44E, from 0.6 GeV/c to 1.6 GeV/c. For <Jet P_T> of 8 GeV/c figure 4.44E implies that the hot jet typically has 9.25 GeV/c of P_T while the second jet has 7.75 GeV/c of P_T.

The difference in cluster content between the two jet-finders again appears when H_1 and H_2 are compared as a function of atomic number. The Gaussian jet-finder, reporting much larger <Jet E_T>'s, produces values of $<H_1>$ and $<H_2>$ nearly independent of nuclear target, indicating that the jets reflect the increase in the total event E_T.

Figure 4.41 $\Delta\phi_{jj}$: Difference in jet ϕ Angle

A) $\Delta\phi_{jj}$ distribution. These curves are shown for $|\Delta\phi_{jet_1}-\Delta\phi_{jet_2}|$ for $1H_2$(dash) and Pb(dotdash) Gaussian jets.
---Cone(solid), Gauss(dash)---
B) α vs. $\langle\Delta\phi_{jj}\rangle$. <Jet P_T>'s over 4.0 GeV/c & $60°\leq\theta^*_{jet_1}\leq 110°$.
C) $\langle\Delta\phi_{jj}\rangle$(nuclear)/$\langle\Delta\phi_{jj}\rangle$($1H_2$) vs. A D) $\langle\Delta\phi_{jj}\rangle$ vs. A
E) $\langle\Delta\phi_{jj}\rangle$ vs <Jet P_T> Cone:H_2=solid,Pb=dot Gauss:H_2=dash,Pb=dotdash

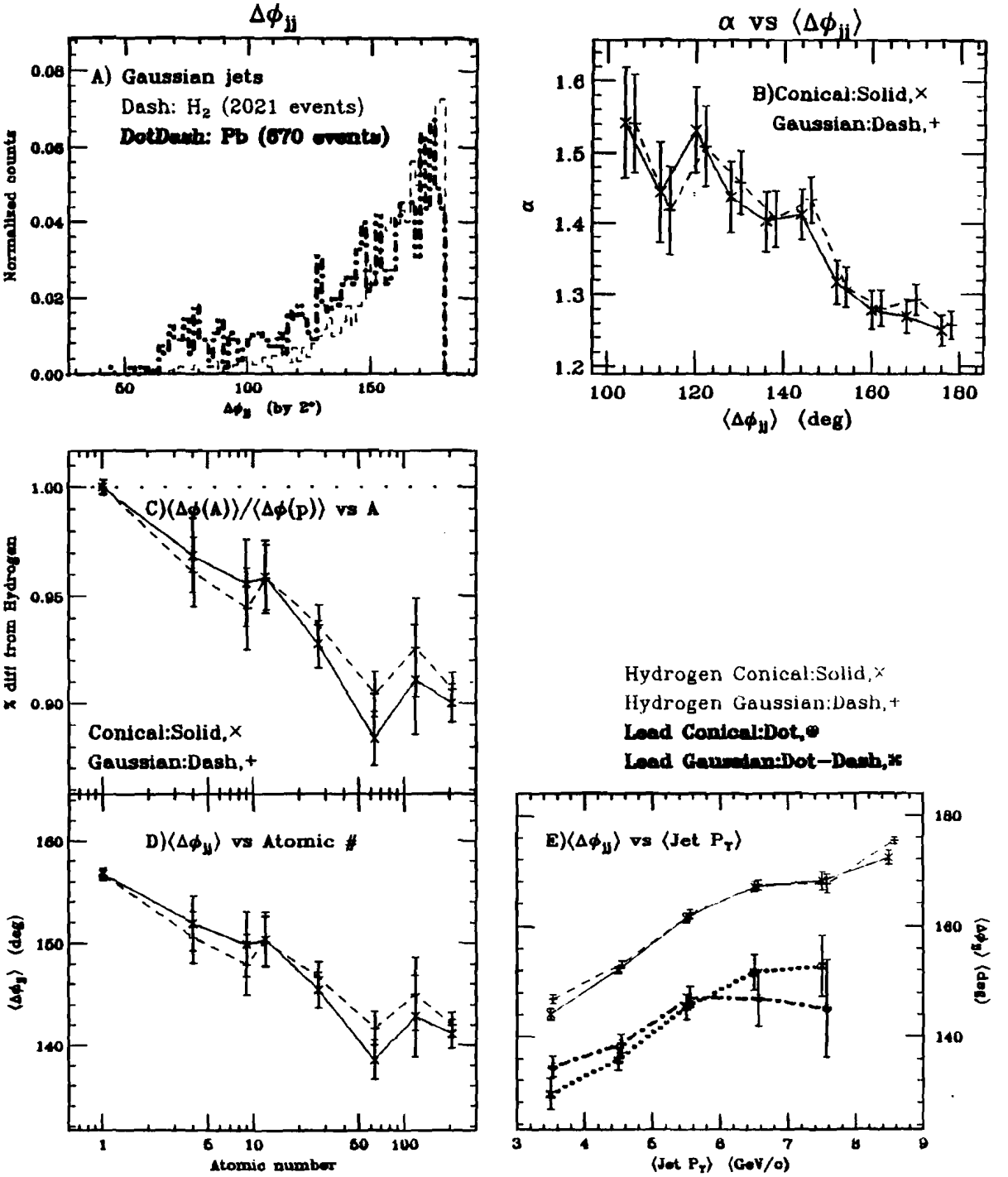

Figure 4.42 $H_1 = E_{Tjet_1}/E_{Tsum}$

A) H_1 distribution for the hydrogen conical(solid) and Gaussian(dash) jet-finders. ---Cone(solid), Gauss(dash)---
B) α vs. $\langle H_1 \rangle$. <Jet P_T>'s over 4.0 GeV/c & $60° \leq \theta^*_{jet_1} \leq 110°$.
C) $\langle H_1 \rangle$(nuclear target)/$\langle H_1 \rangle$(hydrogen) vs. A
D) $\langle H_1 \rangle$ vs. A. Jet-finder E_T definitions separate the curves.
E) $\langle \Delta\phi_{jj} \rangle$ vs <Jet P_T> Cone:H_2=solid,Pb=dot Gauss:H_2=dash,Pb=dotdash

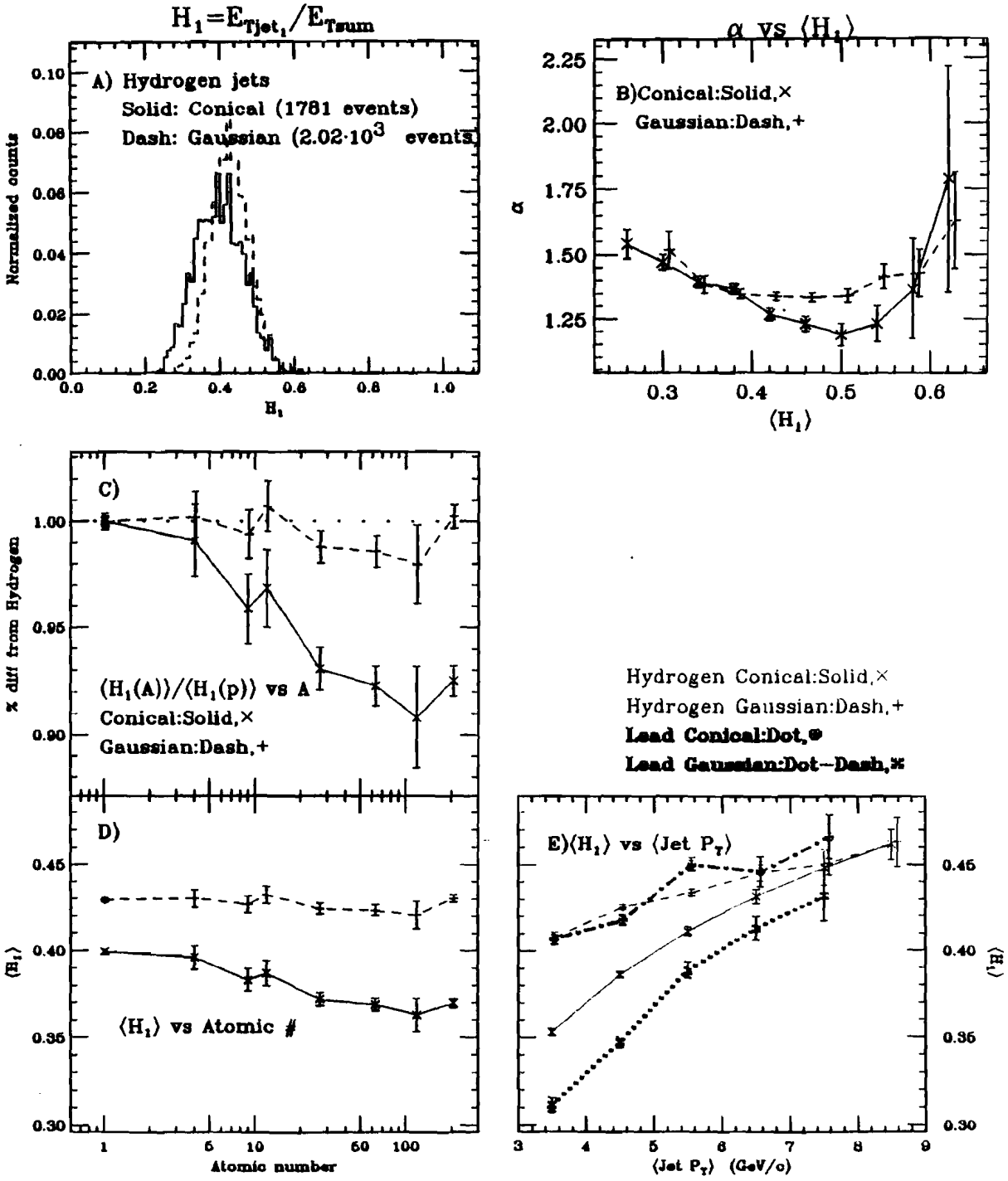

Figure 4.43 $H_2 = (E_{Tjet_1}+E_{Tjet_2})/E_{Tsum}$

A) H_2 distribution for the hydrogen conical(solid) and Gaussian(dash) jet-finders. ---Cone(solid), Gauss(dash)---
B) α vs. $\langle H_2 \rangle$. <Jet P_T>'s over 4.0 GeV/c & $60° \leq \theta^*_{jet_1} \leq 110°$.
C) $\langle H_2 \rangle$(nuclear)/$\langle H_2 \rangle$($1H_2$) vs. A
D) $\langle H_2 \rangle$ vs. A. Jet-finder E_T definitions separate the curves.
E) $\langle H_2 \rangle$ vs <Jet P_T> Cone:H_2=solid,Pb=dot Gauss:H_2=dash,Pb=dotdash

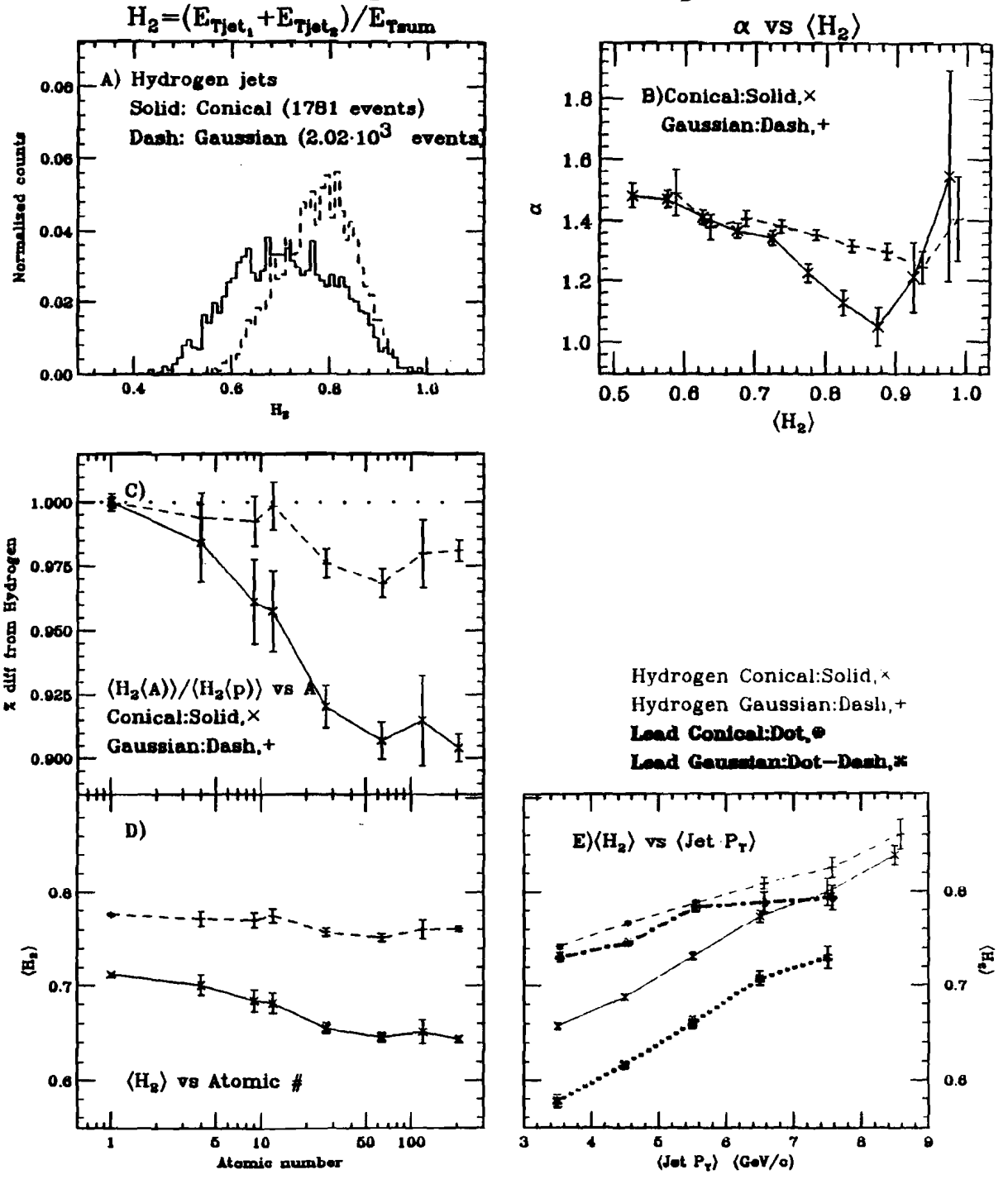

Figure 4.44 ΔP_{Tjj}: P_T balance

A) ΔP_{Tjj} for lH_2(solid) and Pb(dot) jets as found by the conical jet-finder. ---Cone(solid), Gauss(dash)---
B) α vs. $<\Delta P_{Tjj}>$. <Jet P_T>'s over 4.0 GeV/c & $60° \lesssim \theta^*_{jet_1} \lesssim 110°$.
C) $<\Delta P_{Tjj}>$(nuclear)/$<\Delta P_{Tjj}>$(lH_2) vs. A
D) $<\Delta P_{Tjj}>$ vs. A
E) $<\Delta P_{Tjj}>$ vs <Jet P_T> Cone:H_2=solid,Pb=dot Gauss:H_2=dash,Pb=dotdash

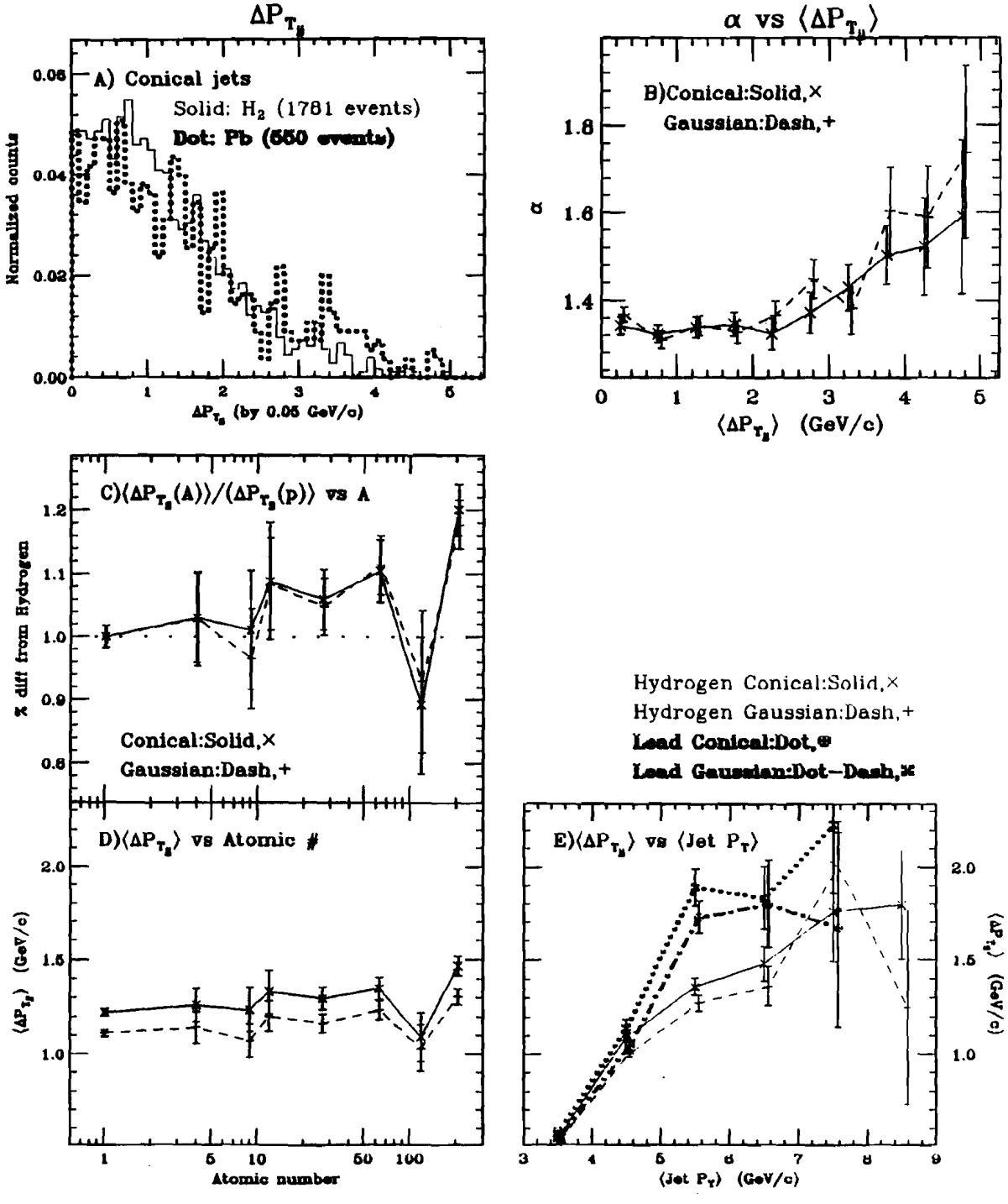

The more limited range of clusters in the conical jet-finder causes both the $<H_1>$ and $<H_2>$ distributions to drop with atomic number. The additional transverse energy available as the target nucleus increases in size shows up outside the 45° cone angle. The $<\Delta P_{Tjj}>$, the difference between the separate jet P_Ts, remains roughly flat with atomic number, figures 4.44C&D, indicating that the cause of the imbalance is either independent of, or scales with, the rising cluster multiplicity available in higher A targets.

Plotting α for H_1, H_2 and ΔP_{Tjj}, figures 4.42-44B, provides reconfirmation that the enhancement decreases as the events become more jet-like. The minimum α value for H_1 occurs when $<H_1>$ equals 0.5, and rises above the minimum for both events unbalanced with the leading jet carrying too much or too little of the total event E_T. H_2 produces the minimum α when the two jets account for nearly all the event energy, as $<H_2>$ approaches 1.0. The data points in the H_2 = 0.975 bin may rise above the minimum value; however, because of limited statistics, any line fit through the H_2 versus $R = \sigma(pA)/A\sigma(pp)$ data is consistent within errors in this bin. $<\Delta P_{Tjj}>$ produces the minimum α value when the jets have balanced P_T to within 2 GeV/c.

The invariant di-jet mass was utilized earlier as the dependent variable to study the jet cluster multiplicity. There it was noted that M_{jj} and <Jet P_T> are nearly proportional (figure 4.13). Figure 4.45 presents this correlation again as well as showing that M_{jj} also increases with atomic number. The M_{jj} versus α shows a drop in α with increasing M_{jj} until M_{jj} equals 8.0 Gev, the minimum total

Figure 4.45 M_{jj}: **Invariant Di-Jet Mass**

A) M_{jj} for the Gaussian jets, lH_2(dash) and **Pb(dotdash).**
---Cone(solid), Gauss(dash)---
B) α vs. $\langle M_{jj} \rangle$. <Jet P_T>'s over 4.0 GeV/c & $60° \leq \theta^*_{jet_i} \leq 110°$.
C) $\langle M_{jj} \rangle$(nuclear)/$\langle M_{jj} \rangle$(lH_2) vs. A
D) $\langle M_{jj} \rangle$ vs. A
E) $\langle M_{jj} \rangle$ vs <Jet P_T> Cone:H_2=solid,Pb=dot Gauss:H_2=dash,Pb=dotdash

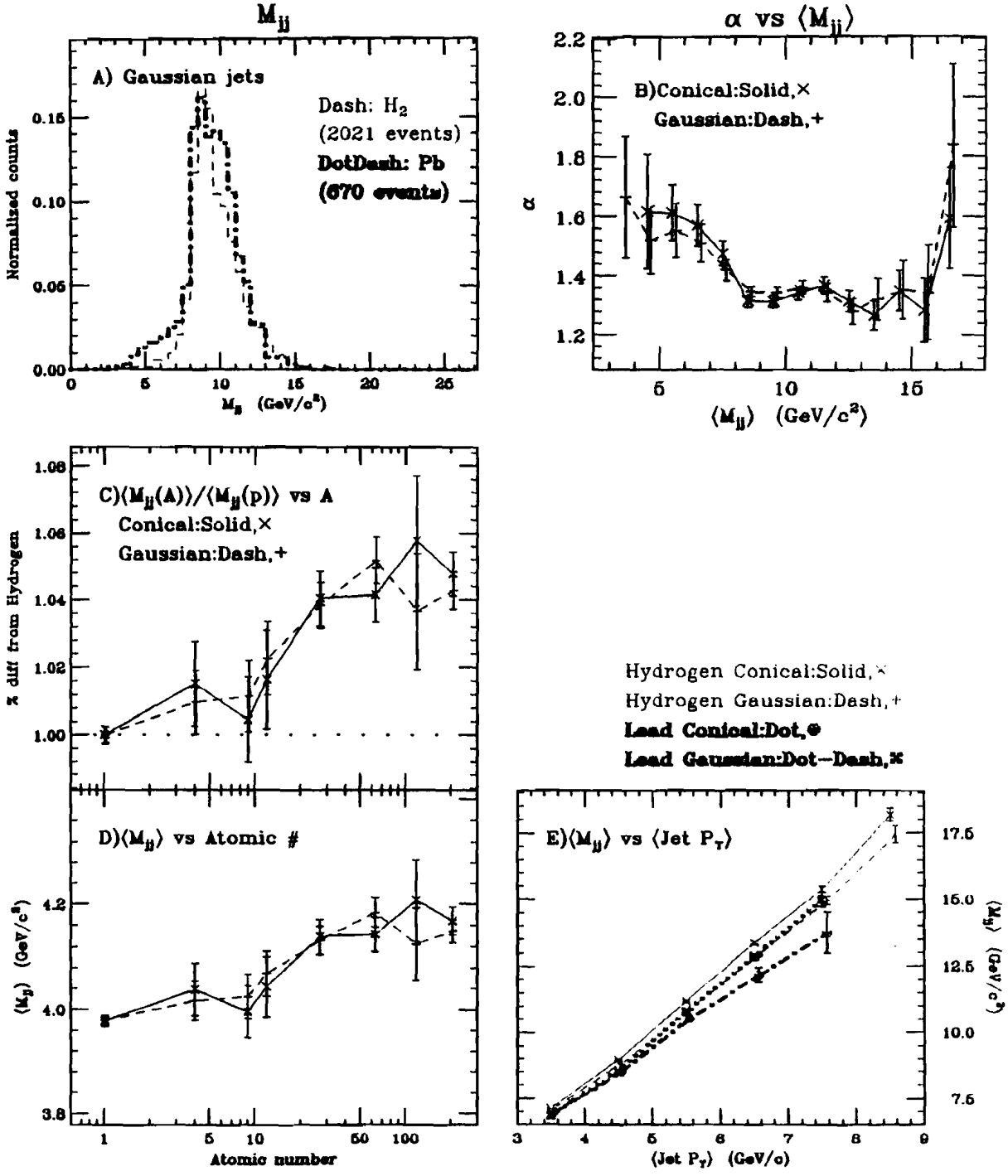

jet P_T represented in the figure, and then remains flat with α near 1.35; near the α value observed for <Jet P_T>.

Krzywicki predicts, in his early nuclear enhancement model based on gluon production within the nucleus [KRZ76], "that any jet structure which might be observed on the side opposite to the large-P_T particle, should be boosted in the direction of motion of the nucleus." In our case the primary jet can be compared to the largest-P_T particle and the away side jet corresponds to the second hottest jet. The hottest jet usually contains the largest available P_T clusters, which lie at large angles; the hotter jet therefore tends to be at larger angles, as shown in figure 4.46A. This θ^* angle grows slightly with atomic number. The second jet can be interpreted as Krzywicki's away side jet; its θ^* grows even faster with increasing A. The difference of the two jets' θ^* angles decrease slightly with atomic number, figure 4.46B; both trends agree with Krzywicki's prediction, but the effects are statistically marginal.

4.4 THE BEAM JET AND INFERRED TARGET JET

The E609 collaboration has previously observed that the energy in the beam jet decreases with atomic number, and that the missing energy does not appear in the main calorimeter [MIE88]. In drawing conclusions about the beam calorimeter one needs to be careful since the difference between the hydrogen and nuclear target position causes the beam calorimeter to sample different solid angles. Not only does the target position and atomic number affect the energy deposition in the beam calorimeter, but the detected energy also depends on the type

Figure 4.46 $\Delta\theta^*_{jj}$

A) θ^* of the jet_1 (solid) and jet_2 (dash) vs. A. $\theta^*_{jet_2}$ increases with A more rapidly than $\theta^*_{jet_1}$.
B) The difference in θ^* of the jet one and jet two, $\Delta\theta^*_{jj}$, takes values that decreases slightly with increasing A. (Conical:solid, Gaussian:dash)

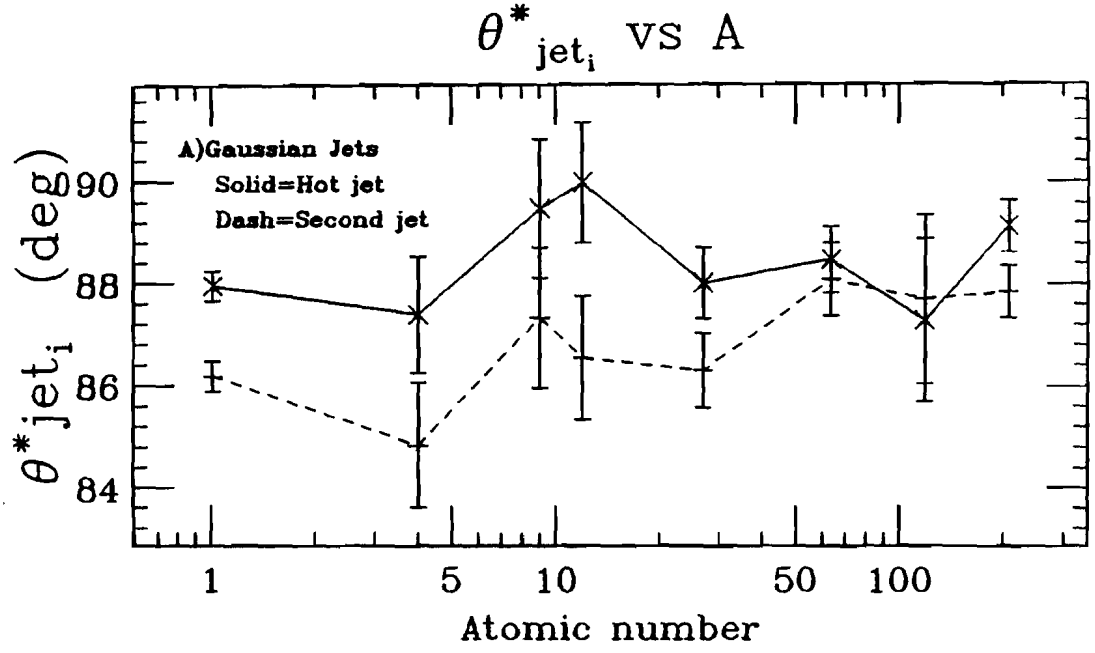

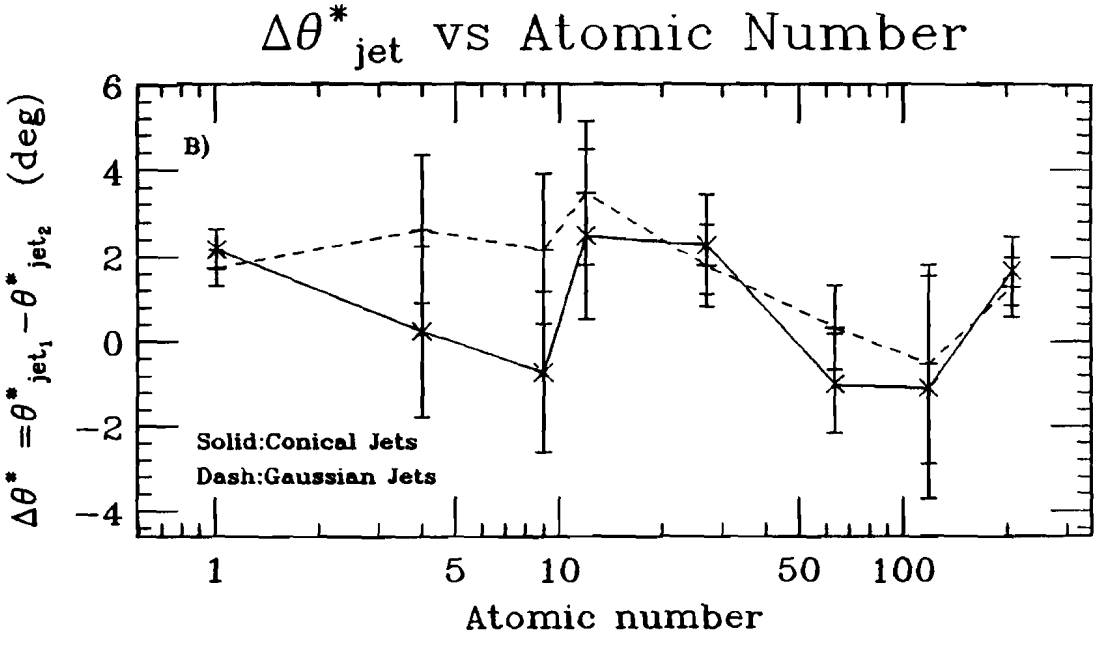

Figure 4.47 **Energy in the Calorimeters**

A) Events passing 2-hi trigger:<$Beam_{Cal}$>(solid), <$Main_{Cal}$>(dots) & <$Total_{Cal}$>(dash) energy vs. A.
Interaction trigger events:<$Beam_{Cal}$> energy(daash) vs. A.
B) <$Beam_{Cal}$>(solid), <$Main_{Cal}$>(dots), & <$Total_{Cal}$>(dash) energy vs. A for 2-hi trigger events with E_T>15 GeV and planarity>0.8.
C) <$Beam_{Cal}$>(solid/daash), <$Main_{Cal}$>(dot/dotdash) & <$Total_{Cal}$> (dash/dotdotdash) energies for the conical/Gaussian jet-finders vs. A for events with <Jet P_T>'s > 4.0 GeV/c.
D) The energy vs. A curves in figure C with $60° \leq \theta^*_{jet_1} \leq 110°$.

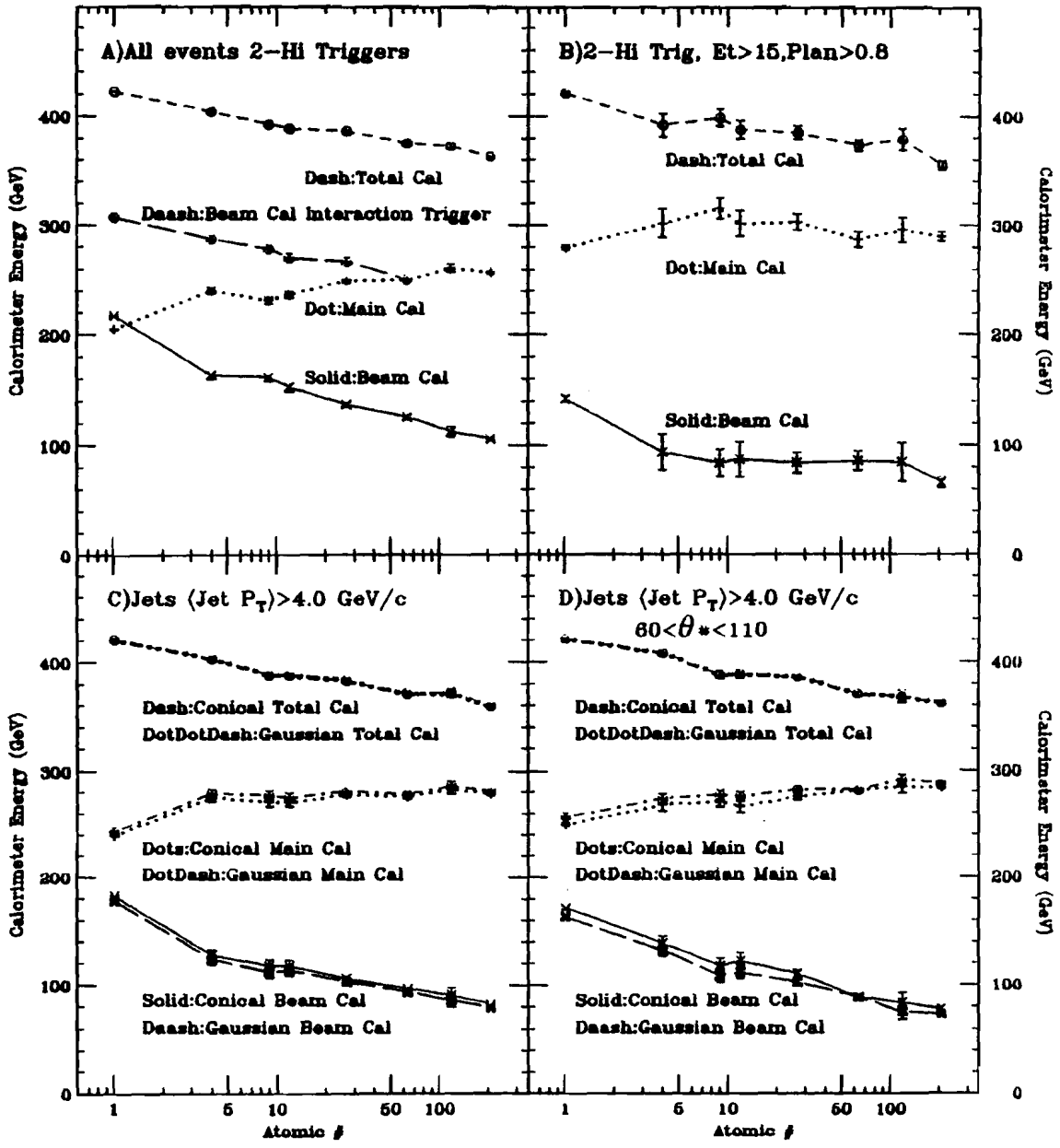

of events selected. Figures 4.47A-D show the mean energy in the main and beam calorimeters as a function of nuclear target for events selected in a variety of manners. Two-high data, taken from the summary tapes without further E_T, planarity, or jet-finding cuts, shows a large discontinuity between the hydrogen and the other nuclear targets. The trend is smooth between these targets when the energy in the calorimeter pair is summed, indicating that the discontinuity is a result of the different solid angle coverage coupled with the energy flow of the selected events. Selecting a different class of events, figure 4.47A also shows beam calorimeter E_T versus A for the interaction trigger (adapted from [MAR89]); the deviation of the hydrogen point from a straight line is minimal. The interaction trigger selects events with a much smaller energy flow to large P_T's. For interaction triggers the different solid angles between the hydrogen and the nuclear targets does not affect the levels of energy measured, one infers that a minimal amount of energy is striking the calorimeter pair where they overlap around $\theta^* = 30°$, while the energy flow to this region for events selected with the two-high trigger is significant.

Figure 4.47B displays a subset of the two-high data, showing events having E_T greater than 15 GeV and a planarity over 0.8. Similar trends appear in [MIE88,MAR89]; energy detected in the calorimeter pair decreases with **A** -- more energy leaks out of the calorimeter coverage into the target fragmentation region. The energy in the beam calorimeter decreases with **A**. (A simple picture giving this effect would be that the larger nuclei absorb more the incident energy; other explanations involve interactions with either the edge of the nucleus or interactions with the nuclear bulk). Finally the

energy in the main calorimeter increases because the energy lost in the beam jet transfers only partially to the target fragmentation region. Normalizing by the solid angle subtended by the beam calorimeter corrects the discontinuity between hydrogen and the rest of the targets, causing the hydrogen to follow the trend set by the other targets [MIE88,MAR89]. However, the discontinuity decreases as the event selection approaches jets of more defined quality; figure 4.47C contains events located by the Gaussian (and conical) jet-finders with <Jet P_T> greater than 4.0 GeV/c while figure 4.47D has the added requirement that the jet θ^* be between 60° and 110°. Each of these event selections decreases the total energy deposited in the beam calorimeter for all targets, and decreases the size of the discontinuity between hydrogen and the other nuclear targets.

One explanation of the decrease in discontinuity is that the selection of events with jet-like properties in the main calorimeter also selects events in which the beam jet becomes more defined. A collimated beam jet deposits all its energy in the beam calorimeter for either target position. One also expects energy deposition in a limited solid angle for the interaction triggers since they represent softer scatters, where the beam jet retains much of its original energy. This explanation fails, however, when one examines the kinematics of the events. In the picture where the entire event consists of two jets at large angles and a narrow beam jet, one would expect all the energy in the main calorimeter to be associated with the two high P_T jets. but there is an additional 100 GeV of energy in the main calorimeter that is not attributed to high P_T jets.

Figure 4.48 E_T in the Calorimeter Rings

A) & B) The E_T in various calorimeter rings. No corrections for the different target positions between lH_2 and the nuclear targets have been made, introducing a systematic error. The nuclear target rings have mean θ^* values of: 30.5°(dots), 40.5°(dotdash), 55°(dash), 77.5°(solid), 96°(dots), 109°(dash), and 125.5°(solid) for massless particles.

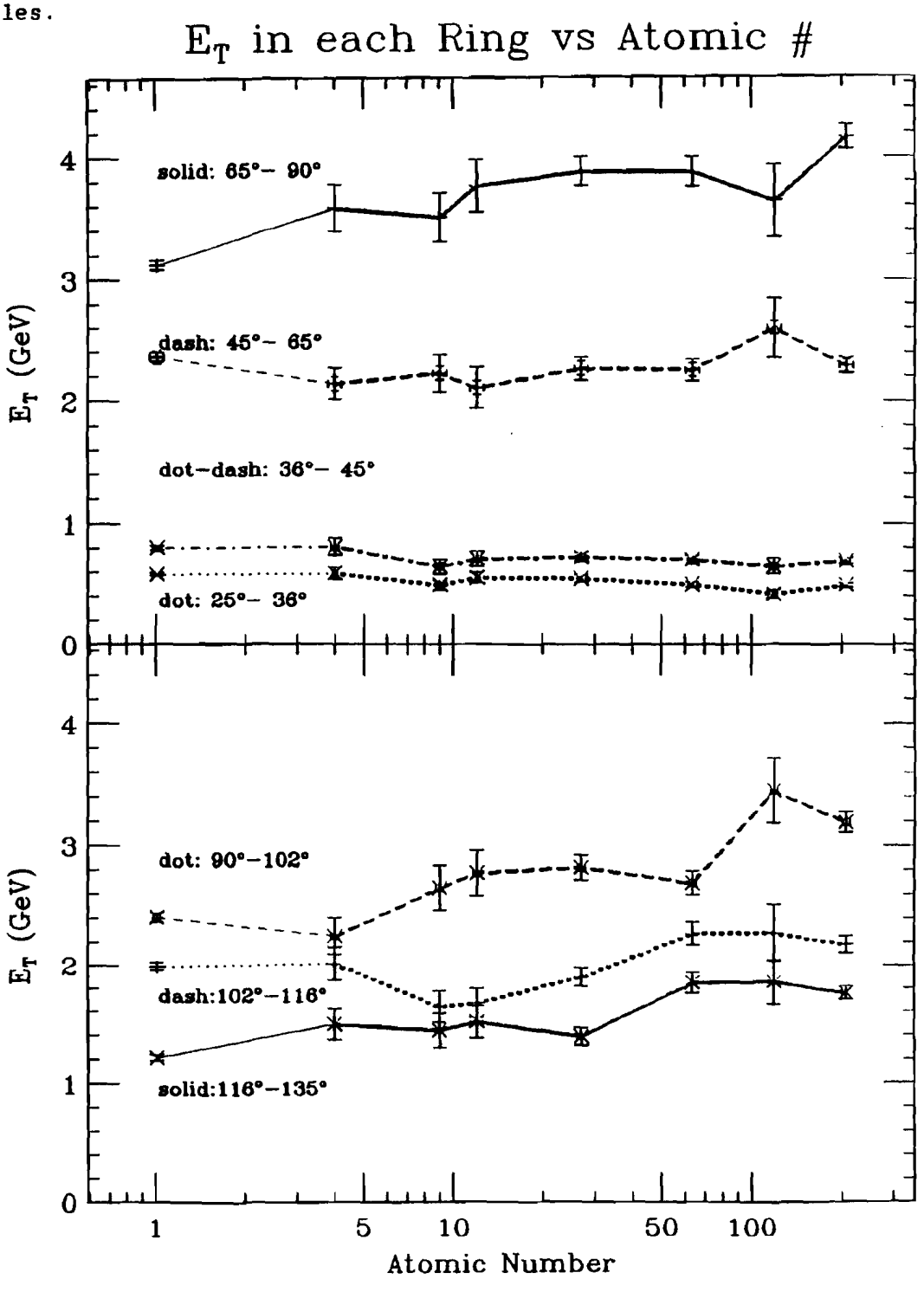

Figure 4.49 **Energy$_{lab}$ in the Calorimeter Rings**

A) & B) The E_{lab} in various calorimeter rings. No corrections for the different target positions between lH_2 and the nuclear targets have been made, introducing a systematic error. The nuclear target rings have mean θ^* values of: 30.5°(dots), 40.5°(dotdash), 55°(dash), 77.5°(solid), 96°(dots), 109°(dash), and 125.5°(solid) for massless particles.

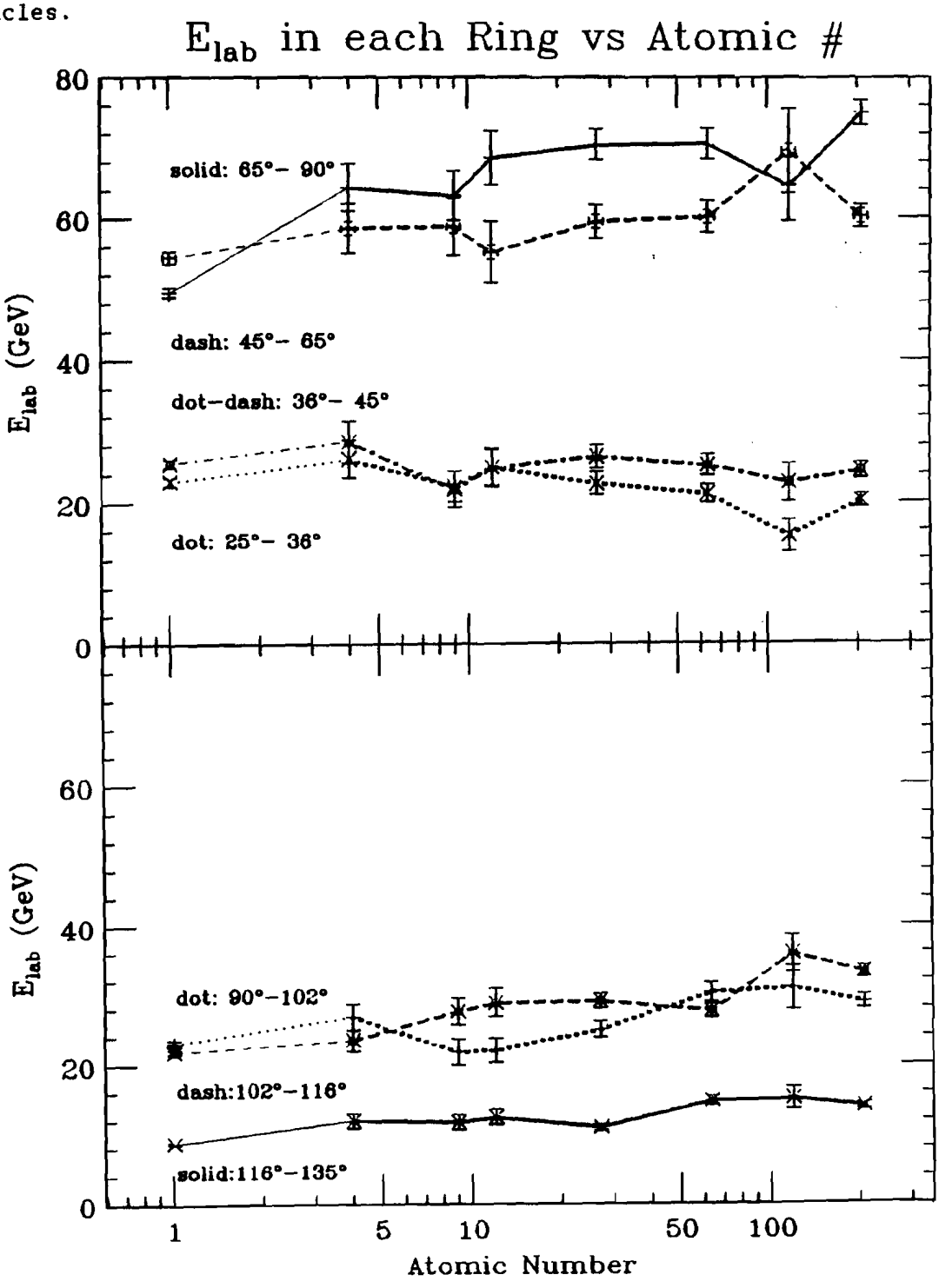

Evidence against additional beam jet spreading as A increases comes from examination of the transverse energy and the lab energy in the various calorimeter rings as a function of atomic number, figures 4.48A&B and figures 4.49A&B. These events were required to have jets with mean P_T greater than 3.0 GeV/c for both the conical and Gaussian jet-finders (the relaxed P_T requirement, historical rather than desired, is somewhat offset by the requirement that *both* jet--finders locate two jets of at least 3.0 GeV/c; our usual cut requires that a single jet-finder locates two jets whose P_T's sum to 8.0 GeV/c). Further, these events had to pass the $60° \leq \theta^*_{jet_i} \leq 110°$ fiducial cut. The hydrogen data points require two (not applied) corrections for the different target-to-calorimeter distances. The larger effect is that the solid angles differ between the rings observed in the center-of-mass at the hydrogen and nuclear target positions, a second, ~5%, effect is that the ring θ^* centers shift between the two target positions, thus the hydrogen points come from different angular regions than the rest of the targets. Both the E_T and E_{lab} fall slightly with atomic number in the inner rings, indicating that additional energy from the beam jet is not flowing into the main calorimeter as A increases. However, at larger θ^* (above 45°), the energy and E_T increase with A. A report on this effect appears in [MIE88].

The total energy in the main calorimeter increases slightly with atomic number, while the energy in the pair of calorimeters drops. One draws the conclusion that the beam jet transfers energy to the target nuclei, and that the energy appears in the target jet and is lost from the E609 calorimeter coverage.

Figure 4.50 α vs. Energy in the Calorimeters

Figure 4.50 shows α as a function of the energy in the beam calorimeter (dots), the main calorimeter (dash) and the sum of the pair of calorimeters (solid) for events with <Jet P_T>'s greater than 4.0 GeV/c and $60° \leq \theta^*_{jet_1} \leq 110°$ as found by the conical jet-finder.

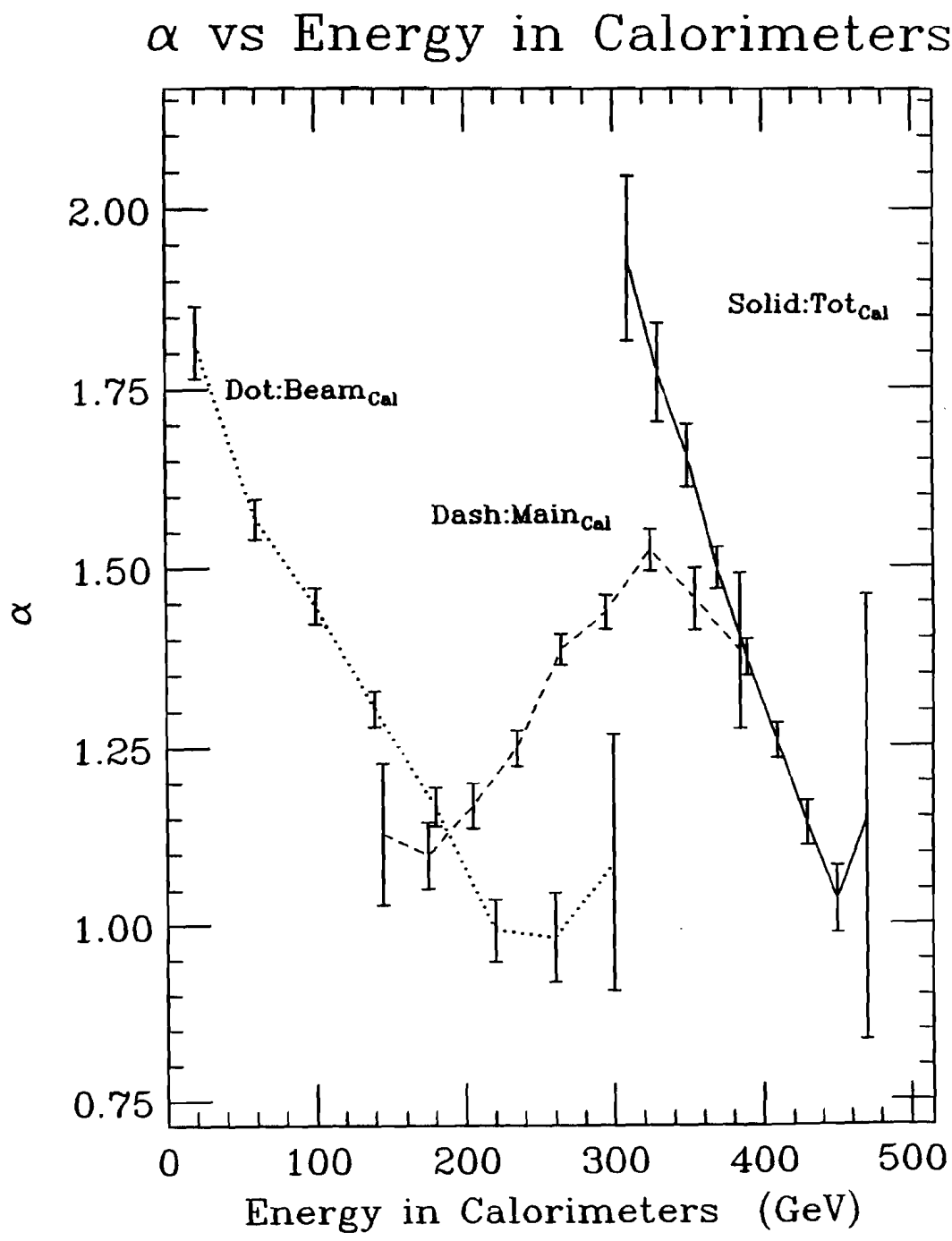

Additional information about the beam jet results from calculating α as a function of calorimeter energy. Figure 4.50 displays the α values for the conical jet-finder for various energy depositions in the beam calorimeter, main calorimeter and calorimeter pair. (Both the conical and the Gaussian jet-finders produce similar α values.) The data is selected from jets with more than 4.0 GeV/c P_T and passing the fiducial cuts. The lowest α value occurs when the collision deposits the least energy in the main calorimeter and the most energy in the beam calorimeter, reflecting interactions with little more than the jets in the main calorimeter. The nuclear enhancement decreases rapidly as the total calorimeter energy increases.

4.5 THE REGION AWAY FROM THE HIGH P_T JETS

The region away from both the high P_T and spectator jets is populated by either wide angle fragments from the triggering jets or by spectator particles from the beam and target jets. Figure 4.51 displays the event E_T left after subtracting the jet clusters' E_T as a function of <Jet P_T> and atomic number. The fewer number of clusters assigned to jets by the conical jet-finder shows up as a much larger increase in unused E_T over the Gaussian jet definition, figure 4.51A. Jets found using the conical method acquire E_T slightly faster than the increase in event E_T, causing the <Unused E_T> to drop slightly with increasing <Jet P_T>, the solid and dotted curves in figure 4.51E. However, for the Gaussian jet-finder <Jet P_T> increases more slowly than the event E_T, as shown by the dashed and dotdashed lines in figure 4.51E. The <Unused E_T> increases for both jet-finders with increasing A; more clusters are available in the event, both inside

Figure 4.51 Unused E_T distribution

A) Unused E_T for the lH_2 conical(solid) and Gaussian(dash) jet--finders. ---Cone(solid), Gauss(dash)---
B) α vs. <Unused E_T>. <Jet P_T>$\geq$4.0 GeV/c & $60° \leq \theta^*_{jet_1} \leq 110°$.
C) <Unused E_T>(nuclear)/<Unused E_T>(lH_2) vs. A
D) <Unused E_T> vs. A
E) <Un: E_T> vs <Jet P_T> Cone:H_2=solid,Pb=dot Gauss:H_2=dash,Pb=dotdash

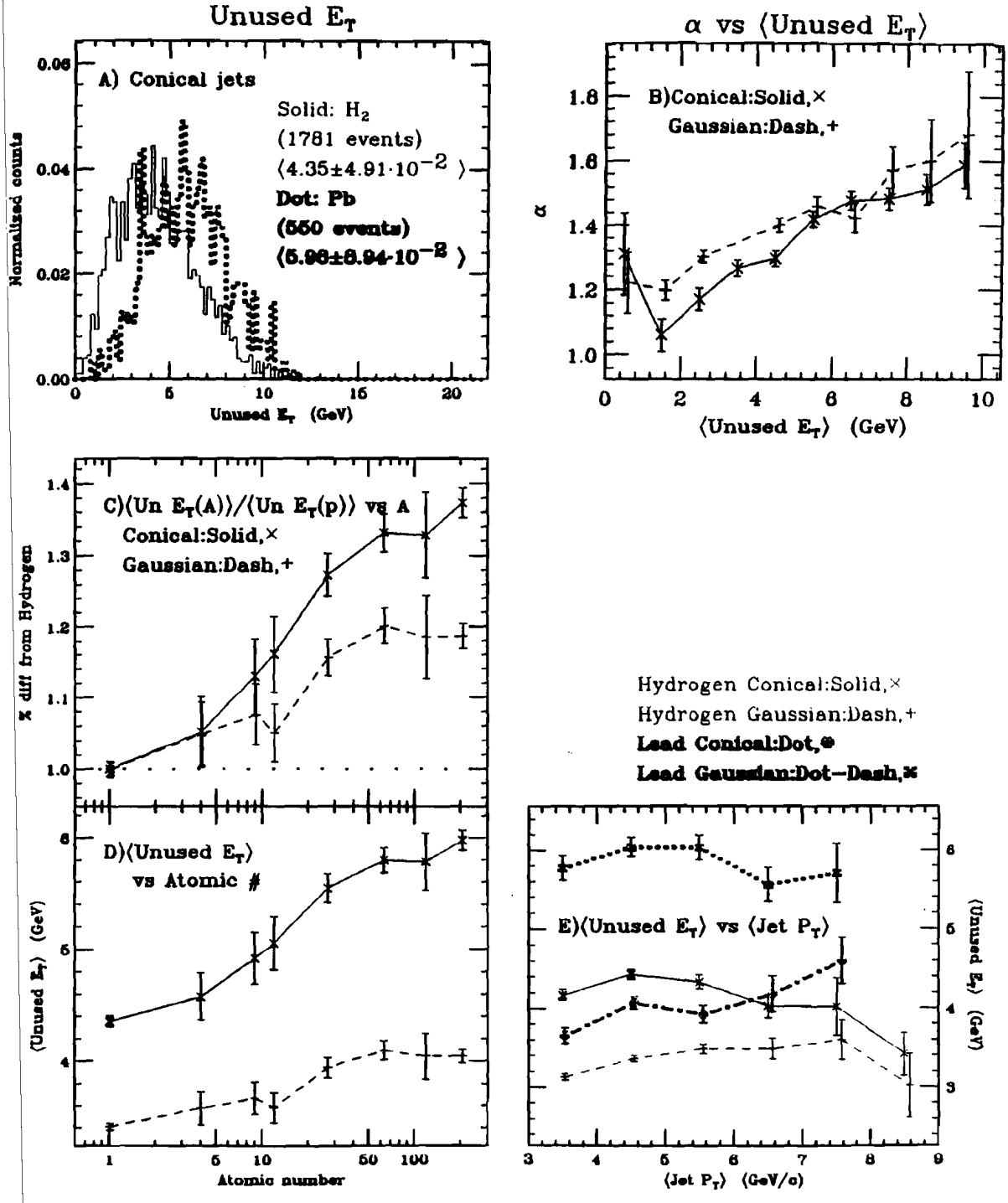

and outside of the jets. The smallest α values result for events when the least E_T lies outside the jet radius.

As the event E_T increases, the changing fraction of the event E_T used by each jet-finder can be extracted from figure 4.52. In this figure the event E_T is shown as a function of the <Jet P_T> for the hydrogen and lead targets. For both targets, a line fit through the data has a slope less than one for the conical jet-finder and a slope greater than one for the Gaussian jet-finder. The higher intercepts for the lead target again result from the increased event multiplicity and accompanying E_T increases from the high A target. The increased multiplicity does not appear entirely in the jets.

To systematically study the phase space not affiliated with specific jets, we have defined a rotated jet region. We first locate the $<\theta^*>$, given by $(\theta_{jet_1}+\theta_{jet_2})/2$, of the jet pair and then define a rotated jet ϕ as the bisecting angle between the two jets. We produce a pair of rotated jet axes, one at $\{<\theta^*>,(\phi_{jet_1}+\phi_{jet_2})/2\}$ and the other at $\{<\theta^*>,180°+(\phi_{jet_1}+\phi_{jet_2})/2\}$. A 45° cone around each of these jet axes determines the number of clusters and their transverse energy in the rotated regions. Figure 4.53, included for reference, shows the number of clusters in the conical jets while figures 4.54 and 4.55 show how the number of clusters and P_T in the rotated regions vary as a function of <Jet P_T> and as a function of atomic number for events with a pair of jets having <Jet P_T> greater than 4 GeV/c.

The number of clusters rises about 5% (from 4.6 to 4.9 clusters for the hotter rotated region and from 3.7 to 3.9 clusters for the less hot region) as the atomic number increases. A similar increase appears as the <Jet P_T> rises for the hydrogen rotated regions and for

Figure 4.52 Event E_T vs. <Jet P_T>

A) Event E_T vs. <Jet P_T> is shown for the hydrogen conical(solid) and Gaussian(dash) jet-finders as well as for the lead conical(dots) and Gaussian(dotdash) jet-finders. Coefficients for straight lines fit through the points are given.
B) The slopes of the conical(solid) and Gaussian(dash) jet-finders of the event E_T vs. <Jet P_T> fits are shown as a function of A.

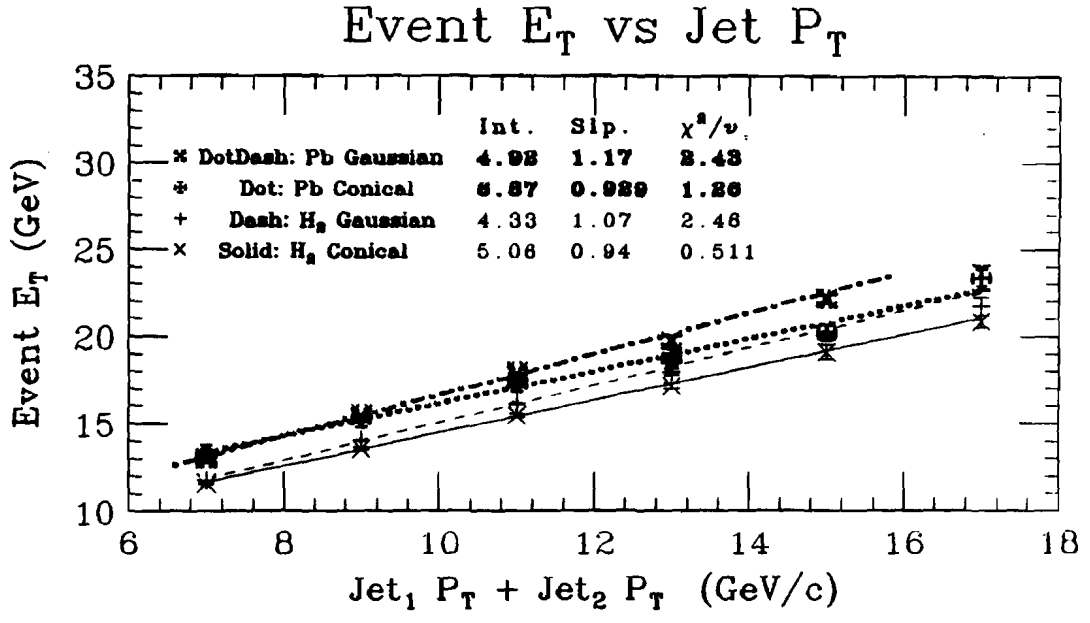

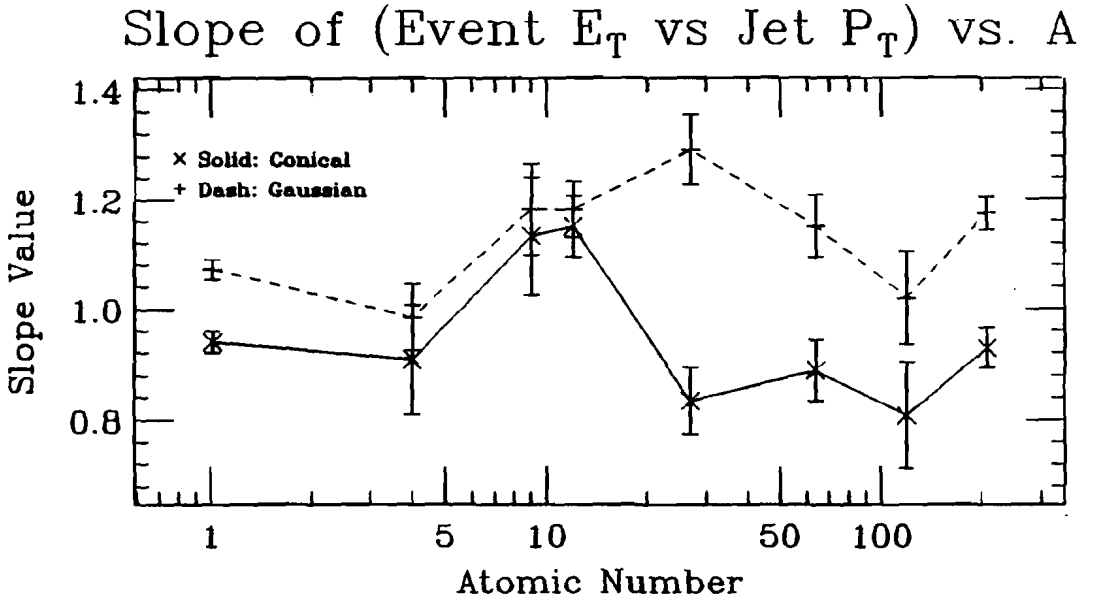

Figure 4.53 # Clusters in Conical Jets

A) # clusters in the jet_1(solid) and jet_2(dash) for the conical jet--finder. ---Jet_1(solid), Jet_2(dash)---
B) α vs <# Clusters in Jet>. <Jet P_T>$\geq$4.0 GeV/c & $60° \leq \theta^*_{jet_1} \leq 110°$.
C) <Jet Cluster#>(nuclear)/<Jet Cluster #>($1H_2$) vs. A
D) <# Clusters in Conical Jet> vs. A
E) <#Cls> vs <Jet P_T> Jet_1:$1H_2$=solid,Pb=dot Jet_2:$1H_2$=dash,Pb=dotdash

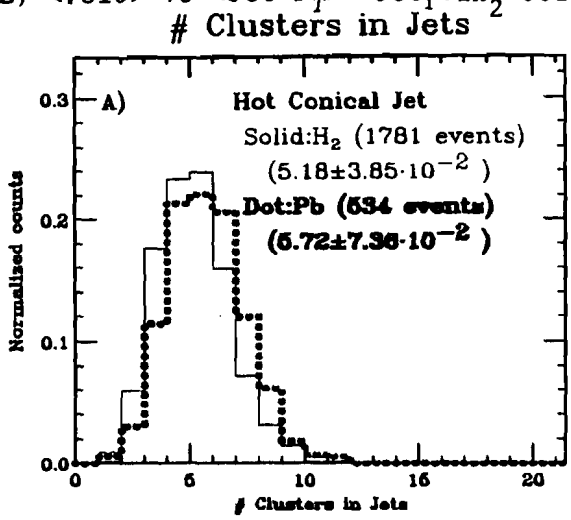

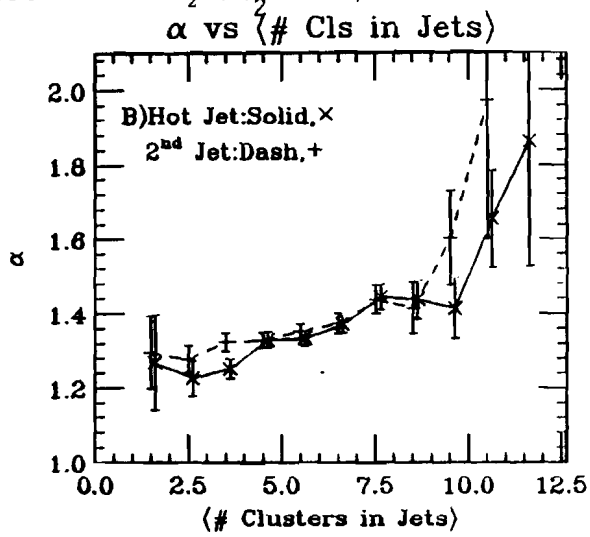

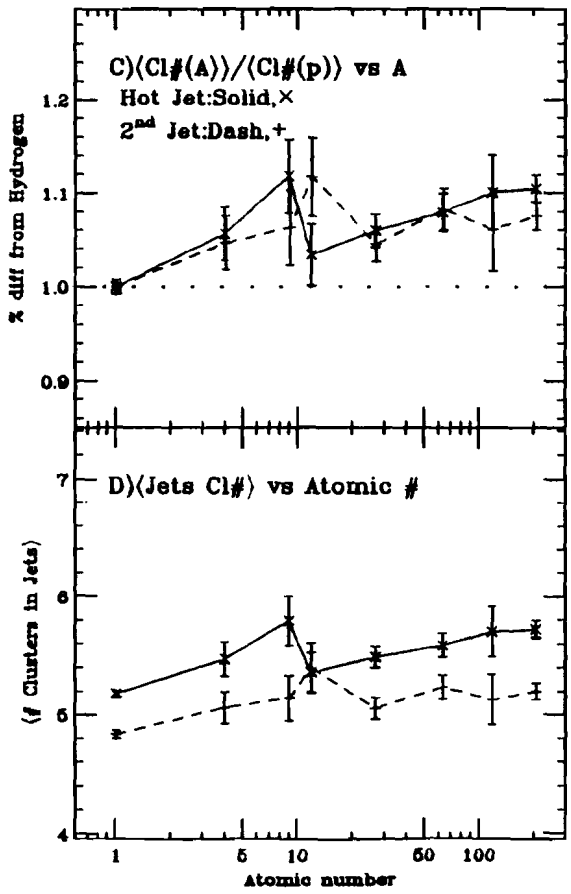

Hydrogen Hot Jet:Solid,×
Hydrogen 2nd Jet:Dash,+
Lead Hot Jet:Dot,✱
Lead 2nd Jet:Dot–Dash,+

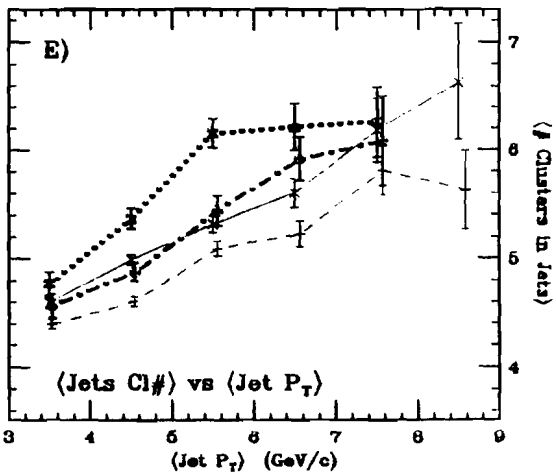

Figure 4.54 # Clusters in Rotated Regions

A) # clusters in the hottest(solid) and other(dash) rotated regions.
---Hot(solid), Second(dash)---
B) α vs <# Cl in rotated area>, <Jet P_T>≥4.0 GeV/c & $60° \leq \theta^*_{jet_1} \leq 110°$.
C) <Rotated area Cl#>(nuclear)/<Rotated area Cl#>($1H_2$) vs. A
D) <# Clusters in Rotated Jet> vs. A
E) <R:#Cls> vs <Jet P_T> Hot:$1H_2$=solid,Pb=dot 2^{nd}:$1H_2$=dash,Pb=dotdash

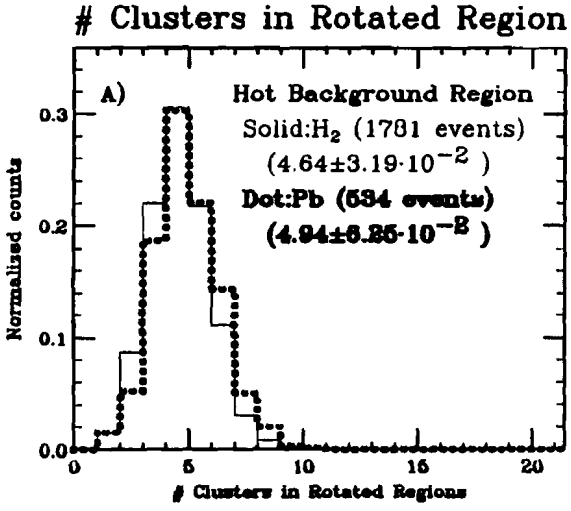

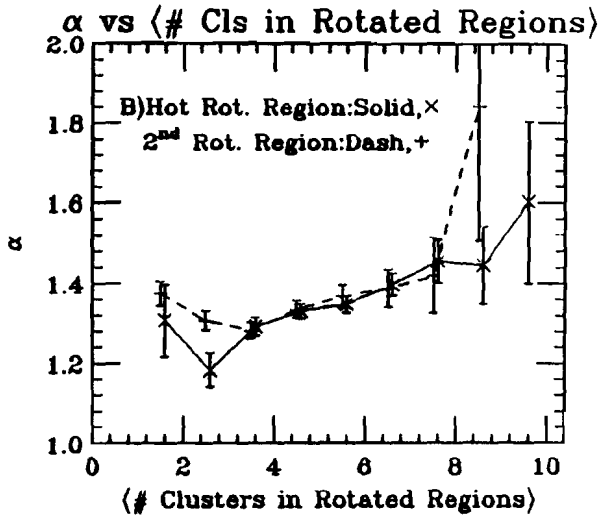

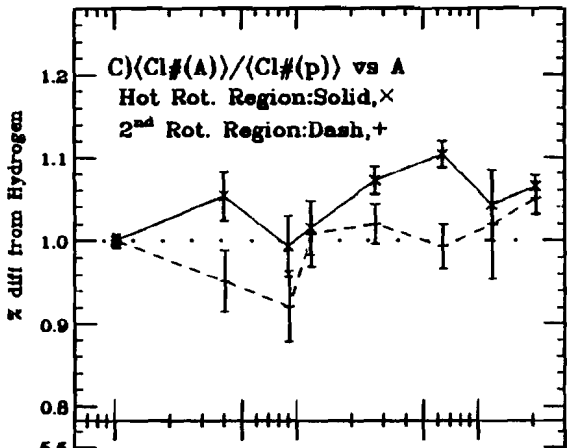

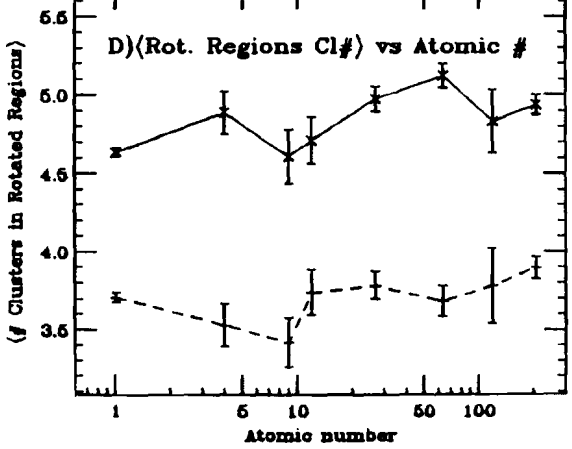

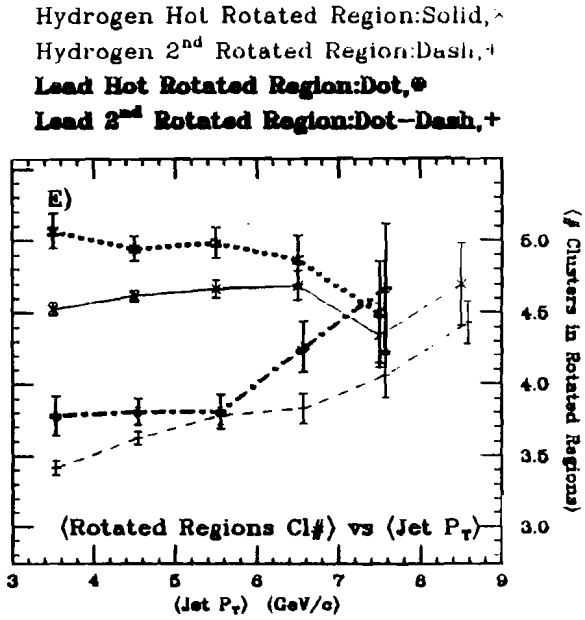

Figure 4.55 **Rotated Region P_T**

A) Rotated Jet P_T in rotated region$_1$ (solid) and region$_2$ (dash).
---Hot(solid), Second(dash)---
B) α vs. <Rotated Jet P_T>. <Jet P_T>$\geq$4.0 GeV/c & $60° \leq \theta^*_{jet_1} \leq 110°$.
C) <Rotated Jet P_T>(nuclear)/<Rotated Jet P_T>($1H_2$) vs. A
D) <Rotated Jet P_T> vs. A
E) <R:P_T> vs <Jet P_T> Hot:$1H_2$=solid,Pb=dot 2^{nd}:$1H_2$=dash,Pb=dotdash

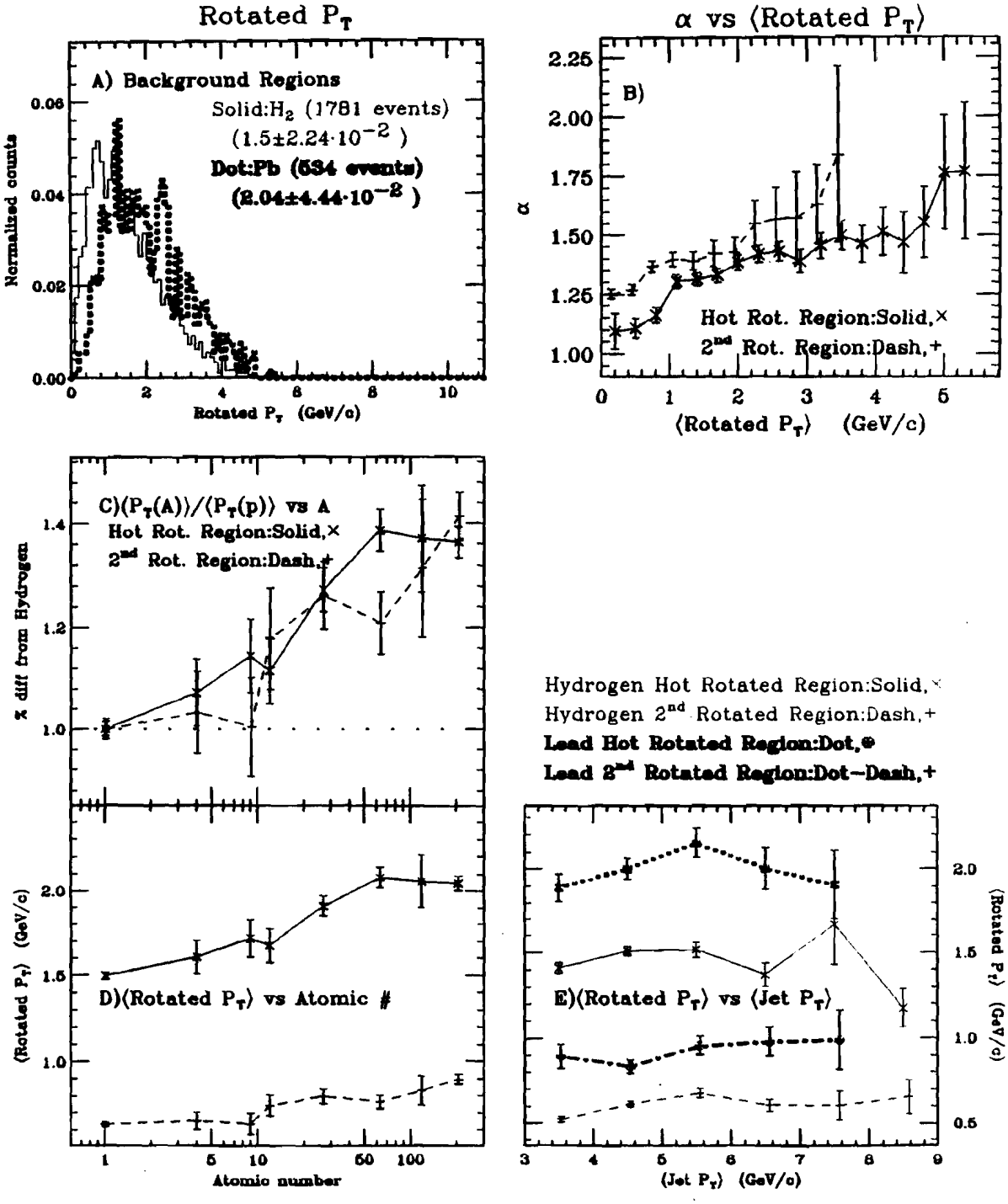

the rotated region with the smaller P_T in it for lead. For events from a lead target, the number of clusters appears to drop (as may the P_T), for the region with the larger quantity of P_T. These results may contain artifacts from the clustering algorithm. Many of the particles in the rotated region carry limited amounts of energy, near the energy region where the clustering algorithm fails.

The P_T in the rotated region also shows an increase with atomic number as well as a slight dependence on <Jet P_T>, as shown in figure 4.55. The rotated P_T increases 40% from a hydrogen target to the lead target. The percentage of increase, tracking the increased availability of particles, is the same for both rotated regions, although the difference in P_T between the regions is nearly 1 GeV/c.

One would expect that a clean 4 jet event, (correlated with limited "nuclear enhancement"), to have a reduced amount of scatter into the rotated region. For the smallest values of P_T and the least number of clusters in the rotated cone, α takes a minimum value near 1.25. As the transverse energy and cluster content in the rotated cone increases α also increases, verified by figures 4.54B & 4.55B. The difference between the α dependence as a function of P_T in the rotated regions diminishes when one recalls that the hot region typically has 1 GeV/c more P_T than the second region. A one GeV/c shift causes the two curves to overlap.

A third method of displaying the activity in the region between jets is to return to figures 4.17 and 4.26, which show plots of the cluster density as a function of $\Delta\phi_{ij}$ and $dE_T/d\Delta\phi$, where $\Delta\phi_{ij}$ is the cluster separation in ϕ from the jet. These curves each contain two peaks, corresponding to the jets, and a plateau across the rotated

Figure 4.56 **Cluster Density near ϕ=90°: $dN/d\Delta\phi$ & $dE_T/d\Delta\phi$**

Events with conical(solid) or Gaussian(dash) jets with <Jet P_T> ≥ 4.0 GeV/c and $60° \leq \theta^*_{jet_1} \leq 110°$.
A) $<dN_{clusters}/d(\Delta\phi)>$ between 80° and 100 ° vs. A
B) $<dE_{T\,clusters}/d(\Delta\phi)>$ between 80° and 100 ° vs. A

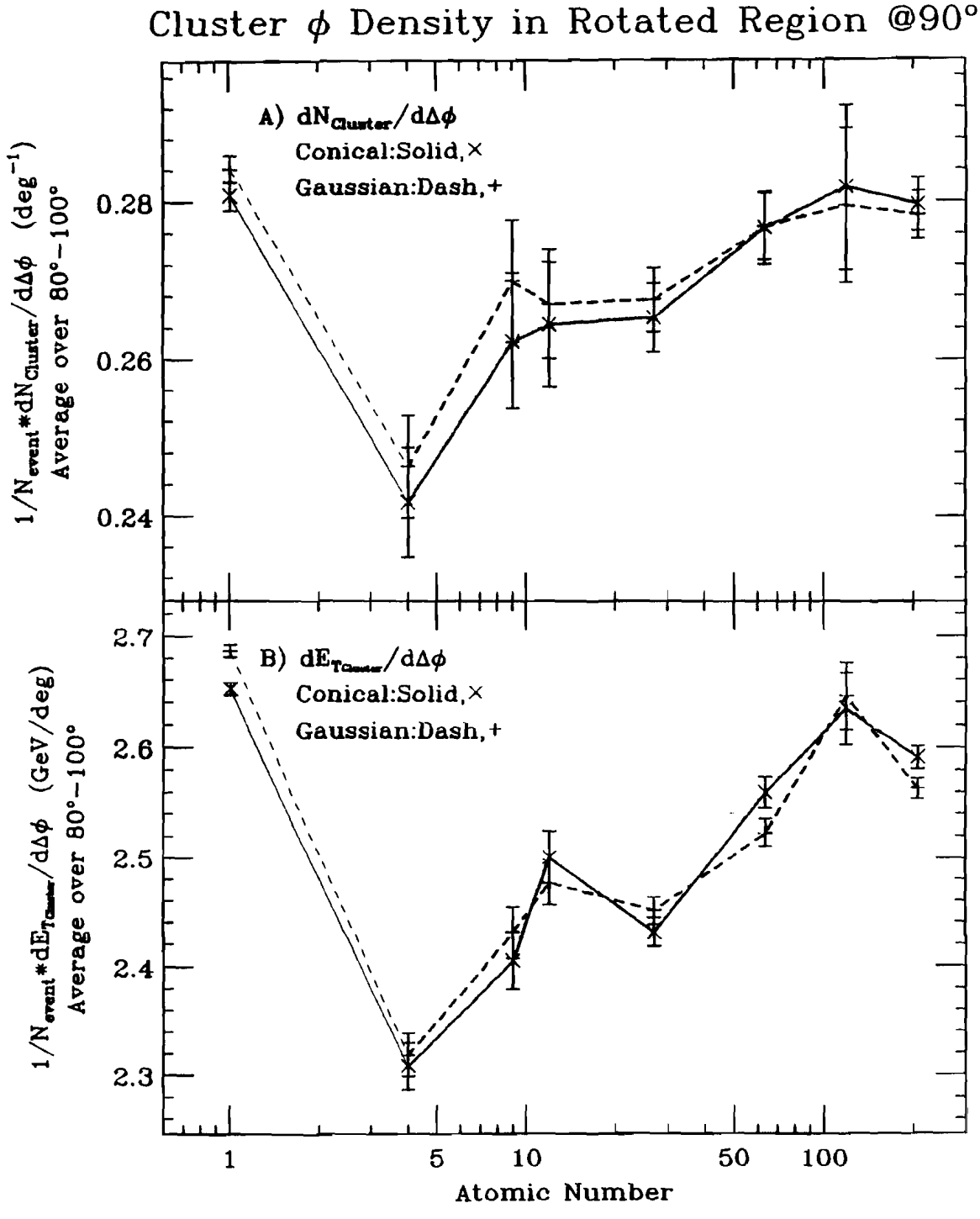

region. Figure 4.56 shows how the cluster density between the jets grows with increasing atomic number. The offset for the hydrogen point may result from the different target positions; the segments for the hydrogen subtend similar ϕ angles but larger θ^* angles, therefore, for a fixed $\Delta\phi$ slice, a larger θ^* band is included for events from hydrogen.

An isotropic background which grows with **A** is a possible explanation for our observed nuclear enhancement. Jets could be identical as a function of **A** and the observed differences arise from a growing background under the jets and included in the jet cone. To study this possibility we selected one of the rotated regions, our measure of the "background level", and then randomly selected one of the high P_T jets from which to subtract this "background". To perform this subtraction, we rotated each cluster in the rotated region 90° to give it the same P_T with respect to the high P_T jet axis as it originally had with respect to the "rotated jet" axis. The energy of the rotated cluster was then subtracted from a nearby jet cluster (the cluster with the most similar angle with respect to the jet axis) by reducing the lab energy of the cluster in the high P_T jet by the lab energy of the rotated cluster. If the rotated cluster had energy larger than the nearest cluster, then additional energy was removed from the next closest jet cluster (and so on). The process was then repeated for the remaining clusters in the rotated region and finally the entire process was performed on the other rotated region, subtracting its energy from the remaining high P_T jet. (Only events passing the fiducial cut and having at least 4 GeV/c <Jet P_T> were considered). This method reduced the total event energy by the

background energy and also roughly reduced the total event E_T by the background E_T. This new set of clusters with effectively "zero background under the jets" was then analyzed in the same manner as an event with a full cluster complement.

In an "ideal" event the jet-finder properly balances any particles lost from the cone angle with extra particles from the spectator jets to reconstruct the true jet energy; "background subtracted" jets from hydrogen will have too low and energy and P_T since the background was previously accounted for. Recall that a Monte Carlo was used to tune the conical jet-finder to determine the optimum cone angle by determining the angle which allowed the found jets to most closely represent the original simulated jets. The Monte Carlo, however, produced only proton-on-proton collisions. If the background grows with A then this method of background subtraction allows a systematic study of this effect. A further caveat exists in that this subtraction does not address the following problem: in the same manner that two particles may strike a single segment to satisfy the trigger, perhaps the background fluctuates underneath the jet to enhance the measured <Jet P_T>. In this case there would be less background in the rotated region and the subtraction would fail to remove its entire effect. Trigger bias probably plays a weak role in the background fluctuation since the trigger requires only a small fraction the the total involved energy.

Given that the sample of "background subtracted jets" represent a rough attempt to remove the background (perhaps over-correcting hydrogen and under-correcting a fluctuating background), we can still infer property changes as a function of A. Figures 4.57-60 display

Figure 4.57 Background Subtracted <Jet P_T>

---Conical Jet-finder(solid),Background Subtracted Jets(dash)---

A) <Back Ground Subtracted Jet P_T> for the lH_2 target.

B) α vs <Bck Sub Jet P_T>, Cone <Jet P_T>$\geq$4.0 GeV/c & $60° \leq \theta^*_{jet_1} \leq 110°$.

C) <Bck Sub Jet P_T>(nuclear)/<Bck Sub Jet P_T>(lH_2) vs. A

D) <Bck Sub Jet P_T> vs. A

E) <Bck Sub Jet P_T> vs <Jet P_T> Cone:H_2=—,Pb=··· Bck-Sub:H_2=--,Pb=··

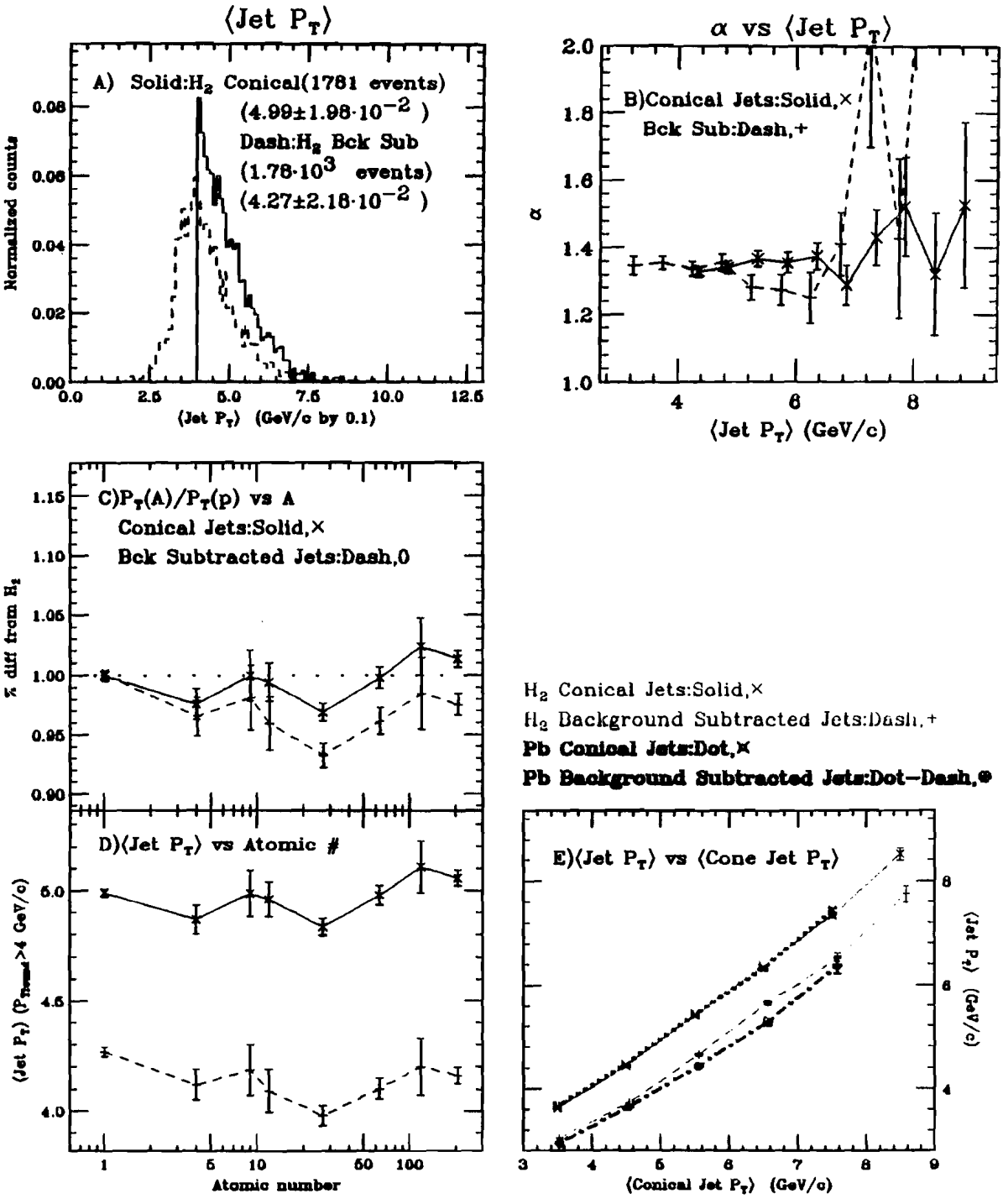

Figure 4.58 Background Subtracted w_{jj}

---Conical Jet-finder(solid),Background Subtracted Jets(dash)---

A) Back Ground Subtracted w_{jj} distribution for $1H_2$.

B) α vs Bck Sub w_{jj}. Cone <Jet P_T>≥4.0 GeV/c & $60° \leq \theta^*_{jet_i} \leq 110°$.

C) Bck Sub w_{jj}(nuclear)/Bck Sub w_{jj}($1H_2$) vs. A

D) Bck Sub w_{jj} vs. A

E) <Bck Sub w_{jj} vs <Jet P_T> Cone:H_2=—,Pb=··· Bck-Sub:H_2=--,Pb=·-

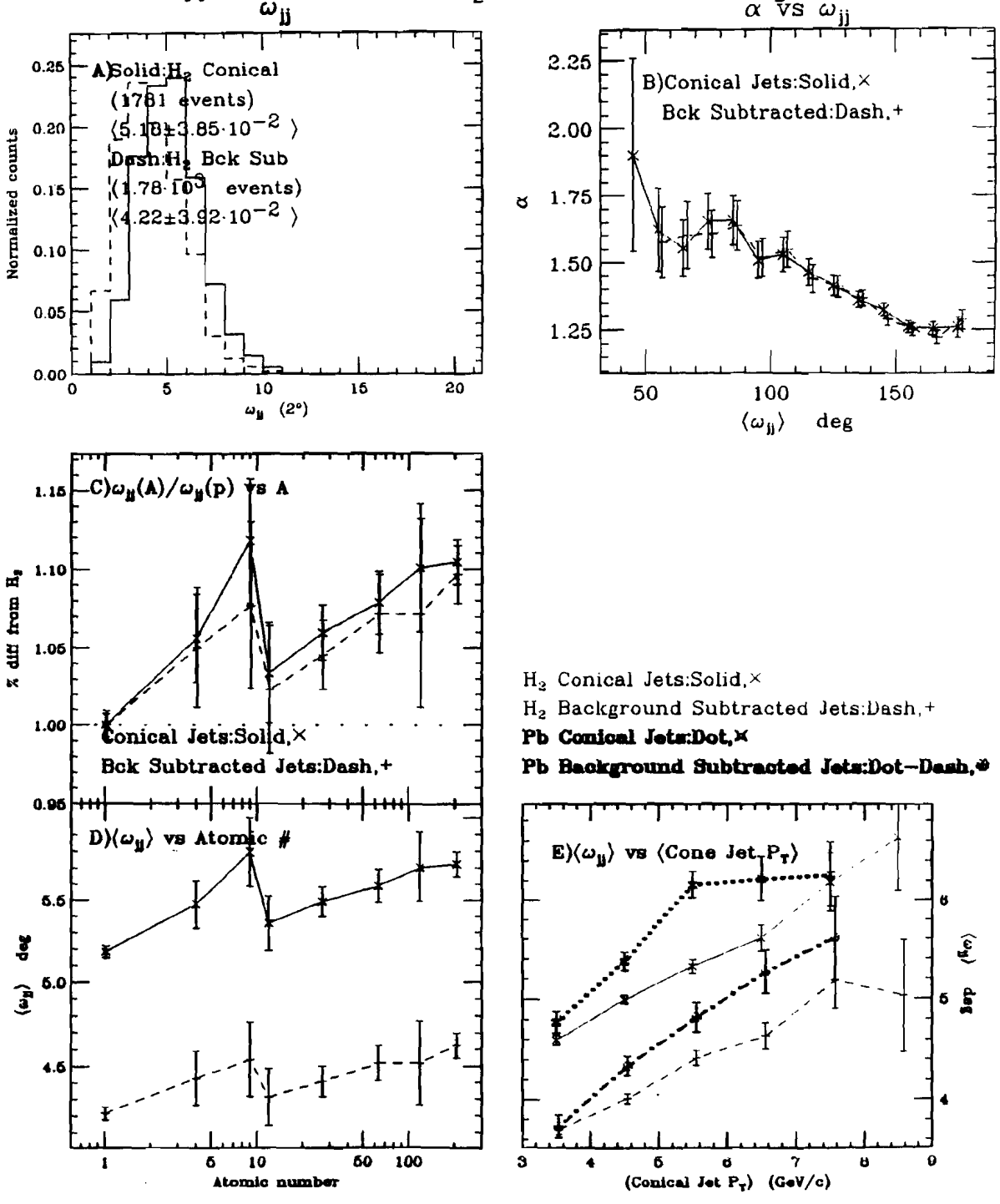

Figure 4.59 **Background Subtracted <Ω>**

---Conical Jet-finder(solid),Background Subtracted Jets(dash)---

A) Background subtracted <Ω> for $1H_2$.

B) α vs Bck Sub <Ω>. Cone <Jet P_T>$\geq$4.0 GeV/c & $60° \leq \theta^*_{jet_1} \leq 110°$.

C) Bck Sub <Ω>(nuclear)/<Ω>($1H_2$) vs. A

D) Bck Sub <Ω> vs. A

E) <Bck Sub <Ω> vs <Jet P_T> Cone:H_2=—,Pb=··· Bck-Sub:H_2=--,Pb=·-

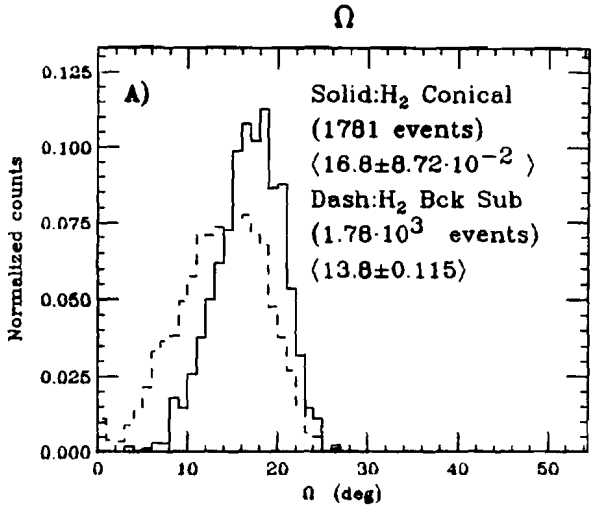

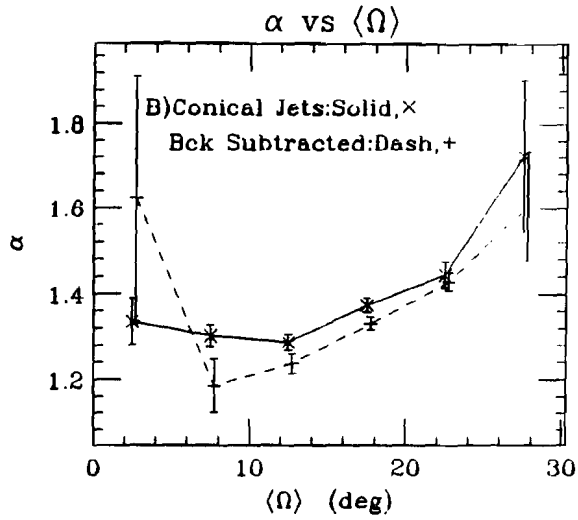

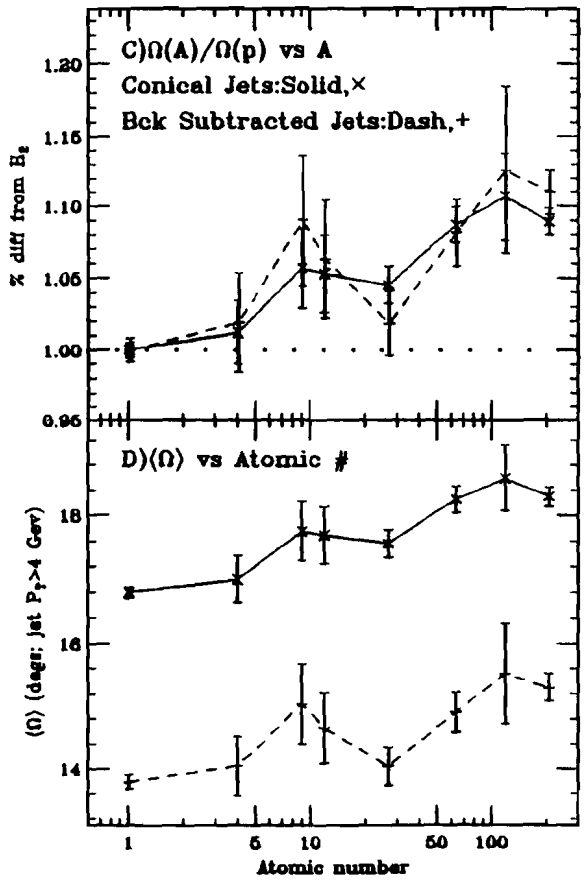

H_2 Conical Jets:Solid,×

H_2 Background Subtracted Jets:Dash,+

Pb Conical Jets:Dot,×

Pb Background Subtracted Jets:Dot—Dash,•

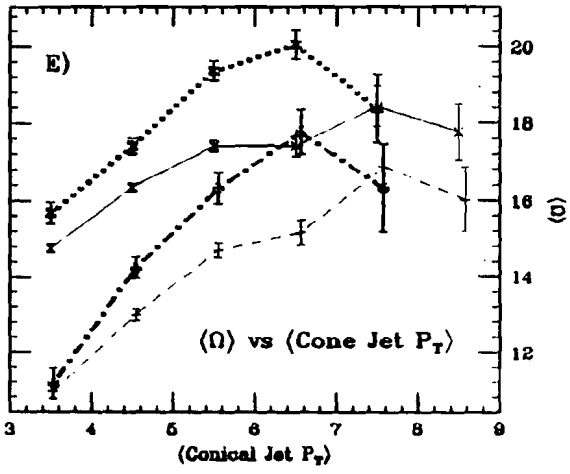

Figure 4.60 **Background Subtracted P_{Tjj}**

---Conical Jet-finder(solid),Background Subtracted Jets(dash)---

A)Background subtracted P_{Tjj} for lH_2.

B) α vs P_{Tjj}. Cone <Jet P_T>$\geq$4.0 GeV/c & $60° \leq \theta^*_{jet_1} \leq 110°$.

C) P_{Tjj}(nuclear)/P_{Tjj}(lH_2) vs. A D) P_{Tjj} vs. A

E) <Bck Sub P_{Tjj} vs <Jet P_T> Cone:H_2=—,Pb=··· Bck-Sub:H_2=--,Pb=··

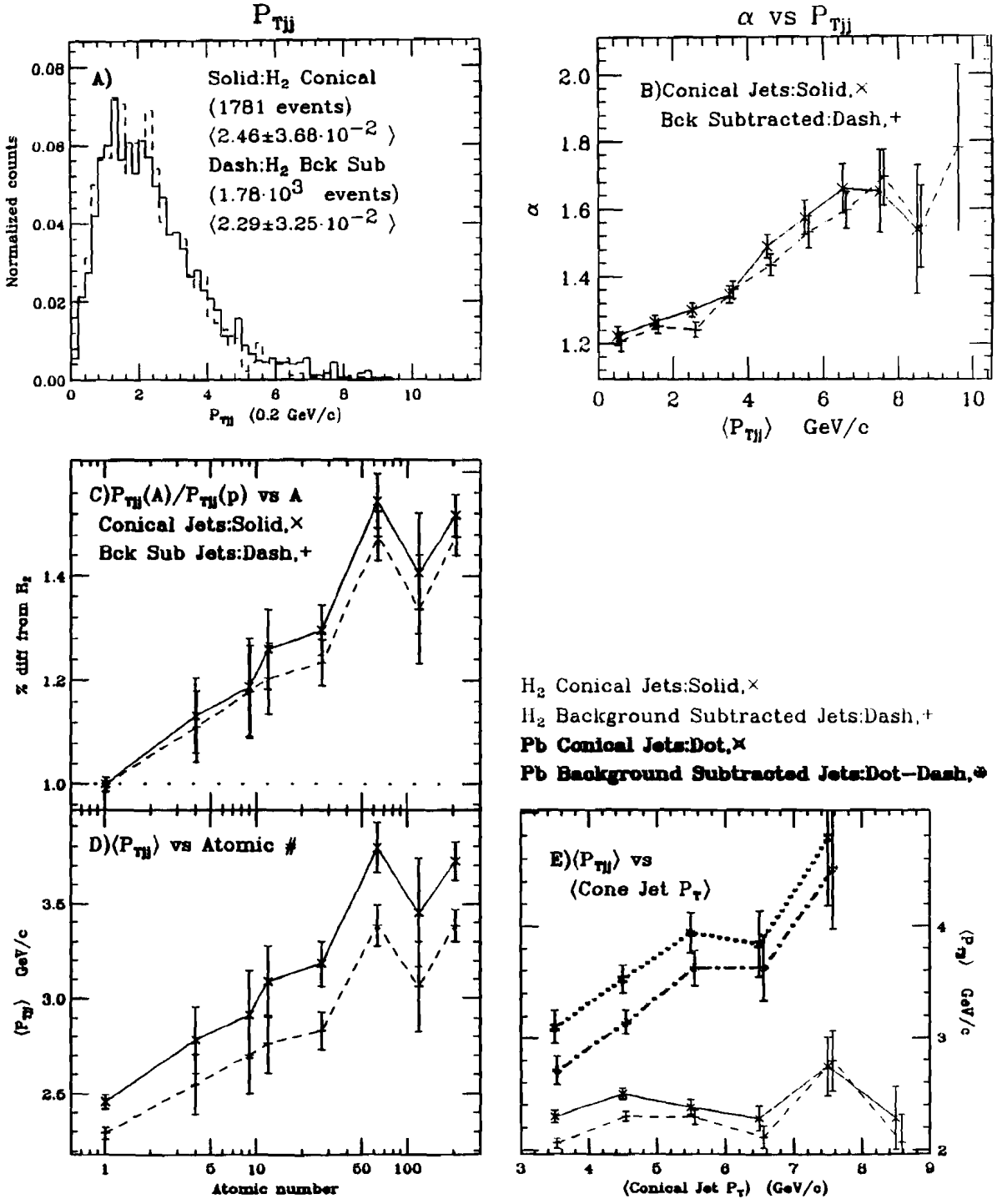

the resulting <Jet P_T>, <Ω>, w_{jj} and ΔP_{Tjj} for these jets. As expected, the background subtracted <Jet P_T> drops below the conical <Jet P_T> since less P_T is available for use in the jets, figure 4.57E. However, even with the removal of the background E_T, α enhancement over 1.0 still appears, figure 4.57B, although its magnitude may be reduced slightly for the higher jet P_T's (the background subtracted data naturally runs out at lower P_T values). The angular properties relating to the jets change only slightly between the background subtracted jets and the conical jets. The angle between the jets, w_{jj}, remains nearly identical, figure 4.58; while the average aperture of the jet pair, <Ω> (where $\Omega = (\Sigma E_i w_i^2 / \Sigma E_i)^{\frac{1}{2}}$) decreases. The aperture decrease is expected since the energy weighting of the clusters is decreased, but the percent change as a function of A, figure 4.59, shows little change with A. Reflecting the similar dependence on A, the background subtracted jets produce α values similar to those from the conical jets; the α values are 5 to 10% smaller but still show nuclear enhancement. The P_T balance between the jets, ΔP_{Tjj}, improves 7% for hydrogen, and even larger amounts for the other nuclear targets, figure 4.60E. In spite of this change in P_{Tjj} the produced α values for the background subtracted jets match those of the conical jets at the ΔP_{Tjj} changes. In general for each variable studied, removing the background does not appear to change the behavior as a function of atomic number. This result implies that the enhancement is due to a change in the physical properties of the jets rather than a changing background.

CHAPTER 5

CONCLUSIONS

High P_T production of jets from 400 GeV/c protons onto eight nuclear targets spanning the range from A equal 1.0 to 207 were measured using a large solid angle calorimeter detector. Jet events were isolated from the larger sample of events collected with the "two-high" trigger using a pair of jet-finders. One jet-finder positioned fixed 45° half-angle angle cones by maximizing the P_T in each cone and interpreting the clusters in the cone as the particles comprising the jet. The other jet-finder smoothed the P_T surface with a Gaussian and identified jets with the peaks in the surface. Parameters for both jet-finders were optimized to reconstruct jets from events generated using a Field/Feynman Monte Carlo. The jet--finders agree except on the jet E_T where the Gaussian definition contains more particles -- and therefore a larger E_T.

The observed ratio $\sigma(pA)/A\sigma(pp)$ when plotted against the atomic number A in a log-log plot roughly produces a straight line fit by A^{α}. Jets show nuclear enhancement; α takes values greater than 1.0, implying coherent effects produce an increased probability of high P_T scatters. One method of attempting to correct for background effects resulting from beam and target spectator fragments reduces the value of α as much as 10%; however the effect persists. The value of α stays roughly constant over the observed <Jet P_T> range of 4-8 GeV/c

at a value near 1.35±0.01. This value is somewhat higher than the α of 1.14±0.02 resulting from the selection of two-high trigger events with planarity $\geq$ 0.8 and $E_T \geq 15$ [MIE88]. A similar analysis of E672, an experiment at 800 GeV/c using a jet-finder, reported an α of 1.6 [STE88]. The different α values highlight the misconception that a single α value describes the nuclear enhancement for "jets". The jet definition and resulting event selection strongly influences the observed α. Selection of jets with increased planarity (by selecting planar events, by choosing low multiplicity, by requiring $\Delta\phi$ near 180°, by asking for jets balanced in P_T...) decreases the size of the enhancement. At planarities near 1.0 the enhancement goes as $A^{1.0}$. Thus the lower α value for jet-like events selected via high E_T and high planarity follows from the difference in selected events resulting from the different "jet" definitions. The large α observed in the E672 data most likely reflects their jet definition.

Given that the exact value of α_{jet} depends on the jet definition, the statement (made in some earlier review articles [TAK79, ZMU81]) that the enhancement for jets is stronger than for single particles requires tempering. High P_T single particles must come from a very specific fragmentation mode, most likely balanced by an unobserved jet. Models explaining the observed α_{jet} values should include the $\alpha_{single\ particle}$ as a subset of the model. Similarly the change in α with jet parameters must be explained. Models which try to describe the process should also explain dependencies on trigger geometry as well as the dependencies of α on the quantum numbers of the triggering particle (recall Cronin observed different α values when he measured production of $\pi^{\pm}$ than when he produced p or $\bar{p}$).

As the atomic number of the target nuclei increases the properties of the jets change; the ϕ angle between the jets ($\Delta\phi_{jj}$) increases, the multiplicity as measured by the clusters increases, the unbalance in the P_T between the two high P_T jet increases, and the jet aperture (Ω) becomes wider. However, for a given A, the two jets remain roughly equal in width. This is shown by displays of $dN_{clusters}/d(\Delta\phi)$ and $dE_{Tclusters}/d(\Delta\phi)$ as a function of the ϕ angle between the clusters and the jet axis. The shape of the distribution is nearly independent of which jet is used as the reference; irregardless of use of the hot jet axis or the second hottest jet axis as ϕ equal to 0 the distributions nearly match, implying the jets have similar widths. For each of these parameters, fits of A^{α} produce α values that decrease as the event properties approach the "ideal" high P_T jet pair scattering, for example α decreases with improving balance in the individual jet P_T's.

Increasing the atomic number of the target nucleus causes the forward energy flow to decrease, and instead of appearing at large transverse angles, the energy misses the calorimeter pair and (by inference) flows into the target fragmentation region. The beam jet appears to transfer its energy to the target and appears in the target fragmentation region rather than to the central or forward regions. calorimeter decreases α increases, and as the energy in the main calorimeter increases α decreases as the total energy observed in both calorimeters decreases toward 400 GeV.

A possible explanation of the differences in jet properties as a function of A starts with the observation that in p-A collisions the particle density increases dramatically with A. The extra particles

may come from the break up of the nuclear target and create a nearly isotropic background of particles at large P_T's. If the jets are created by a parton which has escaped the nucleus without being affected by the nuclear matter, then jets from hydrogen and lead would appear identical, except for the enhanced background of particles. The nuclear enhancement would result from fluctuations of the background under the jets; events where the background fluctuated to create an E_T peak which aligned with the jet E_T peak would appear as even larger E_T jets. Since more background is available as A increases, large energy fluctuations would be more likely for large target nuclei. This in turn would produce α's larger than one. To test this explanation, the region between the jets was studied. In this region, achieved by rotating 90° from the di-jet axis, α might be expected to increase with *decreasing* "background" E_T since the fluctuations producing the high E_T jets would have depleted the regions between the jets. However as the E_T in this region decreases (presumably appearing as increased E_T in the jets) α also *decreases*. We still cannot rule out fluctuations as a source of the enhancements. For example, a rising background that appears mostly under the jets (perhaps as a result of a trigger effect) could produced the observed α behavior. We hope to study the question of fluctuations further.

An attempt to correct for a possible background was made by assuming that the jets appear as energy peaks on top of a uniform background. We measured the energy in the region between the jets and then removed this energy from the high P_T jets. This method of background subtraction can not detect events where the background fluctuates in such a manner that to create an additional energy peak

under the jets. When this type of fluctuation occurs the energy between the jets will give too low an estimate of the background level; background contamination will remain even after this type of subtraction. After applying this limited form of background removal to the data, the differences between jets as a function of atomic number are reduced ~10% but still persist.

The primary difference as A increases can be explained in terms of the addition of more particles from the jet carrying intermediate E_T values. The mean number of particles in the jets increase by 1.2 from hydrogen to lead while the background increases by only 0.4 particles. Additional particles can account for the increased jet P_T, reduced jet coplanarity, and the increased jet aperture observed as A increases.

Conclusions about D(Z) from other authors, implying that the core of the jets from large nuclei vanish [STE88] are clearly over stated. The transverse momentum of the leading particle in the jets stays reasonably constant -- regardless of target nuclei. We observe a dependence of D(Z) on target type which is much smaller than observed in [BROM79], and similar (although still smaller) to that reported in [STE88].

All evidence observed in this jet study is consistent with the quark fragmenting outside the nucleus, after experiencing the enhancement mechanism. The enhancement properties vanish as one selects events which reflect a "clean" quark-nuclear parton scatter (planarity ~1). Of the various models explaining nuclear enhancement, our data does not clearly support any single model over another.

The prediction of increased particle multiplicity from targets of increased A, made by all the models reviewed in chapter one, agrees with the data. All four of Krzywicki's predictions [KRZ79] appear consistent with the data: the jet particle content increases while the average Z decreases. Any effect which decreases the jet coplanarity, in concert with his predicted P_T trend, also increases the nuclear enhancement. His prediction that the θ^* of the softer jet will lie more in the direction of the target with increasing A, or at larger θ^* angles also appears consistent, but the effect is very small. The second jet, corresponding to the softer parton, shifts from an average θ^* angle of 86° for hydrogen to an angle of 88° for the lead target while the hottest jet shifts from an angle of 88° to 89° for these two targets. Krzywicki's final prediction that the enhancement will go to one for any process not involving "sea" particles requires identification sea and non-sea processes for a definitive test. If the highest planarity events result from collisions involving non-sea quarks then this prediction may explain the α response as a function of planarity and the general observation that α=1.0 for the "cleanest events". However, one might also expect that the largest P_T events result from large X_1 and X_2 events, which preclude the involvement of sea-quarks. We observe α to rises (or remain flat) with increasing P_T.

Models using multiple quark pair interaction [TAK79,LAN75] predict increased multiplicities and the widening of the second jet with A. The second jet is nearly always observed wider in each of our measures: $\Omega_2 > \Omega_1$, $w_{i2} > w_{i1}$, and the FWHM of $dN/d\phi$; although the effect is less pronounced in the lead than in the hydrogen data. This

ordering of the jets found by the Gaussian jet-finder may follow from its definition since the "width" of the jet correlates with its E_T. The conical jet-finder, however, fixes the allowed particle angle but again the second jet appears wider than the hottest jet, implying the effect is real. However, the effect does *not* increase with A but decreases slightly.

Zmushko, [ZMU80b], makes a prediction that the increase in cross section will grow dramatically faster than $A^{1.0}$ when the jet P_T exceeds the pp $\sqrt{s}/2$. Our data displays a plateau for <Jet P_T>'s greater than 4 GeV; however, the data runs out well before the 13.7 Gev/c required to test Zmushko's model. His final two predictions appear consistent with the data; the multiplicity increases with increasing A and $\Delta\phi$ degrades away from 180°.

In general our data is consistent with the phenomenological predictions of the models based on multiple scatters in the nucleus. These modules do predict an increase in particle multiplicity within the jets, an increase in $\Delta\phi_{jj}$, and a larger Ω as A increases. Our data support these predictions. The details of the scatter however, are still open to interpretation; none of the models predict the shape of the $\sigma(pA)/A\sigma(pp)$ to flatten at higher A values. To fit our data a series expansion suggested by multiple scattering formalism results in negative coefficients! Further, none of the models discuss the dependence of α on selected events as dictated by jet parameter selection. Our data indicates that multiple scattering may well serve as a good starting hypothesis; however the true nature of jets from nuclei is more complicated than the simple picture postulates.

APPENDIX A

TRACKING EFFICIENCY VS. MULTIPLICITY AND ANGLE

This appendix describes the tracking efficiency as a function of angle and multiplicity. The efficiency determination requires four stages of synthetic track generation, labeled INPUT, GENERATED, FOUND and CUT tracks. The first stage consists of the INPUT tracks, generated according to a given distribution. The second stage uses the input tracks and models the hardware detection, determining a set of chamber hits which combine to make GENERATED tracks. The tracking algorithm then operates on the generated hits, as though the hits were real data, and produces FOUND tracks. A series of cuts reduce the found sample to the final CUT set of tracks. The ratio of the CUT to INPUT tracks gives the final efficiency. Inverting this ratio gives an estimate of the true number (and distribution) of tracks knowing the number in the cut sample of tracks found in the data. The actual efficiency depends on center-of-mass angle, θ^*, and input multiplicity, requiring calculations of both of these variables.

A.1 INPUT TRACKS

The shape of the input track distribution should reflect the true particle θ^* distribution. The two experimental measures, the tracks and the calorimeter clusters, disagree on the number of particles at each angle (figures A.1A and A.2A); the tracking, inefficient at low angles, contains fewer particles below 90 degrees. The cluster distribution, with the ring peaks smoothed out, therefore provides the proper input distribution (figures A.1B and A.2B). Additional large angle tracks strike the chambers but miss the calorimeter. These are accounted for by increasing the distribution above the cluster prediction for θ^* greater than 120 degrees.

The active areas of all the chambers combine to determine the maximum allowed track X and Y angles. The chambers subtend slightly different solid angles, so the maximum slope comes from the center-of-mass X angle of the fourth-largest chamber. This chamber sets the size since every track must have at least four points (plus the vertex point). Similarly, the smallest allowed X angle results from the central gap in the chambers. Table A.1 lists the center-of--mass acceptance angles of the chamber array as well as those of the calorimeter for the two target positions used in our experiment. Figure A.1C, containing input data with 15 tracks per event, shows the X and Y center-of-mass angles generated with a vertex at Z=0.0 cm, the hydrogen target position. The resulting θ^* angles appear in figure A.1D. For comparison, figure A.1D also contains the the final CUT θ^* distribution and the IH_2 data track distribution. Figure A.2 contains similar plots for lead data with vertices at Z=-99.5 cm and Monte Carlo events with 25 input tracks with vertices at Z=-99.5 cm.

Figure A.1 Angular Distribution's of 15 Tracks @ Z=0

A) The distribution of reconstructed tracks(solid) and the clusters(dashed) for two-high data from the hydrogen target with Z=0.
B) Distributions of $1H_2$ cluster(dashed) & 15 simulated tracks(solid).
C) Simulated track X(solid) and Y(dots) distributions.
D) Comparisons of cut tracks from $1H_2$(solid), Monte Carlo input(dash) and Monte Carlo tracks with cuts(dots).

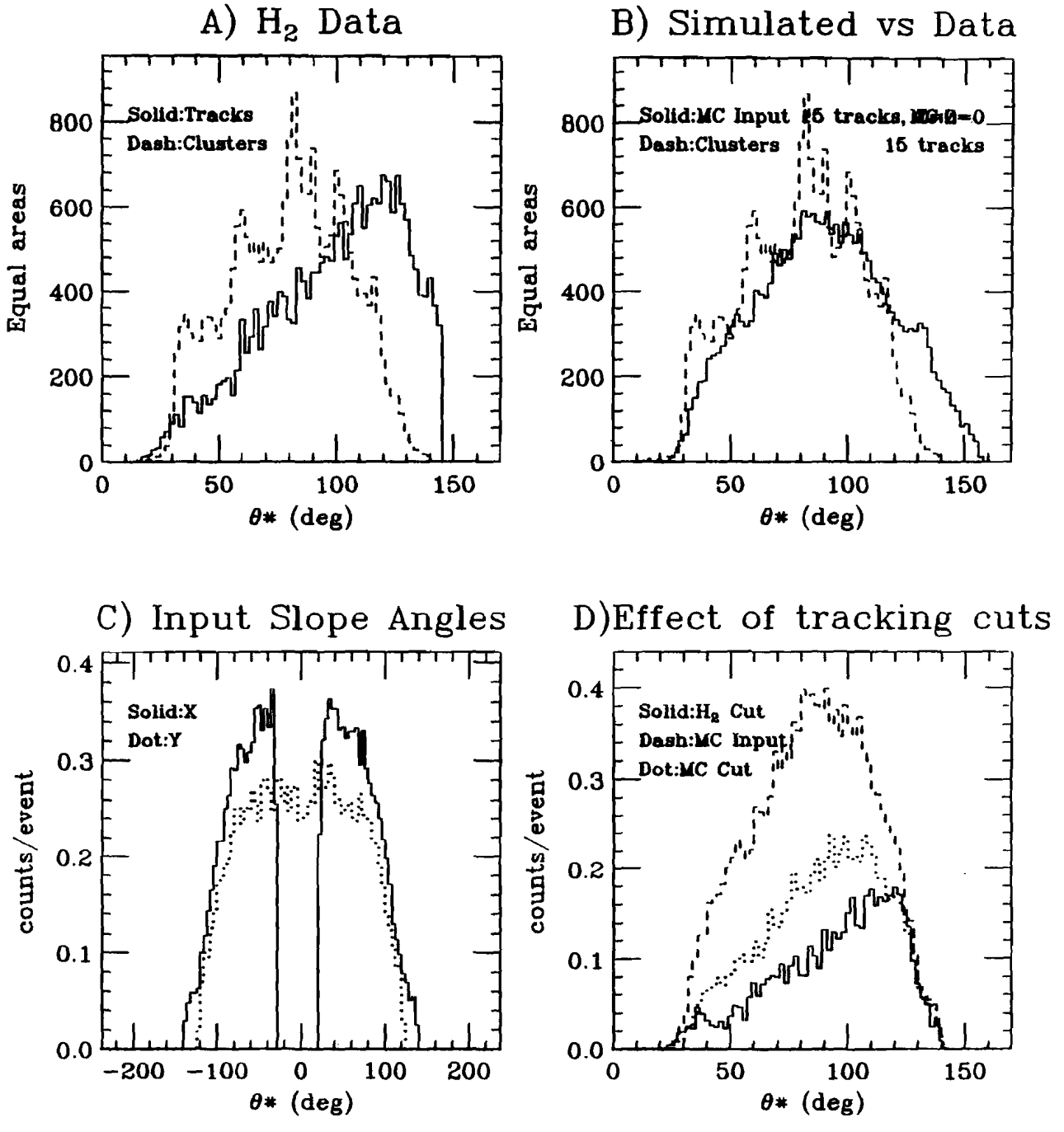

Figure A.2 **Angular Distribution's of 25 Tracks @ Z=-99**

A) The distribution of reconstructed tracks(solid) and the clusters(dashed) for two-high data from the lead target with Z=-99.
B) Distributions of Pb cluster(dashed) & 25 simulated tracks(solid).
C) Simulated track *X*(solid) and *Y*(dots) distributions.
D) Comparisons of cut tracks from lead(solid), Monte Carlo input(dash) and Monte Carlo tracks with cuts(dots).

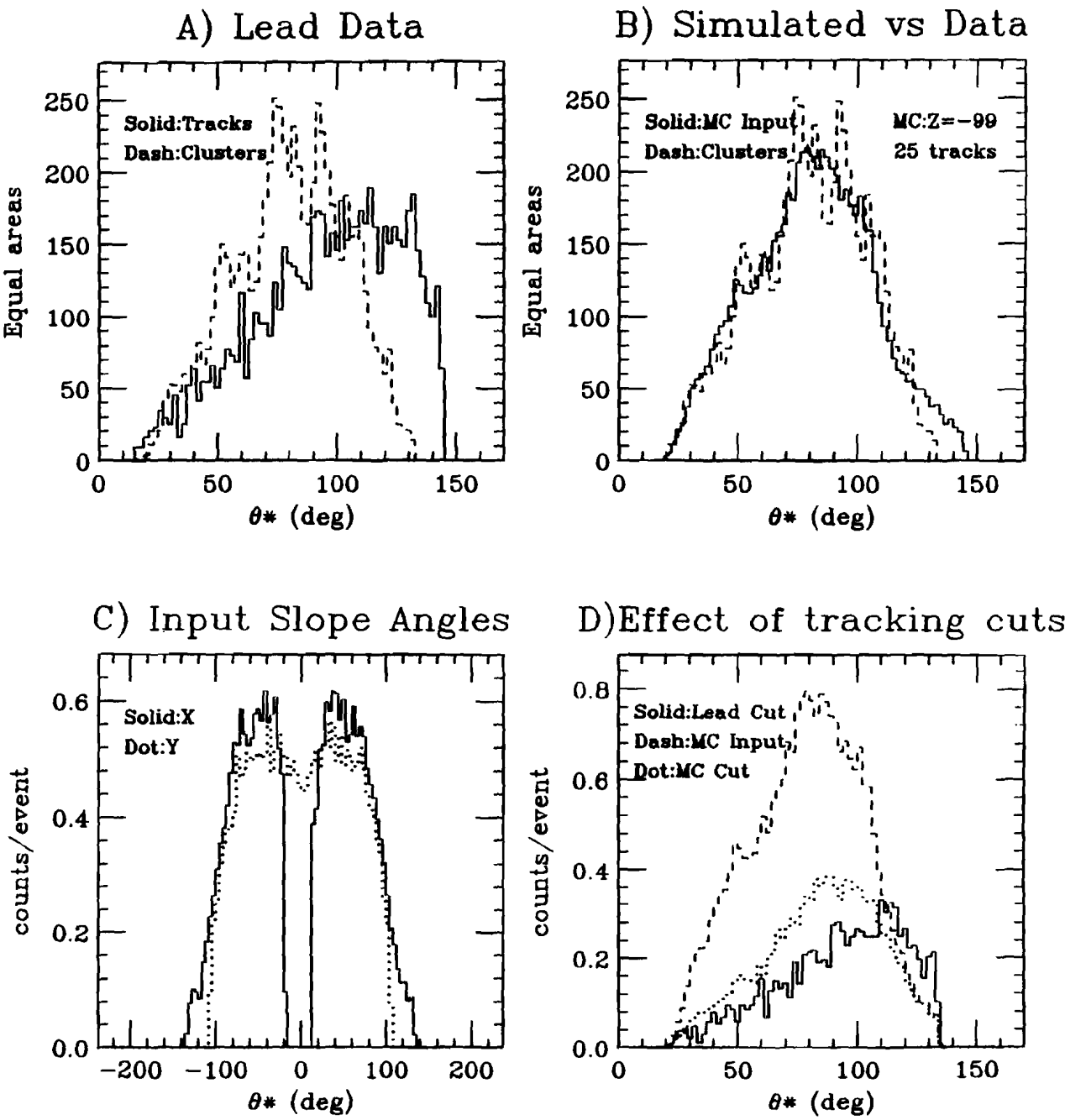

The mean charged particle multiplicity for hydrogen two-high data is 15.2 (23.8 for lead).

TABLE A.1
Chamber and Calorimeter Acceptance

	Chamber *X*-Z plane	Chamber *Y*-Z plane	Calorimeter *X*-Z plane	Calorimeter *Y*-Z plane
Hydrogen	$20.9° < \theta^* < 156°$	$0° < \theta^* < 134°$	$27.8° < \theta^* < 137°$	$26.0° < \theta^* < 122°$
Nuclear	$18.1° < \theta^* < 144°$	$0° < \theta^* < 116°$	$24.7° < \theta^* < 133°$	$22.8° < \theta^* < 116°$

A.2 GENERATED TRACKS

Using the input tracks, the hardware simulation determines which track-chamber intersections (hits) the chambers could record. The major hit loss occurs when two tracks cross the same drift chamber cell. When this happens the sense wire records only the closest hit; a charging TDC ignores additional signal avalanches. (The delay line chambers occasionally give erroneous *X* and *Y* locations when a single cell receives multiple hits. Appendix B.3 discusses the frequency of this error). Tracks missing the active chamber regions cause additional losses of hits between the input and the generated tracks.

The PWC simulation includes a hardware readout feature that groups adjacent wires and reports their average half-wire location and cluster size. Tracks with similar *X* angles blend together producing a single hit. The simulation also adds extra PWC hits to the central region not covered by the tracking acceptance since the PWC is active over this area. The hit loses and gains cancel (within 10%, see §2.2.2) for typical event multiplicities. Combined with a correction

function, this chamber measures the total charged particle multiplicity in the tracking acceptance.

To quantify the chamber detection efficiency, the ratio of detected hits to incident hits, the program tracked actual data and produced an efficiency curve for each chamber as a function of angle. Simulating chamber inefficiency, we deleted points from the generated tracks using the measured inefficiency rate. The simulator modeled the chamber noise by including extra points. Appendices B.1 and B.2 detail these calculations.

The algorithm reproduces the drift chamber resolution by adding to the hit locations a random Gaussian number times an experimental resolution factor. The experimental chamber resolutions were calculated in [KUE84]. To match the quality of the experimental track reconstruction, the simulated points were smeared by the measured resolution increased by a constant factor. The movement of points due to smearing is limited to the cell size. The width of the experimental Gaussian resolution was increased 2.0 times in both the X and Y directions. Appendix B.4 discusses the selection of these parameters. The quantized PWC resolution, resulting from the wire spacing, is accurately simulated by placing hits in bins of an array. Hits near bin edges are placed in both bins, allowing for the possibility of single hit firing 2 wires and simulating the chambers 1/2-wire-space resolution.

Figure A.3A shows the chamber hardware efficiency, (GENERATED/INPUT), for 15 (and 25) input tracks as a function θ^{*} for the Z=0.0 (and Z=-99.5) simulation.

Figure A.3 **Tracking Efficiency Ratios (Summary)**

---15 Tracks @Z=0(Solid) 25 Tracks @Z=-99(Dash)---

A) The ratio of tracks available after hardware losses over the input tracks vs. θ^*.

B) The (# of found tracks)/(# of input tracks) ratio vs. θ^*.

C) The ratio of found passing all cuts over the input tracks vs. θ^*.

D) The "efficiency corrected tracks" over the input tracks vs. θ^*.

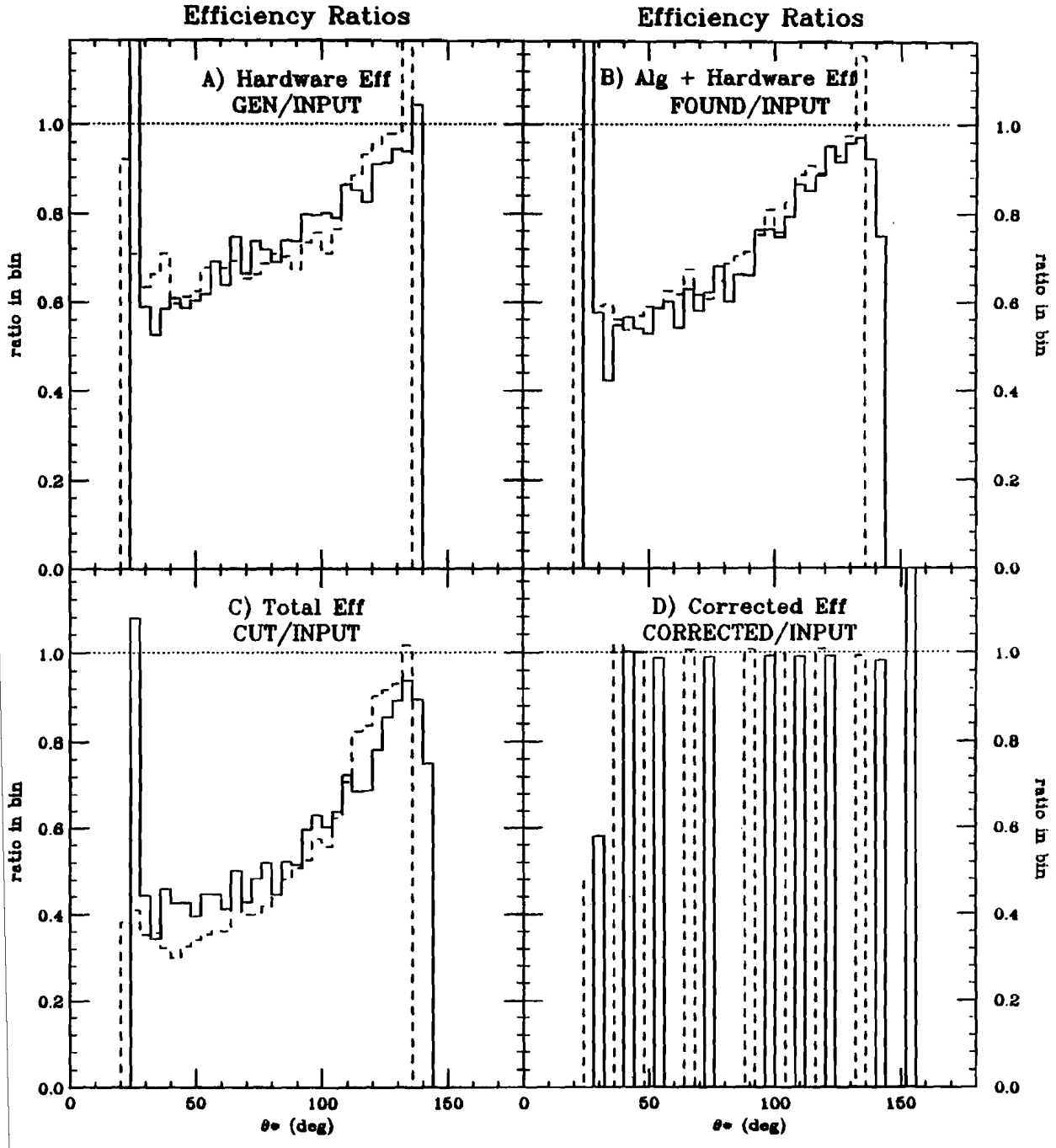

A.3 FOUND TRACKS

Operating on GENERATED hits with simulated drift times and PWC hit locations, the tracking algorithm reconstructs a set of FOUND tracks. Figure A.3B displays the combined efficiency of the hardware and tracking algorithm, (FOUND/INPUT), as a function of the center-of-mass angle. These distributions include some incorrectly reconstructed tracks, removable with additional cuts. The tracking algorithm is discussed in [MOO85].

A.4 CUT TRACKS

A Fortran program uses the FOUND tracks and applies cuts to the sample to produce efficiency histograms. Calculation of θ^* requires tracks to pass four conditions. First, tracks must come from the primary vertex; this excludes tracks not in a vertex or coming from a vertex other than the one with the most tracks. [For events with 15 input tracks 6.06% failed to come from the primary vertex]. Second, every track must have valid slope. Tracks, by definition, have good X slopes however some tracks contain none of the three possible Y points. [For the 15 track sample, 5.24% failed to have any Y information, 8.78% failed the vertex cut and/or Y information cut]. Tracks passing these cuts allow calculation of θ^*; however confidence in this calculation requires cuts three and four. The third cut, on the χ^2/ν of the fit in Y, removes tracks with uncertain Y slopes. Points producing a large Y χ^2/ν usually result from tracks which were incorrectly reconstructed in the X view. The final cut results when the PWC gave the only Y information on the track. Determination of

the Y for a PWC hit usually gives multiple solutions, all equally correct. Normally the unambiguous delay line Y values resolve the ambiguity, however when only the PWC recorded Y information, the correct Y can not be selected; when the possible Y values differ by more than 1.5 cm the track fails the unambiguous reconstruction cut. The ratio of the CUT/INPUT tracks determines the final tracking efficiency displayed in figure A.3C.

A.5 CUT TO INPUT CORRECTION

The ratios in figure A.3C show the tracking efficiency as found by the Monte Carlo. Estimation of the actual number of charged particles intersecting the chamber array from the tracks passing the final cuts in the data requires the inverse process. Tailoring the efficiencies to our application, we subdivide θ^* into 10 angular bins, roughly matching the calorimeter rings (The first ring covers the beam hole and the last ring is beyond the calorimeter's outer edge). For each bin we produced a scatter plot showing the number of input tracks versus the number remaining after cutting, (figure A.4 contains example plots for 15 input tracks at four different angles). For a given number of cut tracks the entries along a row show how many input tracks actually fell in the bin. The ratio of the cut number to the mean input number gives the efficiency. Observing that the mean input values nearly lie on a line, (figure A.5), the slope and intercept of this line give the efficiency correction, symbolically,

TRUE TRACK # = SLOPE * CUT TRACK # + INTERCEPT.

The dotted line in figure A.5 provides a zero correction reference.

The efficiency curves depend strongly on the input multiplicity, requiring separate curves for each multiplicity and angle. Assuming the adjusted number of PWC hits gives the true input multiplicity (see §2.2.2), efficiency corrections use this multiplicity to select the proper correction curve and determine the number of cut tracks in each angle bin. This curve gives the corrected number based on the Monte Carlo efficiency. For intermediate input multiplicities we determine the efficiency by interpolation between calculated Monte Carlo values. Table A.2 gives the slopes, intercepts and the χ^2/ν resulting from the least squares linear fit of the INPUT tracks as a function of the CUT tracks for a variety of input multiplicities as a function of angle.

Application of the correction curve to the CUT tracks produces a CORRECTED set of tracks. Figure A.3D shows the correction efficiency, (CORRECTED/INPUT), for the seven angular bins of the calorimeter rings. A perfect correction would give a ratio of 1.0. Figure A.3D also shows, for reference, the uncorrected tracking efficiency in the beam hole and beyond the calorimeter's edge. The high density of tracks in the inner rings requires a large correction while the outer rings need much smaller corrections. (The ring beyond the edge of the calorimeter actually finds slightly too many tracks due to accidental match-ups). To match the chamber acceptance with that of the calorimeter, we make an additional cut, affecting the 122° to 140°. angular ring, and only consider tracks that hit the calorimeter. This cut removes INPUT, GENERATED and FOUND tracks nearly equally since the outer ring is highly efficient.

Figure A.4 Scatter Plot of Found vs Input Tracks

---Simulated 15 tracks @ Z=0---
A) Tracks in angle bin spanning 52° to 75°.
B) Tracks in angle bin spanning 96° to 110°.
C) Tracks in angle bin spanning 110° to 122°.
D) Tracks in angle bin spanning 122° to 140°.

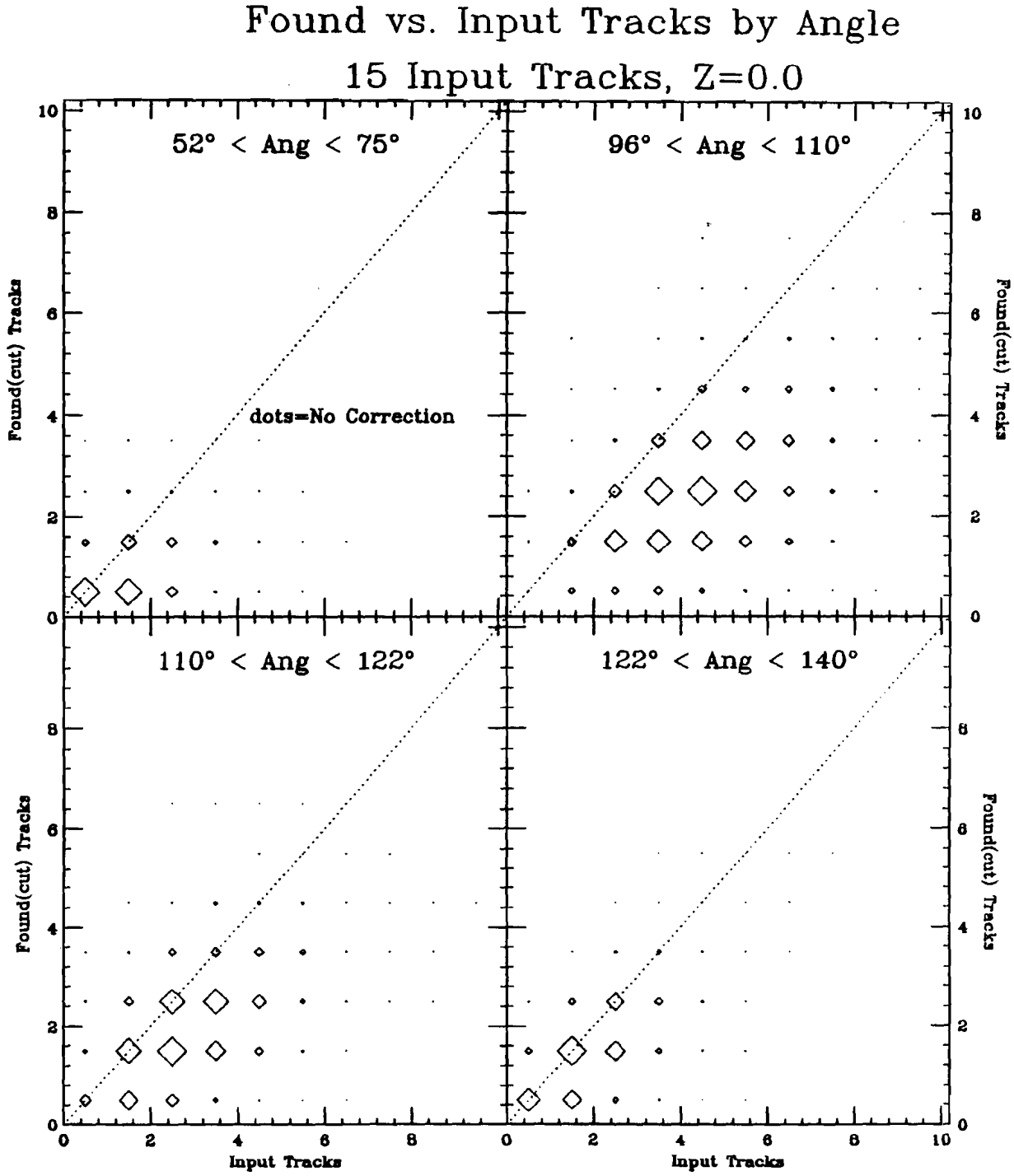

Figure A.5 **Function to Provide Efficiency Correction**

---Simulated 15 tracks @ Z=0---
A) Tracks in angle bin spanning 52° to 75°.
B) Tracks in angle bin spanning 96° to 110°.
C) Tracks in angle bin spanning 110° to 122°.
D) Tracks in angle bin spanning 122° to 140°.

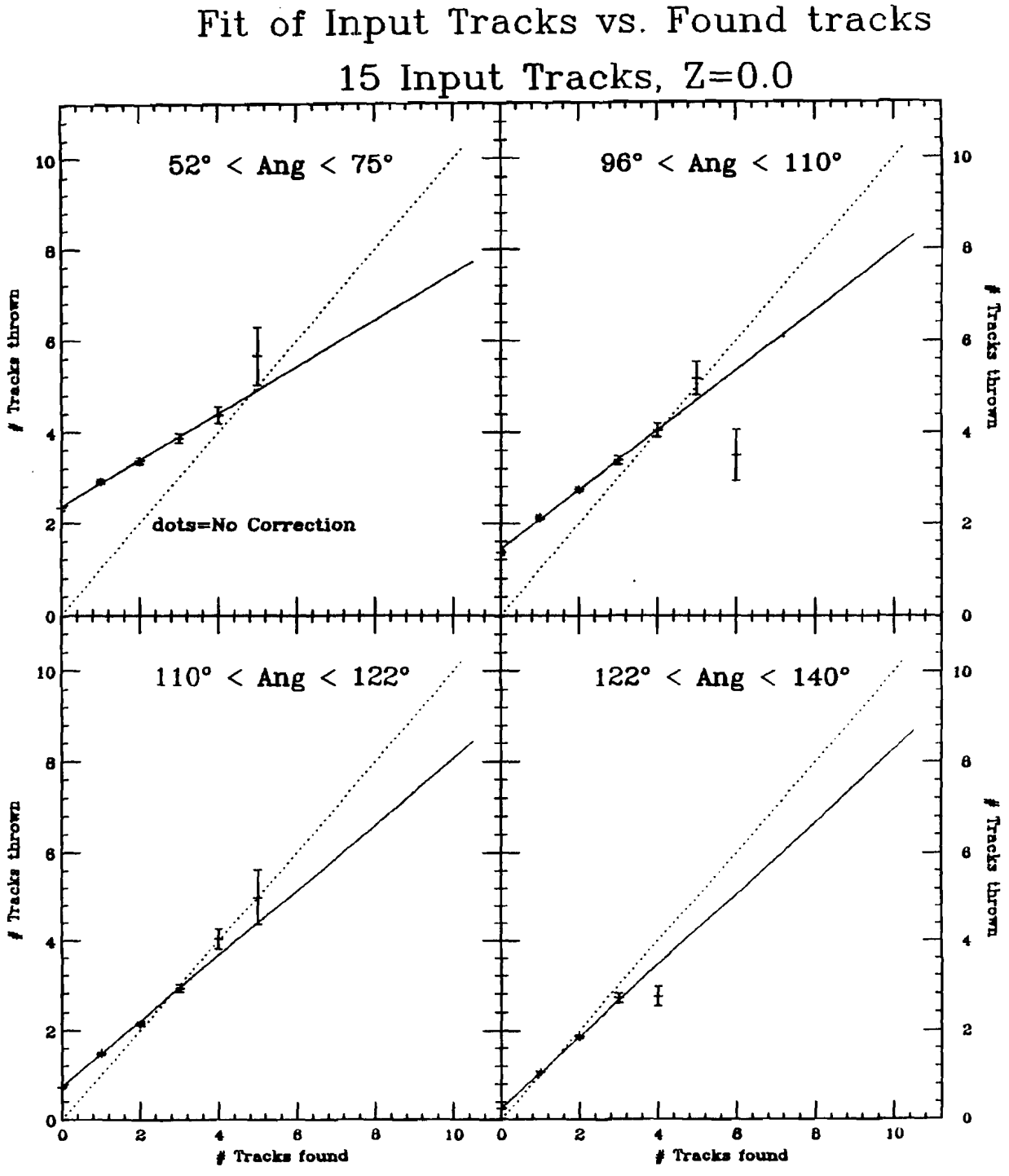

TABLE A.2

Slope and Intercept for Efficiency Corrections

Monte Carlo with a Vertex at Z=0.0 cm

	FOR GENERATED 5 TRACKS			FOR GENERATED 10 TRACKS		
ANGLE	SLOPE	INTERCEPT	χ^2/ν	SLOPE	INTERCEPT	χ^2/ν
40.0	0.5972	0.0905	0.1731	0.5472	0.2308	2.0509
52.0	0.6190	0.1834	0.9008	0.5612	0.4860	0.0013
75.0	0.7155	0.4162	1.9824	0.5928	1.3456	2.5555
96.0	0.7228	0.5196	2.0612	0.6407	1.5691	0.5699
110.0	0.7265	0.3002	2.3034	0.7073	0.7658	0.3424
122.0	0.7633	0.1529	0.7379	0.7349	0.4372	0.9718
140.0	0.8039	0.0671	40.9764	0.7662	0.1526	1.4866

	FOR GENERATED 15 TRACKS			FOR GENERATED 20 TRACKS		
ANGLE	SLOPE	INTERCEPT	χ^2/ν	SLOPE	INTERCEPT	χ^2/ν
40.0	0.4551	0.3841	0.2454	0.3336	0.5996	3.5915
52.0	0.4605	0.8861	1.7833	0.4104	1.2924	1.4420
75.0	0.5094	2.3749	0.6033	0.4628	3.4788	0.6569
96.0	0.5957	2.7360	1.5574	0.5553	4.0807	0.6320
110.0	0.6541	1.4354	2.9955	0.6531	2.1115	1.3793
122.0	0.7331	0.7428	1.3010	0.7213	1.1022	1.1424
140.0	0.8027	0.2573	4.2169	0.8144	0.3515	1.9243

	FOR GENERATED 25 TRACKS			FOR GENERATED 30 TRACKS		
ANGLE	SLOPE	INTERCEPT	χ^2/ν	SLOPE	INTERCEPT	χ^2/ν
40.0	0.3017	0.7441	0.0028	0.2546	0.8890	0.0502
52.0	0.3528	1.7071	3.4312	0.2008	2.1372	0.2117
75.0	0.3650	4.6611	3.7191	0.2599	5.9013	1.0491
96.0	0.5131	5.5558	0.8450	0.3716	7.2426	2.2096
110.0	0.6501	2.8963	0.6675	0.8149	3.4044	1.1376
122.0	0.6759	1.5569	0.1879	0.6466	2.0232	1.0784
140.0	0.7912	0.5318	0.1645	0.7937	0.6359	0.3645

	FOR GENERATED 35 TRACKS			FOR GENERATED 40 TRACKS		
ANGLE	SLOPE	INTERCEPT	χ^2/ν	SLOPE	INTERCEPT	χ^2/ν
40.0	0.3687	1.0600	0.0000	0.4359	1.2099	1.1984
52.0	0.4404	2.4588	0.6057	0.1462	2.7526	0.5630
75.0	0.4161	6.8882	3.1416	0.1574	8.2374	0.3038
96.0	0.4209	8.5149	0.7206	0.5513	9.7896	0.7922
110.0	0.6428	4.4683	1.1364	0.5942	5.4804	1.5207
122.0	0.6847	2.3337	0.1822	0.7468	2.6684	0.9113
140.0	0.8231	0.7702	1.5062	0.8325	0.9894	0.4217

TABLE A.2 - continued
Slope and Intercept for Efficiency Corrections

Monte Carlo with a Vertex at Z=-99 cm

	FOR GENERATED 5 TRACKS			FOR GENERATED 10 TRACKS		
ANGLE	SLOPE	INTERCEPT	χ^2/ν	SLOPE	INTERCEPT	χ^2/ν
36.0	0.6996	0.0680	0.6714	0.7233	0.1757	1.9467
45.0	0.6559	0.1220	1.4409	0.6019	0.3129	0.1111
65.0	0.7825	0.2737	0.9200	0.7609	0.7896	0.7601
90.0	0.8004	0.5348	0.9486	0.7544	1.5644	2.0552
102.0	0.7724	0.2386	2.8306	0.7494	0.6022	1.0540
116.0	0.8460	0.1385	0.7261	0.8891	0.3327	3.5004
135.0	0.8781	0.0367	1.0379	0.8792	0.0815	0.4162

	FOR GENERATED 15 TRACKS			FOR GENERATED 20 TRACKS		
ANGLE	SLOPE	INTERCEPT	χ^2/ν	SLOPE	INTERCEPT	χ^2/ν
36.0	0.6212	0.3483	1.6596	0.5155	0.5391	2.0105
45.0	0.5433	0.5926	1.5290	0.5007	0.8600	0.0277
65.0	0.6824	1.6382	0.7618	0.5705	2.6567	2.0080
90.0	0.7007	2.9457	1.7958	0.6486	4.7340	0.4265
102.0	0.7335	1.1483	1.6714	0.7189	1.7597	0.2882
116.0	0.8340	0.6239	1.0382	0.8345	0.9650	3.5977
135.0	0.8890	0.1337	0.9573	0.8368	0.2213	1.4268

	FOR GENERATED 25 TRACKS			FOR GENERATED 30 TRACKS		
ANGLE	SLOPE	INTERCEPT	χ^2/ν	SLOPE	INTERCEPT	χ^2/ν
36.0	0.5167	0.7228	0.4803	0.3655	0.9815	0.0103
45.0	0.3477	1.2167	1.3161	0.3208	1.4902	1.6517
65.0	0.4920	3.7196	0.3413	0.4468	4.7503	3.5235
90.0	0.5519	6.8010	0.9660	0.4603	8.9247	1.1724
102.0	0.6264	2.6155	2.7240	0.6785	3.2208	0.6165
116.0	0.8430	1.2893	0.4219	0.8481	1.7010	0.6396
135.0	0.9108	0.2355	0.9907	0.8932	0.3017	1.3757

	FOR GENERATED 35 TRACKS			FOR GENERATED 40 TRACKS		
ANGLE	SLOPE	INTERCEPT	χ^2/ν	SLOPE	INTERCEPT	χ^2/ν
36.0	0.4319	1.1393	1.3724	0.4659	1.2680	0.4233
45.0	0.3834	1.7668	1.2692	0.4269	1.9977	0.2348
65.0	0.3572	5.7991	0.5400	0.2277	6.8521	0.7865
90.0	0.4432	0.8319	1.6585	0.3006	3.2990	1.1910
102.0	0.6132	4.1454	1.0737	0.5807	5.0671	0.5149
116.0	0.7928	2.2738	1.1027	0.7741	2.7874	0.9814
135.0	0.8953	0.3674	1.2503	0.8731	0.5111	0.3398

APPENDIX B

TRACKING EFFICIENCY CALCULATION DETAILS

This appendix details the Monte Carlo calculation of chamber inefficiency, noise, delay line position errors, PWC detection efficiency, and the Monte Carlo resolution smearing. All of these corrections are required to calculate the tracking efficiency.

B.1 CHAMBER INEFFICIENCY

Reconstructed tracks from the data give an estimate of chamber efficiency. In the ideal apparatus, each track crossing a chamber produces one hit; however, chamber inefficiencies produce missing hits. We used a sample of clean, "isolated" tracks from the data to study of the chamber efficiency. Whenever multiple tracks cross a common cell they produce tracks with missing points. The sample of isolated tracks contained completely unique cells to avoids hits lost to multiple tracks crossing the same cell. Selecting events containing a single vertex in the target vessel insured correct event reconstruction. Additionally, all isolated tracks were required to come from the vertex and the events contained no more than two non-vertexed tracks. Table B.1 gives the fraction of the events passing these cuts.

TABLE B.1
Events Providing Isolated Tracks

	Number in Cut	% of total	% of last cut
Total Number (in run 3084-6)	12197	100	100
With 1 vertex	9002	73.8	73.8
Vertex in target	4611	37.8	51.2
With enough tracks in vertex*	3860	31.64	83.7

*All tracks but 2 must vertex

Isolated tracks passed the following restrictions: a delta-X-slope cut, a minimum point cut, and proximity to extra track cut. A cut on delta-X-slope, the X slope difference between a track and its nearest neighbor, removes cells with multiple hits. Chamber 3, containing the cell subtending the largest angle (3.2 cm across and 185 cm from the target), has an delta-X slope range of 0.0173 radians. Tracks neighboring each other with X-slopes differing by less than 0.02 radians failed this cut. Isolated tracks contained at least 5 (out of 8) chamber hits plus the vertex, thereby eliminating accidental tracks. Finally, avoiding the non-vertexed tracks, isolated tracks intersect each chamber at least ±3.2 cm from extra track intersections. Table B.2 reports the fraction of tracks passing these three cuts.

TABLE B.2
Fraction of Isolated Tracks Passing Selections

TRACKS	number	% of total	% of last cut
Total track # (run 3084-6)	176844	100	100
Total from useful events	35980	20.3	Full sample
Cleanly separated	11592	32.2	32.2
With 5 + points	9784	27.2	85.2
With no nearby track	9237	25.7	94.4

Because the tracking algorithm is not perfect, some points actually on the track may not be included. For example, whenever a point lies over 3 sigma from the track, the algorithm excludes it even though the point may be part of the track. Removing algorithm bias from the chamber efficiency estimate, a second set of curves, setting an upper efficiency bound, includes track points and any "missed" points. Any time an isolated track passed through a cell that recorded a hit, the second curve includes this hit as a "missed" point. Additionally, regardless of the cell recording the hit, the upper bound includes all hits within 0.2 cm of a track. This chamber efficiency estimate has a large enough road size to contain all possible "missed" points.

An *X*-slope distribution for each chamber comes from the isolated tracks, one entry for each hit along the track. Figure 2.4 displays the ratios resulting from the chamber *X*-slope distribution divided by the total *X*-slope distribution of selected isolated tracks, giving the chamber efficiency as a function of slope. The dotted lines in figure 2.4 include the "missed" points. The true efficiency lies between the two curves.

B.2 CHAMBER NOISE

Two methods were used to estimate the chamber noise. The first, an algorithm-dependent estimate, assumes the unused hits after track reconstruction, result from chamber noise. A second, less algorithm--dependent estimate uses the physically impossible TDC time values.

Track reconstruction utilizes most of the chamber points, however a few extra points remain. Assuming a noise free PWC (valid since the PWC, when out of time, recorded almost no accidental hits) then the unused PWC hits come from tracking inefficiencies. Knowing the number of tracking failures (the extra PWC hits), we calculate the number of noise hits in the other chambers by taking the total of number of extra hits in each chamber minus the number of tracking failures. The percent noise per cell is the mean number of noise hits divided by the number of cells in the chamber. Using events with the reconstructed primary vertex in the target and no more than four non-vertexed tracks, table B.3 gives the percent noise for the chambers based on the track reconstruction. (The numbers in the table exclude points in the gap region of the chambers).

TABLE B.3
Percent Noise/Cell by Track Reconstruction
$1H_2$ DATA (Mean Values in each Chamber)

Chamber	Total Hits	Hits Not Used	% Extra	% Noise	% Noise per Cell
1	11.25	1.351	12.00	0.00	0.00
2	9.08	1.205	13.27	1.27	0.29
3	7.02	1.059	15.09	3.09	0.52
4	12.01	3.130	26.06	14.06	3.67
5	12.33	2.933	23.79	11.79	3.03
6	10.23	2.258	22.07	10.07	2.15
7	9.42	2.044	21.69	9.69	1.83
11	15.38	9.141	59.42	47.42	9.11

Two comments are necessary regarding this calculation. A high noise level in chamber 11 was observed during the run, and is reflected in the calculation here; however this estimation may be an over estimation of the actual noise in the chamber. The two assumptions made in this calculation tend to over estimate the noise.

Recalling the discussion of §2.2.2, our assumption that the PWC detects every track under estimates the total number of tracks. Undetected tracks appear as noise in the other chambers. Secondly, not all the chambers may observe the same number of charged particles. Chamber 11 may appear the noisest in this calculation since it is further from the collision point. The particles have a larger distance to separate, so this chamber responds better to tightly clustered particles (as might be expected to occur in jets). Further, secondary decays are more likely and particles from the target fragments may interact in the momentum analysis magnet and spill into chamber 11. Finally chamber 11 contains active cells at small center-of-mass angles which are inactive in the other chambers. The high number of charged particles detected in this region of the chamber appear as noise since these hits are impossible to reconstruct into tracks without the additional downstream chambers. The original design of the chamber array with 7 chambers downstream of the magnet would have allowed a better estimate of the noise level based on tracking.

A second method to estimate noise utilizes the chambers as individual detectors. In the chamber cells, impossible drift distances result from out-of-time hits or chamber noise. The algorithm, when creating physical distances, excludes impossible values, however a uniform background of noise may also give physical drift distances -- indistinguishable from actual hits. The recorded noise is a function of the raw TDC time, and short times are more numerous than long times, as seen in Figure B.1. Impossibly short raw times, implying long drift distances for TDC's in the common stop mode, occur in

Figures B.1&2 **1)TDC noise** **2)Delay line Errors**

B.1) Noise Estimate for a TDC; the raw times(solid) include a background of noise(dash).
B.2) The frequency of delay line *Y* position errors increases with input multiplicity. Chamber 3(solid) is less affected than chamber 7(dash) since it has smaller cells.

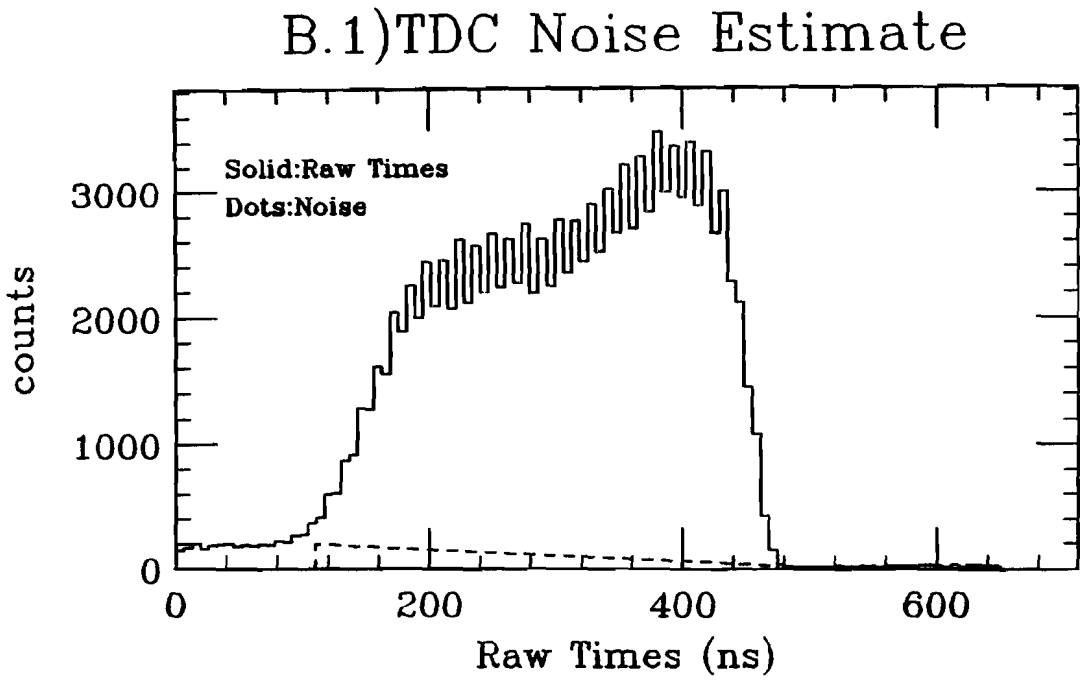

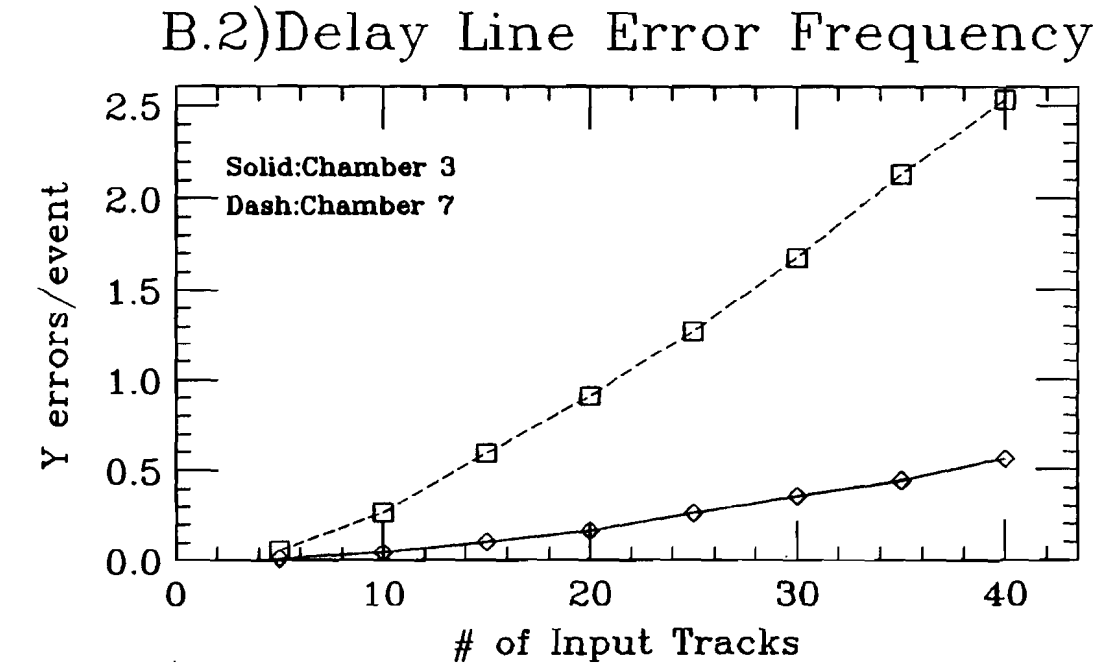

several different ways. For example, short times result when electrons drift across cell boundaries (a long drift distance is correct), when a second interaction occurs after the trigger (the additional electrons start their drift later than expected) or when chamber noise occurs just before readout. Impossibly short drift distances occur when noise in a chamber starts a TDC charging prior to the event trigger or when a previous interaction left electrons in the cell that were not swept away before the current trigger. These sources of noise may also produce physical drift distances. To estimate this effect we approximate the amount of noise in the physical region by assuming that the amount of noise at short raw times decreases linearly to the amount at to long times. If the average number of counts at small (and impossible) times is A and the average at large times is B, then the number of noise counts, N, for the TDC is the area under the trapezoid,

$$N = \frac{1}{2} D (A + B).$$

Where D is number of bins under the useful portion of the distribution. The percent of the total counts that are due to noise is given by the ratio of the noise counts over the total number of physically possible times. To calculate the noise for an entire chamber,

$$\text{Fraction of Chamber Noise} = \frac{\Sigma_i \text{ Noise in TDC}_i}{\Sigma_i \text{ Good TDC}_i \text{ Counts}}.$$

Table B.4 gives the fraction noise for each chamber, for 2 sets of runs. The first set, run numbers 3053-11 thru 3055-5, are for the hydrogen target and an intense beam. The second set, run numbers 3078-5 thru 3082-6, are for the nuclear target with the beam intensity reduced. As expected, the lower beam intensity produces less chamber

noise.

Our Monte Carlo simulated this type of chamber noise by generating a matching distribution of noise hits. It selected a random η from 0.0 to 1.0 and coupled this value with D_{max}, the maximum physical drift time in a cell, and the ratio R = B/A, to generate T, the corresponding drift time of a random noise hit with a matching distribution. The equation for the distribution is:

$$T = \left[\frac{\sqrt{1+\eta(R^2-1)} - 1}{R-1} \right] D_{max}.$$

Values for R, the amount of noise at long times over the amount at short times appear in table B.4 under the column headed "Ratio for M.C.". Calculation of the B/A ratio for a whole chamber is complicated since the individual cells contribute different levels of noise. To include this effect we calculated R for the entire chamber from the sum of the individual ratios of each cell weighted by the number of good drift times in that cell, SUM_i. The sum was then normalized by the total number of good hits in the chamber.

$$R = \text{Ratio for M.C.} = \frac{\sum_i \frac{B_i}{A_i} SUM_i}{\sum_i SUM_i}.$$

The two noise estimates give similar results; the smaller noise estimate for chamber 3 from the estimate based on tracking probably comes from the chamber's inefficiency at small absolute X-slope values (forward center-of-mass angles) observed in appendix B.1. The net effect of noise in the chambers is minimal; even for the worst case there will only be a few extra hits in any chamber due to noise. An

TABLE B.4
Percent Noise/Cell by Raw TDC Noise

Chamber	[High intensity Beam] $^1H_2$ %Noise/Cell	Ratio for M.C.	[Low intensity Beam] Nuclear %Noise/Cell	Ratio for M.C.
2	1.14	4.1689	0.42	6.8563
3	3.12	5.6248	2.46	18.6597
4	1.80	6.5527	1.01	16.6784
5	1.81	6.5599	0.92	16.1983
6	2.00	5.3865	0.89	12.5203
7	1.74	3.5343	0.84	7.8850
11	3.64	7.3251	1.66	10.2567

unmodeled source of noise (accounted for in tracking algorithm) appears as a long series of hits with similar TDC times and is attributed to cross-talk between cells.

B.3 DELAY LINE CHAMBER ERRORS

Normally whenever a track crosses a drift chamber, the chamber records a hit. When several tracks cross the same cell, the hit nearest the sense wire is recorded. The delay line chambers have an added complication because the signal travels up and down the delay line after the avalanche strikes the sense wire. (The delay allows the determination of the hit's Y position). Because of the time lag between avalanche and recording the time, it becomes possible for 2 different hits to combine to give incorrect X and Y locations. The top of the delay line records the following time,

$$\text{Raw Top Time} = T_0 - \frac{L}{V_y} - \left[\frac{d}{V_x} - \frac{Y}{V_y}\right]$$

Where L is the half length of the delay line, V_y is the delay line propagation velocity, V_x is the drift velocity through the gas, Y is the Y of the hit and d is the distance of the hit from the sense wire.

(Recall from §2.2.1.2 that T_0, the maximum drift time in the cell, comes from the TDC's operating in the common stop mode). Similarly the bottom of the delay line records,

$$\text{Bottom Top Time} = T_0 - \frac{L}{V_y} - \left[\frac{d}{V_x} + \frac{Y}{V_y}\right]$$

Erroneous X and Y values result whenever the top and bottom of the delay line record different hits. Using the hardware simulation routine to estimate the magnitude of this effect, figure B.2 shows the increase in number of errors per event with the increase in number of incident tracks; more tracks provide a greater chance for time overlap. The error rate also increases with a larger cell size, explaining why chamber 7, with wider cells, has a higher error rate than chamber 3.

B.4 RESOLUTION SMEARING

To select parameters for the Monte Carlo simulation of the chamber array and the track reconstruction, one might initially assume that the chamber resolution for the Monte Carlo should be the same as that determined for the 1982 data. However the Monte Carlo array of hits reconstruct with a better χ^2/ν than observed in the real data. Decreasing the chamber resolution compensates for this difference and causes the Monte Carlo tracking χ^2/ν to match that observed in the data, see table B.5. Figure B.3 compares the chamber resolution for the hydrogen data with two choices of the σ smear in the Monte Carlo. The resolution is given by a hit position minus the position where the track expects the hit. The amount of smear decreases the resolution, however the FWHM of all the distributions remains similar.

Figure B.3 **Vertex smear for chamber Monte Carlo simulation**

lH_2 Data(solid), M.C. simulation at Z=0, 15 Tracks:σ=1(dot), σ=2(dash) The smear in the Z location of the Monte Carlo tracks result from modeling various chamber and track parameters. Chamber 1 is the PWC. Chambers 2 and 4 are drift chambers. Chamber 3 is a delay line chamber.

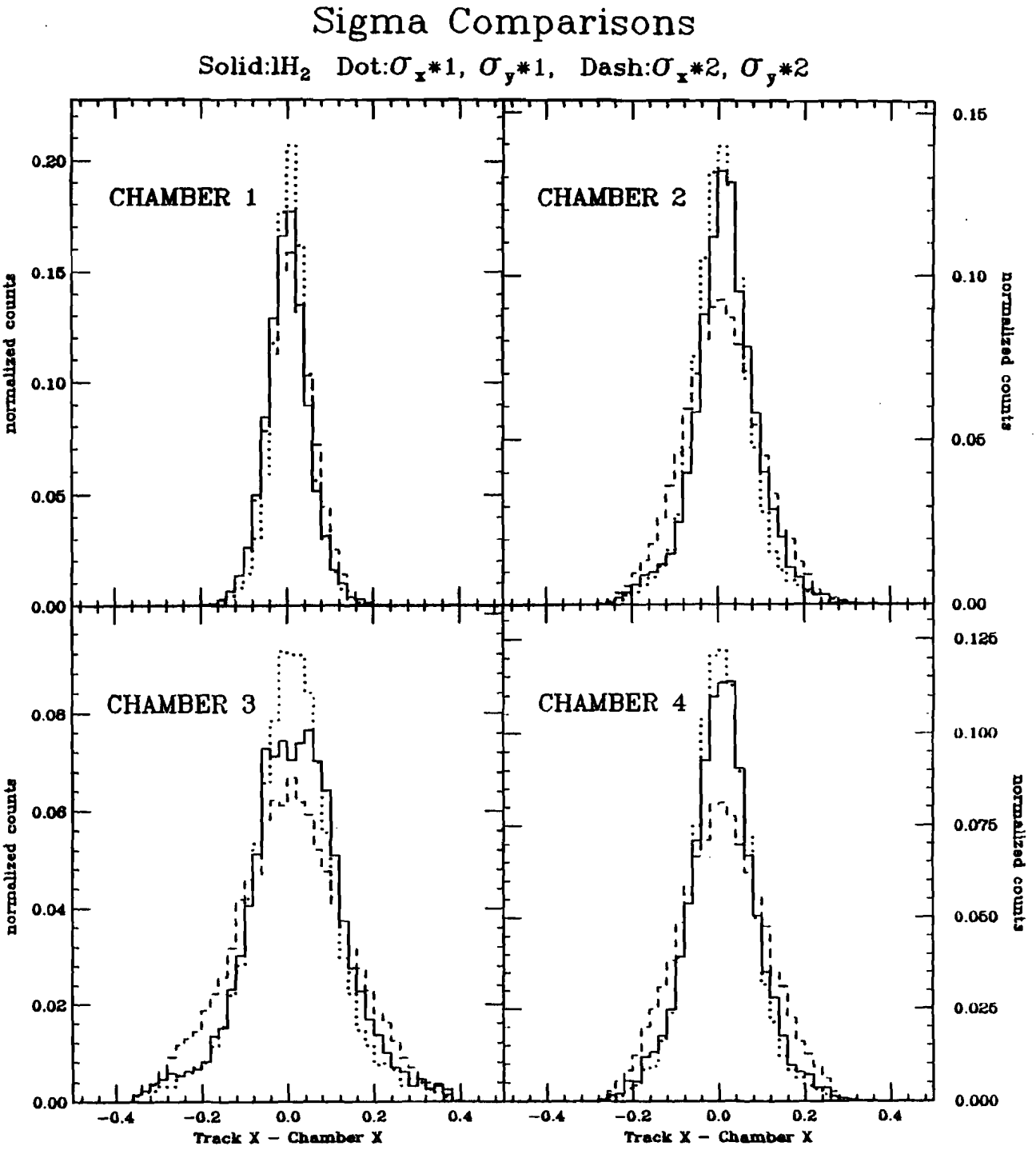

Figure B.3 Cont. **Vertex smear for Chamber Monte Carlo Simulation**

$^1H_2$ Data(solid), M.C. simulation at Z=0, 15 Tracks:σ=1(dot), σ=2(dash) The smear in the Z location of the Monte Carlo tracks result from modeling various chamber and track parameters. Chambers 5,6 and 11 are drift chambers. Chamber 7 is a delay line chamber.

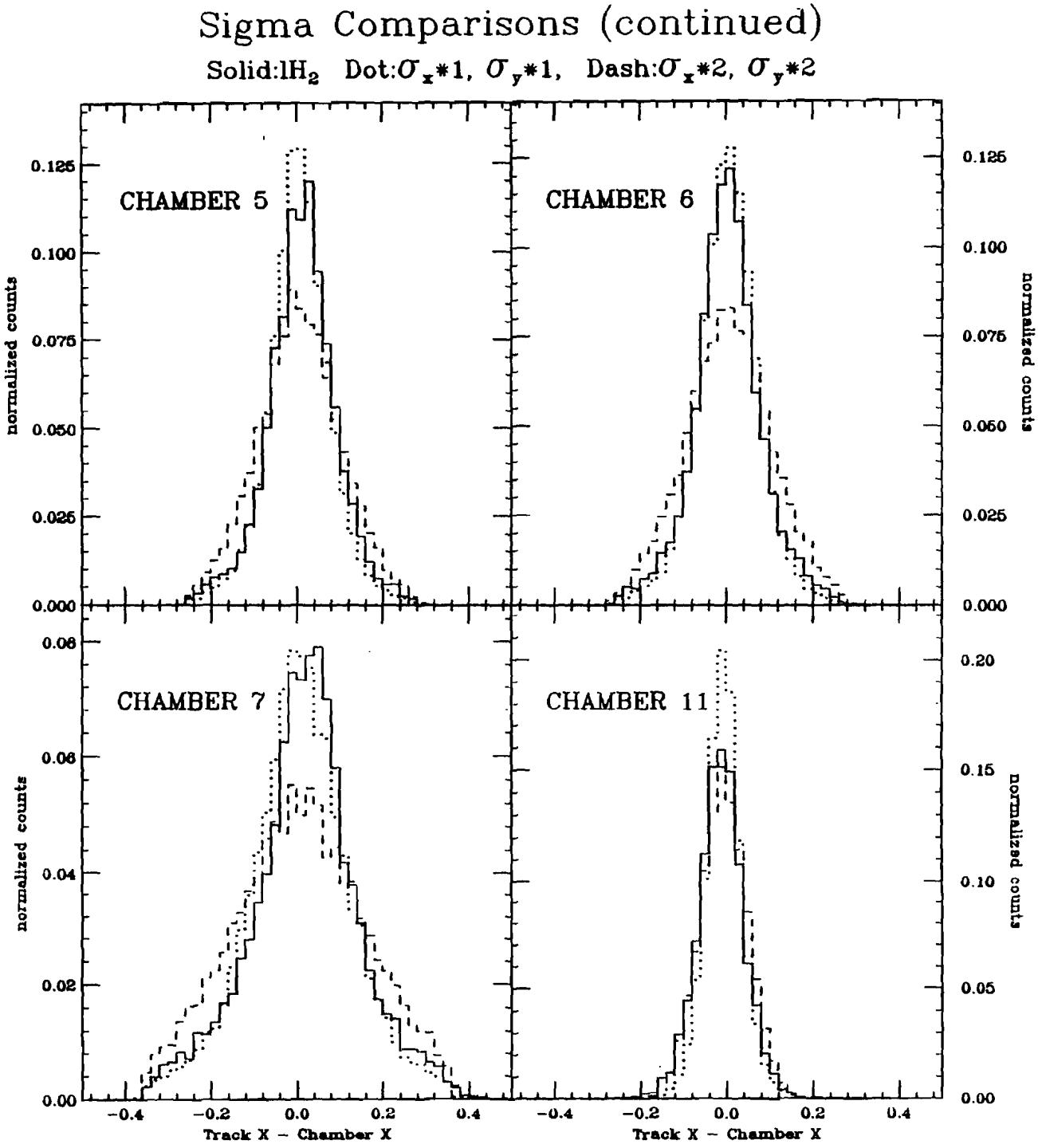

The tracking failures in the data may not come entirely from the deceased resolution. For example the particle flow may fluctuate as a function of θ^*, resulting in a larger charged particle density passing through the chamber at a given angle. The efficiency calculated based on the resolution smearing introduces a uniform uncertainty in the correction rather than an angle-dependant one. Given this limitation, the total number of charged particles measured in the chamber array should only be used to infer details about differences in the multiplicity --rather than as a direct measure of the number of charged particles flowing into the array's active solid-angle.

TABLE B.5
Percent of Tracks Failing Quality Cuts

Input Type	No Y info	Big Y χ^2/ν	Only PWC Y	Not in Vertex	Tracks Lost
Data	6.2	16.5	7.6	7.7	29.5
σ_x*1.0 & σ_y*1.0	3.92	7.61	13.4	2.09	22.0
σ_x*1.5 & σ_y*1.5	4.75	8.49	14.6	3.11	24.7
σ_x*2.0 & σ_y*2.0	5.23	9.93	14.5	4.02	26.6
σ_x*2.5 & σ_y*2.5	6.67	11.9	16.4	5.50	31.0

REFERENCES and BIBLIOGRAPHY

[ABR83] V.V. Abramov *et al.*, Journal De Physique C3, 152 (1983). --p+C,Al,Cu,Sn,Pb→$\pi^{\pm}$,$K^{\pm}$,p,$\bar{p}$ @Serpukhov

[ABR84] V.V. Abramov *et al.*, Z. Phys. C 24, 205 (1984). --p+p,d,C,Al,Cu,Sn,Pb→$\pi^{\pm}$,$K^{\pm}$,p,$\bar{p}$ @Serpukhov

[ÅKE84] T. Åkesson, *et al.*, preprint CERN-EP/84-56 (1984). --Axial Field Spectrometer Collab., ISR at CERN

[ÅKE85] T. Åkesson, *et al.*, preprint CERN-EP/85-164 (1985). --Axial Field Spectrometer Collab., ISR at CERN

[ÅKE82a] T. Åkesson, *et al.*, Phys. Lett. **B110**, 334 (1982). --Axial Field Spectrometer Collab., ISR at CERN

[ÅKE82b] T. Åkesson, *et al.*, Phys. Lett. **B118**, 185 (1982). --Axial Field Spectrometer Collab., ISR at CERN

[ÅKE82c] T. Åkesson, *et al.*, Phys. Lett. **B119**, 464 (1982). --Axial Field Spectrometer Collab., ISR at CERN

[ALB79a] M.G. Albrow, *et al.*, Physica Scriptia **19**, 99-108 (1979). --ISR at CERN

[ALB79b] M.G. Albrow, *et al.*, Nuclear Physics **B160**, 1-41 (1979). --ISR at CERN

[ALT83] M. Althoff, Report No. DESY 83/130, (unpublished): (1983). --e^+e^- Jets from the TASSO experiment

[ANG87] A.L.S. Angelis, *et al.*, Phys. Lett. **B185**, 213 (1987). --BCMOR at ISR using R110 detector pp,dd,$\alpha\alpha$→jets

[ANT79] D. Antreasyan, *et al.*, Phys. Rev. **D19**, 764 (1979). --Chicago-Princeton at Fermilab p+H_2,D_2,Be,Ti,W→$\pi^{\pm}$,$K^{\pm}$,p,$\bar{p}$

[APP85] J.A. Appel, *et al.*, Phys. Lett. **B165**, 441 (1985). --UA2:Emergence of the Two-Jet dominance.

[ARE82] M.W. Arenton, *et al.*, IEEE Trans. Nucl. Sci **NS-29**, 307 (1982). --E609 Development

[ARE84] M.W. Arenton, *et al.*, Phys. Rev. Lett. **53**,1988 (1984). --E609 at Fermilab

[ARE84b] M.W. Arenton, *et al.*, *Proceedings of the Sante Fe Meeting: First Annual Meeting of the Division of Particles and Fields of the American Physical Society* (World Scientific Publishing C., Singapore, 507 (1984). --E609 at Fermilab

[ARE85] M.W. Arenton, *et al.*, Phys. Rev. **D31**,984 (1985). --E609 at Fermilab

[ARN83a] G. Arnison, *et al.*, preprint CERN-EP/83-118 printed in Phys. Lett. **132B**, 214 (1983). --UA1 at CERN

[ARN83b] G. Arnison, *et al.*, Phys. Lett. **B132**, 223 (1983). --UA1 at CERN

[AUR79] P. Aurenche and F.W. Bopp, Z. Physik **C2**, 145 (1979). --Enhancement of high P_T Baryons via Gluons

[B&B70] J.D. Bjorken and S.J. Brodsky, Phys Rev. **D1**, 1461 (1970). --Jet definition

[BAG83a] P. Bagnaia, *et al.*, preprint CERN-EP/83-94 (1983). --UA2 at CERN

[BAG83b] P. Bagnaia, *et al.*, preprint CERN-EP/83-135 (1983). --International Europhysics Conference High Energy Physics, 20-27 July 1983, Brighton (UK)

[BAG84a] P. Bagnaia, *et al.*, Phys. Lett. **B144**, 283 (1984). --UA2 Jet production properties

[BAG84b] P. Bagnaia, *et al.*, Phys. Lett. **B144**, 291 (1984). --UA2 Jet fragmentation properties

[BAR66] M. Bardadin-Otwinowska, *et al.*, Phys. Lett. 21, 351 (1966). --e^+e^- Physics

[BEC76] U. Becker, *et al.*, Phys. Rev. Lett. 27, 1731 (1976). --AGS p-Be,Ti,W+π,K,p+X (α>1.0)

[BER76] G. Berlad, *et al.*, Phys. Rev. **D13**, 161 (1976). --Enhancement from nucleon tubes

[BJO73] J.D. Bjorken, Phys. Rev. **D8**, 4098 (1973). --Theory postulating Jets from high P_T collisions

[BRA79] R. Brandelik, *et al.*, Phys. Lett. **B86**, 243 (1979). --TASSO Collaboration.

[BRA80] R. Brandelik, *et al.*, Phys. Lett. **B89**, 418 (1980). --TASSO Collaboration.

[BROD83] H. Brody, *et al.*, Phys. Rev. **D28**, 2334 (1983). --Wounded-nucleon model fails for high E_T pA

[BROM77] C. Bromberg, *et al.*, Phys. Rev. Lett. **38**, 1447 (1977). --E260 at Fermilab p-Be→jet

[BROM78] C. Bromberg, *et al.*, Nuc. Phys. **B134**, 189 (1978). --E260 at Fermilab p-Be→jet

[BROM79a] C. Bromberg, *et al.*, Phys. Rev. Lett. **42**, 1202 (1979). --E260 at Fermilab p,$\pi\pm$-p,Al→jet

[BROM79b] C. Bromberg, *et al.*, Phys. Rev. Lett. **43**, 561 (1979). --E260 at Fermilab p,$\pi\pm$-p→π,K,p+X

[BROM79c] C. Bromberg, *et al.*, Phys. Rev. Lett. **43**, 565 (1979). --E260 at Fermilab $\pi^{\pm}$,$K^{\pm}$,p,$\bar{p}$-p→jet

[BROM80] C. Bromberg, *et al.*, Nuc. Phys. **B171**,38 (1980). --E260 at Fermilab

[BROW82] B. Brown, *et al.*, Phys. Rev. Lett. **49**, 711 (1982). --E557 at Fermilab

[BROW83] B. Brown, *et al.*, Phys. Rev. Lett. **50**, 11 (1983). --E557 at Fermilab

[BUR87] P.N. Burrows, *et al.*, DESY 87/167, 27 (1987). --e^-p Jet reconstruction and properties at HERA

[CAP78] A. Capella & A. Krzywicki, Phys. Rev. **D18**, 3357 (1978). --Enhancement Model by wounded partons

[CHI83] C.B. Chiu, *et al.*, Phys. Rev. **D25**, 2911 (1983). --Low P_T pA dual topological unitarization theory

[CORC78] M.D. Corcoran, *et al.*, Phys. Rev. Lett. **41**, 9 (1978). --E395 at Fermilab

[CORC80a] M.D. Corcoran, *et al.*, Phys. Rev. Lett. 44, 514 (1980). --E395 at Fermilab

[CORC80b] M.D. Corcoran, *et al.*, Phys. Rev. **D21**, 641 (1980). --E395 at Fermilab

[CORC85] M.D. Corcoran, Phys. Rev. **D32**, 592 (1985). --Field/Feynman 4 jet Monte Carlo vs Data

[CORM82] L.R. Cormell, *et al.*, IEEE Trans. Nucl. Sci. **NS-29**, 307 (1982). --E395 at Fermilab

[CORM85] L.R. Cormell, *et al.*, Phys. Lett. **B105**, 322 (1985). --E609 at Fermilab

[CRO73] J.W. Cronin, *et al.*, Phys. Rev. Lett. **31**, 1426 (1973). --Chicago-Princeton high P_T pA experiment

[CRO75] J.W. Cronin, *et al.*, Phys. Rev. **D11**, 3105 (1975). --CP p+Be,Ti,W+$\pi^{\pm}$,$K^{\pm}$,p,$\bar{p}$

[DeM82] C. De Marzo, *et al.*, Phys. Lett. **B112**, 173 (1982). --NA5 at CERN "selected events show ... no jet-like structure"

[DeM84] C. De Marzo, *et al.*, Nucl. Phys. **B234**, 1 (1984). --NA5 at CERN

[DeM84b] C. De Marzo, *et al.*, Phys. Rev **D29**, 636 (1984). --NA5 at CERN

[ECI79] G. Eichmann and F. Steiner, Z. Physik C1, 353 (1979). --e^+e^- quark jets from Hadron-Ball theory

[F&F77] R.D. Feynman, R.P. Field, Phys. Rev. **D15**, 2590 (1977). --Field/Feynman 4 jet Monte Carlo

[F&F78] R.D. Feynman, R.P. Field, Nucl. Phys. **B136**, 1 (1978). --Field/Feynman 4 jet Monte Carlo (update)

[FF&F77] R.D. Feynman, R.P. Field, and G.C. Fox, Nucl. Phys. **B128**, 1 (1977). --Field/Feynman 4 jet Monte Carlo

[F&P77] G.J. Feldman and M.L. Perl. Phys. Lett. **C33**, 294 (1977). --Review of e^+e^- annihilations above 2 GeV

[FAB77] C.W. Fabjan, *et al.*, Nuclear Inst. and Methods **141**,61 (1977). --Calorimeter response to E&M/Hadronic showers

[FAE82] M.A. Faessler, **Physics in Collisions** Vol 1, ed. Trower and Bellinin, Plenum Press N.Y., 281 (1982). --Review of Hi P_T phenomena in $\alpha\alpha$ and αp collisions

[FAR75] G. Farrar, Phys. Lett. **B56**, 185 (1975). --Extra "Sea" partons in nucleus.

[FEY69] R.P. Feynman, Proceedings of the 3rd Topical Conference on High Energy Collisions of Hadrons, Stony Brook, N.Y., 237 (1969). --Introduction of partons

[FIS75] P.M. Fishbane and J.S. Trefil, Phys. Rev. **D12**, 2113 (1975). --Optical approach to Multiple Scattering Model

[FIS77] P.M. Fishbane, *et al.*, Rev. **D16**, 122 (1977). --Simple multiple scattering Model

[FLE87] J. Fleischman, *Parton-Parton Scattering Determination from Dijet Production in 400 GeV Proton-Proton Collisions* Ph.D. Thesis, University of Pennsylvania (unpublished); (1987). --E609 at Fermilab

[FRE87] S. Fredrikson, *et al.*, Phys. Reports **144**, 187 (1987) --Expt. Review of High-Energy collisions with Nuclei

[FRI83] H.J. Frish, *et al.*, Phys. Rev. **D27**, 1001 (1983). --π^- p→π,K,p,$\bar{p}$ (α>1.0)

[GAR77] D.A. Garbutt, *et al.*, Phys. Lett. **B67**, 355 (1977). --pA→π,K,p (α>1.0)

[GEL64] M. Gell-Mann, Phys. Lett. **8**, 214 (1964). --SU(3) biased on fractional charged quarks

[GLÜ82] M. Glück, E. Hoffman, and E. Reya, Z. Phys. **C13**, 119 (1982). --scale-breaking effects

[GLA58] R.L. Glauber, Lectures in Theoretical Physics, Vol. 1, eds. W.E. Brittin and L.E. Dunham (Interscience, N.Y. 1959) (1958). --Low P_T pA theory based on nuclear screening

[GOM86a] R. Gomez, *et al.*, Second International Workshop on Local Equilibrium in Strong Interaction Physics, Sante Fe, N.M. (1986). --E557 at Fermilab p-p,Be,C,Al,Cu,Pb→jet

[GOM86b] R. Gomez, *et al.*, XXIII International Conference on High Energy Physics, Berkeley, Ca, Abstract No. 1651 (unpub.); (1986). --E557/E672 at Fermilab pp 'small aperture' trigger

[GOM86c] R. Gomez, *et al.*, XXIII International Conference on High Energy Physics, Berkeley, Ca. Abstract No. 1660 (unpub.); (1986). --E557 at Fermilab p-p,Be,C,Al,Cu,Pb→jet

[GOM86d] R. Gomez, *et al.*, XXIII International Conference on High Energy Physics, Berkeley, Ca. Abstract No. 1671 (unpub.); (1986). --E557 at Fermilab

[GOM87] R. Gomez, *et al.*, Phys. Rev. **D35**, 2736 (1987). --E557 at Fermilab p-p,Be,C,Al,Cu,Pb→jet Similar to [GOM86c].

[HAN82] G. Hanson, *et al.*, Phys. Rev. **D26**, 991 (1982). --e^+e^- Mark I at SPEAR

[HOL83] R. Hollebeek, Jets in e^+e^- Annihilation, 11th SLAC Summer Institute on Particle Physics, SLAC-PUB-3242 (1983). --e^+e^- Theory and Experiment Review.

[HSI85] Y.B. Hsiung, *et al.*, Phys. Rev. Lett. 55, 457 (1985). --Fermilab p-Be,Cu,W→π^+,K^+,h^++X (α>1.0)

[JOH83] K.A. Johns, *The Calibration, Response, and Energy Resolution of a Segmented, Sampling Hadron Calorimeter Between 10 and 130 GeV/c*, Master's Thesis, Rice University, (unpublished);
(1983). --Fermilab E609 Detector

[JOH85] K.A. Johns, *A Study of High Transverse Energy Hadron-Hadron Collisions at 400 GeV/c using a QCD Monte-Carlo including Initial and Final State Gluon Bremsstrahlung*, Ph.D. Thesis, Rice University, (unpublished);
(1985). --E609 Data vs. QCD 4 Jet+Gluons Monte Carlo

[JON74] L.W. Jones, *et al.*, Nuclear Inst. and Methods **118**,431
(1974). --Michigan Neutron Calorimeter (E609's Beam Cal)

[KAL79] B.N. Kalinkin,*et al.*, Acta Physica Polonica **B10**, 247
(1979). --Disprove Nuclear Enhancement via "Coherent Tubes"

[KAP78] D.M. Kaplain, *et al.*, Phys. Rev. Lett. **40**, 435
(1978). --Fermilab p+Be,Cu,Pt→$\mu^+ + \mu^-$ +X ($\alpha \simeq 1.0$)

[KAS87] K. Kastella, *et al.*, Phys. Rev. **D36**, 2734
(1987). --A^{α} with hard an *soft* scatters

[KAS89] K. Kastella, *et al.*, Phys. Rev. Lett. **62**, 730
(1989). --A^{α} with low-x gluons

[KIS84] D. Kisielewska, Acta Physica Polonica **B15**, 1111
(1984). --Intranuclear cascade in the target frag. region

[KLU77] L. Kluberg, *et al.*, Phys. Rev. Lett. **38**, 670
(1977). --Chicago-Princeton high P_T pA experiment

[KRZ76] A. Krzywicki, Phys. Rev. **D14**, 152
(1976). --Enhancement by "sea" partons inside nucleus

[KRZ79] A. Krzywicki, *et al.*, Phys. Lett. **B85**, 407
(1979). --Enhancement Model by Gluons with extra E_T

[KUE84] C.E. Kuehn, *Measurement of Leading Charged Particle Charge Ratios in High Transverse Momentum Proton-Proton and Pion-Proton Collisions*, Ph.D. Thesis, University of Wisconsin at Madison, (unpublished);
(1983). --E609 at Fermilab

[KÜH76] J.H. Kühn, Phys. Rev. **D13**, 2948
(1976). --Internal E_T and multiple scattering Model

[LAN75] P.V. Landshoff, J.C. Polkinghorne & D.M. Scott, Phys. Rev. **D12**, 3738
(1975). --Multiple constituent scattering

[LUK77] V.K. Lukyanov, *et al.*, Dubna preprint P2-11049 (1977). --Enhancement Model with Density Fluctuations

[LYK84] G.I. Lykasov, Acta Physica Polonica **B15**, 489 (1984). --Multiple Soft Collision Model for $pA \rightarrow \pi X$

[MAR85] M.R. Marcin, Master's Thesis, Rice University, (unpub.); (1985). --E609 Proton-Nucleon data

[MAR87] M.R. Marcin, E609 Clustering Analysis, (unpublished); (1987). --E609 Towers Clustered into "Particles"

[MAR89] M.R. Marcin, *Study of High Transverse Energy Processes in 400 GeV proton-Nucleus Collisions*, Rice Ph.D., (unpub.); (1989). --E609 at Fermilab

[MCN83] J.A. McNeil, Phys. Rev. D27,292 (1983). --Multiple Scattering analytic approximation

[MIC79] C. Michael, *et al.*, Phys. Lett. **B83**,243 (1979). --Multiple Scattering Model producing leptons

[MIE88] H.E. Miettinen, *et al.*, Phys. Lett. **B207**,222 (1988). --E609 at Fermilab

[MOO85] R.C Moore, *Event Reconstruction Using the Linear Correlation Probability for Fixed Targets at 400 GeV* Master's Thesis, Rice University, (unpublished); (1985). --E609 Tracking

[MOO88] R.C. Moore, Rice Note (1988). --E609 Jet results

[OSB78] L.S. Osborne, *et al.*, Phys. Rev. Lett. **40**, 1624 (1978). --SLAC e-H_2,D_2,Be,C,Cu,Sn$\rightarrow$h+X (α~1.0)

[PAV83] N. Paver, *et al.*, Nuovo Cimento, **A78** 357 (1983). --Multiple scattering with Gluon Enhancement

[PUM75] J. Pumplin and E. Yen, Phys. Rev. **D11**, 1812 (1975). --1st Model using Multiple scattering

[RIO87] M. Riordan, **The Hunting of the Quark**, Touchstone/Pub. ed. by Simon & Schuster Inc., N.Y. (1987)

[SEL79] W.A. Selove, *et al.*, Nuc. Inst. and Meth. **161**, 233 (1979). --E609 Calorimeter

[SHAP84] M. Shapiro, *Inclusive Hadron Production and Two Particle Correlations in --e^+e^- Annihilation at 29 GeV C.o.M. Energy*, Ph.D. Thesis, Lawrence Berkeley Lab., University of California, Berkeley Ca. (unpublished); (1983). --e^+e^- PEP-4 at SLAC

[SHAT84] M.P. Shatz, *A QCD Model of Hadron-Hadron Scattering* Ph.D. Thesis, California Institute of Technology (unpub.); (1984). --Fox,Field,Feynman Monte Carlo

[STE88] C. Stewart, *et al.*, Indiana University, Bloomington, In., (unpublished preprint) (1988). --E557/672 p-p,Be,C,Al,Cu,Pb→jet: A^{α} (α1.6)

[SUK82] U.P Sukhatme and G. Wilk, Phys. Rev. D25, 1978 (1982). --pA& AA Enhancement Model by multiple scattering

[SZW83] R. Szwed, Proceedings from International workshop XI on Gross Properties of Nuclei and Nuclear Excitations, Hirshegg, Austria, CERN-EP/83-50 (1983). --Light Ions and High-Energy Nuclear Physics

[TAK79] F. Takagi, Phys. Rev. Lett. 43, 1296 (1979). --Enhancement Model by multi-quark scattering

[TASSO80] TASSO collaboration, Report No. DESY 79/73, (unpublished); (1980). --e^+e^- TASSO at DESY

[TON85] S.R. Tonse, *Determination of the Atomic Number Dependence of Jet Production from High Transverse Energy pA Collisions at 400 GeV* Master's Thesis, Rice University, (unpub.); (1985). --E609 Fermilab

[TRE80] D. Treleani and G. Wilk, Nuovo Cimento, A60, 201 (1980). --Multiple concurrent & consecutive scattering

[WEB83a] B.R. Webber, XVIII Recontre de Moriond on Proton-Antiproton Collider Physics, La Plange, March 19-25 (1983). --QCD Monte Carlo/Experimental comparison

[WEB83b] B.R. Webber, preprint Ref.TH.3713-CERN (1983). --QCD Monte Carlo/Experimental comparison w/Gluons

[WEB83c] B.R. Webber, Contribution to the XVIII Recontre de Moriond on Proton-Antiproton Collider Physics, La Plange, March 19-25 and CERN TH-3569 (1983). --QCD Monte Carlo with a λ for quarks and gluons

[WOL80] Gunter Wolf, Report No. DESY 80/85, (unpublished) (1980). --e^+e^- Jets from the TASSO experiment

[YOH78] J. K. Yoh, *et al.*, Phys. Rev. Lett. 41, 684 (1978). --Drell-Yan experiment

[YOS79] B.T. Yost , *et al.*, IEEE Trans. Nucl. Sci **NS-26**, 105 (1979). --E395 Development

[ZAL85] K. Zalewski, Ann. Rev. Part. Sci. **35**, 55 (1985). --Review of high energy Hadron-Nucleus collisions

[ZMU80a] V.V. Zmushko, Sov.J. Nucl. Phys. 32(1), 127 (1980). --Detailed Multiple Scattering Model for hadrons

[ZMU80b] V.V. Zmushko, Sov.J. Nucl. Phys. 32(2), 231 (1980). --Multiple Scattering Model patched up for Jets